UNIVERSITY OF BIRMINGHAM

# ADDITIVE MANUFACTURING OF HIGH-STRENGTH ALUMINIUM ALLOYS FOR THERMAL MANAGEMENT APPLICATIONS

By:

FRANCESCO CARERI

A thesis submitted to the University of Birmingham for the degree of

DOCTOR OF PHILOSOPHY

School of Metallurgy and Materials

College of Engineering and Physical Science

University of Birmingham

January 2025

# ABSTRACT

The application of Additive Manufacturing (AM) has demonstrated significant potential in developing complex geometries. With its ability to process a wide range of materials, AM technologies have unlocked unprecedented opportunities for designing high-performance components across several sectors. In aerospace applications, the use of AM, and in particular Laser Powder Bed Fusion (L-PBF), for high-strength Aluminium (Al) alloys offers promising solutions to meet structural and thermal management requirements, including improved efficiency, reduced weight and tailored properties. This doctoral research focuses on advancing L-PBF technologies and optimising high-strength Al alloy materials for innovative thermal management solutions for the aerospace sector.

The study focused initially on optimising L-PBF process parameters for novel thin-walled structures for Heat Exchangers (HXs). Machine Learning (ML) algorithms, such as Neural Networks (NN), were applied to optimise important process parameters, identifying the complex relationships between parameters and properties, and minimising time-intensive experimental campaigns. The optimised parameters enabled the successful manufacture of a novel HX design, demonstrating the feasibility of ML-driven optimisation approaches for aerospace thermal systems. Microstructural and surface quality analyses revealed enhanced accuracy and a defect-free microstructure, mitigating leakage risks and failure during operation. Furthermore, since post-processing is crucial for additively manufactured high-strength Al alloys in aerospace applications, the development of tailored heat treatments (HTs) of high-strength Al alloys was carried out. A novel HT was developed for the high-strength A205 Al alloy, and the obtained microstructure and mechanical properties were compared to the Standard T7 HT and a Commercial HT. A significant reduction in grain size of Rapid HT and Commercial HT compared to the Standard T7 HT was found. The results showed a higher

presence of finer Ω-Al2Cu and ϑ'-Al2Cu precipitates for the Rapid HT than the other HTs, achieving a tensile strength of 465 MPa, compared to the Standard T7 HT (422 MPa) and Commercial HT (449 MPa). Fatigue tests at room temperature and creep tests at 180 °C further confirmed a significant improvement in performance of the newly developed Rapid HT. Finally, mechanical properties were analysed using a strengthening mechanism model to link precipitate formation to observed behaviour.

In addition, a post-processing surface treatment was studied to address the requirements in tribological and corrosion performance of high-strength Al alloys, A205 and AlSi10Mg, in severe environments. In particular, Plasma Electrolytic Oxidation (PEO), was applied to the two investigated alloys produced using L-PBF. The PEO coatings were produced on as-received and polished surfaces. The results demonstrated significant improvements in tribological and corrosion resistance of the coated surface, particularly for pre-treatment surfaces, highlighting the importance of surface preparation for optimising performance.

Finally, an interdisciplinary study was conducted, implementing a novel ML model to optimise the L-PBF process strategy for minimising porosity. A Reinforcement Learning (RL) framework, incorporating thermal modelling principles, accurately identified optimal parameter combinations to reduce defects in the A205 Al alloy. This ML approach reduced reliance on extensive experimental data and simulations. Experimental validation confirmed the effectiveness of the RL approach in improving the reliability of L-PBF processes for high-strength aluminium alloys.

This research demonstrated the potential of combining advanced manufacturing, ML-driven optimisation, and tailored post-processing to enhance the performance of high-strength Al components for aerospace applications, addressing challenges in structural integrity, thermal efficiency, and durability.

**ACKNOWLEDGEMENTS**

First, I would like to express my gratitude to my academic supervisor, Prof Moataz Attallah, for the chance to pursue a PhD in the exciting Additive Manufacturing field. Thanks for your guidance and mentorship. Your insights and expertise have been essential in shaping this research and growing my skills.

I am equally grateful to my industrial supervisor, Dr Raja Khan, for his practical insights and support, which provided me with a unique perspective that bridged the gap between academia and industry.

Also, this PhD would not have been feasible without the funds provided by the Centre for Doctoral Training (CDT) in Topological Design at the University of Birmingham and the National Structural Integrity Research Centre (NSIRC) at TWI Ltd, hence thanks for providing me with this opportunity.

I would also to extend my sincerest thanks to my colleagues at AMPLab, the School of Metallurgy and Materials, and my CDT cohort group for the constructive discussions and insights which have made this journey not only productive but also enjoyable.

Last but not least, I would like to express my deep gratitude to my family, who have always supported me in every choice I have ever made. I'm also heartfelt thanks to my wife, Elena, who began this journey as my girlfriend and has been my unwavering source of love, strength, and support throughout this challenging journey. Your encouragement and patience have been my anchor, and I am endlessly grateful for your belief in me.

# TABLE OF CONTENTS

# LIST OF FIGURES

# LIST OF TABLES

# LIST OF ABBREVIATIONS

| | |
|---|---|
| AI | Artificial Intelligence |
| AM | Additive Manufacturing |
| AMed | Additively Manufactured |
| BB | Bragg-Brentano |
| BC | Beam Compensation |
| BJT | Binder Jetting |
| BSE | Backscatter Electron |
| CAD | Computer-Aided Design |
| CCC | Chromate conversion coatings |
| CD | Contour Distance |
| CEDA | Canny Edge Detection Algorithm |
| CFD | Computational Fluid Dynamics |
| CoF | Coefficient of Friction |
| CTE | Coefficient of Thermal Expansion |
| DED | Direct Energy Deposition |
| DEM | Discrete Element Method |
| DMLS | Direct Metal Laser Sintering |
| DMP | Direct Metal Printing |
| DoE | Design of Experiments |
| $d_p$ | Average Particle Diameter |
| DSC | Differential Scanning Calorimetry |
| EB-PBF | Electron Beam Powder Bed Fusion |
| EBSD | Electron Backscatter Diffraction |
| EDM | Electrical Discharge Machining |
| EDX | X-ray Spectrography |
| EL | Elongation |
| FCC | Face-Centered Cubic |
| FIB | Focused Ion Beam |
| HAADF | Angle Annular Dark-Field |
| HIP | Hot Isostatic Pressing |
| $h_s$ | Hatch Spacing |
| HT | Heat Treatment |
| HX | Heat Exchanger |
| ICP | Inductively Coupled Plasma |
| KP | Keyhole Pore |
| LDH | Layered Double Hydroxides |
| LoF | Lack of Fusion |
| L-PBF | Laser Powder Bed Fusion |
| MAO | Micro-Arc Oxidation |

| | |
|---|---|
| MDP | Markov Decision Process |
| ML | Machine Learning |
| MMC | Metal Matrix Composite |
| MSE | Mean Squared Error |
| MS-ST | Multi-Step Solution Heat Treatment |
| MVC | Microvoid Coalescence |
| n.a. | Not Available |
| NN | Neural Network |
| P | Laser Power |
| PBF | Powder Bed Fusion |
| PBF-LB | Powder Bed Fusion Laser Beam |
| PEO | Plasma Electrolytic Oxidation |
| PFZ | Precipitation-free Zone |
| PSD | Particle Size Distribution |
| RBV | Reduced Building Volume |
| RD | Relative Density |
| ReLU | Rectified Linear Unit |
| RL | Reinforcement Learning |
| SE | Secondary Electron |
| SEM | Scanning Electron Microscopy |
| SL | Sheet Lamination |
| SLA | Stereolithography |
| SLM | Selective Laser Melting |
| SOM | Self-Organizing Map |
| SS-ST | Single-Step Solution Heat Treatment |
| STL | Standard Tessellation Language |
| t | Layer Thickness |
| TCP | Trivalent Chromium Processes |
| TEM | Transmission Electron Microscopy |
| TIP | Thermally-Induced Porosity |
| UAM | Ultrasonic Additive Manufacturing |
| UTS | Ultimate Tensile Strength |
| VED | Volumetric Energy Density |
| VHCF | Very High Cycle Fatigue |
| Vp | Volume Fraction |
| Vs | Scan Speed |
| XCT | X-ray Computed Tomography |
| XRD | X-Ray Diffraction |
| YS | Yield Strength |
| $\lambda$ | Inter-particle Distance |

# List of Publications and Presentations

The following publications and conference presentations are a result of the investigations carried out during the fulfilment of the PhD research and parallelly conducted collaborations.

Scientific Publications

- **Francesco Careri**, Raja H. U. Khan, Catherine Todd, Moataz M. Attallah (2023): "Additive Manufacturing of Heat Exchangers in Aerospace Applications: A Review", Applied Thermal Engineering, 121387. https://doi.org/10.1016/j.applthermaleng.2023.121387.
- **Francesco Careri**, Alessandro Sergi, Pavel Shashkov, Raja HU Khan, Moataz M Attallah (2024): "Plasma electrolytic oxidation (PEO) as surface treatment for high strength Al alloys produced by L-PBF: Microstructure, performance, and effect of substrate surface roughness", Surface and Coatings Technology, 131122. https://doi.org/10.1016/j.surfcoat.2024.131122.
- **Francesco Careri**, Raja HU Khan, Talal Alshammari, Moataz M Attallah (2024): "Development of a Novel Heat Treatment in L-PBF fabricated High Strength A205 Al Alloy: Impact on Microstructure-Mechanical Properties, Materials Science and Engineering: A, 2025, 148278. https://doi.org/10.1016/j.msea.2025.148278.
- **Francesco Careri**, Leonardo Stella, Raja HU Khan, Moataz M Attallah (2024): "Application of Machine Learning in Additive Manufacturing of a Novel Al Alloy Heat Exchanger", The International Journal of Advanced Manufacturing Technology, 2025. https://doi.org/10.1007/s00170-025-15389-y.

- Michele De Lisi, **Francesco Careri**, Usama M Attia, Khamis Essa (2024): "Effect of different additives and sintering regimes on the optical properties of DLP printed translucent alumina", Ceramics International, Vol. 50, issue 14, pp. 26065-26076. https://doi.org/10.1016/j.ceramint.2024.04.348.
- Alessandro Sergi, Raja HU Khan, **Francesco Careri**, Hugh Hamilton, Martina Meisnar, Advenit Makaya, Moataz M Attallah (2024): "Diffusion bonding of dissimilar materials for space applications via hot isostatic pressing", Materials Letters, Vol. 376, 137260. https://doi.org/10.1016/j.matlet.2024.137260.
- Ahmed M Faizan Mohamed, **Francesco Careri**, Raja HU Khan, Moataz M Attallah, Leonardo Stella (2024): "A novel porosity prediction framework based on reinforcement learning for process parameter optimization in additive manufacturing", Scripta Materialia, Vol. 255, 116377. https://doi.org/10.1016/j.scriptamat.2024.116377.

Conference Presentations

- **ISCMM 2021 International Student Conference in Metallic Materials,** 12th – 13th July 2021, Online. Speaker on the study with the title "Process Parameters Development of Aluminium-TiB2 Composite Alloy processed by L-PBF".
- **TMS 2023 152nd Annual Meeting & Exhibition,** 19th – 23rd March 2023, San Diego, California (USA). Speaker on the study with the title "Development of Post-process Heat Treatments Strategy for an Additively TiB2 reinforced AlCu Alloy".
- **TMS 2024 153nd Annual Meeting & Exhibition**, 3rd – 7th March 2024, Orlando, Florida (USA). Speaker on the study with the title "Development of a Digital Twin for Laser Powder Bed Fusion of A205 Al alloy".

# CHAPTER 1. Introduction

Thermal management systems play a critical role in aerospace applications, ensuring the optimal performance and reliability of onboard systems [1]. Aerospace vehicles are subjected to extreme thermal environments, ranging from the intense heat generated by high-speed flight and propulsion systems to the severe cold of outer space. These conditions necessitate the effective dissipation, insulation, and redistribution of heat to maintain the operational integrity of critical components, such as electronics, batteries, and propulsion systems [1-3].

In modern aerospace engineering, lightweight and efficient thermal management systems are indispensable. The increasing demand for lightweight, high-performance materials in aerospace applications [4] has driven extensive research into the development of advanced manufacturing technologies for metal alloys, such as Additive Manufacturing (AM) [5].

AM refers to several manufacturing technologies capable of producing a three-dimensional object by sequentially adding two-dimensional layers of material upon each other until the completion of the design. Unlike the conventional subtractive manufacturing processes, which produce components by removing material from a substrate to reach the final desired shape, AM does not necessitate tools and eliminates issues correlated to the accessibility during manufacturing operation, leading to freedom in the design and advantages in complexity achievable. The general workflow of AM techniques is shown in Figure 1.1.

The design of the component is created using Computer-Aided Design (CAD) software and then is converted into an STL (Standard Tessellation Language) file, which simplifies the geometry into a series of triangles, making it compatible with 3D printers. The STL file is imported into the machine's software for further preparation and slicing, where depending on the vendor of the AM machine and software, part orientation and placement, scanning strategy and process parameters may be conducted either before machine setup or in the same processing

step. The component is then manufactured and removed from the substrate ensuring it is free from any residual material or debris.

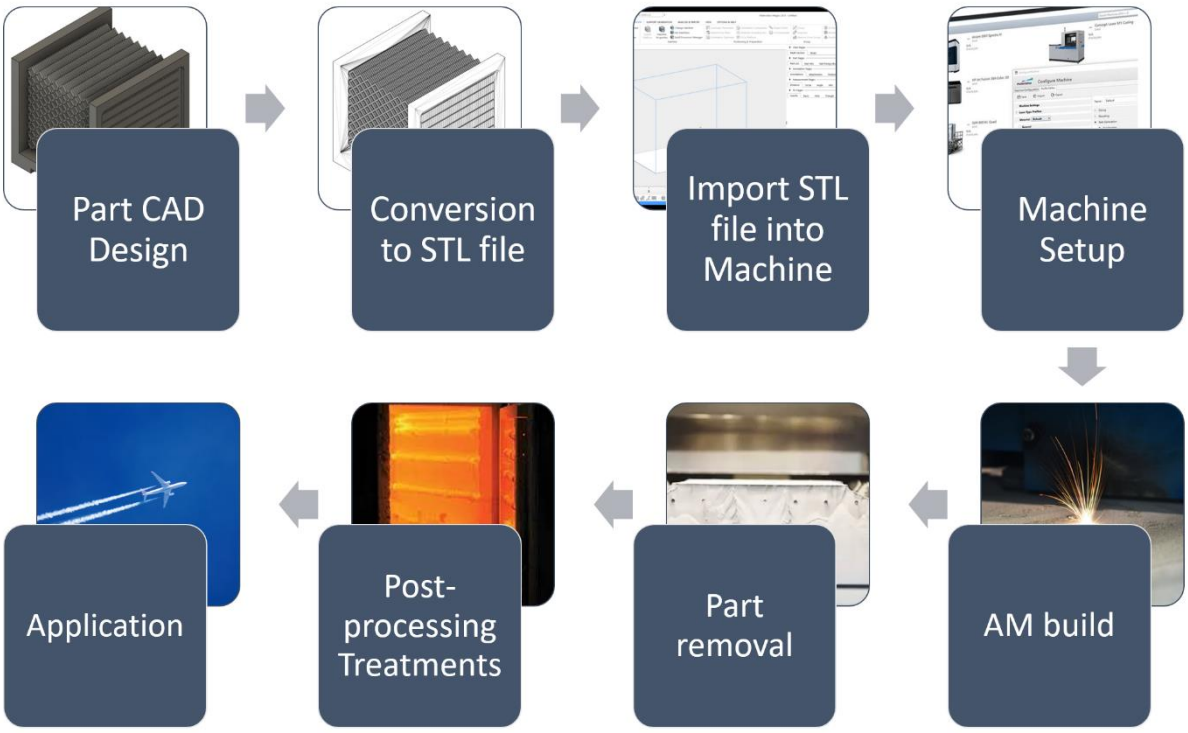


Figure 1.1. Typical flowchart of AM manufacturing steps included in production strategy.

Finally, post-processing treatments may be applied, such as heat treatment, surface finishing, or machining, to enhance the mechanical properties and overall quality before being tested and integrated into the intended application. The building process usually uses feedstock materials in the form of powder or wire, which are either fused or melted with a wide range of energy sources, such as laser or electron beam, either bonded together through different techniques, such as binding agents or high-velocity particle impact.

Laser Powder Bed Fusion (L-PBF) has emerged as one of the most advanced and widely adopted AM technologies, particularly for applications that require high precision, complex geometries, and excellent material properties. The maturity reached by the technology enables the production of advanced designs using lattice structures and topologically optimised components in several aerospace applications. Structural components such as brackets and

joints with optimised designs that reduce weight without compromising strength are manufactured via L-PBF [6, 7]. Turbine blades, nozzles, and combustion chambers for jet engines and rocket systems can be nowadays fabricated using L-PBF [8], leveraging high-performance alloys. In thermal management systems, novel intricate Heat Exchangers (HXs) with integrated cooling channels and complex heat sink designs can be produced by L-PBF to manage the high thermal loads in aerospace applications [9].

Alongside the L-PBF technology, the application of advanced materials [10], such as high-strength Aluminium (Al) alloys, is increasing due to their exceptional thermal conductivity, mechanical strength, and strength-to-weight ratio [11]. The integration of these materials with L-PBF technology unlocks new possibilities for designing compact, high-performance solutions tailored to the stringent requirements of the aerospace field. High-strength Al alloys, with their physical and mechanical properties, are key candidates for use in thermal management systems in aerospace applications. They offer excellent mechanical properties and resistance to environmental degradation while maintaining the lightweight advantage of Al. Using Al which has a low density of approximately 2.7 g/cm$^3$ making it significantly lighter than steel and titanium. The reinforcement through alloying elements, such as Silicon, Copper, and Magnesium, and optimised heat treatments allow for the improvement of several properties [12]. Finally, depending on the reinforcement alloying elements used the thermal and electrical conductivity may slightly decrease, however, remaining close to the high levels of pure Al.

## 1.1 Research Aims and Objectives

Despite its advantages, the successful application of L-PBF to high-strength Al alloys still presents challenges, including increasing reliability and repeatability of the manufacturing process, and optimisation of post-processing treatments. Furthermore, material properties, such as porosity and anisotropy, also affect the performance of additively manufactured components.

Therefore, advancements in areas such as material development, process and post-processing treatment optimisations and in-situ monitoring, are essential to address the challenges and unlock the potential of metal AM in industrial applications.

This research project focuses on advancing knowledge and methodologies for the application of AM technologies for high-strength Al alloys for aerospace applications. In particular, the overall aim of the project was to address existing challenges in the optimisation of process parameters for thin features and post-processing treatments to provide innovative solutions to enhance mechanical performance, surface quality, and microstructural characteristics of advanced materials.

To achieve the stated aim, the following specific objectives have been established:

***Objective 1.*** **To investigate and optimise L-PBF process parameters through ML techniques for the development of reliable and repeatable novel HXs for Aerospace applications.**

A study on the effect of L-PBF process parameters, laser power, scan speed, hatch spacing, beam compensation, and contour distance, on material properties such as density, dimensional and geometrical accuracy, and surface finish, and the application of ML approached for the optimisation of such parameters for the development of a L-PBF manufacturing strategy for novel HXs characterised by complex thin features was carried out. The study provided insight into the role of ML models to predict and optimise process window maps to improve the feasibility and reliability of AM for high-strength Al alloys.

***Objective 2.*** **To analyse the effect of thermal post-processing treatments on material properties and develop a new HT to increase the mechanical properties of A205 Al alloy.**

The evaluation of the influence of several HTs on the microstructure and mechanical behaviour of A205 high-strength Al alloy was carried out. In particular, the development of a new customised HT was performed, and a comparison with currently available HTs was carried out to evaluate surface microstructural features, defect distribution and strengthening phases formation. The study aimed to propose new customised HT solutions for the improvement of the overall mechanical behaviour of A205 Al alloy and provide insight into the effect of different HTs on mechanical performance, including fatigue and creep strength.

***Objective 3.*** **To analyse the effect of surface post-processing treatments on high-strength Al alloys, A205 and AlSi10Mg, to increase tribological and corrosion performance.**

A study of Plasma Electrolytic Oxidation (PEO) as a treatment to change the surface topology of high-strength Al alloy manufactured via L-PBF was carried out. PEO forms a ceramic-like oxide layer. The work focused on the influence of surface condition and type of electrolyte on the generation of oxidised layer and its role in tribological and corrosion performance. The research aims to provide a comprehensive analysis of the effectiveness of PEO coatings in mitigating wear and corrosion, thereby enhancing the operational reliability and durability of A205 and AlSi10Mg alloys for high-performance applications.

***Objective 4.*** **To integrate ML and in particular Reinforcement Learning for the process optimisation and density prediction of high-strength A205 Al alloy.**

The last objective of the research project was an interdisciplinary research focused on the development of new ML approaches to identify the relationships between L-PBF parameters and material properties reducing the experimental campaign usually necessary to achieve this goal. The implementation of an RL model, that does not require any experimental data, was

applied to predict the optimal manufacturing window maps of the high-strength A205 Al alloy for a wide range of process parameters. The aim of the work was to provide insights on the use of advanced ML approaches to reduce time and resource costs for the finding of optimal process parameters for increased manufacturing rate and repeatability of defect-free components produced via AM.

## 1.2 Thesis Structure

This research thesis was structured as below:

In the first Chapter the reader is introduced to the research topic, then focusing on the objectives and goals aimed during the study. Finally, a thesis structure was described.

The second Chapter provides a comprehensive review of the state of the art, focusing on studies related to AM of high-strength Al alloys, and in particular L-PBF. It also examines the application of ML applications in process prediction and monitoring, as well as post-processing treatments such as heat and surface treatments.

The third Chapter outlines the methodology used in the research. The chapter describes the material preparation, process involved, and testing methods, including mechanical, tribological and corrosion tests. Furthermore, the description of advanced characterisation techniques, and microscopy, together with surface 3D reconstruction was discussed.

The fourth Chapter focused on the application of ML techniques, and in particular Computer Vision and Neural Networks as optimisation tools for L-PBF process parameters and their impact on the fabrication of complex thin features for novel HXs in aerospace applications. The ML models were trained using experimental data and used to predict the density and accuracy of the A205 Al alloy of several thin features. Furthermore, the optimised parameters were employed to assess the feasibility and reliability of the L-PBF process as a manufacturing

strategy for complex HXs characterised by hollow-walled lattice structures impossible to manufacture using traditional manufacturing routes.

The fifth Chapter investigates the effect of HTs on the microstructure and mechanical performance of high-strength A205 Al alloy. A novel HT was developed for the specific alloy and a comparison with the currently available HTs in terms of hardness, strength, and microstructural evolution was analysed. The influence on the microstructure was correlated to the mechanical performances, providing insights into the novel HT potential for performance enhancement of the alloy.

The sixth Chapter evaluates the role of Plasma Electrolytic Oxidation (PEO) as surface treatment for improving the tribological and corrosion performance of additively manufactured high-strength Al alloys, A205 and AlSi10Mg. The effect of different surface and PEO conditions on the evolution and properties of the oxidised layer formed was assessed and the benefits achieved through PEO treatment were highlighted.

The seventh Chapter explores the use of the RL model to identify the optimal L-PBF process parameters for the density of a high-strength Al alloy. An RL framework based on mathematical modelling of the L-PBF process was developed and implemented to dynamically explore a 3D space generated by the combination of laser power, scan speed, and hatch spacing with the aim of achieving defect-free parts. The chapter discusses the model's development, validation, and results, demonstrating its potential for reducing the experimental burden on optimisation process control problems.

The eighth and final Chapter summarises the key findings of the research project, presenting a broad conclusion to the thesis. It highlights the major results of each chapter, and therefore the contributions of the research project to the field. The chapter also provides recommendations for future work directions.

# References

[1] M. Williams, A. Muley, J. Bolla, H. Strumpf, Advanced Heat Exchanger Technology for Aerospace Applications, SAE International, 2008.

[2] K. Kasim, A. Muley, M. Stoia, F. Ladeinde, Advanced Heat Transfer Devices for Aerospace Applications, ASME 2017 International Mechanical Engineering Congress and Exposition, 2017.

[3] B. Sundén, J. Fu, Chapter 6 - Aerospace Heat Exchangers, in: B. Sundén, J. Fu (Eds.) Heat Transfer in Aerospace Applications, Academic Press, 2017, pp. 89-115.

[4] B. Cantor, H. Assender, P. Grant, Aerospace materials, CRC Press, 2015.

[5] B. Blakey-Milner, P. Gradl, G. Snedden, M. Brooks, J. Pitot, E. Lopez, M. Leary, F. Berto, A. Du Plessis, Metal additive manufacturing in aerospace: A review, Materials & Design, 209 (2021) 110008.

[6] A. Dagkolu, I. Gokdag, O. Yilmaz, Design and additive manufacturing of a fatigue-critical aerospace part using topology optimization and L-PBF process, Procedia Manufacturing, 54 (2021) 238-243.

[7] P.I. Pradeep, V.A. Kumar, A. Sriranganath, S.K. Singh, A. Sahu, T.S. Kumar, P.R. Narayanan, M. Arumugam, M. Mohan, Characterization and Qualification of LPBF Additively Manufactured AISI-316L Stainless Steel Brackets for Aerospace Application, Transactions of the Indian National Academy of Engineering, 5 (2020) 603-616.

[8] P. Gradl, D.C. Tinker, A. Park, O.R. Mireles, M. Garcia, R. Wilkerson, C. McKinney, Robust Metal Additive Manufacturing Process Selection and Development for Aerospace Components, Journal of Materials Engineering and Performance, 31 (2022) 6013-6044.

[9] F. Careri, R.H. Khan, C. Todd, M.M. Attallah, Additive manufacturing of heat exchangers in aerospace applications: a review, Applied Thermal Engineering, (2023) 121387.

[10] R.R. Boyer, J.D. Cotton, M. Mohaghegh, R.E. Schafrik, Materials considerations for aerospace applications, MRS Bulletin, 40 (2015) 1055-1066.

[11] P. Rambabu, N. Eswara Prasad, V.V. Kutumbarao, R.J.H. Wanhill, Aluminium Alloys for Aerospace Applications, in: N.E. Prasad, R.J.H. Wanhill (Eds.) Aerospace Materials and Material Technologies : Volume 1: Aerospace Materials, Springer Singapore, Singapore, 2017, pp. 29-52.

[12] P.A. Rometsch, Y. Zhu, X. Wu, A. Huang, Review of high-strength aluminium alloys for additive manufacturing by laser powder bed fusion, Materials & Design, 219 (2022) 110779.

# CHAPTER 2. Literature Review

This chapter is part of a scientific review paper that has been published in the Journal 'Applied Thermal Engineering'. The paper's details and co-authors' contributions are outlined below.

**Francesco Careri,** Raja H.U. Khan, Catherine Todd, Moataz M. Attallah, Additive manufacturing of heat exchangers in aerospace applications: a review, Applied Thermal Engineering, Volume 235, 2023, 121387, ISSN 1359-4311, https://doi.org/10.1016/j.applthermaleng.2023.121387.

**Francesco Careri:** Conceptualisation, Methodology, Investigation, Data curation, Visualisation, Writing – original draft, Writing - review and editing.

**Raja H.U. Khan:** Funding acquisition, Supervision, Writing – review and editing.

**Catherine Todd:** Writing – review and editing.

**Moataz M. Attallah:** Conceptualisation, Funding acquisition, Supervision, Writing – review and editing.

The published paper was modified from the published version to include further background. In particular, the following Sections are original, and not included in the published review paper:

Section 2.6 discusses the Application of Machine Learning in Additive Manufacturing.

Section 2.8.1 discusses the influence of Additive Manufacturing, and in particular L-PBF, on the microstructure, anisotropy and texture effect of Al alloys.

## Abstract

The current review is mainly focused on exploring Additive Manufacturing (AM) methods suitable for the fabrication of complex-shaped compact Heat Exchangers (HXs) used in the aerospace industry. The introduction of AM technologies, thanks to the freedom of design and the ability to produce topologically optimised complex parts, aims at the production of high-efficiency HXs. These new HXs are characterised by very thin features and a substantial reduction in the weight of the parts compared to the products conventionally manufactured, maintaining a leak-proof structure and excellent mechanical properties. The current L-PBF systems along with software packages are not yet fully ready for the creation of thin leak-proof features needed for highly efficient complex-shaped compact HXs and most of the studies in the literature are in the initial development stages. This literature review covers the current advanced manufacturing technologies which can be employed to manufacture the new generation of compact HXs, with particular reference to the L-PBF. The advantages and the current challenges of the AM processes are described. Furthermore, the state-of-art of topological optimisation and CFD analysis as design tools to support the production of additively manufactured were critically analysed. Finally, new criteria of how to down-select compact HX materials for AM in the aerospace industrial sector are presented, with particular attention to Al alloys.


## 2.1 Introduction

Heat exchangers (HXs) are indispensable in several applications. In general, a heat exchanger (HX) is used to transfer heat between fluids, usually in motion, to get rid of the excessive heat generated during a process or operation of a component. In particular, in aerospace applications, HXs are essential to ensure the proper functioning of ultra-high bypass ratio turbofan engines.

In particular, air-to-oil HXs are often used to cool the oil that lubricates the internal rotating components of aeroengines. For this, HX is inserted in the front part of the aero-engine, typically on the fan-case, as expressed in Figure 2.1 and must necessarily operate at high temperatures, severe corrosion and wear conditions, mostly for aircraft with longer standstill times in areas with ocean-atmosphere, dynamic vibrations and long periods of operation [1].

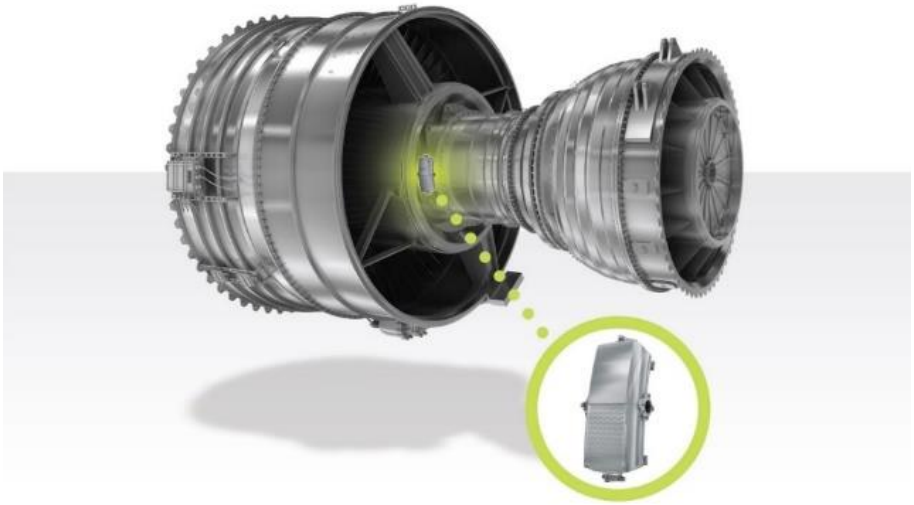

Figure 2.1. Conventional HX for an aero-engine (courtesy of Meggitt Plc.) [2].

Due to the complex heat transfer surfaces within the external case, aerospace HXs are conventionally produced through a long process, by assembling thin plates by brazing or diffusion bonding. Brazing is a joining process that uses a filler metal with a lower melting point than the base materials being joined. The process creates a strong bonding and increases properties such as corrosion resistance but it is not completely suitable for very large components with several joints and requires highly skilled and experienced operators to achieve optimal results. The innovative diffusion bonding, allows a better and easier union between the metallic parts, leading to high-performance compact HXs. In particular, this process consists of applying high temperature and high pressure to bond the plates with no melting or deformation

of the shape. However, the process requires specialised equipment and a long process time. Furthermore, the success of the joining relies on surface preparation and close contact between the surface, restricting the range of application for complex geometries. Over the years, the aerospace industry has achieved great technological improvements and nowadays the components of an HX are made more efficiently in order to minimise waste [3]. However, the development of new and more efficient HXs is still ongoing. It is of primary importance to reduce the final weight of the component, by acting on the size/weight, while the performance in terms of thermal efficiency must reach high levels [4]. Consequently, there are several main objectives during the design and manufacture of an HX that result in challenges from an engineering and production cost point of view.

Today's requirements for the correct manufacture and operational life of all components used in the aerospace field, whether civil or military, together with the most stringent rules on environmental impact have forced the industry in the sector to a new vision of HXs, leading to the modelling of complex systems that very often cannot be achieved through conventional manufacturing techniques due to their limited versatility in modelling geometries with complex features. Furthermore, this new regulation has led to the consideration of new types of manufacturing technologies and, therefore, materials with a high density/strength ratio.

This study proposes to fill the gap in a description of the evolution of HXs and manufacturing techniques necessary for the correct production of the new generation of HXs. In particular, a detailed description of AM techniques, with particular attention to Laser-Powder Bed Fusion, and the advantages and limitations of these new manufacturing technologies are provided. In addition, the wide range of materials and post-processing strategies currently used are also explored with particular interest in advanced Aluminium alloys.

## 2.2 Heat Exchangers (HXs)

Heat Exchangers (HXs) are widely present in all major industrial fields being an essential component of most engineering systems. The design is often a complex balance between maximising the surface area of the part and minimising the pressure drop within the part.

Usually, HXs can be classified in various ways, such as based on transfer mechanism, nature of the process, fluid flow, and compactness. In particular, this review focuses on compact heat exchangers. Compact HXs are characterised by a large amount of heat exchange surface per unit of volume. Maximising heat transfer by minimising the total volume of the component is the basis of the design of a compact HX. These compact HXs have found wide use in the aerospace and aeronautical sectors thanks to the combination of relatively small volumes and consequently low weight and high thermal efficiency [5].

### 2.2.1 Current status, challenges and the future direction of technology

Compact HXs are mainly used in the aviation and automotive industries. In particular, given the stringent requirements of aeronautical and aerospace applications, the most commonly used HXs are of the finned plate type. The particular design is indeed easily achievable by brazing the fins and can be easily designed according to the predefined characteristics of the final application. Cross-flow plate HXs have prevailed in the aerospace industry thanks to their compactness, high performance, and ease of system integration [6].

The scientific community is still exploring new design tools and manufacturing methods to address the existing limitations of these HXs and maximise the thermal efficiency coupled with an extreme compactness and low weight of the components. Many details of an HX are ultimately driven not by the performance requirements, but by manufacturing capability. Understanding the influence of variables such as pitch, fin height, and fin thickness is therefore

essential to repeatedly produce a lightweight, high-performance HX [7]. In the past, numerous studies on the correlation between fin shape and thermal efficiency [8-12] have led to the design of new HXs. Conventionally, the types of fins used are the result of sheet metal forming or bending processes, and the geometries must allow easy joining on the final component. This reduces the possible combinations of geometries to be used for the generation of new and more functional HXs.

Modern industry has now reached a level of technological advancement that guarantees the overcoming of the limits described above. In particular, the combination of two new technologies, topological optimisation in the design phase and AM in the construction phase, has allowed the expansion of the production space of HXs, increasing the possible categories and, with some limitations, potentially helping to improve the performance for aerospace and other applications.

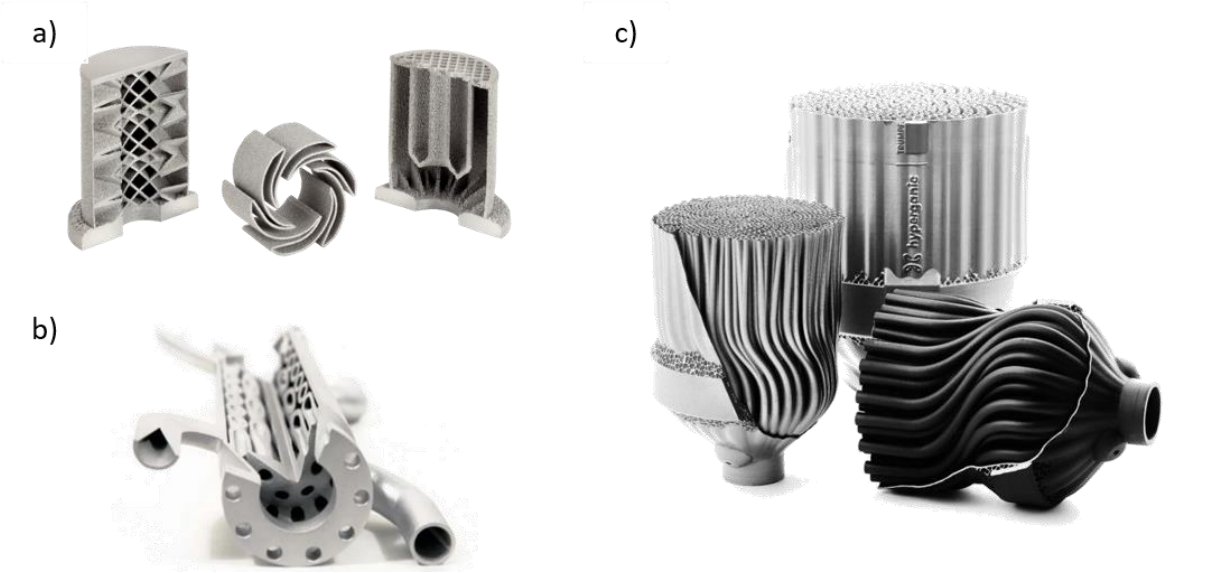


Figure 2.2. Novel HXs produced using optimisation models and AM. a) 3D printed HXs (courtesy of Mott Corporation, Farmington, CT, USA) [13], b) monolithic HXs printed (courtesy of Stratasys Ltd.) [14], c) new generation of heat transfer components (courtesy of Hyperganic Group GmbH) [15].

Topological optimisation is a mathematical technique that uses variable design parameters and constraint conditions for the generation of shapes that guarantee the maximisation or

minimisation of one or more objective functions. In particular, to satisfy the constraint condition, the maximum or minimum value of the objective function has been reached by adjusting the value of the project parameter, which is the achievement of optimisation [16]. This useful tool, coupled with advanced computational modelling software and AM technology, can create HX designs with optimised surfaces and low weight, some examples of which are shown in Figure 2.2.

The increased need to maximise heat dissipation and performance has introduced new visions of HX design. The use of lattice structures, for example, was proven to be a possible method to enhance the heat transfer and consequently the efficiency of an HX [17]. A lattice structure is a structure composed of solid struts, topologically ordered in a periodic arrangement called a cell that is repeated one or more times [18]. The lattice structures guarantee remarkable mechanical resistance resulting in highly efficient load support systems and also provide interesting possibilities for crossflow heat exchange. The heat coming from the hot fluid is locally dissipated through the reticular structure by conduction and convection thanks to a crossflow of a cold fluid that propagates through the passages of the pores. The combination of high thermal conduction and convection and low flow resistance in empty areas of the lattice structure results in highly efficient heat exchange [19-21]. Traditionally, lattice structures are produced using conventional manufacturing techniques, which have many limits in the number of architectures [17]. The introduction of modern AM techniques, on the other hand, has expanded the possible geometries that can be created [22, 23]. Currently, investigations on the use of hollow structures are ongoing. The combination with a lattice structure crystalline structure could significantly increase thermal efficiency. These new hollow-walled HXs, manufactured via AM have great potential for industrial development, but the relationships between heat transfer, losses, and type of structure still need to be properly evaluated [24, 25].

Nevertheless, some limits of lattice structures and thin features manufacturability through AM remain a challenge that scientific research is still trying to face. The limits in minimum and maximum inclination, thickness, and accuracy do not always guarantee the realisation of the intricate and thin geometry of complex architectures.

## 2.3 Additive Manufacturing of HXs

AM is a modern manufacturing process that offers great flexibility and opportunities to create new products with complex geometries. AM is starting to have a great impact in recent decades in industrial sectors where products are difficult to make with traditional manufacturing techniques, and where the waste of raw materials is very high. Furthermore, the introduction of AM has made it possible to implement techniques such as topological optimisation, allowing an increase in performance by reducing the weight of the components. Consequently, the use of these processes for manufacturing components in the aerospace sector has increased the opportunities for innovation and provided new ways of manufacturing HXs.

### 2.3.1 AM technologies to manufacture HXs

According to the standard ISO/ASTM 52900:2021 [26], there are currently 7 (seven) categories of AM processes, and they are described in Table 2.1. Most of these technologies are useful tools for creating prototypes, but not all are suitable for metal materials and the production of reliable components to be put in operation. Four of these technologies can produce metal final parts, and are Direct Energy Deposition (DED), Powder Bed Fusion (PBF), binder jetting (BJT), and sheet lamination (SL). In particular, BJT is a process in which a printhead selectively deposits a liquid binding agent on a thin layer of powder particles (ceramic, metal and composites). Repeated layer by layer, the process can manufacture complex components. The binder is then extracted through a curing and sintering process. Usually, the final density of

parts produced by BJT is lower than with PBF technologies with a large amount of porosity due to the binder removal process [27]. It is commonly used for ceramics HXs due to its complex manufacturability.

DED is a process that concentrates a high energy source to melt metals which are supplied in the form of a powder or wire. The focal point of energy, usually a laser, is also where the material is released. As a result, localised melting occurs, followed by rapid solidification. A nozzle moves to create the shape of the single layer, and the part is built layer by layer. The process is characterised by a high deposition volume capacity per unit of time but also presents some problems concerning residual stresses and high surface roughness [28]. Although DED is able to produce large components, the poor final surface and dimensional accuracy of the products make the process unsuitable for the production of HX characterised by thin features.

Ultrasonic Additive Manufacturing (UAM), is considered a technology that falls into the SL category. This technology uses ultrasonic friction to join thin metal sheets. Then, the layer is worked through subtractive processes to create the desired geometry. The process is repeated layer by layer until the generation of the final component [29]. Through this technology, it is possible to join dissimilar metals and is therefore advantageous in the aerospace sectors where lightweight and performance in harsh environments due to the high altitude and speed, and weather conditions are essential. Consequently, many ongoing studies on the development of UAM for the manufacturing of HXs are trying to demonstrate the technology's great manufacturing capabilities and investigate its limitations [30].

PBF, is by far, the most widely used AM approach for large-scale production of metal parts. Its popularity is largely due to the inherent simplicity of the process coupled with the wide range of materials available. PBF technologies generally use a laser or an electron beam as a source of thermal energy. Nowadays, both sources are considered valid from an industrial production

point of view and the selection of the optimal system is only a function of the technical, economic, and process characteristics of the intended application. Therefore, PBF is the most common HXs manufacturing process [31-34].

Table 2.1. Current definition of categories for AM processes [26].

| **AM Processes Categories** | | |
|---|---|---|
| **BJT** | **Binder Jetting** | Process in which a liquid bonding agent is selectively deposited to join powder materials |
| **DED** | **Directed Energy Deposition** | Process in which focused thermal energy is used to fuse materials by melting as they are being deposited |
| **MEX** | **Material Extrusion** | Process in which material is selectively dispensed through a nozzle or orifice |
| **MJT** | **Material Jetting** | Process in which droplets of feedstock material are selectively deposited |
| **PBF** | **Powder Bed Fusion** | Process in which thermal energy selectively fuses regions of a powder bed |
| **SHL** | **Sheet Lamination** | Process in which sheets of material are bonded to form a part |
| **VPP** | **Vat Photopolymerisation** | Process in which liquid photopolymer in a vat is selectively cured by light-activated polymerisation |

Electron Beam Powder Bed Fusion (EB-PBF) is a process that uses an electron beam as a source of thermal energy and base material in the form of a metal powder. A representation, both real and schematic, is described in Figure 2.3. This electron beam is directed by a series of magnetic lenses on different points to create several pools of fusion at the same time. The use of magnetic lenses makes the EB-PBF incompatible with ferrous metals due to possible magnetic interference. A drawback of the electron beam energy source is the necessary creation of a vacuum within the system prior to the manufacturing process. Creating the vacuum is relatively

time-consuming to respond to processes using a protective gas environment but results in several advantages during manufacturing. The vacuum environment guarantees easy control of the temperatures involved in the process which results in a thermally stable operating environment even at high temperatures [35]. The high level of energy used in the process is able to provide high melting capacity and productivity. The materials used in an EB-PBF process are relatively few and, for the most part, refractory and resistant materials, including niobium, molybdenum, tungsten, zirconium, titanium, their alloys and many others [36]. EB-PBF is therefore particularly beneficial to the aeronautical and aerospace industries, creating new opportunities for both prototyping and low-volume manufacturing. Nevertheless, disadvantages such as the complex physics of the process and the not yet understood relationship between process parameters and repeatability of the characteristics of the parts produced, make this process unstable in the industrial field. Several scientific research has been carried out to give a broader overview of the technology, the mechanical and surface properties downstream of the process, and numerical analyses [37].

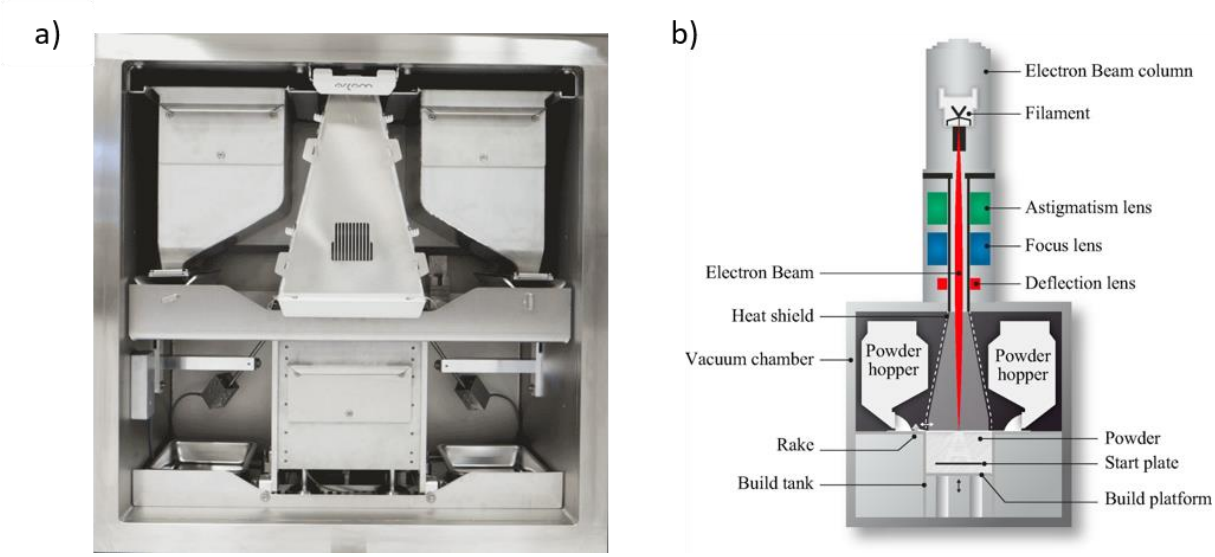


Figure 2.3. EB-PBF process. a) view of the process chamber of a commercial GE Additive Arcam EBM (courtesy of GE Additive) [38] and b) schematic representation of the EB-PBF process [39].

The machines currently on the market are shown in Table 2.2. The current market is seeing an increasing number of commercial and non-commercial machines available. In particular, five manufacturers produce twelve different commercial machine models.

Table 2.2. Commercial EB-PBF machines on the market [40].

| Company | Country | Systems | Build Volume [mm] | Material | EB Power [kW] |
|---|---|---|---|---|---|
| **GE Additive Arcam** | Sweden | A2X | 200 x 200 x 380 | Ti, Ni alloy, Ti aluminide | 3 |
| | | Q10 plus | 200 x 200 x 180 | Ti, Co-Cr, Cu | 3 |
| | | Q20 plus | 350 Φ x 380 | Ti | 3 |
| | | Spectra L | 350 Φ x 430 | Ti | 4.5 |
| | | Spectra H | 250 Φ x 430 | Ti, Ti aluminide, Ti alloy, SS | 6 |
| **Freemelt** | Sweden | ONE | 100 Φ x 100 | Non-magnetic | 0 - 6 |
| **Tianijin Qingyan ZhishuTechnology Co., Ltd (Qbeam)** | China | Lab 200 | 200 x 200 x 240 | Ti alloy, superalloy, Cu alloy, refractory | 3 |
| | | Med 200 | 200 x 200 x 240 | Ti | 3 |
| | | Aero 350 | 350 x 350 x 400 | Ti alloy, Ni-alloy, Cu alloy, Ti aluminide | 3 |
| **Xi'an Sailong Metal Materials Co., Ltd** | China | S200 Production | 200 x 200 x 200 | Ti alloy, Ti-Al, SS, refractory | 3 |
| | | Y150 Biomedical | 150 x 150 x 180 | Ti alloy, Co-Cr, Ta, Ta ally | 3 |
| **Tada Electric (Mitsubishi Electric Group)** | Japan | EZ300 | 250 x 250 x 300 | n.a. | 6 |

Laser Powder Bed fusion (L-PBF) technique, represented in Figure 2.4, consists of depositing through a recoater a layer of powder of defined thickness, contained in the powder chamber, in the build chamber. Subsequently, a laser beam is directed to the areas of interest through a lens mechanism and generates a melt pool, while an inert gas (usually Argon) removes the fumes created by the melting of the material and the excess powder. This step is repeated several times, to create, layer-by-layer, the final solid body [41-43].

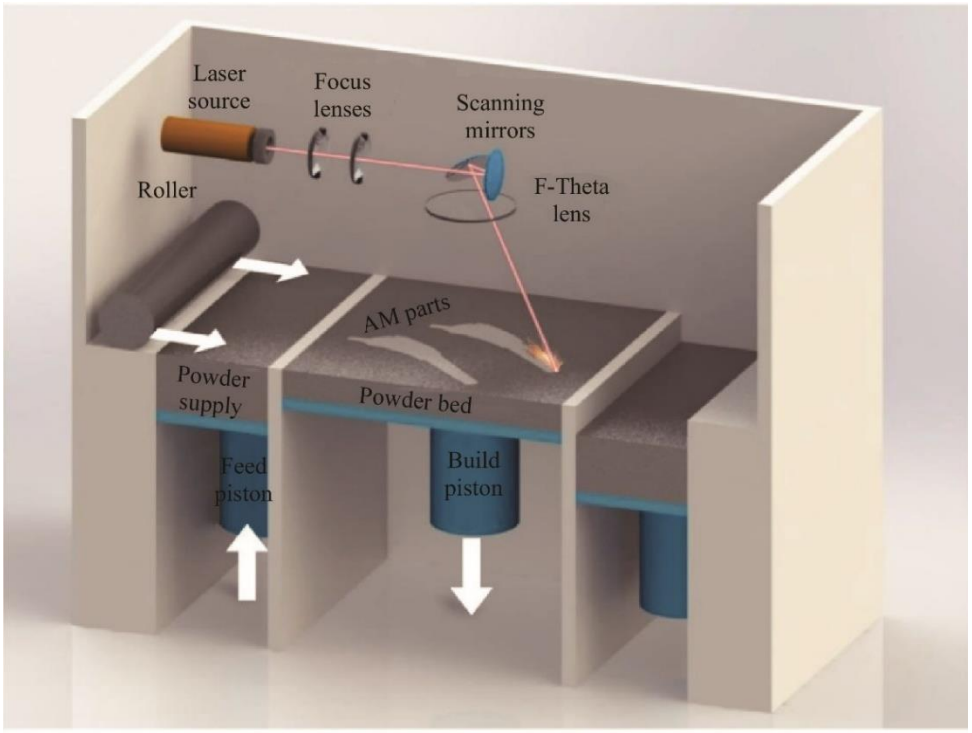


Figure 2.4. Schematic representation of a L-PBF process [44].

A broader overview of the physical process and the influence of process parameters is given in the below sub-section 2.3.2.

### 2.3.2 L-PBF system and process parameters influence

Powder Bed Fusion Laser Beam (PBF-LB), more commonly known as Laser Powder Bed Fusion (L-PBF), also previously called Selective Laser Melting (SLM), is an AM process that uses a laser beam as a heat source to fuse metal powders. The starting point of the process is the creation of a 3D CAD model, subsequently divided numerically into several finished layers, through a software process called slicing. For each sliced layer, a scan pattern is computed, defined as a laser path to trace the component outline and fill sequence. Each layer is then sequentially recreated by fusing sections of the CAD model onto a layer of powder using a laser beam. After creating each layer, the powder is distributed evenly from a recoated and the process is repeated. Layer by layer, the melted powder particles solidify to form a component

[45]. Several features have made this process the most widely used metal AM technology in the world. The build chamber is filled with inert gas, usually argon, in order to prevent oxidation and ensure good quality of the manufactured components. Consequently, the flow of argon plays an important role in the final mechanical and surface properties of the parts. Using a homogeneous layer thickness helps to control and improve the quality of the built part. The use of a recoater facilitates the control of the deposited layer of powder which is uniformly distributed on the printing platform and therefore allows a controlled feeding of the material. Finally, the laser beam allows the use of different powers ranging from a few Watts to kW and allows the correct choice of parameters for the creation of an efficient melt pool of different materials [46, 47]. The high flexibility offered by the L-PBF technology within a wide range of metallic materials allows the manufacturing of components characterised by customised geometries and complex internal features. L-PBF can create complex gradient structures to reduce the necessity to combine several components to manufacture a tailored part. These advantages are behind the strong growth of this technology and have promoted the wide adoption of this process in various industries in recent years [48]. In particular, sectors such as aerospace and automotive look to this technology as the potential development of better and lighter components for use in the operational field. Consequently, the use of the L-PBF process as a means of producing lighter and more efficient HXs is one of the many scientific studies of the past decades. Given the considerable size of a conventional compact HX, it is essential to look for machines that simultaneously have a large printing plate and a large number of lasers that can be used simultaneously. This makes the production process attractive because it guarantees high production volumes in acceptable building times. Furthermore, since HXs have thin section features, it is necessary to consider the minimum thicknesses capable of being

manufactured by the machines. The main manufacturers and systems currently on the market are listed below in Table 2.3.

Table 2.3. Commercial L-PBF systems [48-51].

| Company | Country | Systems | Build Volume [mm] | Fibre Laser Power [W] | Minimum Feature Size [µm] |
|---|---|---|---|---|---|
| **EOS GmbH** | Germany | M 300-4 | 300 x 300 x 400 | 4 x 400 | 100 |
| | | M 400-4 | 400 x 400 x 400 | 4 x 400 | |
| **GE Additive Concept Laser** | Germany | M Line Factory | 500 x 500 x 400 | 4 x 400 or 4 x 1000 | n.a. (laser beam adjustable between100 -500) |
| | | X Line 2000R | 800 x 400 x 500 | 2 x 1000 | |
| **SLM Solution Group AG** | Germany | SLM® 500 | 500 x 280 x 365 | 4 x 400 or 4 x 700 | 150 |
| | | SLM® 800 | 500 x 280 x 850 | 4 x 400 or 4 x 700 | |
| | | NXG XII 600 | 600 x 600 x 600 | 12 x 1000 | |
| **3D Systems, Inc.** | USA | DMP Factory 500 Solution | 500 x 500 x 500 | 3 x 500 | 300 |
| **Renishaw plc.** | UK | RenAM 500Q | 250 x 250 x 350 | 4 x 500 | n.a. |
| **TRUMPF GmbH + Co. KG** | Germany | TruPrint 5000 | 300 Φ x 400 | 3 x 500 | n.a. (laser beam adjustable between150 -500) |
| **VELO3D** | USA | Sapphire XC | 600 Φ x 550 | 8 x 1000 | 150 |
| **Additive Industries** | Netherlands | MetalFABG2 | 420 x 420 x 400 | 4 x 500 | n.a. |
| **PrimaAdditive** | Italy | Print Genius 250 | 258 x 258 x 350 | 2 x 500 | 100 |

The main process parameters characteristic of the L-PBF are the laser power, the scanning speed, the spacing of the hatching, the thickness of the layer, and the scan strategy and are represented in Figure 2.5. These are used to calculate a fundamental process parameter called Volumetric Energy Density (VED) and are described by Equation 2.1 [52].

$$VED = \frac{P}{v \cdot h \cdot t}$$ Equation 2.1

where P is the laser power, v is the scan speed, h is the hatch spacing, and t is the layer thickness, respectively. The optimisation of process parameters is necessary to obtain dense materials and minimise defects. Furthermore, the combination of parameters influences the mechanical properties [53], surface roughness [54-56] and process time of the components additively produced through L-PBF.

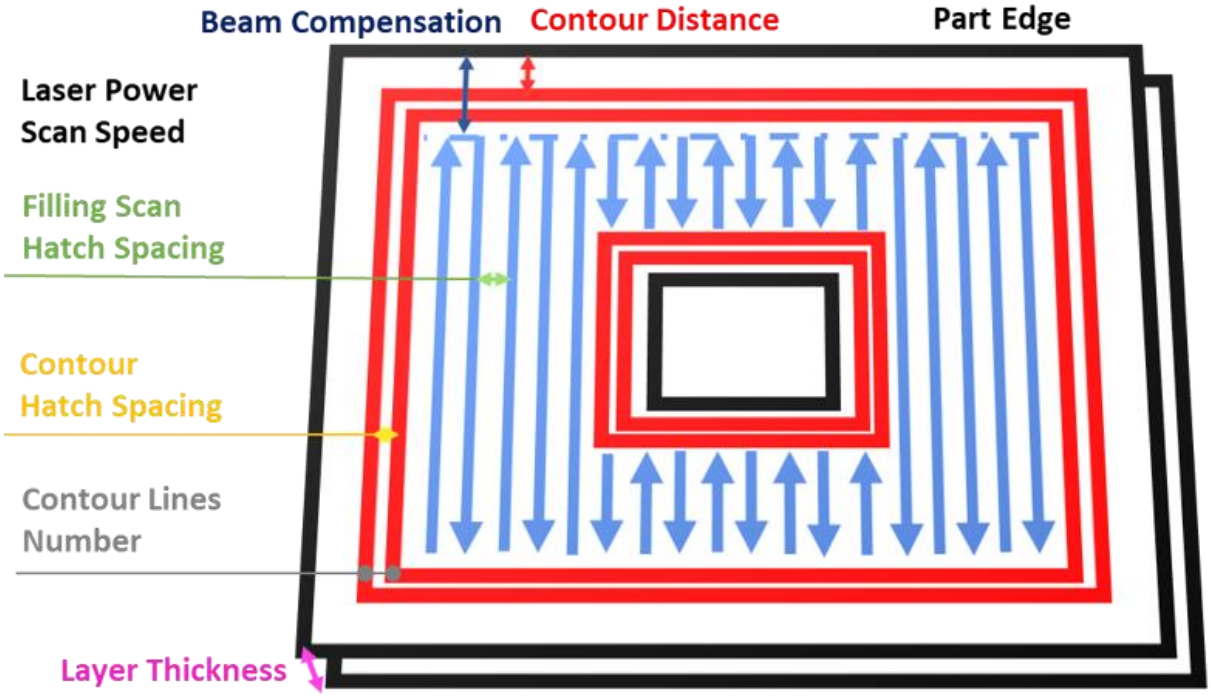


Figure 2.5. Common process parameters for an L-PBF technology.

The effects of process parameters on defects in additive technology have been the subject of study by the scientific community and the relationship can be schematised as in Figure 2.6. Porosity is the most common defect encountered during an L-PBF process and can be distinguished in several configurations. Lack of fusion occurs when insufficient energy is applied, leading to incomplete fusion of the metal powder. Incorrect energy can cause balling phenomena, leading to an incomplete and disconnected laser track, and keyhole phenomena.

Finally, if the energy sent by the system is too high, it is possible to run into problems of evaporation of alloying elements, the absence of which decreases the mechanical properties of the final component.

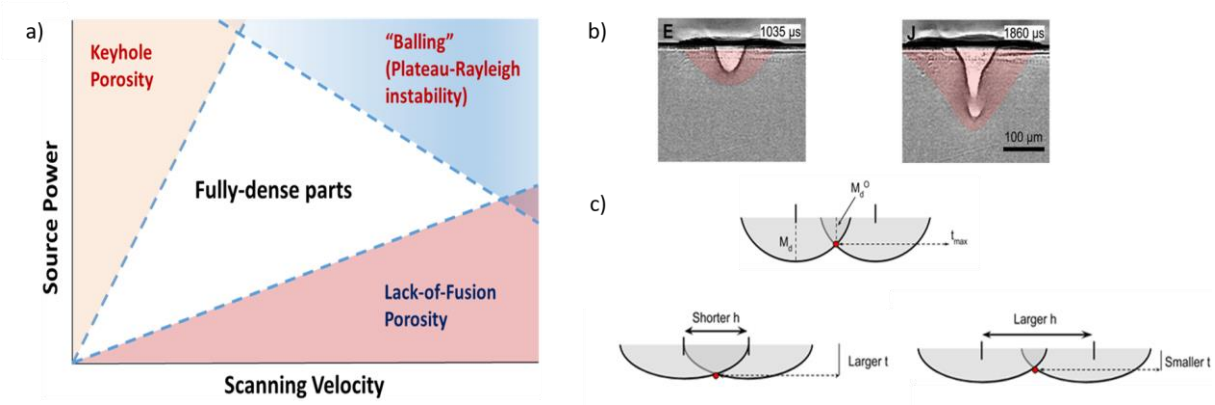


Figure 2.6. Influence of process parameters on porosity defect of L-PBF technology. a) Graphic representation of the influence; b) key-hole defect; c) lack of fusion defect [57].

Other challenges that characterise L-PBF are the distortions of the components caused by the same residues accumulated during the construction of the parts. The residual stresses are due to the high thermal gradients that occur during the process, caused by the localised heating of the material. This heating causes an initial expansion of the layer followed by a subsequent shrinkage on the parts adjacent to the melt pool formation zone and therefore creates a heat-affected zone. During the construction of the subsequent layers, this phenomenon is repeated, and the component accumulates residual stress which could cause the detachment of the part from the substrate and subsequent distortion. Despite the numerous scientific studies focused on understanding the origin of residual stresses and their eventual control, it is still impossible to obtain a stress-free part and the components must be treated with appropriate thermal stress relaxation treatments before being removed from the substrate [57]. The current solutions to the problems described above are summarised in Table 2.4.

Table 2.4. Common solutions to the defects caused by L-PBF process parameters.

| Defect | First Approach | Second Approach |
|---|---|---|
| **Keyhole** | Reducing laser power | Increasing scan speed<br>Remelting |
| **Lack of fusion** | Reduce hatch spacing<br>Reduce layer thickness | Reduce scan speed<br>Increase laser power<br>Remelting |
| **Evaporation** | Reducing laser power<br>Increase scan speed | Increase hatch spacing<br>Increase layer thickness |
| **Residual Stress** | Chess (island) scan strategy<br>Use heated substrate | Process in which thermal energy selectively fuses regions of a powder bed |

The microstructures of additively processed materials are generally described by anisotropic mechanical properties due to the dendritic and non-equiaxial microstructure typical of L-PBF. Further problems caused by the incorrect use of optimised process parameters and the formation of dendritic structures are unwanted segregations and precipitations during a process. The presence of segregation zones of alloying elements and the presence of undesired phases can lead to the failure of a component in the operational phase and therefore result in production waste.

## 2.4 Modeling and simulation for thermal applications

Various tools have been generated and evolved for the solution of technical and engineering problems. In particular, modelling and simulation are used to develop realistic scenarios and predict the behaviour of a component. The modelling and simulation of heat transfer phenomena is a rapidly growing field. It can be used to improve the operation of existing systems, achieve enhanced results, increase efficiency, and optimise processes. The modelling and simulation of heat transfer is a powerful tool that can be used to improve the design and operation of many engineering systems. In the design of heat exchangers, modelling and simulation can be used to optimise the design for maximum efficiency and minimum weight

and volume. This section highlights the state-of-art of heat transfer analysis and optimisation in various HXs applications via a modelling and simulation approach.

### 2.4.1 Current status and future direction

The thermal aspects of heat exchangers are complex and challenging to solve. Therefore, many attempts and efforts are needed to realise lightweight, cost-effective HXs capable of exhibiting enhanced efficiencies and environmental performances. These conventional methods for heat exchanger design and development are time-consuming and expensive. Modelling, and in particular CFD simulation, has emerged as a cost-effective alternative that provides a quick solution in the design phase of HXs. CFD software is versatile and can be used to predict the performance of heat exchangers, identify areas of potential problems, and optimise the design of heat exchangers. Many modelling software is available for thermal analysis and extensive work has been carried out to study and analyse the behaviour of the models for predicting the thermal aspects and optimisation of HXs. One of the most important challenges in CFD simulations of HXs is the accurate prediction of the flow field, typically turbulent and three-dimensional. Another challenge is the accurate prediction of heat transfer rates. The heat transfer rates in an HX are affected by a number of factors, including the flow conditions, the geometry, and the properties of the fluids. The commercially available software uses different methods to solve the equations governing these properties but predicting all the factors is not always achievable and it can lead to errors in the predictions of HX properties [58-60].

The use of Artificial Intelligence (AI) in control systems has become increasingly important in the past two decades. AI-based techniques can be used to improve the performance of control systems, making them more efficient and reliable. They can also be used to develop new types of control systems that are not possible with traditional methods. AI and computer science models, such as machine learning, can be used to investigate the performance of heat

exchangers avoiding experimental and time-consuming computational approaches [61, 62]. These methods are able to make accurate predictions and are relatively fast, making them valuable tools for engineers. A significant amount of research is being conducted on using AI techniques, to predict and control the performance of HXs [63-65]. AI techniques can be used to develop models that can predict the performance of HXs under different operating conditions. This information can then be used to optimise the design of heat exchangers and to improve their efficiency. They can also be used to develop control systems that can automatically adjust the operating conditions of HXs to ensure that they are operating at their optimum performance. The state of the art of modelling and simulations of HXs is constantly evolving. New models and algorithms are constantly being developed and updated in order to achieve more accurate and detailed predictions of the performance of thermal devices and simplify the simulation tools for the flow of fluids and heat transfer in HXs. Furthermore, the use of AI techniques and machine learning to predict and control the performance of heat exchangers is a promising area of research with the potential to improve the design, operation, and efficiency of heat exchangers.

### 2.4.2 Tools for AM HXs thermal aspects optimisation

The introduction of AM techniques has increased the use of tools such as topological optimisation and simulation software to enhance the thermal aspects of the HXs. The result is a structure designed to withstand the loads applied in the operational phase, minimising the constituent material. Topological optimisation design and CFD software were introduced in the structural design phase of high-performance, light and multifunctional structures and are nowadays widely used in sectors such as aerospace, automotive, etc. [66].

Topologically optimised structures are generally characterised by complex geometric configurations. Therefore, conventional processes (e.g. machining, casting) are not suitable for

their manufacture. AM enables the freedom of design for lightweight structures and the manufacturing of highly complex internal geometries in a single step, difficult or impossible to achieve with traditional manufacturing methods. [67, 68]. The work of Saltzman et al. [3] illustrates the potential of AM as a single-step manufacturing process for HXs. The authors successfully replicated a conventional aircraft oil cooler HX design using AM techniques. The findings of this study revealed a high surface roughness in the additively manufactured component but demonstrated excellent accuracy in replicating the complex features of the original design. Through comprehensive experimental analysis, the authors evaluated the impact of the significant surface roughness on the pressure drop and heat transfer performance of the additively manufactured HXs compared to their traditionally manufactured counterparts. Despite the presence of typical additive manufacturing defects such as pores and lack of fusion, the produced HXs completed the experimental tests and exhibited superior performance compared to the conventionally manufactured HXs currently in production. However, using CT analysis, several nucleation of cracks were found that could cause component failure. In subsequent work [3], the same author highlighted how some channels for the transport of the hot fluid (oil) were compromised and/or blocked. Furthermore, the results of the experimental test indicated that the significant surface roughness of AM HXs led to a higher pressure drop when compared to conventionally manufactured HXs. However, it was observed that the heat transfer performance of the additively manufactured HXs improved significantly. Significant limitations still need to be overcome in order to make of AM a reliable manufacturing method for industrial HXs. However, the study by Saltzman et al. exemplifies the feasibility of using AM as a single-step manufacturing process for HXs.

The use of topological optimisation has the potential to significantly impact the design of heat exchangers (HXs), offering opportunities to enhance efficiency and performance in HX

applications beyond what is achievable with traditional manufacturing methods. The main objectives in the optimisation of an HX are the maximisation of the thermal efficiency, and the minimum pressure drops while maintaining compact dimensions and lightness. Furthermore, the attention on the part of the scientific community [28, 58, 60, 69, 70] has increased in recent decades and the development of more powerful finite element and computational fluid dynamics (CFD) software has allowed the introduction of methodologies that, together with topological optimisation, guarantee an overall in the entire decision-making phase of new optimised HXs. The fundamental role of CFD analysis is underscored in the study conducted by Da Silva et al. [71]. The authors employed L-PBF to manufacture a compact HX and subsequently validated the CFD numerical results through an experimental campaign focused on pressure drops and heat transfer. The findings revealed a strong correlation between the numerical and experimental outcomes, emphasising the significance of numerical analysis during the design phase of HXs.

The application of algorithms for the optimisation of the shape and features makes the design process intuitive and helps in the research of optimal solutions [72]. In the study conducted by Moon et al. [73], a shape optimisation genetic algorithm was employed to design a novel HX that could be produced using AM techniques. The genetic algorithm aimed to enhance thermal efficiency by maximising the total surface area while adhering to design constraints. The geometry of the newly developed HX surpassed the limitations of conventional manufacturing methods and was successfully manufactured using L-PBF with an Al alloy. By comparing the additively manufactured HX with a commercial tube-in-tube device as a baseline, the experimental analysis demonstrated a significant improvement in the overall performance of the newly optimised HX. Moreover, when compared to traditional heat exchangers such as shell-and-tube and brazed plate configurations designed for considerably higher heat transfer,

the optimised HX exhibited comparable performance. This notable performance enhancement of the genetically optimised HX can be attributed to its internal architecture, which cannot be achieved using conventional design and manufacturing approaches.

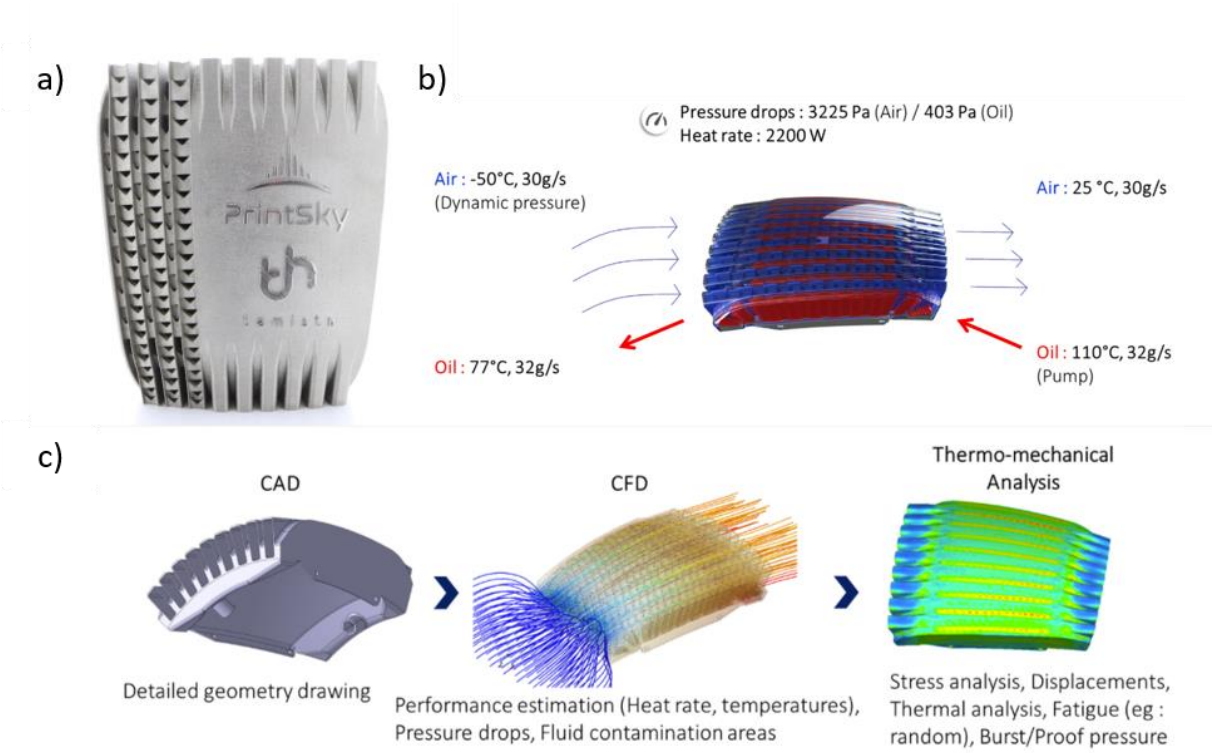


Figure 2.7. Topological optimisation and CFD analysis of novel HXs (courtesy of TEMISTh) [74]. a) additively produced component; b) boundary condition for the CFD analysis; c) phases of CFD numerical approach.

The project developed by three different consortiums, Temisth [75], AddUp [76], and Sogeclair [77], depicted in Figure 2.7, represents another example. The project [74] aimed to study the topological optimisation of a compact air-to-oil HX using CFD models and the thermal efficiency of the component. The material selected was Inconel 718, a heavier and less conductive material than other alloys such as Al alloys. The authors justified the choice by highlighting how the use of this material through AM allows the creation of thin features excluding leaking defects. However, no experimental test was yet performed to assess the real performance of the component during the operation.

Feppon et al. [78] and Dixit et al. [79], in their works, depicted in Figure 2.8, studied the thermal aspects of the generation of HXs using different approaches.

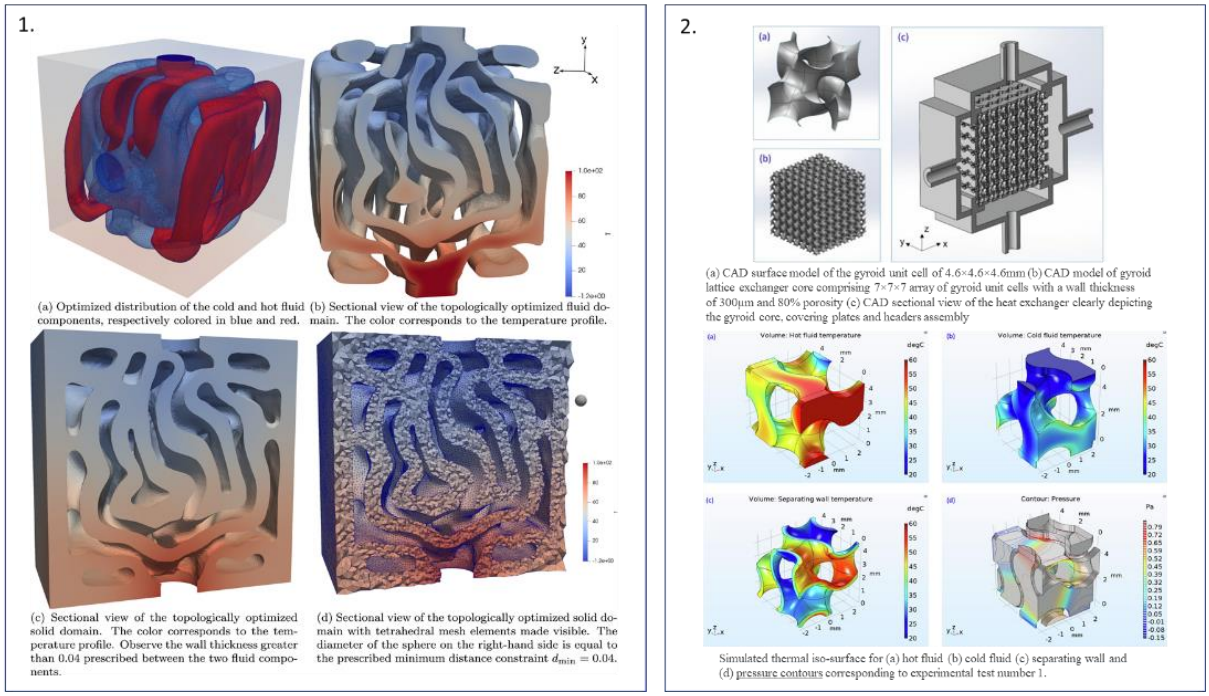


Figure 2.8. Representation of optimisation analysis of thermal aspects for the new generation of optimised HXs. Work of Feppon et al. [78] on the left; Dixit et al. [79] on the right.

The work of Feppon et al. [78] proposed the constitution of a 2D and 3D optimisation model to modify the HX shape incrementing the thermal properties. Based on the correlation between the velocity and pressure of the fluid, together with a convection-diffusion equation for the temperature fields, the new optimisation tool guarantees the optimisation of the geometrical design taking into account constraints such as input and output, thickness and non-penetration of the components. Although the mathematical method used was purely constructed to optimise the shape through the optimisation of only heat transfer, not considering the influence of constraints such as pressure drop, it was successfully applied to different types of HXs. The newly generated designs, represented in Figure 2.8 on the left, are not achievable through conventional manufacturing processes but the AM is able to produce the innovative designs generated by the algorithm. However, also in this case, the authors didn't perform any

validation of the model experimentally, leading to gaps in the real validation of both AM manufacturing reliability and operational performance of the new design.

In the work of Dixit et al. [79], depicted in Figure 2.8 on the right, a new-generation liquid-to-liquid HX using a gyroids lattice structure was manufactured and tested to prove the ability of AM to create complex geometries characterised by thin features. Both experimental and numerical methods were used to analyse and assess the thermal aspects of the HX. The AMed HX was proved to be leak-proof highlighting the feasibility of the AM process to generate thin walls characterised by 300 μm in thickness. Furthermore, the new design showed a high increment in thermal efficiency compared with a conventional HX. The authors emphasised how the increase in thermal properties of the new generation of HXs produced by AM is attributed to the large contact surface density characteristic of the new topological geometries used by modern numerical models.

The available studies and the lack of experimental analysis of the performance of additively manufactured HXs and the comparison with the traditionally manufactured counterpart indicates a non-maturity of the AM method as mass production of HXs. However, ongoing investigations in the fabrication of complex internal features, coupled with the advancements in AM technologies have the potential for achieving a high level of reliability. Specifically, L-PBF, considered the most prominent AM technique, is expected to reach levels of advancements to be embraced in the production of HXs, leading to extensive adoption and standardisation of the technology.

## 2.5 Technological challenges for AM of HXs

L-PBF is a complex process and requires studies to address the limitations in the fabrication of thin elements. In particular, it is very difficult to create a high-quality, defect-free thin wall or generally a thin feature with a thickness of less than 200-300 μm. In addition, conventional

manufacturing methods such as stamping have demonstrated the capability to fabricate plate fins with typical thicknesses ranging from 46 to 200 μm [1]. However, AM has not yet achieved the technical maturity and production quality required for the mass production of these critical attributes necessary for the development of high-performance heat exchangers [80]. Different types of sources are the cause of the problems. Shrinkage can cause cracks and total breakage of a thin part. Furthermore, in the case of thin-section pipes characterised by complex geometry, the viability of the duct could be compromised by the entrapment of powder and/or inclusions of unfused powder attached to the internal walls. This translates into an increase in internal surface roughness and a decrease in the properties of heat exchange. In addition, the limitations in the additive process must be considered when designing a component to be made via an additive process and summarised by Mani et al. [81]. Consequently, preliminary studies for the optimisation of process parameters for the production of thin features to be used in HXs are generally carried out.

### 2.5.1 Manufacturing of thin features for HXs

The L-PBF process does not seem yet suitable for guaranteeing repeatability in the production of thin sections. In particular, the accuracy error increases with the reduction of the thickness dimension of the manufactured component. Significant dimensional variations have been identified between sections in both the horizontal and vertical planes. Furthermore, it has been observed that the distortion of the walls decreases as the thickness of the printed object increases. The work of Wu et al. [82] aimed to generate design guidelines for optimising thin section walls taking into account all possible combinations of L-PBF process parameters. A schematic representation of the work performed by the authors is described in Figure 2.9.

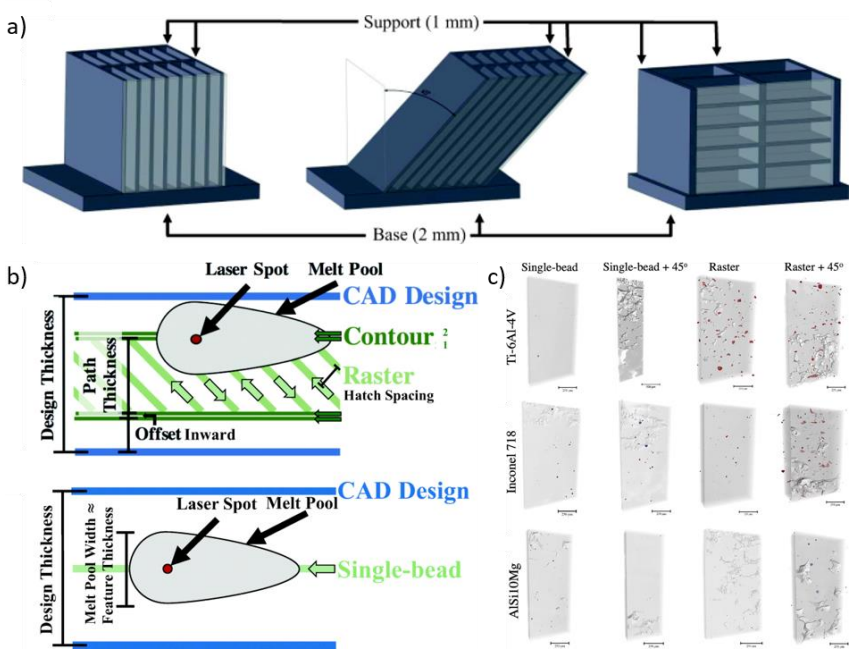


Figure 2.9. Influence of L-PBF process parameters on the generation of thin walls [82]; a) schematic representation of the geometries studied in the work; b) schematic representation of different scan strategies for the AM process; c) porosity calculated through µSCT of different materials for the additively produced thin walls.

Based on the selected parameters, it was observed that a notable lack of fusion occurred primarily when employing a single laser scan approach. The resulting wall thickness of approximately 100 µm was consistent across all three materials investigated in this study, namely Ti6Al4V, Inconel 718, and AlSi10Mg. Furthermore, a maximum inclination angle of 60 degrees was successfully produced for the AlSi10Mg and Ti6Al4V, while only an angle of 45 degrees was able to achieved for the Inconel 718. Two scan strategies, raster and single laser track can be used to produce thin sections, and the correlation between each scan strategy and thermal and shrinkage issues, inclination angle and wall dimension controlling factors was assessed. Porosity was analysed using CT scan technology and a process map for the fabrication of the thin walls correlated to laser power and scan speed was developed. Finally, the surface quality was analysed, discovering a direct relation between the inclination angle and material.

Tan et al. [83] and Hassanin et al. [84] analysed the influence of Contour Distance (CD) and Beam Compensation (BC) on the geometrical accuracy of thin designs such as lattice structure

and micro-channels respectively. In both studies, the authors highlighted the challenges in finding the optimal process parameters to improve simultaneously the dimensional accuracy and general quality of the features. Consequently, the construction of thin features through L-PBF and AM processes, in general, is particularly difficult and still a challenge for the scientific community.

### 2.5.2 Powder removal

Another important challenge for the manufacturing of additively manufactured HXs is the cleaning of complex internal channels. The powder entrapped or sintered in the channels needs to be removed before further post-processing operations and the completion of the manufacturing process. Most of the channels of optimised HXs and/or hollow lattice HXs have no opening or outlet, and therefore powder removal becomes a challenge. There are not many studies in the literature addressing this important issue. Two possible methods underlie the few studies focusing on the problem, design redesign, and the use of equipment and methods after AM of the component.

An example of the first approach is the work of Gutmann et al. [85] in which a reactor for continuous difluoromethylation for the nuclear field has been redesigned to favour the elimination of residual powder due to the AM process. The work is summarised in Figure 2.10a. The component was made of SS316L stainless steel via L-PBF and the geometry included a series of holes in the connection points of the channels to facilitate the powder removal at the end of the process. After cleaning the reactor using the ultrasonic technique, the holes were closed by laser beam welding. Analyses performed on the reactor have confirmed the success of this manufacturing strategy.

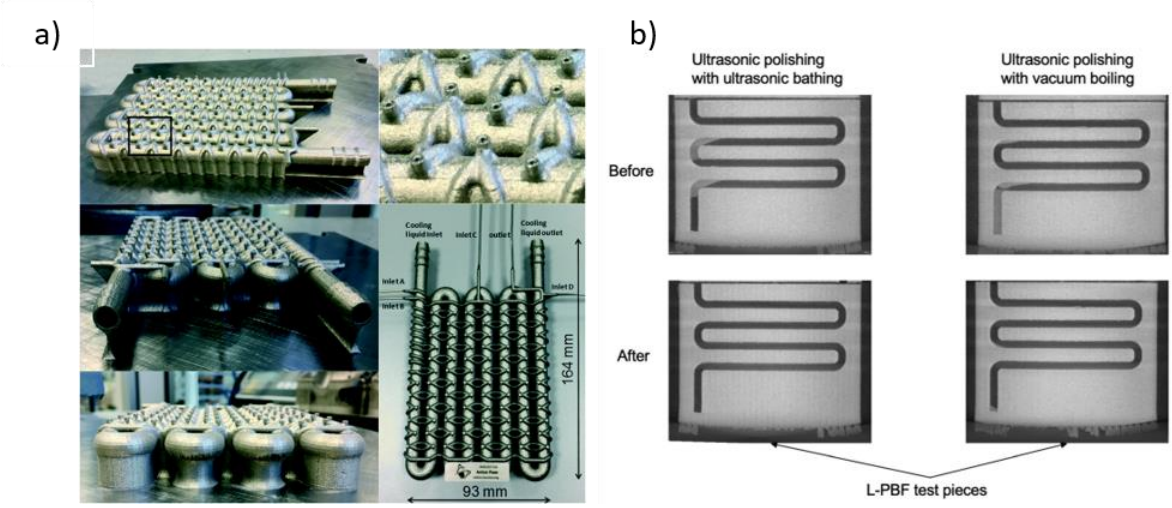


Figure 2.10. Powder removal approach. a) first approach: redesign of a component [85]; b) second approach: using a post-processing strategy [86].

Hunter et al. [86] proposed in their work a method to detect and remove the powder entrapped in complex features fabricated via L-PBF. In particular, X-ray computed tomography (XCT) and weighing were used to inspect and assess quantitatively the successful ratio of their powder removal methods. A traditional method of ultrasonic polishing with ultrasonic bathing was compared with a new and innovative technique of vacuum boiling. The results of the work of Hunter et al. are represented in Figure 2.10b. In particular, the vacuum boiling strategy involved a depressurised container with the component submerged in water. After the air is evacuated from the container, a heat source brought the water to boiling point causing the formation of water bubbles. The water bubbles help the removal of the powder, and the technique was demonstrated to completely freeing the ducts. This method is easy to implement but cannot be used for metallic materials, especially in powder form, which reacts easily in contact with water or air, such as Al and its alloys. Al reacts with water to produce hydrogen gas due to its highly negative redox potential. Scientific studies have found that the result of this reaction can be a significant accumulation of gaseous hydrogen, even for small concentrations of material.

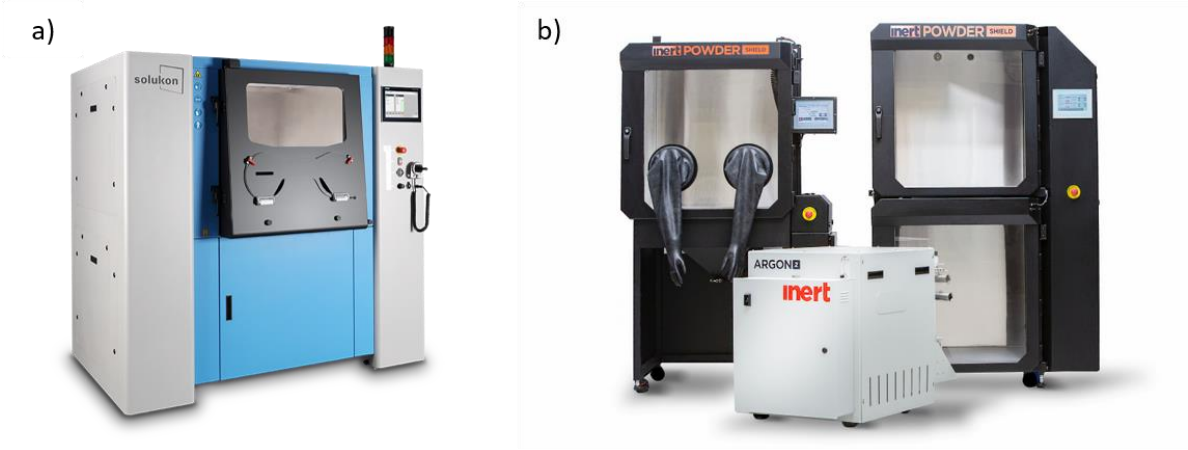


Figure 2.11. Two commercial depowdering systems for AM. a) Solukon SFM-AT800/-S (courtesy of Solukon Maschinenbau GmbH) [87] and b) Inert Technology PowderShield (courtesy of Inert Technology) [88].

Table 2.5. Main features and characteristics of two depowdering systems [89].

| Feature | Solukon SFM-AT800/-S | Inert PowderShield |
|---|---|---|
| **Table size** | 800 x 400 mm | Φ 533 mm |
| **Max weight** | 300 kg | 50 kg |
| **Vibration** | Yes | Yes |
| **Programmable vibration** | Yes | No |
| **Access for loading build plates** | Yes | No |
| **Inert gas** | Yes – optional | Yes – included |
| **Motorised axes of movement** | 2 axes | None |
| **Maximum rotation/tilt of axes** | 360 degrees | 45 degrees |
| **Robot loading** | Yes | No |

Considering the large, exposed surface of a metal powder particle, the reaction in aqueous environments could lead to the formation of high levels of hydrogen with the achievement of high pressures. This can pose the risk of fire or explosion in wet powder removal systems [90, 91]. Therefore, industrial-grade equipment was developed for the purpose to remove the powder from parts fabricated via AM. These specialised depowdering stations, exemplified in Figure 2.11 and detailed in Table 2.5, consist typically of a wide range of components designed to facilitate the removal of residual powder from the build plate.

Typically operating within a controlled environment that employs inert gas, these stations incorporate filters, sieving components, and various other features to ensure the integrity and quality of the extracted powder.

### 2.5.3 Fundamental properties of AM HXs

When it comes to HXs, different properties need to be analysed to evaluate the performance of an HX during the operational phases. In particular, for HXs produced through AM, scientific attention is focused on surface roughness, microchannels and thin walls, surface geometry, laminar and/or turbulent behaviour, corrosion and finally thermal efficiency. HXs, such as those used in an aircraft engine, operate at temperatures around 200 °C and are not subjected to very high loads. Consequently, they do not require high mechanical properties but surface and geometric properties suitable for heat dissipation. With the technological advancement of AM processes, great improvements can be achieved in the quality of surface quality and realisation of small thicknesses with precision, but scientific research is still far from total mastery of these characteristics [33, 34].

#### 2.5.3.1 Leak-free integrity

Leak-free features are essential for increasing the heat exchange between the two fluids at different temperatures in compact high-performance HXs [32]. AM reduces the risk of leaks as it eliminates the manufacturing step of assembling various thin-section components. However, it also has the disadvantage of possible losses caused by the formation of defects such as porosity and inadequate union of the layers. Defects such as pores and voids could be weak structural points where the fluid can escape from the duct, mixing with the second liquid. In particular, considering the manufacturing of thin features, a small defect can damage the entire component. Despite the increased interest from the aeronautics and aerospace sectors in new

compact HXs characterised by thin features, the study of the leaking problem has not yet attracted the attention of the scientific community. Few studies including that of Sabau et al. [92] performed leaking tests to ensure the success of the additive process, but no author has yet started the research on the correlation between the leaking, its known causes and targeted optimisation to solve this critical issue.

New systems have recently been developed which aim to eliminate internal pores within a printed material through a sequential process, the so-called vacuum impregnation systems. Initially, the component is immersed in a resin bath, while placed inside an autoclave. Subsequently, a vacuum is created to evacuate the air from the component, thereby facilitating the ingress of resin into the voids. Once the impregnation process is completed, the component is withdrawn from the bath, and surplus resin is extracted to ensure optimal impregnation levels. [93].

#### 2.5.3.2 Surface roughness

Surface Roughness is considered the most important characteristic in different types of HX configurations produced by metal AM. The roughness plays a double role as it influences both the actual dimensions of the produced feature (pipe, wall) and the behaviour of the fluid. Usually, a high roughness is synonymous with a significant deviation of the fabricated dimensions from the intended design, especially as the dimensions approach the fabrication limits of the AM machine [33, 94]. Many studies [95-98] also demonstrated that high internal roughness of channels increases pressure drops and turbulent behaviour, compared to the traditionally manufactured fins and channels. On the other hand, the performance in terms of heat transfer between traditionally and additively manufactured are in most cases comparable. In their work, Geete and Pathak [99] numerically analysed the effect of the internal roughness of pipes made of different materials on the performance of HXs. In particular, three different

surface roughness values were considered and through CFD simulations with predefined boundary conditions, the rate of heat transfer was calculated as output. The authors have shown that a low roughness improves the properties of thermal exchange and they have also settled the influence of the different materials, steel, Cu and Al. According to the study, both surface and material influence heat transfer and pressure drop. In particular, for steel pipe, the authors analysed a linear relation between surface roughness and properties, while, Aluminium and Copper show similar non-linear trends. The results highlighted copper pipes with smooth internal surfaces as the best conditions to enable high thermal performances. Consequently, the objective of many recent research studies [55, 100-104] was the optimisation of the parameters of the AM technologies for the tailoring of the surface roughness downstream of the additive process. In particular, Poncelet et al. [102] analysed the influence of L-PBF process parameters on the vertical roughness and hardness of AlSi10Mg thin walls. The authors used a Design of Experiments (DoE) to test different values of the main process parameters, laser power and scan speed during the construction of thin walls characterised by a thickness of 600 μm and ultra-thin walls produced by two single laser tracks. In particular, regarding the ultra-thin walls manufactured using parallel tracks, the offset or distance between melt pools has been identified as a crucial factor in reducing roughness. Larger offsets between melt pools consistently prove advantageous in minimising roughness levels. This can be attributed to the wetting phenomenon that occurs between a melt pool and the adjacent solidified melt pool, resulting in a slight liquid overflow. Everything was compared taking into consideration the final hardness of the as-built steps to understand the relationship between roughness optimisation and mechanical properties of the components. The results showed that the ideal process values for a low roughness were those close to the formation of the keyhole phenomenon. Consequently, the mechanical properties evaluated in terms of hardness are lower than the average values of an as-built

AlSi10Mg. For thin walls, the scanning strategy also plays a crucial role and using a scan contour before a bulk contour seems to give better quality to the surfaces. Finally, the authors believe that further studies must be carried out to determine if the lower levels of hardness and therefore mechanical properties affect the reliability of thin and ultra-thin walls.

#### 2.5.3.3 Fatigue performance

The fatigue performance of additively manufactured materials has been the subject of extensive research and investigation [105, 106]. Several factors such as microstructure, residual stresses, and surface roughness influence the fatigue life of any material. In particular, research has focused on specific metals and alloys commonly used in AM, such as titanium alloys, stainless steels, Aluminium alloys, and nickel-based superalloys. These studies [107-109] have examined the influence of AM process parameters, microstructure, defects, and post-processing treatments on the fatigue performance of these materials. However, the fatigue behaviour of heat exchangers, composed of several complex and thin features, is influenced by other several factors. The combination of cyclic loads at high temperatures and elevated working pressure may give rise to structural concerns. In recent times, the assessment of fatigue in heat exchangers has predominantly relied on numerical simulations. Limited attention has been given to experimental investigations of fatigue in plate and shell heat exchangers, with Martins et al. [110] being one of the few researchers to undertake such studies.

A substantial number of studies have been conducted on the low-cycle performance of thin walls manufactured through AM processes. These studies [111, 112] have identified several influential factors affecting the fatigue behaviour of these features. The initial microstructure, often exhibiting anisotropic characteristics, as well as metallurgical defects like porosity and lack of fusion, play a significant role in fatigue performance. Moreover, AM processes tend to result in higher surface roughness compared to conventional manufacturing methods. Extensive

research has demonstrated the detrimental impact of elevated surface roughness on the fatigue properties of additively manufactured thin features. However, these limitations can be mitigated through various post-processing treatments, including Hot Isostatic Pressing (HIP), machining, and heat treatments [113]. Nevertheless, a comprehensive understanding of the influence of AM process parameters, microstructure, defects, and post-processing treatments remains incomplete. Ongoing research efforts are focused on further characterising and enhancing the fatigue resistance and reliability of metal AM thin features.

#### 2.5.3.4 Corrosion resistance

Corrosion is a major problem affecting HXs. Corrosion can be caused by several factors including environmental conduction, the fluids used, and wear and erosion. Corrosion failure is quite common during the operational life of an HX, and maintenance and repair costs can be quite long and expensive, especially when it comes to air to oil compact HXs used in the aerospace field [114]. These components in particular are subject to severe environmental conditions, especially in the presence of sea and ocean routes where the strong concentration of salt mist can accelerate the degradation rate of metals. Consequently, the study of the phenomenon of corrosion, and the search for methods, traditional and innovative, for the protection of exposed surfaces, is ongoing. In particular, the effects of post-thermal treatment, surface finishing and coating treatments on the corrosion behaviour of additively manufactured materials are nowadays widely assessed [115, 116].

#### 2.5.3.5 Post thermal treatments

Due to the intrinsic phenomena during an additive process of L-PBF, the components produced require post-thermal treatments to improve the properties of the material. Generally, the microstructure and mechanical properties of the as-fabricated materials (prior heat treatments) produced through AM are inferior to the counterparts made through traditional manufacturing

techniques of casting or forging. The particular thermal cycle of AM processes is characterised by the sudden heating caused by the laser, followed by a rapid cooling and a second melting which simultaneously involves the next layer with a remelting of the underlying and previously solidified layers. These thermal cycles are repeated during the formation of every single layer of an L-PBF process and cause large thermal gradients that form residual stresses on the component. If the stress levels reached are high, a distortion of the geometry of the piece can occur which can lead to damage and malfunction of the product [117, 118].

Several approaches have been evaluated to solve this problem. In particular, the use of post thermal treatments for the relaxation of residual stresses remains the most adopted solution in the scientific and industrial fields. Studies [119, 120] have indeed shown that post-AM thermal treatment would drastically reduce the dislocation density, which therefore translates into a significant reduction in residual stress.

Post thermal treatments for L-PBF parts are also widely used to increase other material properties, such as mechanical properties and resistance to corrosion and wear [121, 122]. The use of post thermal treatments on materials additively manufactured gives properties comparable to or even superior to those of conventional materials. Homogenisation and solution treatments make the microstructure homogeneous and allow the elongated dendritic grains typical of the additive process to be transformed into equiaxed grains. They also allow the diffusion of segregated alloying elements. While through the ageing treatments, the formation of precipitates takes place, which helps to increase the mechanical properties of the material [123-125]. Furthermore, oxidation phenomena occur during thermal treatments which form a protective oxide layer on a wide range of materials. This helps to increase the performance in terms of corrosion and wear resistance [124-126].

## 2.6 Application of Machine Learning in Additive Manufacturing

Machine Learning (ML) is a particular field of AI, under the wide umbrella of Data Science [127]. The first ML models were initially introduced in the 1950s but only in the 1990s, following advancements in Computer Science, ML and its rise as an essential and remarkable field. Nowadays, the application of ML algorithms in several industrial and academic fields made this discipline a cornerstone of modern technology [128]. The foundation of ML relies upon its ability to model and analyse highly complex problems, finding the nonlinear relationship between input data and outcomes, and leading to the development of statistical analysis and optimisation tools, essentials for data-intensive sectors.

ML methods can be categorised into three broad categories: i) Supervised Learning; ii) Unsupervised Learning; iii) Reinforcement Learning. Each of these categories is tailored to specific types of problems, represented in Figure 2.12.

Supervised learning is the most applied category of ML. It uses sets of data, consisting of input parameters associated with output results, to train models able to map the correlation between data and outcomes through iterative processes, leading to the prediction of the input parameters corresponding to a desired outcome [129, 130]. Supervised learning is applied to several problems that fall into regression and classification tasks, where the aim is to predict continuous values or categorise data into discrete classes, respectively. The algorithms used for these types of problems are linear regression, decision trees, and neural networks (NN). All of the models applied to supervised learning are directly correlated to the quantity of data, and their accuracy increases with an increase in data provided for the training, which can be expensive and time-

consuming to retrieve. However, the models, in particular NN can be tuned with a smaller dataset using hyperparameters, reducing the need for a large amount of experimental data.

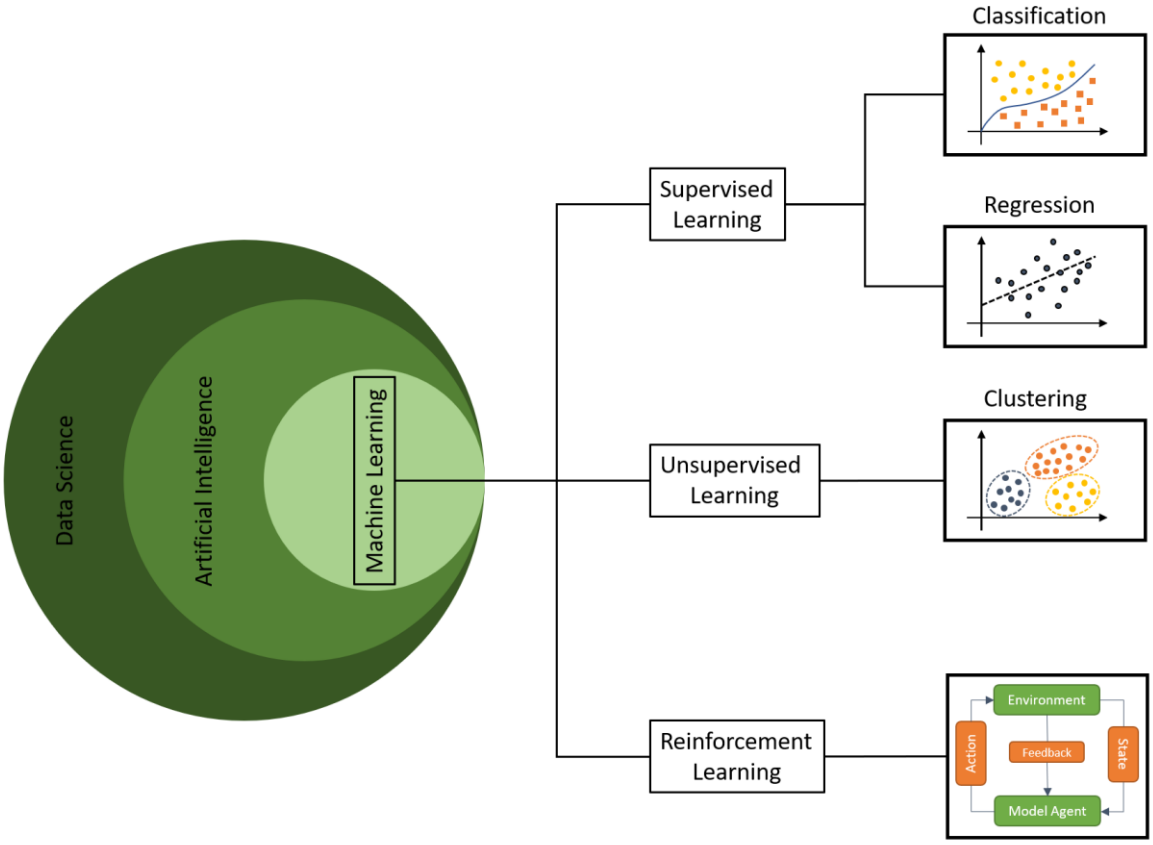


Figure 2.12. Umbrella of Data Science. Artificial intelligence is encompassed within the broader domain of data science, which also includes the field of machine learning. Machine learning comprises various models and techniques, such as supervised learning (including classification and regression), unsupervised learning (such as clustering), and reinforcement learning.

Unsupervised learning aims to discover hidden patterns between data and outputs. It is usually applied to clustering and anomaly detection problems, using algorithms such as k-means clustering, and hierarchical clustering [129]. These algorithms are able to analyse data whose identities are not available or hard to define. However, the results of unsupervised learning models can be challenging to interpret compared to supervised methods, as there are no explicit labels to validate the identified patterns.

Reinforcement Learning (RL) is a particular ML method where an agent interacts with an environment to learn actions based on rewards. Unlike supervised or unsupervised learning, RL

focuses on decision-making through trial-and-error processes. The agent receives feedback in the form of rewards or penalties based on its actions, which guides its learning toward optimal behaviour. RL is able to optimise complex, multi-step problems, and it is currently applied to robotics, game strategy development, and process optimisation. The limits of RL lie in the high computational burden and engineering of reward functions and environment development to ensure meaningful outcomes [131].

The application of ML in AM can increase the reliability of the process, leading to high final product quality. In particular, due to the high number of process parameters in an AM process, ML models can be trained to simulate and predict optimal configuration strategies to minimise defects and increase mechanical properties [132, 133]. Furthermore, ML is extensively capable of detecting defects leading to quality control of the AM process. By applying image recognition techniques, or other pattern recognition algorithms, ML can identify anomalies, such as spatter, delamination, or voids, in real time.

Focusing on the L-PBF process, ML models, such as NNs, have been already employed to predict the outcomes of several combinations of process parameters affecting the part density, surface finish, microstructure and mechanical properties [134]. Marrey et al. [135] used experimental data associated with the influence of process parameters on porosity, microstructure and mechanical properties to train an artificial NN and they were able to identify the process windows of defect-free for the 316L correlated to good mechanical performance. Phadke et al. [136] applied NN algorithms for the optimisation of process parameters for the dimensional accuracy of AlSi10Mg. The authors used an experimental dataset to train models characterised by different numbers of neurons in each hidden layer, successfully developing a model capable of predicting quite accurately the process parameters associated with high dimensional accuracy.

Furthermore, unsupervised learning algorithms have been applied to real-time monitoring and defect detection of the L-PBF process. The use of ML techniques alongside equipment such as thermal and speed cameras registering during the build can enable the implementation of feedback loops, where process parameters are adjusted in real time to prevent or reduce defect formation, significantly improving the process reliability. Taherkhani et al. [137] adopted an unsupervised learning model to identify the generation of porosity during the L-PBF process. Using a photodiode the acquisition of melt pool light intensity was carried out and a customised Self-Organizing Map (SOM) algorithm was used to classify disturbances in the signal, then associated with the presence of defects. The results of the study highlighted the ability of the ML approach to detect porosity from 100 μm, characterised by different shapes and distributions.

Finally, RL has shown significant potential to address the complex optimisation of the L-PBF process. The significant advantage of this model lies in the absence of training data since the algorithm can learn based on rewards associated with specific actions taken in a designed environment. Furthermore, RL frameworks can perform multi-objective optimisation, making this ML model capable of exploring optimised solutions for high overall part quality. Dharmadhikari et al. [138] introduced a model-free RL framework for optimising laser power and scan velocity combinations in a DED process to achieve a desired melt pool depth. The authors employed a type of off-policy RL algorithm known as Q-learning, to navigate the process parameter space and the environment was represented by a digital twin based on the Eagar-Tsai thermal model, which simulated the DED process. The Q-learning algorithm successfully identified optimal process parameters, with optimal predicted parameters closely matching experimental observations.

Vaghefi et al. applied a similar approach to the L-PBF process, optimising the combination of power and scan speed to achieve a desired melt pool depth target. The RL algorithm used in the study was able to identify the optimal process window for the material using FEM simulations validated through experimental data.

Both studies demonstrated the robustness and adaptability of RL models for AM optimisation. However, RL requires efficient models to simulate the phenomena occurring during an L-PBF process, which not always are available in the literature. The use of experimental data and FEM simulations can reduce but not eliminate the need for reliable mathematical or empirical models.

## 2.7 Materials selection for AM HXs

A wide range of materials is suitable for the production of HXs. The main characteristics to consider are density, thermal conductivity, AM processability, and finally cost. The selection of the most suitable material is carried out based on the component requirements, the type of operating environment and the boundary conditions [31].

In particular, the AM metal alloys mainly used are stainless steel, employed for HXs operating at high temperatures and corrosive environments; Nickel (Ni)-based alloys and Titanium (Ti) alloys are used in the application at very high temperatures; Al alloys applied in fields where the main requirement is lightweight, and the operating temperatures don't exceed 250 °C; Copper (Cu) alloys are high suitable materials thanks to its high thermal conductivity but are not yet mature due to their poor processability via AM [139] and reaction with esters in oil [140].

A basic comparison between the principal materials used for the manufacturing of HXs is summarised in Table 2.6.

Table 2.6. Comparison of general properties for the selected materials [141-143].

| Material | Density [g/cm$^3$] | Specific Thermal Conductivity [W/mK] | Melting Point (°C) | AM Friendly (from 1, poor, to 10, excellent) | Powder Average Price (£/kg) |
|---|---|---|---|---|---|
| **Aluminium** | 2.70 | 205 | 660 | 6 | 2.67 |
| **Stainless Steels** | 8.00 | 16 | 1530 | 10 | 2.53 |
| **Nickel** | 8.90 | 94 | 1453 | 8 | 25.86 |
| **Titanium** | 4.51 | 22 | 1670 | 9 | 44.89 |
| **Copper** | 8.96 | 401 | 1084 | 4 | 4.20 |

In the following sections, the characteristics of the main materials presented above are described.

### 2.7.1 Stainless Steels

Stainless Steels have always been used in a wide range of industrial applications thanks to their excellent mechanical properties, corrosion resistance and relatively low costs [144]. Therefore, they are a good material candidate for the production of HXs. The challenges in the AM process of Stainless Steel have already been overcome by the scientific community and often additive components subjected to heat treatments possess superior properties compared to their conventional counterpart. Many studies have focused on the evaluation of microstructural, mechanical and corrosion properties of these alloys, and in particular, 316L austenitic stainless steel resulted in the most used and suitable for aeronautical and aerospace applications [145]. Many works on the processability of 316L via AM and in particular L-PBF are available. The typical microstructure deriving from an additive process for 316L is composed of elongated dendritic grains along the building plane. This particular microstructure gives superior mechanical properties to the as-built material. Revilla et al. [146] have shown excellent corrosion properties of 316L processed by AM, showing higher oxide stability than the conventional one and similar resistance. Furthermore, 316L has been demonstrated as suitable

for the fabrication of thin features, by Yang et al. [147]. 316L is therefore a good candidate for the selection of the most suitable material for HXs. However, the high density of the material and the non-exceptional thermal properties must be considered. Consequently, this material and more generally the stainless steels are not ideal for the manufacture of HXs for aeroengines in aerospace applications but can be taken into consideration for other HX types in several industrial fields.

### 2.7.2 Ni-based Alloys

Ni-based alloys are widely used in the aerospace field thanks to their superior mechanical properties at high and very high temperatures [148]. For this reason, they are also selected for the manufacturing of HXs. In particular, Inconel 625 and Inconel 718 are the most known Ni-based superalloys. Recent studies [149-151] have demonstrated the feasibility of features such as thin walls via these materials and the influence of AM process parameters. Consequently, given the great corrosive and wear properties of these alloys, Inconel 625 and Inconel 718 would be excellent candidates for guaranteeing superior properties to HXs. However, the continuing need to reduce the total weight of aircraft makes this material not suitable for manufacturing air to oil compact HXs, and they are mostly used in the hot stages of aero engines.

### 2.7.3 Ti Alloys

The best-known Ti alloy used in various industrial sectors is the Ti6Al4V. It is a material with high strength, low density, high fracture toughness, excellent corrosion resistance and superior biocompatibility [152]. Originally, the Ti6Al4V alloy was developed for structural applications in the aerospace field as this light, but strong alloy allows a reduction of the weight of highly loaded structures maintaining the reliability of the structural components [152, 153]. Current

scientific research in the feasibility of thin-walled features has used Ti6Al4V in several studies as the processability and the influence of the optimal parameters on the microstructure, mechanical and thermal properties, and corrosive and fatigue performance has been assessed for some time. Recent studies, such as the work of Chen et al. [154] and Gockel et al. [155] focused on the analysis of the correlation between melt pool and thin features and the discovery of techniques for the tailoring of the microstructure and properties during the production of thin sections. In particular, Chen et al. [154] also focused on the evaluation of thermal phenomena that lead to the formation of residual stresses and the effects on the final geometry of thin walls. The authors pointed out that during the fabrication of thin walls, deformations accumulate, causing the geometry to vary. The greater the height of the features, the greater the deviation from the nominal value. The critical point is the middle of the wall, with the deformation which then tends to stabilise up to an average value. Consequently, this material is a promising material for the construction of HXs.

### 2.7.4 Cu Alloys

Copper and its alloys are very suitable for heat transfer applications but present many challenges. They are sensitive to impurities and the AM printability is very low due to the high surface reflectivity and low laser absorption. Furthermore, the high thermal gradient can result in delamination and bending during the AM process [139, 156]. Nevertheless, in recent years, many attempts to investigate the manufacturability of AM of Cu alloys have been registered, in particular for heat transfer applications. Several studies have employed Cu alloys with added alloying elements to reduce reflectivity and improve absorption properties. These investigations have focused on the additive manufacturing of different heat sink configurations and small-scale heat exchanger concepts. Subsequently, a comparative analysis was conducted to assess the performance of these printed structures in relation to their traditionally manufactured

counterparts. [32, 157]. Furthermore, AM of Cu alloys was implemented for high flux applications in the aerospace field. In the last decade, several studies [158] on a wide range of applications were reported, with particular interest in combustion chambers for liquid rocket engines [159, 160]. AM of Cu alloys for aerospace offers the potential for lightweight, complex, and customised components with enhanced mechanical, thermal, and electrical properties. However, research, testing, and validation to ensure the suitability and performance of AM copper alloy parts for specific aerospace applications are still ongoing.

### 2.7.5 Al Alloys

Al alloys are most commonly used for air-oil HXs due to their high thermal conductivity, low density, and low cost relative to other metallic materials [148]. Al alloys are available in wrought and cast form and can be divided into two groups, heat treatable and not [161, 162]. In AM, the most suitable Al powders are usually based on cast alloys due to similar material properties necessary for both AM and casting processes, such as castability, low shrinkage, and no solidification or liquation cracking. In particular, the use of near-eutectic metal alloys increases processability through AM and allows for a reduction of defects such as porosity and segregations thanks to greater fluidity and therefore better management of the melt pool solidification phase. Moreover, given the complex chemical composition used today, a near-eutectic alloy allows a better homogenisation of the alloying elements and greater stability of the matrix and the constituent phases [163, 164]. In contrast, wrought alloys are not suitable for AM as they require a long solidification range which can generate hot cracking [165]. The interaction between each alloying element of an Al matrix material determines the response and the final properties of the alloy [166].

## 2.8 L-PBF of Al Alloys

Current challenges with Al processed via AM include the material's high reflectivity [167] and thermal conductivity which can result in high levels of porosity. In L-PBF the most common Al alloys are near eutectic Al-Si alloys such as AlSi10Mg, AlSi12, A357 and A356 [168]. New Al alloys to be considered as have been customised for L-PBF processes as a variant of casting alloys are Airbus Scalmalloy® and A205. The chemical composition of these alloys is described in Table 2.7.

Table 2.7. Chemical composition (wt.%) of Al alloys [169-171].

| | **AlSi10Mg** | **A205** | **Scalmalloy®** |
|---|---|---|---|
| **Al** | **Balance** | **Balance** | **Balance** |
| **Si** | 9.00 – 11.00 | < 0.10 | < 0.40 |
| **Mg** | 0.25 – 0.45 | 0.20 – 0.33 | 4.00 – 4.90 |
| **Cu** | < 0.05 | 4.20 – 5.00 | < 0.10 |
| **Ti** | < 0.15 | 3.00 – 3.85 | < 0.15 |
| **Fe** | < 0.25 | < 0.08 | < 0.40 |
| **Zn** | < 0.10 | - | < 0.25 |
| **Mn** | < 0.45 | - | 0.30 – 0.80 |
| **Pb** | < 0.05 | - | - |
| **Ni** | < 0.05 | - | - |
| **Sn** | < 0.05 | - | - |
| **B** | - | 1.25 -1.55 | - |
| **Ag** | - | 0.60 – 0.90 | - |
| **Sc** | - | - | 0.60 – 0.80 |
| **Zr** | - | - | 0.20 – 0.50 |

**AlSi10Mg** is a hypoeutectic casting grade alloy. The Si content, see Table 7, allows for the solidification cracking phenomenon to be controlled with the solidification range being refined to a window of just 30°C [168, 172]. Si has high absorptivity and low reflectivity in comparison to Al, improves molten Al fluidity, lowers solidification shrinkage, and lowers the coefficient of thermal expansion, all of which improve the AM processability of Al [173-175]. AlSi10Mg can consistently produce material with a density above 99% with a variety of parameters. The

alloy gains much of its strength from the ultrafine microstructure formed by the rapid solidification SLM processing and from needle-like β''-$Mg_2Si$ precipitates. The properties of AlSi10Mg when produced by SLM, have higher strength than cast or wrought equivalents due to the ultrafine structure and maintain a good UTS at elevated temperatures. It has therefore gained applications in aerospace as a low-cost equivalent to Ti alloys, and in motorsport and automotive to allow for greater design freedoms in HXs and engine block components. AlSi10Mg is commonly heat-treated using the standardised T6 process comprising of solution heat treating followed by artificial ageing [176, 177]. In particular, Aboulkhair et al. [176] demonstrate the effect of the T6 treatment on additively manufactured AlSi10Mg, highlighting a decrease of the ultimate tensile strength (UTS) in return for an increase in ductility.

**A205** has another designation, A205, which is a metal matrix composite based on an Al-Cu system with the addition of Ti and boron (B), present as the ceramic, Ti diboride (TiB2), as represented in Table 2.7 [178, 179]. The addition of TiB2 changes the alloy to a mass feeding mechanism which allows for homogenous grain formation across the material, negating the need for interdendritic feeding. The presence of the $TiAl_3$ phase in A205 alloy yields a grain refinement effect, resulting in the formation of fine equiaxed α-Al grains that nucleate around $TiAl_3$ particles. This phenomenon contrasts with the formation of coarse columnar grains, enhancing the mechanical properties of the material [178, 180]. Furthermore, $TiB_2$ has a grain refinement effect, to a lesser extent than $TiAl_3$, but is suspected to restrict the growth of the grains which leads to an ultrafine homogenous structure with high UTS at room temperature. A205 rivals 7000 series alloys in strength and preserves good ductility, while also retaining UTS at elevated temperatures up to 250 °C better than other AM Al-alloys.

**Scalmalloy®** is an Al, magnesium (Mg), scandium (Sc), and zirconium (Zr) alloy, see Table 2.7, based on the 5000 series of Al-alloys [181]. It has a bimodal microstructure with fine

equiaxed grains separated by coarser columnar grains, where the addition of Sc to the hyper eutectic point (eutectic at 0.4-0.55 wt.%) provides grain refinement and an increase in strength, as well as the addition of Mg, provided solid solution hardening in the form of $Al_8Mg_5$ precipitate due to the lack of Si presence [171, 182]. Sc is an extremely expensive element with a single source which translates into a significantly more expensive alloy to the point where it no longer competes effectively with Ti-alloys. Furthermore, the elevated temperature properties, while still acceptable, are not as impressive as either AlSi10Mg or A205.

### 2.8.1 Effect of L-PBF process on the Material's Microstructure

The thermal history during L-PBF influences the final microstructure. In particular, the material is subject to a directional heat source and high thermal gradients. Generally, the laser power and scan speed affect the solidification rate, leading to the formation of a fine microstructure, constituted of columnar dendrites, evolved along the build direction. This final microstructure is different from the typical coarse microstructures developed by conventional manufacturing [183, 184]. Hadadzadeh et al. [185], like many other studies [183, 186-188], have shown that the average width of the columnar grains of the material processed by L-PBF is very fine, usually less than 5-6 μm, while the average grain size of the casted material is much higher, around to 150 μm, with predominantly equiaxed grains [189].

Figure 2.13 shows the typical microstructure of the as-fabricated Al alloys, AlSi10Mg, A205, and Scalmalloy®. As shown in Figure 2.13a the microstructure of AlSi10Mg produced with L-PBF is mainly composed of elongated grains, which grow nearly perpendicular to the building direction, following the thermal gradient. The unidirectional growing of grains reduces the isotropy of the material, affecting the mechanical properties. AlSi10Mg in as-fabricated condition exhibits anisotropic tensile and fatigue performance, with higher ductility in the plane perpendicular to the build direction rather than the plane parallel to it [190]. The alignment of

the elongated grain provides weaker interlayer bonding when loaded in the same direction as the grains [191]. Optimising the L-PBF process parameters and changing the scanning strategy can mitigate the issue but a fully isotropic behaviour of the material can be achieved only with full post-thermal treatments, including homogenisation and artificial ageing [192].

Scalmalloy® shows, in Figure 2.13b, a typical bi-modal microstructure. Due to the melting pool formation and overlap, the solidification mechanism generates either elongated grains along the build direction in the middle of the meltpool or a fine grain structure without any preferential grain orientation mostly concentrated on the boundaries [193].

The more uniform grain structure, characterised by fine equiaxed grains, prevents the development of a strong structure reducing the anisotropy typical of the Al alloys produced by L-PBF, achieving uniform strength and ductility across both build directions [194]. Furthermore, the addition of Sc and Zr promotes the formation of Al3(Sc, Zr) precipitation during the L-PBF process and under thermal post-processing strategies, preventing texture changes and guaranteeing stable and high performance of the material at high operation temperatures [195, 196].

In some cases, the generation of microstructure characterised by equiaxed fine grains is instead induced by the addition of alloying elements in the chemical composition of the alloy. This is the case with the AlCu-$TiB_2$ alloy, known as the A205, shown in Figure 2.13c. The addition of reinforcing alloys such as Ti Diborate ($TiB_2$), called nanoparticle grain refiners, leads to a decrease in the final average size of the grains, even lower than the classical values obtained by L-PBF [197, 198]. Martin et al. [197] analysed the effect of introducing $TiB_2$ nanoparticles and highlighted how the final microstructure is completely different from both casting and traditional additively manufactured materials.

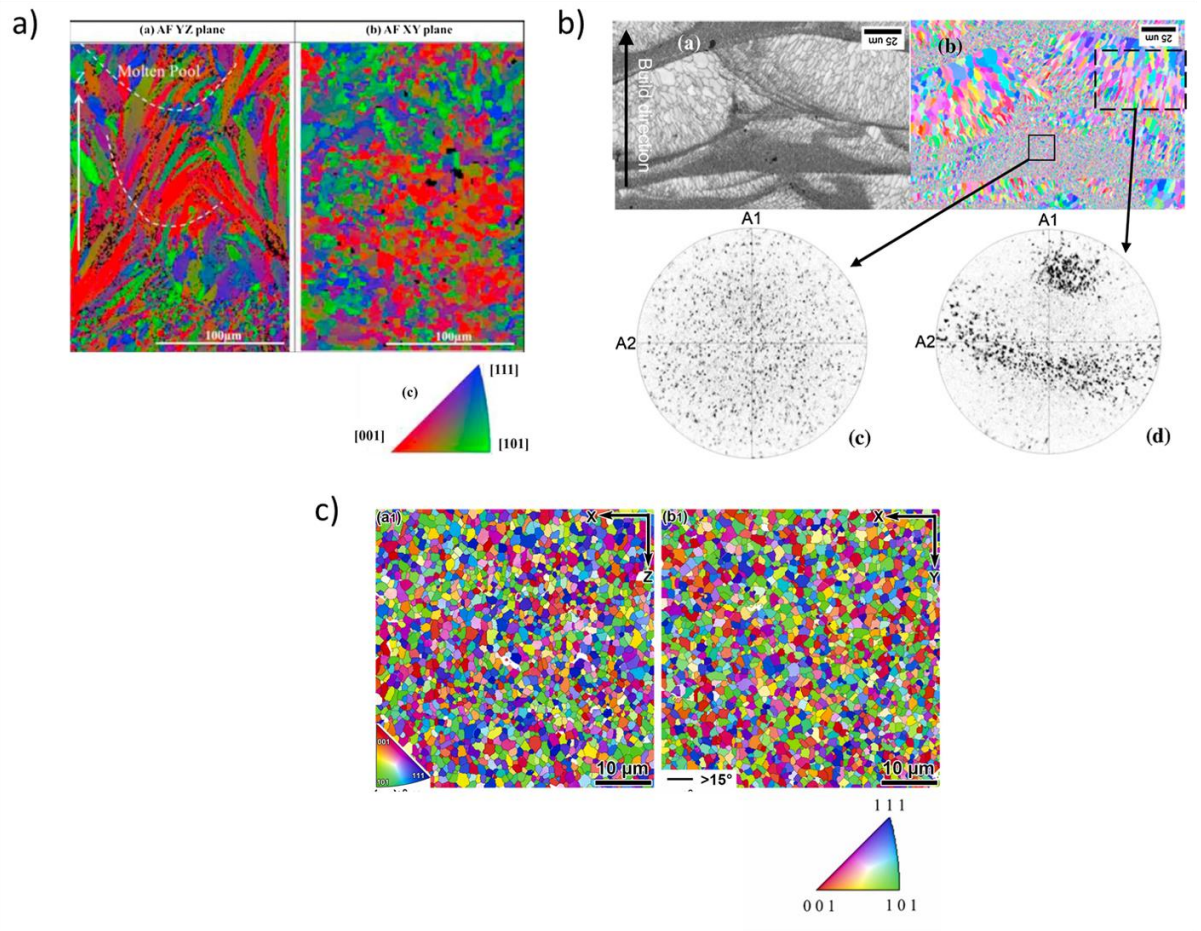


Figure 2.13. EBSD microstructure of different L-PBF Al alloys. In particular, a) EBSD imager of L-PBF AlSi10Mg [199]; b) EBSD imager of L-PBF Scalmalloy® [200]; c) EBSD imager of L-PBF A205 [201].

A205 alloy shows uniform equiaxed microstructure, with a fine average grain size, resulting in isotropic behaviour. However, the residual stresses generated during the L-PBF manufacturing process can still introduce slight anisotropy in the as-fabricated material [202]. Residual stresses and therefore anisotropy can be reduced using an optimised scanning strategy, increasing the overall tensile and fatigue performance of the alloy. Nevertheless, A205 achieve superior mechanical properties when subjected to post-thermal treatments of solution and artificial ageing, leading to the formation of ϑ'-$Al_2Cu$ and S'-$Al_2CuMg$ precipitates [203, 204].

### 2.8.2 Mechanical Properties

The mechanical properties of additive components are still a subject of investigation due to the distinctive columnar microstructure resulting from the L-PBF process. Specifically, the absence of standards poses a challenge in accurately characterising materials fabricated through AM techniques. Consequently, the scientific community has tried to respond to the need for analysis and explanation of mechanical properties using several methods. Several studies have analysed the effect of the building direction on tensile mechanical properties. In particular, Ponnusamy et al. [205] collected several studies highlighting a horizontal building direction as the best configuration. Read et al. [206] on the other hand, together with the mechanical properties of the AlSi10Mg alloy using the optimal parameters obtained through an experimental campaign, also evaluated the creep properties at high temperatures. In particular, according to the authors, the build direction does not seem to influence the tensile or creep resistance of the material, achieving higher performance than the conventional counterpart.

A comparative evaluation of the mechanical properties between additively manufactured and conventionally cast materials has been collected and presented in Table 2.8.

Table 2.8. Differences in mechanical properties of additively and cast Al alloy [170, 207-210].

| **Material** | | | **AlSi10Mg** | | **A205** | | **Scalmalloy®** | |
|---|---|---|---|---|---|---|---|---|
| **Configuration** | | | **As-built** | **Cast** | **As-built** | **Cast** | **As-built** | **Cast** |
| **Mechanical Properties** | **YS at RT** | **MPa** | 230 | 230 | 385 | 220 | 306 | - |
| | **UTS at RT** | **MPa** | 460 | 270 | 410 | 370 | 334 | - |
| | **Elongation (RT)** | **%** | 6.3 | 2.5 | 15 | 20 | 12 | - |
| | **Fatigue Strength at Troom** | **MPa** | 110 | 76 | 150 | 120 | - | - |
| | **Young's Modulus (RT)** | **GPa** | 66 | 71 | 74 | 71 | 65 | - |

### 2.8.3 Tribology and Corrosion

Nowadays, the corrosion protection mechanism for AM material holds significant importance. Surface roughness, microstructure, and post-thermal treatment are essential to increase the corrosion property of a material. A high-quality surface or a surface treatment of polishing can help to decrease the corrosion rate in the air and marine environment but it is difficult to achieve for highly complex geometries and internal features [211, 212]. Regarding the post-thermal treatments, different temperatures and times, together with the type of thermal treatment (solution, ageing, etc.) attribute different properties and therefore different corrosion performances [213, 214]. Extensive research efforts have been dedicated to the investigation of AlSi10Mg alloy [215-217] as it is the most widely used and studied Al alloy, while for the other Al alloys, few studies have been discovered [218].

Other mechanisms for corrosion protection are available for AM materials. Conversion coating is used to achieve the full protective properties of Al alloys. Chromate conversion coatings (CCCs) have been commonly applied as a surface finishing process, but they soon have to be replaced due to the toxic and carcinogenic effects of hexavalent chromium compounds. Recently, a new conversion coating has been developed, known as Trivalent Chromium Processes (TCP) [219, 220]. Also, another mechanism called Layered double hydroxides (LDHs) seems to be a new and healthy alternative to the chromate-based coating [221]. Organic coatings provide protection to the surface thanks to the pigments in the coating, acting as a barrier between the material and the external environment. For example, polymers such as polypyrrole (PPy), polythiophene (PTh) and polyaniline (PANI) are often used to generate organic coatings to prevent corrosion of Al and its alloys [222]. Besides, silica-based organic-inorganic hybrid nanocomposite films have been developed using sol-gel methods to generate coating against corrosive environments [223, 224]. Finally, Al anodising is a process that uses

electrochemical reactions to generate a protective oxidised layer on the surface of the metal materials. Plasma Electrolytic Oxidation (PEO) [225] is the most common and used in recent years. In particular, this last coating is an eco-friendly treatment that allows the formation of an Alumina oxide ($Al_2O_3$) coating that guarantees stable and long-term superior properties of resistance to corrosion and wear. However, studies on the PEO coating of additively manufactured high-strength Al alloys are limited to AlSi10Mg while a lack of research was discovered for the A205 Al alloy.

### 2.8.4 Effect of post-thermal treatments

The post-thermal treatments of Al alloys are performed to eliminate various manufacturing defects and impurities, to obtain recrystallisation and to improve the mechanical properties and the behaviour of the material during the life cycle. Al alloys are generally subjected to solution and quenching treatments, followed by artificial ageing treatments. The solution treatment involves maintaining the material at a high temperature to allow the diffusion of the alloying elements in the matrix. It is usually followed by water quenching which involves rapid cooling in order to obtain an oversaturated structure of alloying elements and can significantly impact the success of the treatment. Failure to control factors, such as the temperature and agitation of the hardening medium, the immersion speed, and the orientation of the part, can result in the formation of internal bubbles caused by pore growth and lead to permanent deformations. Finally, the ageing treatment consists of a medium-long permanence of the material and medium-low temperatures to allow the precipitation of the strengthening phases and increase the final mechanical properties of the component. The most common post-thermal treatments of Al alloys are T6 and T7 heat treatments, described in Figure 2.14. In particular, the HT T7 involves an ageing step characterised by higher temperature and shorter duration compared to

the HT T6, in order to achieve significant grain growth increasing the material's creep resistance.

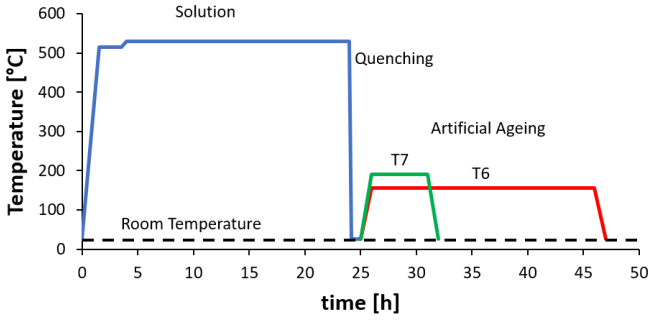


| Solution Treatment | Artificial Ageing Treatment | | |
|---|---|---|---|
| | T [°C] | t [h] | Designation |
| 515 °C for 2 h then 530 °C for 20 h | 155 | 20 | T6 |
| | 190 | 5 | T7 |

Figure 2.14. Conventional thermal treatments for Al alloy produced by casting, following the ASM handbook standard [226].

Limited information on the properties of materials made through AM after thermal treatments is available in the literature. These have been summarised in Table 2.9. While for the AlSi10Mg and A205 alloys, the standard thermal treatments are known for the corresponding conventional materials made by casting, for the Scalmalloy® alloy they do not exist. Consequently, ad hoc thermal treatments have been studied for this alloy, and the proposed thermal treatment consists of a single step of 4 h at a temperature of 325 °C [227], considered in Table 2.9, or a hot isostatic pressing (HIP). A recent study published by Kuo et al. [228] confirmed 325 °C as the ideal thermal treatment temperature to favour the formation of $Al_3Sc$ precipitates which give superior properties to the heat-treated alloy.

Numerous studies are focusing on the optimisation of post-additive thermal treatments for numerous AM metal alloys including Al alloys [229] and particular attention is focused on the study of the effects of standard treatments [230-232]. Among the conventional thermal treatments suitable for the AlSi10Mg alloy produced with additive processes, stress relief is the most used in the industrial field. The treatment is usually carried out at a temperature of around 300 °C for a period of 2 hours, and guarantees better ductility and resistance to fatigue, with deterioration of the mechanical properties [233].

Table 2.9. Mechanical properties of Al alloys fabricated by L-PBF, differences between as-built and heat-treated materials [170, 207-210, 234].

| **Material** | | | **AlSi10Mg** | | **A205** | | **Scalmalloy®** | |
|---|---|---|---|---|---|---|---|---|
| **Configuration** | | | **As-built** | **HT T6** | **As-built** | **HT T7** | **As-built** | **HT** |
| **Mechanical Properties** | **Max Operating Temp** | **°C** | 200 | | 230 | | 250 | |
| | **YS at RT** | **MPa** | 230 | 250 | 385 | 445 | 306 | 480 |
| | **YS at 200 °C** | **MPa** | - | - | - | 311 | - | 139 |
| | **YS at 230 °C** | **MPa** | - | - | - | 215 | - | 71 |
| | **UTS at RT** | **MPa** | 460 | 310 | 410 | 511 | 334 | 530 |
| | **UTS at 200 °C** | **MPa** | - | - | - | 331 | - | 163 |
| | **UTS at 250 °C** | **MPa** | - | - | - | 224 | - | 78 |
| | **Elongation (RT)** | **%** | 6.3 | 11 | 15 | 11 | 12 | 13 |
| | **Young's Modulus (RT)** | **GPa** | 66 | 69 | 74 | 79 | 65 | 70 |

Many studies in [176, 235] highlighted the unsuitability of the standard post-thermal treatments for L-PBF Al alloys as they lead to a decrease in the mechanical properties of the material such as hardness and tensile strength. Consequently, the evaluation of new customised post-thermal treatment is ongoing [236, 237] to assess the ideal thermal cycle for tailoring the microstructure and maximising the mechanical performance of Al alloys.

## 2.9 Summary and Identified Research Gaps

Heat Exchangers are typically produced through conventional manufacturing strategies. AM and in particular L-PBF allow the generation of complex geometries for mass production of components with short lead time. AM, with the help of advanced tools such as topological optimisation, CFD modelling, and ML approaches, is able to optimise the shape guaranteeing lighter and more performant HXs, tailoring the mechanical and corrosion properties of the components. Academia and industry are currently confronting challenges in the design and production of new generations of HXs. The objective of this review was to provide a

comprehensive overview of the current status and challenges in the design and manufacturing of new HXs using AM technology. In particular, the ability of AM to produce thin complex features could revolutionise the aerospace sector by generating compact HXs, with high efficiency and less weight, but is not yet mature. L-PBF as a winning strategy is a much-debated topic in the scientific field due to many technological limits that still need to be overcome. First, the optimisation of process parameters for the manufacture of a leak-proof with thin-walled features has yet to be reliable and repeatable. Moreover, a thorough understanding of the effects of L-PBF process parameters on the surface roughness, microstructure and density of fabricated Heat Exchangers has not yet been achieved. Furthermore, a careful analysis for the selection of suitable materials for L-PBF is still necessary to manufacture high-quality components, guaranteeing repeatability, reproducibility, and traceability. The principal material candidates were reviewed and the AM feasibility was evaluated. Particular attention was focused on the most common material, high-strength Aluminium alloys, which maintain high mechanical strength even at high temperatures and severe environments. Microstructure, mechanical properties and the influence of post-thermal treatments on the performance of these alloys produced using L-PBF were provided. Therefore, the following gaps were identified and addressed in this doctoral research work:

- The application of ML-driven approaches for the optimisation of the process has shown significant potential. However, further research is needed to address the optimisation of high-strength Al alloys and the prediction of optimal process parameters for ensuring dimensional accuracy in the fabrication of thin-walled features. These aspects are critical for enhancing the performance and manufacturing feasibility of aerospace components produced using L-PBF technology.

- HTS strategies play a significant role in meeting the stringent mechanical performance requirements of aerospace applications, especially under severe environmental conditions. However, the lack of standardised HTs for additively manufactured high-strength Al alloys, and in particular the A205 alloy, remains a significant gap. Limited studies on the impact of standard HTs, designed for cast materials, and the attempts to develop novel HTs were found in the literature. Moreover, the influence of such heat treatments on key properties such as tensile strength, fatigue resistance, and creep performance, as well as their correlation with microstructural evolution remains still to be fully understood.
- The PEO process has emerged as an eco-friendly and efficient surface treatment method to improve both the tribological and corrosion performance of Al alloys, generating a protective uniform layer of alumina on the material surface. While its application is well-established for conventionally manufactured Al alloys, a lack of comprehensive studies evaluating its influence on additively manufactured high-strength Al alloys was found in the literature, particularly for the A205 alloy. Additionally, further investigation is required to understand the effect of surface preparation on the PEO process and the impact on the performance of components in harsh environments.

## Acknowledgements

*This work is part of the C-AM AOHE project funded by the European Union's Horizon H2020-CS2-CFP08-2018-01 research and innovation program under grant agreement No 831880. This work was also supported in part by the EPSRC Centre for Doctoral Training in Topological Design, funded by the UK Engineering and Physical Sciences Research Council (grant EP/S02297X/1) based at the University of Birmingham.*

# References

[1] B. Sundén, J. Fu, Chapter 6 - Aerospace Heat Exchangers, in: B. Sundén, J. Fu (Eds.) Heat Transfer in Aerospace Applications, Academic Press, 2017, pp. 89-115.

[2] Meggitt, Advanced Thermal Systems Technology. Step-changing technology for next generation energy efficient ultra-high bypass ratio (UHBR) aero engines. https://www.meggitt.com/insights/step-changing-technology-for-the-next-generation-of-aero-engines/ (accessed on 15 June 2022).

[3] D. Saltzman, M. Bichnevicius, S. Lynch, T.W. Simpson, E.W. Reutzel, C. Dickman, R. Martukanitz, Design and evaluation of an additively manufactured aircraft heat exchanger, Applied Thermal Engineering, 138 (2018) 254-263.

[4] M. William, A. Muley, J. Bolla, H. Strumpf, Advanced Heat Exchanger Technology for Aerospace Applications, SAE International, (2008).

[5] C. Balaji, B. Srinivasan, S. Gedupudi, Chapter 7 - Heat exchangers, in: C. Balaji, B. Srinivasan, S. Gedupudi (Eds.) Heat Transfer Engineering, Academic Press, 2021, pp. 199-231.

[6] K. Kasim, A. Muley, M. Stoia, F. Ladeinde, Advanced Heat Transfer Devices for Aerospace Applications, ASME 2017 International Mechanical Engineering Congress and Exposition, 2017.

[7] M. Williams, A. Muley, J. Bolla, H. Strumpf, Advanced Heat Exchanger Technology for Aerospace Applications, SAE International, 2008.

[8] D. Southall, R. Le Pierres, S.J. Dewson, Design considerations for compact heat exchangers, Proceedings of ICAPP, ICAPP, 2008, pp. 8-12.

[9] P. Moorthy, A.N. Oumer, M. Ishak, Experimental Investigation on Effect of Fin Shape on the Thermal-Hydraulic Performance of Compact Fin-and-Tube Heat Exchangers, IOP Conference Series: Materials Science and Engineering, 318 (2018) 012070.

[10] M.I.N. Ma'arof, G.T. Chala, H. Husain, M.S.S. Mohamed, Influence of fins designs, geometries and conditions on the performance of a plate-fin heat exchanger-experimental perspective, Journal of Mechanical Engineering and Sciences, 13 (2019) 4368-4379.

[11] M. Göltaş, B. Gürel, A. Keçebaş, V.R. Akkaya, O.V. Güler, Improvement of thermo-hydraulic performance with plate surface geometry for a compact plate heat exchanger manufactured by additive manufacturing, International Journal of Heat and Mass Transfer, 188 (2022) 122637.

[12] A. Menéndez Pérez, C. Fernández-Aballí Altamirano, R. Borrajo Pérez, Parametric analysis of the influence of geometric variables of vortex generators on compact louver fin heat exchangers, Thermal Science and Engineering Progress, 27 (2022) 101151.

[13] Mott, 3D Printed Heat Exchangers. https://mottcorp.com/product/3d-printed-products/3d-printed-heat-exchangers/ (accessed on 16 February 2022).

[14] Stratatys, Advancing Thermal Management with Additive Manufacturing. https://www.stratasysdirect.com/-/media/files/direct/white-papers/thermal-management-white-paper_web.pdf (accessed on 16 February 2022).

[15] Hyperganic, The Heat Exchanger, Algorithmic Engineering of heat exchangers. https://www.hyperganic.com/press-and-stories/2/ (accessed on 20 June 2023).

[16] J. Yao, A Review of Industrial Heat Exchange Optimization, IOP Conference Series: Earth and Environmental Science, 108 (2018) 042036.

[17] I. Kaur, P. Singh, Critical evaluation of additively manufactured metal lattices for viability in advanced heat exchangers, International Journal of Heat and Mass Transfer, 168 (2021) 120858.

[18] T. Maconachie, M. Leary, B. Lozanovski, X. Zhang, M. Qian, O. Faruque, M. Brandt, SLM lattice structures: Properties, performance, applications and challenges, Materials & Design, 183 (2019) 108137.

[19] H.N.G. Wadley, D.T. Queheillalt, Thermal Applications of Cellular Lattice Structures, Materials Science Forum, 539-543 (2007) 242-247.

[20] K.J. Maloney, K.D. Fink, T.A. Schaedler, J.A. Kolodziejska, A.J. Jacobsen, C.S. Roper, Multifunctional heat exchangers derived from three-dimensional micro-lattice structures, International Journal of Heat and Mass Transfer, 55 (2012) 2486-2493.

[21] N. Lebaal, A. Settar, S. Roth, S. Gomes, Conjugate heat transfer analysis within in lattice-filled heat exchanger for additive manufacturing, Mechanics of Advanced Materials and Structures, (2020) 1-9.

[22] L.-Y. Chen, S.-X. Liang, Y. Liu, L.-C. Zhang, Additive manufacturing of metallic lattice structures: Unconstrained design, accurate fabrication, fascinated performances, and challenges, Materials Science and Engineering: R: Reports, 146 (2021) 100648.

[23] D. Jafari, W.W. Wits, The utilization of selective laser melting technology on heat transfer devices for thermal energy conversion applications: A review, Renewable and Sustainable Energy Reviews, 91 (2018) 420-442.

[24] J.Y. Ho, K.C. Leong, T.N. Wong, Additively-manufactured metallic porous lattice heat exchangers for air-side heat transfer enhancement, International Journal of Heat and Mass Transfer, 150 (2020) 119262.

[25] J. Noronha, M. Qian, M. Leary, E. Kyriakou, M. Brandt, Hollow-walled lattice materials by additive manufacturing: Design, manufacture, properties, applications and challenges, Current Opinion in Solid State and Materials Science, 25 (2021) 100940.

[26] I.A. 52900, Additive manufacturing - General principles - Fundamental and vocabulary, 2021.

[27] I. Gibson, D. Rosen, B. Stucker, M. Khorasani, Binder Jetting, in: I. Gibson, D. Rosen, B. Stucker, M. Khorasani (Eds.) Additive Manufacturing Technologies, Springer International Publishing, Cham, 2021, pp. 237-252.

[28] T. Vaneker, A. Bernard, G. Moroni, I. Gibson, Y. Zhang, Design for additive manufacturing: Framework and methodology, CIRP Annals, 69 (2020) 578-599.

[29] A. Hehr, M. Norfolk, A comprehensive review of ultrasonic additive manufacturing, Rapid Prototyping Journal, 26 (2020) 445-458.

[30] NasaJPL, Ultrasonic Welding Makes Parts for NASA Missions, Commercial Industry. https://www.jpl.nasa.gov/news/ultrasonic-welding-makes-parts-for-nasa-missions-commercial-industry (accessed on 04 November 2022).

[31] E. Klein, J. Ling, V.C. Aute, Y. Hwang, R. Radermacher, A Review of Recent Advances in Additively Manufactured Heat Exchangers, (2018).

[32] J.R. McDonough, A perspective on the current and future roles of additive manufacturing in process engineering, with an emphasis on heat transfer, Thermal Science and Engineering Progress, 19 (2020) 100594.

[33] I. Kaur, P. Singh, State-of-the-art in heat exchanger additive manufacturing, International Journal of Heat and Mass Transfer, 178 (2021) 121600.

[34] S.A. Niknam, M. Mortazavi, D. Li, Additively manufactured heat exchangers: a review on opportunities and challenges, The International Journal of Advanced Manufacturing Technology, 112 (2021) 601-618.

[35] M. Leary, Chapter 11 - Powder bed fusion, in: M. Leary (Ed.) Design for Additive Manufacturing, Elsevier, 2020, pp. 295-319.

[36] S. Rahmati, 10.12 - Direct Rapid Tooling, in: S. Hashmi, G.F. Batalha, C.J. Van Tyne, B. Yilbas (Eds.) Comprehensive Materials Processing, Elsevier, Oxford, 2014, pp. 303-344.

[37] X. Gong, T. Anderson, K. Chou, Review on powder-based electron beam additive manufacturing technology, Manufacturing Review, 1 (2014) 2.

[38] GEAdditive, EBM MAchine Solutions. https://www.ge.com/additive/additive-manufacturing/machines/ebm-machines (accessed on 23 February 2022).

[39] M. Galati, L. Iuliano, A literature review of powder-based electron beam melting focusing on numerical simulations, Additive Manufacturing, 19 (2018) 1-20.

[40] M. AM, Unrealised potential: The story and status of Electron Beam Powder Bed Fusion, 2020. https://www.metal-am.com/articles/unrealised-potential-the-story-and-status-of-electron-beam-powder-bed-fusion-3d-printing/. (accessed on 23 February 2022).

[41] T.D. Ngo, A. Kashani, G. Imbalzano, K.T.Q. Nguyen, D. Hui, Additive manufacturing (3D printing): A review of materials, methods, applications and challenges, Composites Part B: Engineering, 143 (2018) 172-196.

[42] A.B. Badiru, V.V. Valencia, D. Liu, Additive Manufacturing Handbook: Product Development for the Defense Industry, 1st edition ed., CRC Press, 2017.

[43] A. Gebhardt, Layer Manufacturing Processes, in: A. Gebhardt (Ed.) Understanding Additive Manufacturing, Hanser, 2011, pp. 31-63.

[44] H. Shipley, D. McDonnell, M. Culleton, R. Coull, R. Lupoi, G. O'Donnell, D. Trimble, Optimisation of process parameters to address fundamental challenges during selective laser melting of Ti-6Al-4V: A review, International Journal of Machine Tools and Manufacture, 128 (2018) 1-20.

[45] W.E. King, A.T. Anderson, R.M. Ferencz, N.E. Hodge, C. Kamath, S.A. Khairallah, A.M. Rubenchik, Laser powder bed fusion additive manufacturing of metals; physics, computational, and materials challenges, Applied Physics Reviews, 2 (2015) 041304.

[46] E. Santecchia, S. Spigarelli, M. Cabibbo, Material Reuse in Laser Powder Bed Fusion: Side Effects of the Laser—Metal Powder Interaction, Metals, 10 (2020) 341.

[47] S. Sun, M. Brandt, M. Easton, 2 - Powder bed fusion processes: An overview, in: M. Brandt (Ed.) Laser Additive Manufacturing, Woodhead Publishing, 2017, pp. 55-77.

[48] I. Yadroitsev, I. Yadroitsava, A. Du Plessis, 2 - Basics of laser powder bed fusion, in: I. Yadroitsev, I. Yadroitsava, A. du Plessis, E. MacDonald (Eds.) Fundamentals of Laser Powder Bed Fusion of Metals, Elsevier, 2021, pp. 15-38.

[49] PrimaAdditive, Technologies - Powder bed Fusion. https://www.primaadditive.com/it/tecnologie/powder-bed-fusion (accessed on 23 February 2022).

[50] AM Metal, SLM Solutions launches 12-laser metal Additive Manufacturing machine. https://www.metal-am.com/slm-solutions-launches-12-laser-metal-additive-manufacturing-machine/ (accessed on 23 February 2022).

[51] Additive Industries, A New Metal Additive Manufacturing Era | The MetalFABG2. https://www.additiveindustries.com/metalfabg2 (accessed on 05 April 2023).

[52] G.V. de Leon Nope, L.I. Perez-Andrade, J. Corona-Castuera, D.G. Espinosa-Arbelaez, J. Muñoz-Saldaña, J.M. Alvarado-Orozco, Study of volumetric energy density limitations on the IN718 mesostructure and microstructure in laser powder bed fusion process, Journal of Manufacturing Processes, 64 (2021) 1261-1272.

[53] S. Chowdhury, N. Yadaiah, C. Prakash, S. Ramakrishna, S. Dixit, L.R. Gupta, D. Buddhi, Laser powder bed fusion: a state-of-the-art review of the technology, materials, properties &

defects, and numerical modelling, Journal of Materials Research and Technology, 20 (2022) 2109-2172.

[54] J.C. Snyder, K.A. Thole, Effect of Additive Manufacturing Process Parameters on Turbine Cooling, ASME Turbo Expo 2019: Turbomachinery Technical Conference and Exposition, 2019.

[55] J.C. Snyder, K.A. Thole, Tailoring Surface Roughness Using Additive Manufacturing to Improve Internal Cooling, Journal of Turbomachinery, 142 (2020).

[56] J.C. Snyder, K.A. Thole, Understanding Laser Powder Bed Fusion Surface Roughness, Journal of Manufacturing Science and Engineering, 142 (2020).

[57] J.P. Oliveira, A.D. LaLonde, J. Ma, Processing parameters in laser powder bed fusion metal additive manufacturing, Materials & Design, 193 (2020) 108762.

[58] M.M. Aslam Bhutta, N. Hayat, M.H. Bashir, A.R. Khan, K.N. Ahmad, S. Khan, CFD applications in various heat exchangers design: A review, Applied Thermal Engineering, 32 (2012) 1-12.

[59] B. Sundén, Computational Fluid Dynamics in Research and Design of Heat Exchangers, Heat Transfer Engineering, 28 (2007) 898-910.

[60] C. Abeykoon, Compact heat exchangers – Design and optimization with CFD, International Journal of Heat and Mass Transfer, 146 (2020) 118766.

[61] A. Jamal, R. Syahputra, Heat exchanger control based on artificial intelligence approach, International Journal of Applied Engineering Research (IJAER), 11 (2016) 9063-9069.

[62] J. Krzywanski, A general approach in optimization of heat exchangers by bio-inspired artificial intelligence methods, Energies, 12 (2019) 4441.

[63] M. Mohanraj, S. Jayaraj, C. Muraleedharan, Applications of artificial neural networks for thermal analysis of heat exchangers – A review, International Journal of Thermal Sciences, 90 (2015) 150-172.

[64] M. Sridharan, Chapter 15 - Applications of artificial intelligence techniques in heat exchanger systems, in: L. Pekař (Ed.) Advanced Analytic and Control Techniques for Thermal Systems with Heat Exchangers, Academic Press, 2020, pp. 325-334.

[65] M. Ghalandari, M. Irandoost Shahrestani, A. Maleki, M. Safdari Shadloo, M. El Haj Assad, Applications of intelligent methods in various types of heat exchangers: a review, Journal of Thermal Analysis and Calorimetry, 145 (2021) 1837-1848.

[66] J. Zhu, H. Zhou, C. Wang, L. Zhou, S. Yuan, W. Zhang, A review of topology optimization for additive manufacturing: Status and challenges, Chinese Journal of Aeronautics, 34 (2021) 91-110.

[67] E. Dalpadulo, F. Gherardini, F. Pini, F. Leali, Integration of Topology Optimisation and Design Variants Selection for Additive Manufacturing-Based Systematic Product Redesign, Applied Sciences, 10 (2020) 7841.

[68] K. Salonitis, S.A. Zarban, Redesign Optimization for Manufacturing Using Additive Layer Techniques, Procedia CIRP, 36 (2015) 193-198.

[69] COMSOL, Comparing Optimization Methods for a Heat Sink Design for 3D Printing. https://www.comsol.com/blogs/comparing-optimization-methods-for-a-heat-sink-design-for-3d-printing/ (accessed on 23 February 2022).

[70] E.M. Dede, Multiphysics topology optimization of heat transfer and fluid flow systems, proceedings of the COMSOL Users Conference, 2009.

[71] R.P.P. da Silva, M.V.V. Mortean, K.V. de Paiva, L.E. Beckedorff, J.L.G. Oliveira, F.G. Brandão, A.S. Monteiro, C.S. Carvalho, H.R. Oliveira, D.G. Borges, V.L. Chastinet, Thermal

and hydrodynamic analysis of a compact heat exchanger produced by additive manufacturing, Applied Thermal Engineering, 193 (2021) 116973.

[72] V.K. Patel, V.J. Savsani, M.A. Tawhid, Thermal Design and Optimization of Heat Exchangers, Thermal System Optimization, Springer, 2019, pp. 33-98.

[73] H. Moon, D.J. McGregor, N. Miljkovic, W.P. King, Ultra-power-dense heat exchanger development through genetic algorithm design and additive manufacturing, Joule, 5 (2021) 3045-3056.

[74] Temisth, AddUp, Sogeclair, HEWAM – Heat Exchanger with Additive Manufacturing. http://temisth.com/hewam-heat-exchanger-with-additive-manufacturing/ (accessed on 26 February 2022).

[75] Temisth, http://temisth.com/ (accessed on 26 February 2022).

[76] AddUp Global Additive Solutions, https://addupsolutions.com/ (accessed on 26 February 2022)

[77] Sogeclair, https://sogeclair.com/ (accessed on 26 February 2022).

[78] F. Feppon, G. Allaire, C. Dapogny, P. Jolivet, Body-fitted topology optimization of 2D and 3D fluid-to-fluid heat exchangers, Computer Methods in Applied Mechanics and Engineering, 376 (2021) 113638.

[79] T. Dixit, E. Al-Hajri, M.C. Paul, P. Nithiarasu, S. Kumar, High performance, microarchitected, compact heat exchanger enabled by 3D printing, Applied Thermal Engineering, 210 (2022) 118339.

[80] A. Muley, M. Stoia, D. Van Affelen, V. Reddy, V. Duggirala, S. Locke, Recent Advances in Thin-Wall Additively Manufactured Heat Exchangers, ASME 2021 International Mechanical Engineering Congress and Exposition, 2021.

[81] M. Mani, P. Witherell, Design Rules for Additive Manufacturing: Literature Review and Research Categorization, (2017).

[82] Z. Wu, S.P. Narra, A. Rollett, Exploring the fabrication limits of thin-wall structures in a laser powder bed fusion process, The International Journal of Advanced Manufacturing Technology, 110 (2020) 191-207.

[83] C. Tan, S. Li, K. Essa, P. Jamshidi, K. Zhou, W. Ma, M.M. Attallah, Laser Powder Bed Fusion of Ti-rich TiNi lattice structures: Process optimisation, geometrical integrity, and phase transformations, International Journal of Machine Tools and Manufacture, 141 (2019) 19-29.

[84] H. Hassanin, L. Finet, S.C. Cox, P. Jamshidi, L.M. Grover, D.E.T. Shepherd, O. Addison, M.M. Attallah, Tailoring selective laser melting process for titanium drug-delivering implants with releasing micro-channels, Additive Manufacturing, 20 (2018) 144-155.

[85] B. Gutmann, M. Köckinger, G. Glotz, T. Ciaglia, E. Slama, M. Zadravec, S. Pfanner, M.C. Maier, H. Gruber-Wölfler, C. Oliver Kappe, Design and 3D printing of a stainless steel reactor for continuous difluoromethylations using fluoroform, Reaction Chemistry & Engineering, 2 (2017) 919-927.

[86] L.W. Hunter, D. Brackett, N. Brierley, J. Yang, M.M. Attallah, Assessment of trapped powder removal and inspection strategies for powder bed fusion techniques, The International Journal of Advanced Manufacturing Technology, 106 (2020) 4521-4532.

[87] Solukon, Depowdering Metals SFM-AT800/-S. https://www.solukon.de/en/depowdering-metal/sfm-at800-s/ (accessed on 11 May 2023).

[88] Inert Technologies, 3D Printing Depowdering With Powdershield. https://www.inertcorp.com/powdershield/ (accessed on 24 February 2022).

[89] Metal AM, Powder removal: The Achilles heel of powder bed-based metal Additive Manufacturing. https://www.metal-am.com/articles/powder-removal-in-powder-bed-based-metal-3d-printing/ (accessed on 24 February 2022).

[90] A.V. Parmuzina, O.V. Kravchenko, Activation of aluminium metal to evolve hydrogen from water, International Journal of Hydrogen Energy, 33 (2008) 3073-3076.

[91] Y. Wang, K. Xu, L. Li, Inhibition of the reaction between aluminium dust and water based on the HIM, RSC Advances, 7 (2017) 33327-33334.

[92] A.S. Sabau, A. Bejan, D. Brownell, K. Gluesenkamp, B. Murphy, F. List, K. Carver, C.R. Schaich, J.W. Klett, Design, additive manufacturing, and performance of heat exchanger with a novel flow-path architecture, Applied Thermal Engineering, 180 (2020) 115775.

[93] Aerospace & Defense Technology, Curing the Porosity Problem in Additive Manufacturing. https://www.aerodefensetech.com/component/content/article/adt/features/articles/39675 (accessed on 26 February 2022).

[94] A.M. Ralls, P. Kumar, P.L. Menezes, Tribological Properties of Additive Manufactured Materials for Energy Applications: A Review, Processes, 9 (2021) 31.

[95] D. Saltzman, S. Lynch, Flow-Field Measurements in a Metal Additively Manufactured Offset Strip Fin Array Using Laser Doppler Velocimetry, Journal of Fluids Engineering, 143 (2021).

[96] D. Saltzman, S. Lynch, Overall Pressure Loss and Heat Transfer Performance of Additively Manufactured Offset Strip Fins Used in Compact Heat Exchangers, Journal of Thermal Science and Engineering Applications, 14 (2022).

[97] T.M. Baker, M.P. Manahan, S.P. Lynch, E.W. Reutzel, Effect of Hydraulic Diameter and Surface Roughness on Additively-Manufactured Offset Strip Fin Heat Exchanger Performance,

ASME 2022 Heat Transfer Summer Conference collocated with the ASME 2022 16th International Conference on Energy Sustainability, 2022.

[98] K.A. Thole, S.P. Lynch, A.J. Wildgoose, Chapter Five - Review of advances in convective heat transfer developed through additive manufacturing, in: J.P. Abraham, J.M. Gorman, W. Minkowycz (Eds.) Advances in Heat Transfer, Elsevier, 2021, pp. 249-325.

[99] A. Geete, R. Pathak, Effect of surface roughness on the performance of heat exchanger, SN Applied Sciences, 1 (2019) 901.

[100] L. Cao, J. Li, J. Hu, H. Liu, Y. Wu, Q. Zhou, Optimization of surface roughness and dimensional accuracy in LPBF additive manufacturing, Optics & Laser Technology, 142 (2021) 107246.

[101] J. Jiang, Y. Ma, Path Planning Strategies to Optimize Accuracy, Quality, Build Time and Material Use in Additive Manufacturing: A Review, Micromachines, 11 (2020) 633.

[102] O. Poncelet, M. Marteleur, C. van der Rest, O. Rigo, J. Adrien, S. Dancette, P.J. Jacques, A. Simar, Critical assessment of the impact of process parameters on vertical roughness and hardness of thin walls of AlSi10Mg processed by laser powder bed fusion, Additive Manufacturing, 38 (2021) 101801.

[103] C. Silbernagel, A. Aremu, I. Ashcroft, Using machine learning to aid in the parameter optimisation process for metal-based additive manufacturing, Rapid Prototyping Journal, 26 (2019) 625-637.

[104] C.K. Stimpson, J.C. Snyder, K.A. Thole, D. Mongillo, Scaling Roughness Effects on Pressure Loss and Heat Transfer of Additively Manufactured Channels, Journal of Turbomachinery, 139 (2016).

[105] R. Molaei, A. Fatemi, Fatigue Design with Additive Manufactured Metals: Issues to Consider and Perspective for Future Research, Procedia Engineering, 213 (2018) 5-16.

[106] A.B. Spierings, T.L. Starr, K. Wegener, Fatigue performance of additive manufactured metallic parts, Rapid Prototyping Journal, 19 (2013) 88-94.

[107] J.W. Pegues, S. Shao, N. Shamsaei, N. Sanaei, A. Fatemi, D.H. Warner, P. Li, N. Phan, Fatigue of additive manufactured Ti-6Al-4V, Part I: The effects of powder feedstock, manufacturing, and post-process conditions on the resulting microstructure and defects, International Journal of Fatigue, 132 (2020) 105358.

[108] A.D. Brandão, J. Gumpinger, M. Gschweitl, C. Seyfert, P. Hofbauer, T. Ghidini, Fatigue Properties Of Additively Manufactured AlSi10Mg – Surface Treatment Effect, Procedia Structural Integrity, 7 (2017) 58-66.

[109] M. Pelegatti, D. Benasciutti, F. De Bona, A. Lanzutti, M. Magnan, J. Srnec Novak, E. Salvati, F. Sordetti, M. Sortino, G. Totis, E. Vaglio, On the factors influencing the elastoplastic cyclic response and low cycle fatigue failure of AISI 316L steel produced by laser-powder bed fusion, International Journal of Fatigue, 165 (2022) 107224.

[110] G.S.M. Martins, R.P.P.D. da Silva, L. Beckedorff, A.S. Monteiro, K.V. de Paiva, J.L.G. Oliveira, Fatigue performance evaluation of plate and shell heat exchangers, International Journal of Pressure Vessels and Piping, 188 (2020) 104237.

[111] C.-H. Yu, A. Leicht, R.L. Peng, J. Moverare, Low cycle fatigue of additively manufactured thin-walled stainless steel 316L, Materials Science and Engineering: A, 821 (2021) 141598.

[112] N. Spignoli, G. Minak, Influence on Fatigue Strength of Post-Process Treatments on Thin-Walled AlSi10Mg Structures Made by Additive Manufacturing, Metals, 2023.

[113] N. Ahmad, S. Shao, M. Seifi, N. Shamsaei, Additively manufactured IN718 in thin wall and narrow flow channel geometries: Effects of post-processing and wall thickness on tensile and fatigue behaviors, Additive Manufacturing, 60 (2022) 103264.

[114] W. Faes, S. Lecompte, Z.Y. Ahmed, J. Van Bael, R. Salenbien, K. Verbeken, M. De Paepe, Corrosion and corrosion prevention in heat exchangers, Corrosion reviews, 37 (2019) 131-155.

[115] R. Siva, G. Mageshwaran, S. Kallat, J. Jeevahan, Experimental investigation on the effect of corrosion and erosion on the shell and tube-type heat exchanger, International Journal of Ambient Energy, 42 (2021) 816-822.

[116] P. Renner, S. Jha, Y. Chen, A. Raut, S.G. Mehta, H. Liang, A Review on Corrosion and Wear of Additively Manufactured Alloys, Journal of Tribology, 143 (2021).

[117] Y. Liu, Y. Yang, D. Wang, A study on the residual stress during selective laser melting (SLM) of metallic powder, The International Journal of Advanced Manufacturing Technology, 87 (2016) 647-656.

[118] L. Mugwagwa, I. Yadroitsava, N.W. Makoana, I. Yadroitsev, 9 - Residual stress in laser powder bed fusion, in: I. Yadroitsev, I. Yadroitsava, A. du Plessis, E. MacDonald (Eds.) Fundamentals of Laser Powder Bed Fusion of Metals, Elsevier, 2021, pp. 245-276.

[119] S.-g. Chen, H.-j. Gao, Y.-d. Zhang, Q. Wu, Z.-h. Gao, X. Zhou, Review on residual stresses in metal additive manufacturing: formation mechanisms, parameter dependencies, prediction and control approaches, Journal of Materials Research and Technology, 17 (2022) 2950-2974.

[120] D. Xie, F. Lv, Y. Yang, L. Shen, Z. Tian, C. Shuai, B. Chen, J. Zhao, A Review on Distortion and Residual Stress in Additive Manufacturing, Chinese Journal of Mechanical Engineering: Additive Manufacturing Frontiers, 1 (2022) 100039.

[121] H.M. Khan, Y. Karabulut, O. Kitay, Y. Kaynak, I.S. Jawahir, Influence of the post-processing operations on surface integrity of metal components produced by laser powder bed

fusion additive manufacturing: a review, Machining Science and Technology, 25 (2021) 118-176.

[122] C. Li, Z.Y. Liu, X.Y. Fang, Y.B. Guo, Residual Stress in Metal Additive Manufacturing, Procedia CIRP, 71 (2018) 348-353.

[123] A. Martin, M. San Sebastian, E. Gil, C.Y. Wang, S. Milenkovic, M.T. Pérez-Prado, C.M. Cepeda-Jiménez, Effect of the heat treatment on the microstructure and hardness evolution of a AlSi10MgCu alloy designed for laser powder bed fusion, Materials Science and Engineering: A, 819 (2021) 141487.

[124] S. Papula, M. Song, A. Pateras, X.-B. Chen, M. Brandt, M. Easton, Y. Yagodzinskyy, I. Virkkunen, H. Hänninen, Selective Laser Melting of Duplex Stainless Steel 2205: Effect of Post-Processing Heat Treatment on Microstructure, Mechanical Properties, and Corrosion Resistance, Materials, 12 (2019) 2468.

[125] C. Zitelli, P. Folgarait, A. Di Schino, Laser Powder Bed Fusion of Stainless Steel Grades: A Review, Metals, 9 (2019) 731.

[126] H. Chen, C. Zhang, D. Jia, D. Wellmann, W. Liu, Corrosion Behaviors of Selective Laser Melted Aluminum Alloys: A Review, Metals, 10 (2020) 102.

[127] B. Mahesh, Machine learning algorithms-a review, International Journal of Science and Research (IJSR).[Internet], 9 (2020) 381-386.

[128] I.H. Sarker, Machine Learning: Algorithms, Real-World Applications and Research Directions, SN Computer Science, 2 (2021) 160.

[129] M. Alloghani, D. Al-Jumeily, J. Mustafina, A. Hussain, A.J. Aljaaf, A systematic review on supervised and unsupervised machine learning algorithms for data science, Supervised and unsupervised learning for data science, (2020) 3-21.

[130] S.B. Kotsiantis, I. Zaharakis, P. Pintelas, Supervised machine learning: A review of classification techniques, Emerging artificial intelligence applications in computer engineering, 160 (2007) 3-24.

[131] R. Nian, J. Liu, B. Huang, A review On reinforcement learning: Introduction and applications in industrial process control, Computers & Chemical Engineering, 139 (2020) 106886.

[132] L. Meng, B. McWilliams, W. Jarosinski, H.-Y. Park, Y.-G. Jung, J. Lee, J. Zhang, Machine Learning in Additive Manufacturing: A Review, JOM, 72 (2020) 2363-2377.

[133] S.S. Razvi, S. Feng, A. Narayanan, Y.-T.T. Lee, P. Witherell, A Review of Machine Learning Applications in Additive Manufacturing, ASME 2019 International Design Engineering Technical Conferences and Computers and Information in Engineering Conference, 2019.

[134] X. Qi, G. Chen, Y. Li, X. Cheng, C. Li, Applying Neural-Network-Based Machine Learning to Additive Manufacturing: Current Applications, Challenges, and Future Perspectives, Engineering, 5 (2019) 721-729.

[135] M. Marrey, E. Malekipour, H. El-Mounayri, E.J. Faierson, A Framework for Optimizing Process Parameters in Powder Bed Fusion (PBF) Process Using Artificial Neural Network (ANN), Procedia Manufacturing, 34 (2019) 505-515.

[136] N. Phadke, R. Raj, A. Kumar Srivastava, S. Dwivedi, A. Rai Dixit, Modeling and parametric optimization of laser powder bed fusion 3D printing technique using artificial neural network for enhancing dimensional accuracy, Materials Today: Proceedings, 56 (2022) 873-878.

[137] K. Taherkhani, C. Eischer, E. Toyserkani, An unsupervised machine learning algorithm for in-situ defect-detection in laser powder-bed fusion, Journal of Manufacturing Processes, 81 (2022) 476-489.

[138] S. Dharmadhikari, N. Menon, A. Basak, A reinforcement learning approach for process parameter optimization in additive manufacturing, Additive Manufacturing, 71 (2023) 103556.

[139] Q. Jiang, P. Zhang, Z. Yu, H. Shi, D. Wu, H. Yan, X. Ye, Q. Lu, Y. Tian, A Review on Additive Manufacturing of Pure Copper, Coatings, 11 (2021) 740.

[140] M.H.N. Parameswaran, A. Anand, S.R. Krishnamurthy, A Comparison of Corrosion Behavior of Copper and Its Alloy in Pongamia pinnata Oil at Different Conditions, Journal of Energy, 2013 (2013) 932976.

[141] The Engineering Toolbox, Solid, Liquid, and Gases - Thermal Conductivities. https://www.engineeringtoolbox.com/thermal-conductivity-d_429.html (accessed on 27 February 2022).

[142] Psyclops, Density of materials.; http://www.psyclops.com/tools/technotes/materials/density.html (accessed on 27 February 2022).

[143] MetalMiner, MetalMiner Prices: Price feeds, embedded forecasts, should-cost models, 2022. https://agmetalminer.com/metal-prices/. (accessed on 27 February 2022).

[144] A. Zadi-Maad, R. Rohib, A. Irawan, Additive manufacturing for steels: a review, IOP Conference Series: Materials Science and Engineering, IOP Publishing, 2018, pp. 012028.

[145] N. Haghdadi, M. Laleh, M. Moyle, S. Primig, Additive manufacturing of steels: a review of achievements and challenges, Journal of Materials Science, 56 (2021) 64-107.

[146] R.I. Revilla, M. Van Calster, M. Raes, G. Arroud, F. Andreatta, L. Pyl, P. Guillaume, I. De Graeve, Microstructure and corrosion behavior of 316L stainless steel prepared using

different additive manufacturing methods: A comparative study bringing insights into the impact of microstructure on their passivity, Corrosion Science, 176 (2020) 108914.

[147] Z. Yang, Y. Yu, Y. Wei, C. Huang, Crushing behavior of a thin-walled circular tube with internal gradient grooves fabricated by SLM 3D printing, Thin-Walled Structures, 111 (2017) 1-8.

[148] B. Cantor, H. Assender, P. Grant, Aerospace materials, CRC Press, 2015.

[149] M. Karmuhilan, S. Kumanan, A Review on Additive Manufacturing Processes of Inconel 625, Journal of Materials Engineering and Performance, (2021).

[150] A.N. Jinoop, C.P. Paul, S.K. Mishra, K.S. Bindra, Laser Additive Manufacturing using directed energy deposition of Inconel-718 wall structures with tailored characteristics, Vacuum, 166 (2019) 270-278.

[151] P.R. Gradl, D.C. Tinker, J. Ivester, S.W. Skinner, T. Teasley, J.L. Bili, Geometric feature reproducibility for laser powder bed fusion (L-PBF) additive manufacturing with Inconel 718, Additive Manufacturing, 47 (2021) 102305.

[152] S. Liu, Y.C. Shin, Additive manufacturing of Ti6Al4V alloy: A review, Materials & Design, 164 (2019) 107552.

[153] E. Uhlmann, R. Kersting, T.B. Klein, M.F. Cruz, A.V. Borille, Additive Manufacturing of Titanium Alloy for Aircraft Components, Procedia CIRP, 35 (2015) 55-60.

[154] C. Chen, Z. Xiao, H. Zhu, X. Zeng, Deformation and control method of thin-walled part during laser powder bed fusion of Ti–6Al–4V alloy, The International Journal of Advanced Manufacturing Technology, 110 (2020) 3467-3478.

[155] J. Gockel, J. Fox, J. Beuth, R. Hafley, Integrated melt pool and microstructure control for Ti–6Al–4V thin wall additive manufacturing, Materials Science and Technology, 31 (2015) 912-916.

[156] T.J. Horn, D. Gamzina, Additive Manufacturing of Copper and Copper Alloys, in: D.L. Bourell, W. Frazier, H. Kuhn, M. Seifi (Eds.) Additive Manufacturing Processes, ASM International, 2020, pp. 0.

[157] X. Tang, X. Chen, F. Sun, P. Liu, H. Zhou, S. Fu, The current state of CuCrZr and CuCrNb alloys manufactured by additive manufacturing: A review, Materials & Design, 224 (2022) 111419.

[158] B. Blakey-Milner, P. Gradl, G. Snedden, M. Brooks, J. Pitot, E. Lopez, M. Leary, F. Berto, A. du Plessis, Metal additive manufacturing in aerospace: A review, Materials & Design, 209 (2021) 110008.

[159] P.R. Gradl, T.W. Teasley, C.S. Protz, M.B. Garcia, D. Ellis, C. Kantzos, Advancing GRCop-based Bimetallic Additive Manufacturing to Optimize Component Design and Applications for Liquid Rocket Engines, AIAA Propulsion and Energy 2021 Forum, American Institute of Aeronautics and Astronautics, 2021.

[160] P. Gradl, C. Protz, K. Cooper, C. Garcia, D. Ellis, L. Evans, GRCop-42 Development and Hot-fire Testing Using Additive Manufacturing Powder Bed Fusion for Channel-Cooled Combustion Chambers. https://ntrs.nasa.gov/api/citations/20190030461/downloads/20190030461.pdf (accessed on 02 July 2023).

[161] W.D. Callister, An introduction: material science and engineering, John Wiley and Sons Inc, (2007).

[162] J. Davis, ASM specialty handbook, Aluminum and aluminum alloys, (1993) 207-216.

[163] G. Rödler, F.G. Fischer, J. Preußner, V. Friedmann, C. Fischer, A. Weisheit, J.H. Schleifenbaum, Additive manufacturing of high-strength eutectic aluminium-nickel alloys –

Processing and mechanical properties, Journal of Materials Processing Technology, 298 (2021) 117315.

[164] D. Zhang, S. Sun, D. Qiu, M.A. Gibson, M.S. Dargusch, M. Brandt, M. Qian, M. Easton, Metal alloys for fusion-based additive manufacturing, Advanced Engineering Materials, 20 (2018) 1700952.

[165] J.C. Benedyk, Additive Manufacturing od Aluminium Alloys, 2018. https://www.lightmetalage.com/news/industry-news/3d-printing/article-additive-manufacturing-of-aluminum-alloys/. (accessed on 27 February 2022).

[166] C. Kliemt, Thermo-mechanical Fatigue of Cast Aluminium Alloys for Engine Applications Under Severe Conditions, Heriot-Watt University, 2012.

[167] S.C. Altıparmak, V.A. Yardley, Z. Shi, J. Lin, Challenges in additive manufacturing of high-strength aluminium alloys and current developments in hybrid additive manufacturing, International Journal of Lightweight Materials and Manufacture, 4 (2021) 246-261.

[168] A. Aversa, G. Marchese, A. Saboori, E. Bassini, D. Manfredi, S. Biamino, D. Ugues, P. Fino, M. Lombardi, New Aluminum Alloys Specifically Designed for Laser Powder Bed Fusion: A Review, Materials, 12 (2019) 1007.

[169] 3T Additive Manufacturing Ltd., Aluminium A20XTM Material Data Sheet. https://www.3t-am.com/sites/threeT/files/Aluminium%20A20X_Datasheet.pdf (accessed on 02 March 2022).

[170] EOS GmbH, EOS Aluminium AlSi10Mg Material Data Sheet. https://www.eos.info/03_system-related-assets/material-related-contents/metal-materials-and-examples/metal-material-datasheet/aluminium/material_datasheet_eos_aluminium-alsi10mg_en_web.pdf (accessed on 02 March 2022).

[171] M. Awd, J. Tenkamp, M. Hirtler, S. Siddique, M. Bambach, F. Walther, Comparison of Microstructure and Mechanical Properties of Scalmalloy® Produced by Selective Laser Melting and Laser Metal Deposition, Materials, 11 (2018) 17.

[172] M.L. Montero-Sistiaga, R. Mertens, B. Vrancken, X. Wang, B. Van Hooreweder, J.-P. Kruth, J. Van Humbeeck, Changing the alloy composition of Al7075 for better processability by selective laser melting, Journal of Materials Processing Technology, 238 (2016) 437-445.

[173] M.A. Green, Self-consistent optical parameters of intrinsic silicon at 300K including temperature coefficients, Solar Energy Materials and Solar Cells, 92 (2008) 1305-1310.

[174] W.R. Osório, N. Cheung, J.E. Spinelli, P.R. Goulart, A. Garcia, The effects of a eutectic modifier on microstructure and surface corrosion behavior of Al-Si hypoeutectic alloys, Journal of Solid State Electrochemistry, 11 (2007) 1421-1427.

[175] W.M. Haynes, CRC Handbook of Chemistry and Physics, CRC Press, 2016.

[176] N.T. Aboulkhair, I. Maskery, C. Tuck, I. Ashcroft, N.M. Everitt, The microstructure and mechanical properties of selectively laser melted AlSi10Mg: The effect of a conventional T6-like heat treatment, Materials Science and Engineering: A, 667 (2016) 139-146.

[177] A.I.H. Committee, ASM Handbook, ASM International, 1990.

[178] L. Xi, D. Gu, S. Guo, R. Wang, K. Ding, K.G. Prashanth, Grain refinement in laser manufactured Al-based composites with TiB2 ceramic, Journal of Materials Research and Technology, 9 (2020) 2611-2622.

[179] H.R. Kotadia, G. Gibbons, A. Das, P.D. Howes, A review of Laser Powder Bed Fusion Additive Manufacturing of aluminium alloys: Microstructure and properties, Additive Manufacturing, 46 (2021) 102155.

[180] B.S. Murty, S.A. Kori, M. Chakraborty, Grain refinement of aluminium and its alloys by heterogeneous nucleation and alloying, International Materials Reviews, 47 (2002) 3-29.

[181] P. Rometsch, Q. Jia, K. V. Yang, X. Wu, 14 - Aluminum alloys for selective laser melting – towards improved performance, in: F. Froes, R. Boyer (Eds.) Additive Manufacturing for the Aerospace Industry, Elsevier, 2019, pp. 301-325.

[182] Z. Ahmad, The properties and application of scandium-reinforced aluminum, JOM, 55 (2003) 35-39.

[183] N.T. Aboulkhair, M. Simonelli, L. Parry, I. Ashcroft, C. Tuck, R. Hague, 3D printing of Aluminium alloys: Additive Manufacturing of Aluminium alloys using selective laser melting, Progress in Materials Science, 106 (2019) 100578.

[184] Y. Li, D. Gu, Parametric analysis of thermal behavior during selective laser melting additive manufacturing of aluminum alloy powder, Materials & Design, 63 (2014) 856-867.

[185] A. Hadadzadeh, B.S. Amirkhiz, S. Shakerin, J. Kelly, J. Li, M. Mohammadi, Microstructural investigation and mechanical behavior of a two-material component fabricated through selective laser melting of AlSi10Mg on an Al-Cu-Ni-Fe-Mg cast alloy substrate, Additive Manufacturing, 31 (2020) 100937.

[186] S.I. Shakil, A. Hadadzadeh, B. Shalchi Amirkhiz, H. Pirgazi, M. Mohammadi, M. Haghshenas, Additive manufactured versus cast AlSi10Mg alloy: Microstructure and micromechanics, Results in Materials, 10 (2021) 100178.

[187] C.A. Biffi, P. Bassani, J. Fiocchi, M. Albu, A. Tuissi, Selective laser melting of AlCu-TiB2 alloy using pulsed wave laser emission mode: processability, microstructure and mechanical properties, Materials & Design, 204 (2021) 109628.

[188] S. Lathabai, Chapter 2 - Additive Manufacturing of Aluminium-Based Alloys and Composites, in: R.N. Lumley (Ed.) Fundamentals of Aluminium Metallurgy, Woodhead Publishing, 2018, pp. 47-92.

[189] B.K. Milligan, S. Roy, C.S. Hawkins, L.F. Allard, A. Shyam, Impact of microstructural stability on the creep behavior of cast Al–Cu alloys, Materials Science and Engineering: A, 772 (2020) 138697.

[190] P. Li, Y. Kim, A.C. Bobel, L.G. Hector, A.K. Sachdev, S. Kumar, A.F. Bower, Microstructural origin of the anisotropic flow stress of laser powder bed fused AlSi10Mg, Acta Materialia, 220 (2021) 117346.

[191] E. Strumza, O. Yeheskel, S. Hayun, The effect of texture on the anisotropy of thermophysical properties of additively manufactured AlSi10Mg, Additive Manufacturing, 29 (2019) 100762.

[192] N. Limbasiya, A. Jain, H. Soni, V. Wankhede, G. Krolczyk, P. Sahlot, A comprehensive review on the effect of process parameters and post-process treatments on microstructure and mechanical properties of selective laser melting of AlSi10Mg, Journal of Materials Research and Technology, (2022).

[193] J. Bi, Z. Lei, Y. Chen, X. Chen, N. Lu, Z. Tian, X. Qin, An additively manufactured Al-14.1Mg-0.47Si-0.31Sc-0.17Zr alloy with high specific strength, good thermal stability and excellent corrosion resistance, Journal of Materials Science & Technology, 67 (2021) 23-35.

[194] S.I. Shakil, L. González-Rovira, L. Cabrera-Correa, J. de Dios López-Castro, M. Castillo-Rodríguez, F.J. Botana, M. Haghshenas, Insights into laser powder bed fused Scalmalloy®: investigating the correlation between micromechanical and macroscale properties, Journal of Materials Research and Technology, 25 (2023) 4409-4424.

[195] L. Cabrera-Correa, L. González-Rovira, J. de Dios López-Castro, M. Castillo-Rodríguez, F.J. Botana, Effect of the heat treatment on the mechanical properties and microstructure of Scalmalloy® manufactured by Selective Laser Melting (SLM) under certified conditions, Materials Characterization, 196 (2023) 112549.

[196] J. Bi, Z. Lei, Y. Chen, X. Chen, Z. Tian, X. Qin, J. Liang, X. Zhang, Effect of Al3(Sc, Zr) and Mg2Si precipitates on microstructure and tensile properties of selective laser melted Al-14.1Mg-0.47Si-0.31Sc-0.17Zr alloy, Intermetallics, 123 (2020) 106822.

[197] J.H. Martin, B.D. Yahata, J.M. Hundley, J.A. Mayer, T.A. Schaedler, T.M. Pollock, 3D printing of high-strength aluminium alloys, Nature, 549 (2017) 365-369.

[198] Y.K. Xiao, Z.Y. Bian, Y. Wu, G. Ji, Y.Q. Li, M.J. Li, Q. Lian, Z. Chen, A. Addad, H.W. Wang, Effect of nano-TiB2 particles on the anisotropy in an AlSi10Mg alloy processed by selective laser melting, Journal of Alloys and Compounds, 798 (2019) 644-655.

[199] N.O. Larrosa, W. Wang, N. Read, M.H. Loretto, C. Evans, J. Carr, U. Tradowsky, M.M. Attallah, P.J. Withers, Linking microstructure and processing defects to mechanical properties of selectively laser melted AlSi10Mg alloy, Theoretical and Applied Fracture Mechanics, 98 (2018) 123-133.

[200] A.B. Spierings, K. Dawson, P. Dumitraschkewitz, S. Pogatscher, K. Wegener, Microstructure characterization of SLM-processed Al-Mg-Sc-Zr alloy in the heat treated and HIPed condition, Additive Manufacturing, 20 (2018) 173-181.

[201] F. Jiang, L. Tang, S. Li, H. Ye, M.M. Attallah, Z. Yang, Achieving strength-ductility balance in a laser powder bed fusion fabricated TiB2/Al–Cu-Mg-Ag alloy, Journal of Alloys and Compounds, 945 (2023) 169311.

[202] M. Ghasri-Khouzani, H. Karimialavijeh, M. Pröbstle, R. Batmaz, W. Muhammad, A. Chakraborty, T.D. Sabiston, J.P. Harvey, É. Martin, Processability and characterization of A20X aluminum alloy fabricated by laser powder bed fusion, Materials Today Communications, 35 (2023) 105555.

[203] J. Fiocchi, A. Tuissi, C.A. Biffi, Heat treatment of aluminium alloys produced by laser powder bed fusion: A review, Materials & Design, 204 (2021) 109651.

[204] M. Zamani, S. Toschi, A. Morri, L. Ceschini, S. Seifeddine, Optimisation of heat treatment of Al–Cu–(Mg–Ag) cast alloys, Journal of Thermal Analysis and Calorimetry, 139 (2020) 3427-3440.

[205] P. Ponnusamy, R.A. Rahman Rashid, S.H. Masood, D. Ruan, S. Palanisamy, Mechanical properties of SLM-printed aluminium alloys: a review, Materials, 13 (2020) 4301.

[206] N. Read, W. Wang, K. Essa, M.M. Attallah, Selective laser melting of AlSi10Mg alloy: Process optimisation and mechanical properties development, Materials & Design (1980-2015), 65 (2015) 417-424.

[207] MakeItFrom, https://www.makeitfrom.com/material-properties/A201.0-A201.0-T7-A12010-Cast-Aluminum (accessed on 07 March 2022).

[208] Eckart, A20X™ – the strongest aluminium alloy. Worldwide. https://eckart.net/de/en/microsite/am (accessed on 07 March 2022).

[209] MakeItFrom, EN AC-43000 (AlSi10Mg(a)) Cast Aluminum. https://www.makeitfrom.com/material-properties/EN-AC-43000-AlSi10Mga-Cast-Aluminum (accessed on 07 March 2022).

[210] D. Koutny, D. Skulina, L. Pantělejev, D. Paloušek, B. Lenczowski, F. Palm, A. Nick, Processing of Al-Sc aluminum alloy using SLM technology, Procedia CIRP, 74 (2018) 44-48.

[211] P. Fathi, M. Mohammadi, X. Duan, A.M. Nasiri, Effects of Surface Finishing Procedures on Corrosion Behavior of DMLS-AlSi10Mg_200C Alloy Versus Die-Cast A360.1 Aluminum, JOM, 71 (2019) 1748-1759.

[212] A. Leon, E. Aghion, Effect of surface roughness on corrosion fatigue performance of AlSi10Mg alloy produced by Selective Laser Melting (SLM), Materials Characterization, 131 (2017) 188-194.

[213] T. Rubben, R.I. Revilla, I. De Graeve, Influence of heat treatments on the corrosion mechanism of additive manufactured AlSi10Mg, Corrosion Science, 147 (2019) 406-415.

[214] A. Zakay, E. Aghion, Effect of Post-heat Treatment on the Corrosion Behavior of AlSi10Mg Alloy Produced by Additive Manufacturing, JOM, 71 (2019) 1150-1157.

[215] G. Sander, J. Tan, P. Balan, O. Gharbi, D. Feenstra, L. Singer, S. Thomas, R. Kelly, J.R. Scully, N. Birbilis, Corrosion of additively manufactured alloys: a review, Corrosion, 74 (2018) 1318-1350.

[216] L. Girelli, M. Tocci, L. Montesano, M. Gelfi, A. Pola, Investigation of cavitation erosion resistance of AlSi10Mg alloy for additive manufacturing, Wear, 402-403 (2018) 124-136.

[217] A. Leon, A. Shirizly, E. Aghion, Corrosion Behavior of AlSi10Mg Alloy Produced by Additive Manufacturing (AM) vs. Its Counterpart Gravity Cast Alloy, Metals, 6 (2016) 148.

[218] P. Wang, A. Gebert, L. Yan, H. Li, C. Lao, Z. Chen, K. Kosiba, U. Kühn, S. Scudino, Corrosion of Al-3.5Cu-1.5 Mg–1Si alloy prepared by selective laser melting and heat treatment, Intermetallics, 124 (2020) 106871.

[219] Y. Guo, G.S. Frankel, Characterization of trivalent chromium process coating on AA2024-T3, Surface and Coatings Technology, 206 (2012) 3895-3902.

[220] R. Saillard, S. Zanna, A. Seyeux, B. Fori, J. Światowska, C. Blanc, P. Marcus, Influence of ageing on the corrosion behaviour of 2024 aluminium alloy coated with a trivalent chromium conversion layer, Corrosion Science, 182 (2021) 109192.

[221] A.C. Bouali, M. Serdechnova, C. Blawert, J. Tedim, M.G.S. Ferreira, M.L. Zheludkevich, Layered double hydroxides (LDHs) as functional materials for the corrosion protection of aluminum alloys: A review, Applied Materials Today, 21 (2020) 100857.

[222] R.M. Bandeira, J. van Drunen, A.C. Garcia, G. Tremiliosi-Filho, Influence of the thickness and roughness of polyaniline coatings on corrosion protection of AA7075 aluminum alloy, Electrochimica Acta, 240 (2017) 215-224.

[223] M. Zheludkevich, I.M. Salvado, M. Ferreira, Sol–gel coatings for corrosion protection of metals, Journal of Materials Chemistry, 15 (2005) 5099-5111.

[224] H. Takahashi, M. Sunada, T. Kikuchi, M. Sakairi, S. Hirai, Formation of Al-Si Composite Oxide Films on Aluminum by Electrophoretic Sol-Gel Coating / Anodizing, in: P. Marcus, V. Maurice (Eds.) Passivation of Metals and Semiconductors, and Properties of Thin Oxide Layers, Elsevier Science, Amsterdam, 2006, pp. 685-690.

[225] F. Simchen, M. Sieber, A. Kopp, T. Lampke, Introduction to Plasma Electrolytic Oxidation—An Overview of the Process and Applications, Coatings, 10 (2020) 628.

[226] Heat Treating of Aluminum and Its Alloys, in: G.E. Totten (Ed.) Heat Treating of Nonferrous Alloys, ASM International, 2016, pp. 0.

[227] A.B. Spierings, K. Dawson, K. Kern, F. Palm, K. Wegener, SLM-processed Sc- and Zr-modified Al-Mg alloy: Mechanical properties and microstructural effects of heat treatment, Materials Science and Engineering: A, 701 (2017) 264-273.

[228] C.N. Kuo, P.C. Peng, D.H. Liu, C.Y. Chao, Microstructure Evolution and Mechanical Property Response of 3D-Printed Scalmalloy with Different Heat-Treatment Times at 325 °C, Metals, 11 (2021) 555.

[229] S. Baig, S.R. Ghiaasiaan, N. Shamsaei, Effect of Heat Treatment on the Microstructure and Mechanical Properties of LB-PBF AlSi10Mg and Scalmalloy, Light Metals 2021, Springer, 2021, pp. 119-125.

[230] X. Yu, L. Wang, T6 heat-treated AlSi10Mg alloys additive-manufactured by selective laser melting, Procedia Manufacturing, 15 (2018) 1701-1707.

[231] A. Sarentica, Conventional heat treatment of additively manufactured AlSi10Mg, 2019.

[232] V. Mára, J. Krčil, L. Pilsová, Problematic of heat treatment and its influence on mechanical properties of selectively laser melted AlSi10Mg alloy, The International Journal of Advanced Manufacturing Technology, (2022).

[233] B.J. Mfusi, N.R. Mathe, L.C. Tshabalala, P.A. Popoola, The Effect of Stress Relief on the Mechanical and Fatigue Properties of Additively Manufactured AlSi10Mg Parts, Metals, 9 (2019) 1216.

[234] Carpenter Additive, Scalmalloy Data Sheet. https://f.hubspotusercontent10.net/hubfs/6205315/Resources/Data%20Sheets/20210624--Scalmalloy_Datasheet_Digital_F.pdf (accessed on 07 March 2022).

[235] F. Belelli, R. Casati, F. Larini, M. Riccio, M. Vedani, Investigation on two Ti–B-reinforced Al alloys for Laser Powder Bed Fusion, Materials Science and Engineering: A, 808 (2021) 140944.

[236] L. Girelli, M. Tocci, M. Gelfi, A. Pola, Study of heat treatment parameters for additively manufactured AlSi10Mg in comparison with corresponding cast alloy, Materials Science and Engineering: A, 739 (2019) 317-328.

[237] F. Belelli, R. Casati, M. Riccio, A. Rizzi, M.Y. Kayacan, M. Vedani, Development of a Novel High-Temperature Al Alloy for Laser Powder Bed Fusion, Metals, 11 (2021) 35.

# CHAPTER 3. Methodology

This chapter outlines the methodologies used to produce, characterise and evaluate the high-strength Al alloys of the research. The experimental procedures were designed to ensure the reliability of the data acquired. Each subchapter details the techniques applied to investigate a specific area of characterisation. A wide range of processes and characterisations were employed during the study and are described below.

## 3.1 Materials

The high-strength Al alloys used in this study were A205 and AlSi10Mg. Both materials were obtained in metal powder form, from different suppliers. The details and properties of each powder are described below.

The batch of gas-atomised A205 spherical powder was supplied by Aeromet Ltd., now acquired by Eckart, an Altana group. The batch of AlSi10Mg, produced using plasma atomisation, was instead acquired from TECKNA Advanced Materials.

The analysis of particle size for metal powder used in L-PBF is crucial for optimising the process and achieving high-standard components. Particle size distribution (PSD) directly influences powder flowability, packing density, and laser absorption, which affect the meltpool formation and therefore the final properties of the fabricated components [1, 2]. The powder size distribution of the acquired materials was measured according to standard ASTM B822-20 [3] and the results are shown in Figure 3.1. Both materials are characterised by a Gaussian distribution with a peak near a powder size of 30 - 40 μm. In particular, the average powder sizes calculated for the analysed distribution were 33.29 μm and 39.97 μm for A205 and AlSi10Mg alloys, respectively. The results highlighted the good quality of the acquired powder, suitable for the L-PBF process.

a)

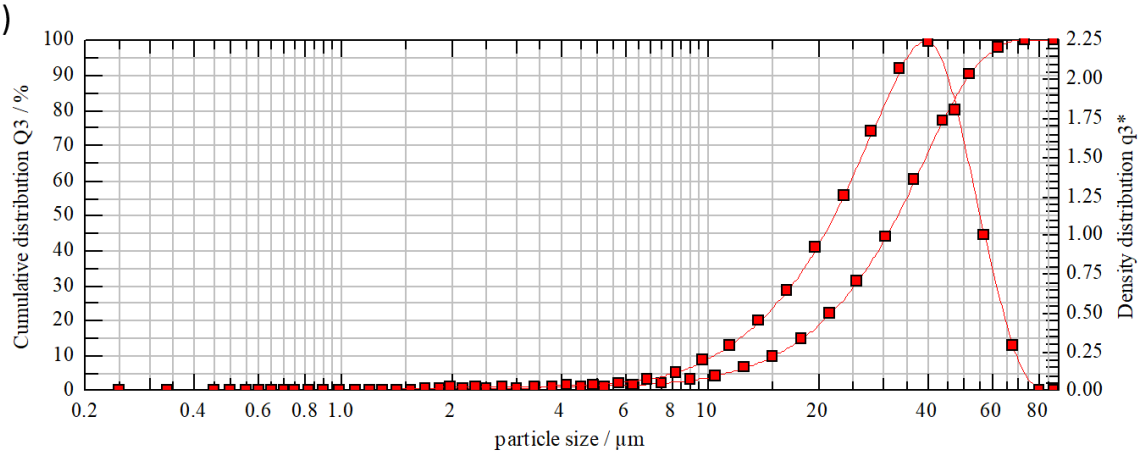


b)

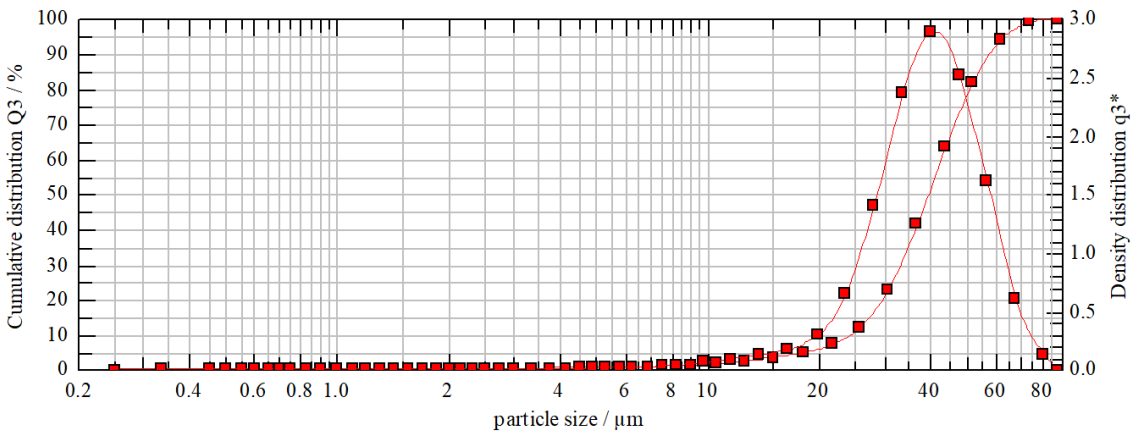


c)

| Material | D10 (µm) | D50 (µm) | D90 (µm) |
|---|---|---|---|
| A205 alloy | 15.22 | 32.79 | 51.43 |
| AlSi10Mg alloy | 23.83 | 39.24 | 58.05 |

Figure 3.1. Powder particle characterisation for high-strength Al alloys used in the study. Powder size distribution for a) A205 alloy and b) AlSi10Mg alloy; c) powder size values for A205 and AlSi10Mg alloys.

Additionally, the morphology of the powder was assessed using Scanning Electron Microscopy (SEM) to analyse the sphericity, surface, and presence of agglomerates which could impact negatively on the deposition and melting of the layers. The images captured through SEM are shown in Figure 3.2. Both powders are characterised by spherical geometry, and no large presence of agglomerations or satellites was found. In particular, the A205 alloy showed higher concentrations of smaller particles, which could decrease the spreadability, but overall both powders were considered free from defects.

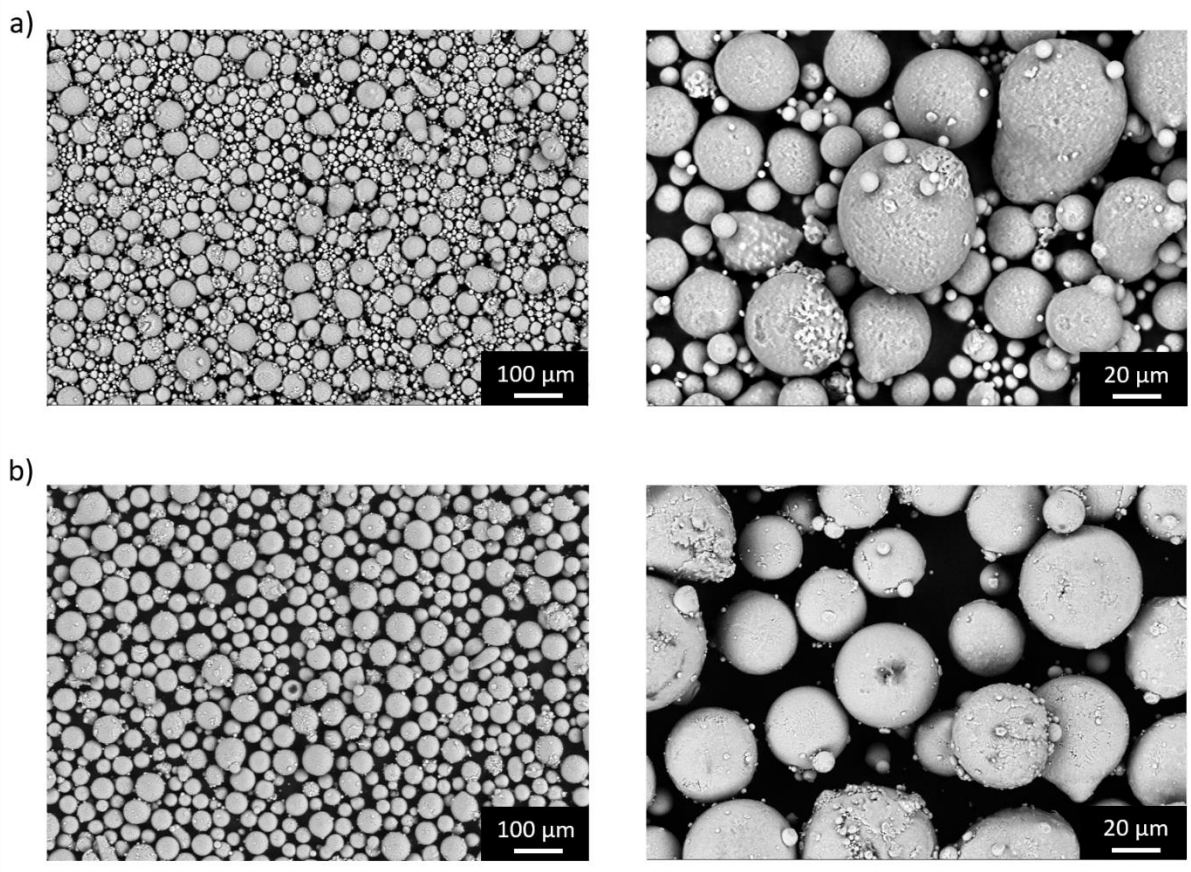


Figure 3.2. Morphology characterisation for the high-strength Al alloys used in the study. SEM images at different magnifications for a) A205 alloy and b) AlSi10Mg alloy.

Finally, the chemical composition of the powder was analysed to quantify each alloy present in the material. The analysis was carried out using Inductively Coupled Plasma (ICP) according to the standard ASTM E3061-17 [4]. The results are presented in Table 3.1.

Table 3.1. Chemical composition for the high-strength Al alloys used in the study, A205 and AlSi10Mg.

| **Chemical Composition [w%]** | | | | | | | | | |
|---|---|---|---|---|---|---|---|---|---|
| **Material** | **Al** | **Si** | **Mg** | **Cu** | **Fe** | **Ti** | **B** | **Ag** | **Ni** |
| **A205** | Bal. | 0.1 | 0.24 | 4.49 | 0.04 | 2.4 | 0.91 | 0.71 | - |
| **AlSi10Mg** | Bal. | 11 | 0.45 | <0.1 | - | - | - | - | <0.05 |

## 3.2 L-PBF Systems

Two L-PBF systems were used in the study, Concept Laser M2 Cusing and SLM 500 HL. Both machines are very similar in characteristics and working operation. The details of each machine are presented below.

### 3.2.1 Concept Laser M2 Cusing

The Concept Laser M2 Cusing is produced and distributed by GE Additive. It is equipped with a single continuous fibre laser source with a maximum power of 400W. Laser power calibration was performed regularly during the study, maintaining an optimal laser spot of 67 μm and a Gaussian laser beam distribution. All manufacturing processes were performed under an inert atmosphere using argon, with a level of oxygen less than 0.1%. The system was equipped with a powder handling chamber where the set-up of the build was carried out. In particular, powder sieving, powder pouring on the powder feeding area, and substrate levelling were performed for each build. Two different building volume kits were used in the study. The optimisation of process parameters was carried out using a Reduced Building Volume (RBV) characterised by a building envelope of 90 x 90 x100 mm in length, width and height, respectively. The other builds were carried out using the maximum build volume chamber of 250 x 250 s 280 mm. The powder spreading was performed using a flexible rubber blade. An image of the Concept laser M2 Cusing is presented in Figure 3.3.

Prior to the build, the design to be manufactured was designed using CAD software such as Solidworks and Autodesk Fusion 360, and exported in STL format. Then, the files were imported into the slices software compatible with the machine, Materialise Magics, where the settings of layer thickness, BC, CD, and scanning strategy were set. Finally, the sliced files were imported into the L-PBF system, where the process parameters were set.


Figure 3.3. Concept Laser M2 Cusing system [5].

During the set-up, the substrate in Al alloy was fixed to the building platform and the powder of both the powder feeding and build platform was levelled. Once the set-up was completed, the entire module was moved to the processing chamber on the right side of the machine, accommodating the laser and mirror system. When the build was completed, the module was moved back to the handling chamber and filled with argon. The powder was collected, and the substrate was removed from the machine.

In particular, the A205 Al alloy was manufactured using exclusively the Concept Laser M2 Cusing.

### 3.2.2 SLM 500 HL

The SLM 500 HL is an industrial L-PBF system produced and distributed by Nikon SLM Solutions. The machine is characterised by a 500 x 280 x 325 mm build envelope, and a dual-beam setup, with a 400 W and 1000 W laser firing from the same print head. The system version

used in this study had two such print heads, making it possible for 2 lasers to work in tandem, each for half of the build volume, with a central area of overlap. Figure 3.4 shows a representation of the SLM 500 HL system.


Figure 3.4. SLM 500 HL system [6].

The machine was supplied with an automated powder management technology, using a continuous conveyance system, decreasing the overall setup and manufacturing time. A single chamber was used for both preparation and printing, while a separate glovebox was used for depowdering and substrate setup. As for the other L-PBF system, the manufacturing of samples was carried out in an inert gas atmosphere, argon, with a level of oxygen less than 0.02%. The setup included the placement of an Al alloy substrate on the building platform, carried out in the glovebox. The substrate was then placed inside the machine from the left side. The powder spreading was carried out using a gravity recoater equipped with a flexible rubber blade. After

the levelling of the powder on the substrate, the build was initialised. As for the Concept Laser M2 Cusing the components were first designed using CAD software and then imported to Materialise Magics to create the sliced file compatible with the SLM 500 HL system.

All lasers of the machine were regularly tested and calibrated. In particular, the 400 W lasers were characterised by a Gaussian profile and an average laser spot size of 80 μm, while the 1000 W lasers were composed of many small laser beams converging to the same point, increasing the average total spot size, characterised by an average evaluated diameter of 630 μm. The SLM 500 HL offered a wide selection of process parameters compared to the Concept Laser M2 Cusing, including up-skin and down-skin process parameters, and scanning strategies.

The SLM 500 HL, due to its limit in changing metal powder due to its size and automated conveying system, was employed for the manufacturing of the AlSi10Mg alloy.

## 3.3 Machine Learning Approaches

In this study, Machine Learning (ML) approaches were applied in an interdisciplinary context, combining principles from material science and data science to enhance data analysis and prediction accuracy. The application of diverse fields allowed for the optimisation of L-PBF process parameters, enabling efficient identifications of the relationship between material properties and the L-PBF processing system. This subchapter outlines the ML-based techniques employed in this study.

### 3.3.1 Computer Vision

An Artificial Intelligence (AI) driven approach was used to analyse the extensive dataset of SEM images collected during the study, with a particular focus on Computer Vision techniques. Computer Vision enables the digital processing of data derived from images, video, and other

visual sources, facilitating more precise and efficient data analysis [7]. The particular method used in the study was the development of a Canny Edge Detection Algorithm (CEDA) [8], to analyse images of structures produced during the study, captured using SEM microscopy. This approach provided an improvement in the accuracy and speed of data analysis.

Initially, each image was converted to greyscale, assigning a pixel value from 0 (black) to 255 (white). The CEDA algorithm was then applied to detect the edges of the structure under analysis. The pixel length of the scale bar related to the image was measured and converted by dividing it by the pixel count, and subsequently, the scale bar was removed from the image to avoid any interference with the measurement process. The CEDA was then performed and the coordinates of the detected edges were acquired along all the structures to calculate the overall average measurement.

### 3.3.2 Neural Networks (NN)

The Neural Network (NN) [9] developed in this work was used for the optimisation study of L-PBF process parameters of the high-strength Al alloys. The NN featured two hidden layers, each including five nodes. Each of the nodes within the hidden layer and the output layer was defined by an activation function and an associated set of weights, used to increase the efficiency of the model.

Two NNs were used in this study. The first NN was employed to predict optimal L-PBF process parameters (laser power, scan speed, and hatch spacing) for density, aiming for the discovery of a good processability window for the material. The second NN was used to understand the relationship between BC and CD and the geometrical and dimensional accuracy of thin features. The model was applied to predict the optimal parameters, fixing the other L-PBF process parameters.

For both NNs, the activation functions applied were the Rectified Linear Unit (ReLu) and the sigmoid function [10]. Each hidden layer node utilised the ReLU function, chosen for its computational efficiency, while the sigmoid function was employed in the output layer to enhance model reliability in predicting RD. The Mean Squared Error (MSE) was selected as the cost function, being widely used in neural networks, with backpropagation applied to further refine model performance [9, 11]. Given the limited experimental data available for both optimisation studies, hyperparameter tuning was conducted to improve model accuracy. This tuning process helped to minimise the risks of overfitting and underfitting, enhancing the robustness of the NN models.

## 3.4 Characterisation Methods for L-PBF Process Analysis

This subchapter provides a detailed overview of the characterisation techniques employed in this study to analyse and understand the material properties critical to my research objectives. Each technique was selected based on its suitability for investigating specific aspects of the materials, such as structural, chemical, mechanical, and others.

### 3.4.1 Metallurgical Preparation

The samples were initially sectioned, either along the build direction, on plane XZ, or orthogonal to the build direction, on plane XY. The sectioning was carried out using either an Electrical Discharge Machining (EDM) or a precision saw cutting machine, a Buehler IsoMet 5000. Then the samples were manually mounted using cold resin, or placed in an automatic system, the Presidon ML-P mounting machine, to be mounted in conductive bakelite. The samples were then subjected to several cycles of grinding and polishing using a Struers Tegramin-25 system. In the first grinding step, a disc with different roughness was employed, from a grade of #120 to #4000, and water was used as a cooling and grinding liquid. Later on,

the polishing was divided into two steps, where the first was performed using a DAC disc with 3 µm diamond suspension, while the second step was carried out using a CHEM disc and a silica suspension of 0.25 µm to ensure an acceptable surface finishing scratch-free suitable for all the several characterisation techniques.

### 3.4.2 Density and Porosity Measurements

The methodologies employed to analyse the density of the material after the manufacturing via L-PBF were Archimedes density and porosity analysis. The Archimedes density measurement was used to determine the bulk density based on Archimedes' principle. The tests were carried out following the standards ASTM F3637-23 [12] and ASTM B311-22 [13].

Each sample was first weighed in air and then in a liquid of known density, in this case, ethanol. Looking at the temperature of the liquid the correlated density was used and the density measurement was calculated using the following Equation 3.1.

$$Archimedes\ Density = \frac{m_{air}}{m_{air} - m_{liq}} \rho_{liq} \qquad \text{Equation 3.1}$$

The analysis of density was also carried out in further detail at a microstructural level using microscopy images of the sectioned samples. Images were acquired using different types of microscopy, in particular optical microscope and SEM, and then quantitatively analysed using ImageJ, a Java-based processing software designed for scientific purposes. The porosity analysis in ImageJ involved several steps. First, each image was converted to greyscale, to enhance the contrast between solid material and pores. Then the image was subjected to a threshold to highlight any voids inside the image. Once the right threshold was set, the software calculated the area fraction of the voids in relation to the total area analysed.

### 3.4.3 Microscopy

The study involved the use of several microscopy techniques, each tailored for a specific purpose. In particular, optimal microscopy, SEM, and optical profilometers were employed to evaluate a wide range of properties of the material, from pores to microstructural changes, and from surface roughness to fractography analysis.

Optical microscopy was carried out using a digital microscope, the Keyence VHX-7000 4K, capable of acquiring images in a wide range of magnifications and equipped with a motorised stage and image stitching tool. The optical microscope was used to capture images for relative density analysis and corrosion analysis, allowing for the identification of defects' size and distribution.

SEM was employed to achieve a higher resolution in the analysis of the material properties. The SEM used in the study, the HITACHI TM4000, was equipped with both backscatter electron (BSE) and secondary electron (SE) to acquire a wide range of structural details. BSE was used to gain insights into the composition through the difference in contrast of the different element compositions, while SE provided a high resolution of the surface topography, allowing for detailed analysis of features such as fractography, and grain boundaries. Additionally, energy-dispersive X-ray spectrography (EDX) was used to perform elemental analysis of specific regions of interest.

Finally, an Alicona InfiniteFocus profilometer was used to obtain quantitative data on the surface. The optical profilometer provides three-dimensional surface measurements combining both microscopy and contact profilometry. The Alicona system was employed to acquire measurements of surface roughness, tribological tracks and corrosion analysis, crucial for understanding the performance of the material in critical conditions.

### 3.4.4 Electron Backscatter Diffraction (EBSD)

Electron Backscatter Diffraction (EBSD) measurements were carried out to analyse the grain size and generate IPF maps for microstructural samples. In particular, a JEOL JCM-7000F equipped with EBSD was used in the study. The analysis was carried out using a step size of 0.1 μm, at a magnification of x10000 using a tension voltage of 20 kV. Texture measurements were performed using the IPF maps, but the aim of the EBSD mapping was the calculation of grain size.

The raw data was initially processed using the software ATEX. This tool helped in refining and cleaning the EBSD map, increasing the EBSD data quality. Then, the grain size measurement was calculated using the ATEX software, which gives in return the average, and min & max of the grain size of the map.

### 3.4.5 Transmission Electron Microscopy (TEM)

The TEM analysis was carried out during the study of the development of a new heat treatment for the A205 alloy. The TEM analysis was conducted with the support of the Henry Royce Institute through the Student Equipment Access Scheme, at the University of Sheffield, using a JEOL JEM-F200 equipped with EDX.

The samples for the TEM were generated using a Focused Ion Beam (FIB) technique, allowing for the fabrication of very thin specimens, ideal for TEM analysis. TEM-EDX were performed at high magnification in order to verify the presence of precipitation in the material, while High Angle Annular Dark-Field (HAADF) imaging was carried out at different magnifications to identify the presence and quantitatively assess the size and distribution of phases in the material.

### 3.4.6 X-ray Diffraction (XRD)

The structural characterisation of the alloys was performed using the X-Ray Diffraction (XRD) technique. XRD is a non-destructive analytical method that provides information on the phase composition and crystallographic structure of a material. The XRD system used in the study was a benchtop PROTO AXRD.

In this study, the XRD system was equipped with a copper line-focus X-ray tube. The analysis was carried out using a Bragg-Brentano (BB) geometry. Furthermore, the parameters used during the analysis were characterised by an angle range of 2θ between 20° and 100°, with a step size of 0.05° and a dwell time of 1 s. All the acquired raw data were then processed using the crystallographic software CrystalDiffract.

### 3.4.7 Micro-Hardness

The evaluation of the hardness of the material was carried out using Vickers micro-hardness testing. The semi-automated micro-hardness machine equipped with a Vickers indenter used in the study was a Wilson VH1202.

The samples were polished before the hardness analysis and the indentations were performed using both manual location and pattern, such as lines, and matrix. A load of 0.1 Kg and a minimum distance of two times the biggest diagonal was used during the testing. After each indentation optical images were acquired automatically from the software, at a magnification of x50. The software was then automatically evaluating the value of the diagonals, and calculating the correlated hardness. Each measurement was then manually validated, and if necessary, the measurement of the diagonal was manually adjusted. Multiple measurements were taken across the sample to ensure statistical reliability and to capture potential variations in hardness due to microstructural differences.

### 3.4.8 Differential Scanning Calorimetry (DSC)

Differential Scanning Calorimetry (DSC) was employed as a thermal analysis technique to investigate the phase transitions of the materials studied. The results acquired through DSC played an essential role in the design and development of heat treatments. The DSC system used in the study was a Netzsch STA 449 F3 Jupiter.

In this study, DSC measurements were performed using a heating a cooling cycle between room temperature and a max temperature of 550°C, using a heating and cooling rate of 10 °C/min. A pure Al was used as reference material, and the test was performed in an inert atmosphere using argon.

## 3.5 Post-Processing Treatments

The study of the influence of post-processing treatments on the material's performance was evaluated, focused in particular on heat treatments and surface treatments. These post-processing treatments enable the tailoring of the material's mechanical, thermal, tribological and corrosion properties to meet specific application requirements. The post-processing treatments applied in the study are explained below.

### 3.5.1 Heat Treatments

Heat treatment is a critical process for heat-treatable Al alloys, allowing for the enhancement of properties such as strength, hardness, and ductility by altering the alloy's microstructure. In this study, heat treatment procedures of solution and quenching, and artificial ageing were performed on the A205 Al alloy to study the influence on the material microstructure and mechanical properties. Typical solution temperatures for Al alloys are in the range of 500°C - 550°C for a long time, allowing alloying elements to dissolve into the matrix. Usually, solution treatments are followed by quenching in water or glycol to "freeze" the alloying elements in a

supersaturated solid solution, avoiding the precipitation of phases and creating a positive condition for the following step of artificial ageing. Typical temperatures of the latter are in the range of 150°C - 200°C for extensive dwell times, allowing the precipitation of strengthening phases [14].

The heat treatments evaluated in the study were several. In particular, a standard T7 HT, and a commercial HT, were applied to the Al alloy. Furthermore, the development of an optimised HT was performed and compared to the existing ones. Solution HT was carried out using a Carbolite Gero CWF 1200 furnace, equipped with Molybdenum heating elements, and the quenching was performed using water. Finally, the artificial ageing step was performed using an industrial Elite convection oven.

### 3.5.2 Surface Treatment

The surface treatment employed in this study was the Plasma Electrolytic Oxidation (PEO) process. PEO is an advanced eco-friendly electrochemical process that forms a hard, ceramic-like oxide layer on the surface of light metals such as Al alloys, enhancing the hardness, tribological and corrosion resistance of the materials [15].

The PEO process includes the immersion of the metal substrate in an alkaline electrolyte solution and the application of a high-voltage current, either pulsed DC or AC, across the electrolyte. Due to the high voltage, plasma micro-discharges are generated on the metal surface, causing localised melting and oxidation. This high-energy reaction promotes the growth of a dense and porous oxide layer, which becomes strongly bonded to the substrate due to the high-temperature conditions. The oxide layer typically consists of aluminium oxide ($Al_2O_3$), providing excellent hardness and corrosion resistance. A representation of the schematic process is represented in Figure 3.5. For this study, the PEO coatings were applied to both Al alloys, A205 and AlSi10Mg. The treatment was performed on samples with different

surface preparations, in particular as-fabricated and polished. For the polished configuration, samples underwent initial grinding and polishing to significantly lower the surface roughness introduced by the L-PBF process.

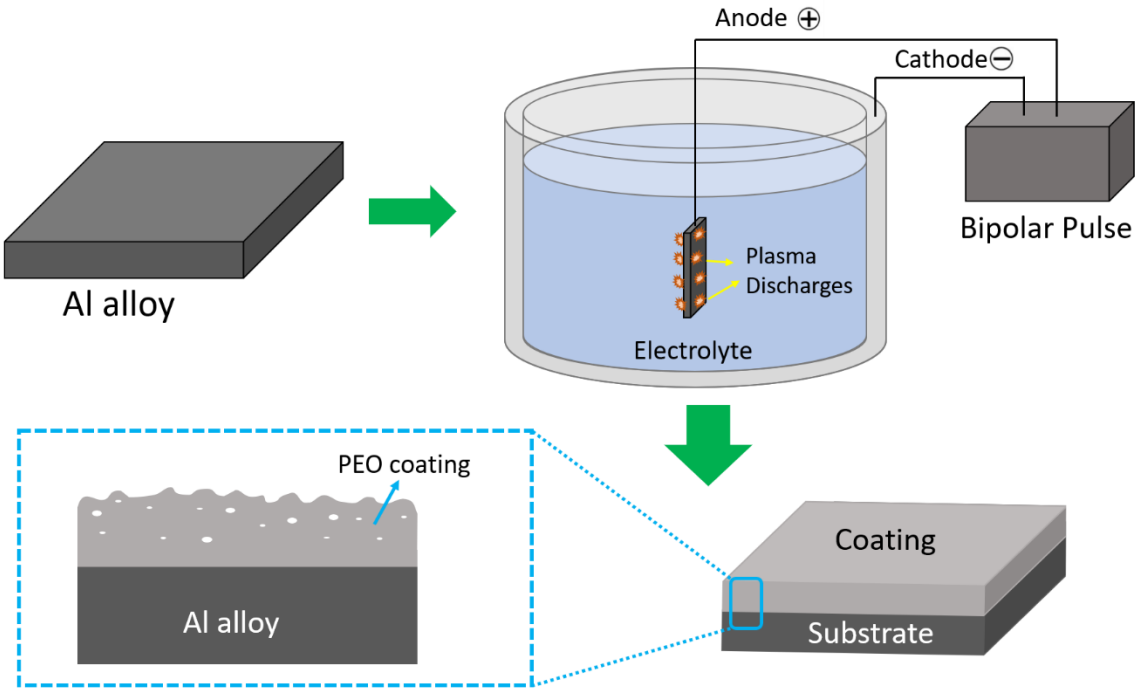


Figure 3.5. Schematisation of Plasma Electrolytic Oxidation (PEO) process.

The PEO treatment was conducted by Cambridge Nanolitic Limited, a company specialising in advanced coating technologies. The PEO coating was applied using three distinct alkaline electrolytes, each containing varied concentrations of phosphate and silicate. The electrolytes used were as follows:

- Lean (L) electrolyte: An alkaline solution with less than 1 g/l of phosphate and less than 0.5 g/l of silicate.
- Medium (M) electrolyte: An alkaline solution with less than 1 g/l of phosphate and up to 1.5 g/l of silicate.
- Rich (R) electrolyte: An alkaline solution containing up to 2.5 g/l of phosphate and 5 g/l of silicate.

The A205 alloy samples were successfully coated with all three electrolyte types, while only the Rich (R) electrolyte was suitable for the AlSi10Mg alloy, due to its high silicon content.

For all samples, the PEO process was carried out using a "soft sparking" electrical mode, employing bipolar pulse sequences with applied voltages reaching up to 650 V.

## 3.6 Mechanical Testing

The performance of the materials studied was evaluated using different mechanical testing methods. Mechanical tests are essential to understand how materials respond under various loading conditions, which is crucial for assessing materials' suitability in specific applications. In this study, tensile, fatigue and creep testing were performed to investigate the materials' performances, and are described below.

### 3.6.1 Tensile testing

In this study, uniaxial tensile tests were conducted, applying a controlled tensile force, to determine properties such as ultimate tensile strength, yield strength, and elongation. The tensile testing was performed using a Zwick/Roell 1484. The system was characterised by a load cell of 100 kN, designed for both tensile and compression testing. An extensometer was already present in the machine, making setup operations easier. Furthermore, the software interface included the setup of all the important factors for the testing.

The tensile tests were carried out using dogbone specimens fabricated in both vertical and horizontal directions. The design of the specimen and the tensile test were designed and conducted according to the standard ASTM E8/E8M – 22 [16]. The tests were performed at room temperature, with three repetitions for each condition, at a loading rate of 0.39 mm/min. An extensometer was attached to the gauge length of the specimen to record displacement

throughout the duration of the test. Fractographic analysis was conducted using SEM to examine fracture surfaces.

### 3.6.2 Fatigue testing

Fatigue testing was performed to evaluate the material's resistance to cyclic loading, assessing its behaviour under repeated stresses below the ultimate tensile strength. In particular, in this study, the specimens were subjected to high-cycle fatigue testing at room temperature using an electromagnetic resonance fatigue machine. This type of machine uses a mechanical resonator in connection with an electromagnetic drive to generate a resonant frequency vibration that drives the cyclic loading of the sample. The machine is designed to operate at the material's or machine's natural resonant frequency, with typical resonant frequencies in the range of 20-300 Hz. For the Al alloys used in the study, a frequency of 78-80 Hz was reached for all the tested conditions. The particular design of this machine allows for reaching millions of cycles within a short period, making it highly efficient for fatigue testing. The fatigue test specimens were designed and evaluated in accordance with standard ASTM E466 – 21 [17] and were tested in both vertical and horizontal orientations. Testing of all the specimens, horizontal and vertical, was carried out under a fixed load set to 60% of the yield strength (180 MPa) of the as-fabricated vertical condition. Three repetitions were conducted for each orientation at room temperature. Fractographic analysis was conducted using SEM to examine fracture surfaces.

### 3.6.3 Creep testing

Creep testing was used to assess the material's ability to resist deformation under constant load at elevated temperatures over a prolonged period, critical in components that operate in environments where prolonged exposure to stress can lead to gradual deformation and failure. In this study, the uniaxial creep test in force control mode employs a high load to minimise the

duration of the test. Creep tests were performed using an Instron 8862, on specimens manufactured along the horizontal direction only, to minimise the effect of metallurgical defects. The creep test was conducted on specimens designed and evaluated in accordance with standard ASTM E139–11 [18]. A uniaxial load of 200 MPa was applied at a constant temperature of 180°C. The specimens were subjected to a preload until the target test temperature was reached, followed by a stabilisation period of 30 minutes to ensure uniform temperature distribution. The elongation was recorded for the entire duration of the test.

## 3.7 Tribological testing

Tribological testing is essential for evaluating the wear resistance and frictional behaviour of materials, particularly in applications where surface durability and low friction are critical. In this study, a linear reciprocating ball-on-disk test, schematised in Figure 3.6b, was conducted to investigate the tribological properties of the materials. The wear tests were conducted following the standard ASTM G133-22 [19], using a Phoenix Tribology Tester, depicted in Figure 3.6a.

The tests employed $Al_2O_3$ balls with a diameter of 10 mm as the counterpart. The tests were performed at room temperature using a fixed load of 10 N, and a sliding velocity of 5 mm/s, for a total of 500 cycles. The coefficient of friction (CoF) was measured using the dedicated software provided with the tribometer.

Images of the wear tracks were captured using scanning electron microscopy (SEM) and an Alicona optical profilometer to assess wear characteristics and surface degradation. Additionally, the Alicona profilometer was used to calculate the wear volume loss and wear rate for each testing condition.

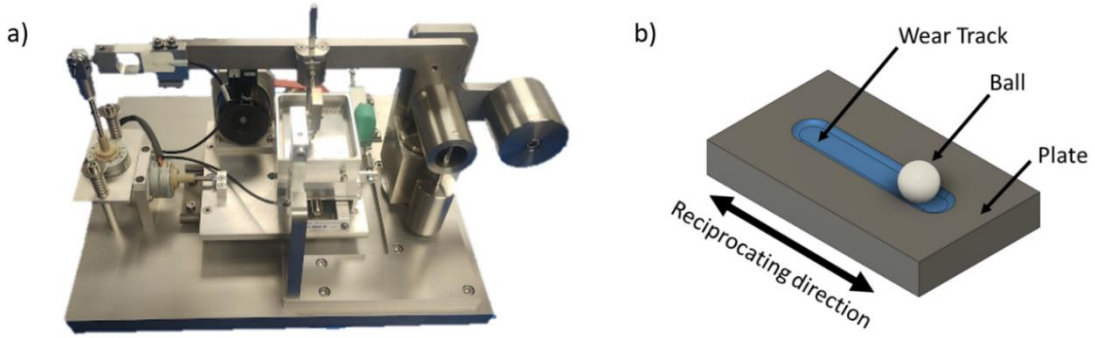


Figure 3.6. Tribology testing system. a) tribological system used in the study, a Phoenix Tribology Tester; b) Schematisation of Linearly Reciprocating Ball-on-Flat Sliding Wear.

In particular wear loss was calculated as the volume of the wear track, while the wear rate was determined in compliance with standard ASTM G133-22 [19], expressed as the wear volume loss per unit sliding distance, calculated by multiplying the linear slide distance by the total test duration.

## 3.8 Corrosion testing

The performance of the materials in severe environments was evaluated through corrosion testing, and, in particular, the Salt Fog Test. The salt fog test is widely used to evaluate the corrosion resistance of materials and coatings by introducing them into a simulated corrosive environment that accelerates the natural corrosion process. This method is particularly relevant in assessing materials used in marine, automotive, and aerospace applications, where exposure to salt and humidity is common. An overview of the salt fog test is represented in Figure 3.7. During the test, the specimens are placed in a sealed chamber where a continuous mist of a saline solution, typically 5% sodium chloride (NaCl), is sprayed. This salt fog creates a highly corrosive environment, simulating prolonged exposure to saline conditions.

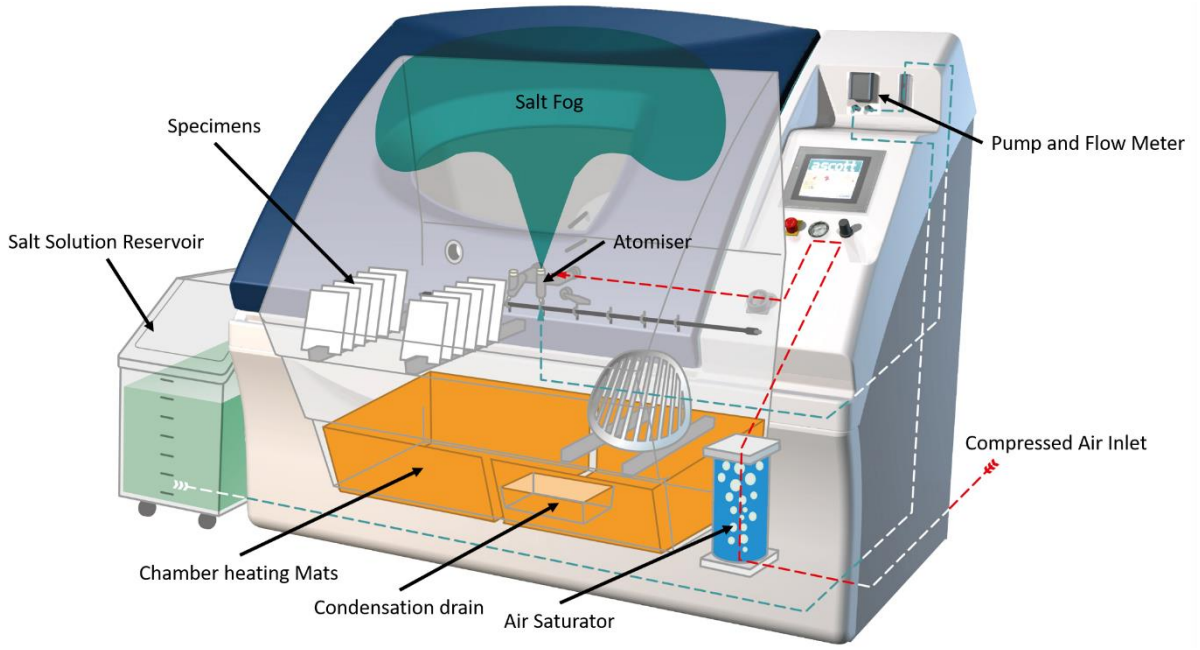


Figure 3.7. Schematisation of the Salt Fog Test, detailing the components of the system and the operations [20].

In this study, the salt fog test was carried out externally, in a calibrated salt fog chamber in TWI Ltd, Cambridge. Testing was conducted in accordance with standard ASTM B117-19 [21], using an exposure period of 96 hours in a saline environment created by dissolving sodium chloride in deionised water. The saline liquid was generated using water and a saline concentration of 4.0 – 6.0 % by weight, and the pH value of the atomised salt solution was constantly monitored and was in the range of 6.5 – 7.2. The chamber temperature was kept between 33°C and 37°C, while the collection rate of atomised salt solution was around 1.0 – 3.0 ml/hour. The samples were first weighted using a precision scale with an accuracy of four decimal places, and then placed in the chamber. Visual inspections were conducted at 24-hour intervals to monitor and document the effects of the salt environment on the samples. After the completion of the test, the specimens were removed from the chamber, rinsed with clean running water to eliminate any surface salt deposits and subsequently dried. Corrosion products were then removed following the standard ASTM G1-03 [22] by placing the samples in an ultrasonic bath containing a solution of $HNO_3$ in water (at a concentration of 70% by volume)

at 90°C for a duration of 10 minutes. Following this cleaning procedure, the specimens were weighted using the precision scale in order to calculate the mass loss. The average corrosion rate was then determined based on the mass loss, as specified in the standard ASTM G1-03 [22], providing a quantitative measure of material degradation under the test conditions. Finally, the samples were examined using a digital microscope to assess the extent of damage incurred during the salt fog test. This high-resolution imaging allowed for detailed visualisation and documentation of corrosion features, providing insights into the surface degradation and morphological changes caused by exposure to the salt environment.

# References

[1] S.E. Brika, M. Letenneur, C.A. Dion, V. Brailovski, Influence of particle morphology and size distribution on the powder flowability and laser powder bed fusion manufacturability of Ti-6Al-4V alloy, Additive Manufacturing, 31 (2020) 100929.

[2] L. Haferkamp, L. Haudenschild, A. Spierings, K. Wegener, K. Riener, S. Ziegelmeier, G.J. Leichtfried, The Influence of Particle Shape, Powder Flowability, and Powder Layer Density on Part Density in Laser Powder Bed Fusion, Metals, 11 (2021) 418.

[3] A. B822-20, Standard Test Method for Particle Size Distribution of Metal Powders and Related Compounds by Light Scattering, 2020.

[4] A. E3061-17, Standard Test Method for Analysis of Aluminum and Aluminum Alloys by Inductively Coupled Plasma Atomic Emission Spectrometry (Performance Based Method), 2017.

[5] GEAdditive, M Line L-PBF Printer, https://www.colibriumadditive.com/printers/l-pbf-printers/m-line. (accessed on 25 January 2025).

[6] N.S. Solutions, SLM Systems, https://nikon-slm-solutions.com/slm-systems/. (accessed on 25 January 2025).

[7] J. Chai, H. Zeng, A. Li, E.W.T. Ngai, Deep learning in computer vision: A critical review of emerging techniques and application scenarios, Machine Learning with Applications, 6 (2021) 100134.

[8] J. Canny, A Computational Approach to Edge Detection, IEEE Transactions on Pattern Analysis and Machine Intelligence, PAMI-8 (1986) 679-698.

[9] M. Paliwal, U.A. Kumar, Neural networks and statistical techniques: A review of applications, Expert Systems with Applications, 36 (2009) 2-17.

[10] T. Szandała, Review and Comparison of Commonly Used Activation Functions for Deep Neural Networks, in: A.K. Bhoi, P.K. Mallick, C.-M. Liu, V.E. Balas (Eds.) Bio-inspired Neurocomputing, Springer Singapore, Singapore, 2021, pp. 203-224.

[11] C.M. Bishop, Neural networks and their applications, Review of Scientific Instruments, 65 (1994) 1803-1832.

[12] A. F3637-23, Standard Guide for Additive Manufacturing of Metal — Finished Part Properties — Methods for Relative Density Measurement, 2023.

[13] A. B311-22, Standard Test Method for Density of Powder Metallurgy (PM) Materials Containing Less Than Two Percent Porosity, 2022.

[14] Heat Treating of Aluminum and Its Alloys, in: G.E. Totten (Ed.) Heat Treating of Nonferrous Alloys, ASM International, 2016, pp. 0.

[15] C. Berlanga-Labari, M.V. Biezma-Moraleda, P.J. Rivero, Corrosion of Cast Aluminum Alloys: A Review, Metals, 10 (2020) 1384.

[16] A. E8/E8M-22, Standard Test Methods for Tension Testing of Metallic Materials, 2022.

[17] A. E466-21, Standard Practice for Conducting Force Controlled Constant Amplitude Axial fatigue test of Metallic Materials, 2021.

[18] A. E139-11, Standard Test Methods for Conducting Creep, Creep-Rupture, and Stress-Rupture Tests of Metallic Materials, 2018.

[19] A. G133-22, Standard Test Method for Linearly Reciprocating Ball-on-Flat Sliding Wear, 2022.

[20] Ascott-Analytical, CCT Chambers – Salt Spray Mode – how it works, https://www.ascott-analytical.com/how-chambers-work/cct-chambers-salt-spray-mode-how-it-works/. (accessed on 25 November 2024).

[21] A. B117-19, Standard Practice for Operating Salt Spray (Fog) Apparatus, 2019.

[22] A. G1-03(2017)e1, Standard Practice for Preparing, Cleaning, and Evaluating Corrosion Test Specimens, 2017.

# CHAPTER 4. Application of Machine Learning in Optimisation of L-PBF technology for Al alloys

This chapter is part of a scientific paper that has been published in the Journal 'The International Journal of Advanced Manufacturing Technology'. The paper's details and co-authors' contributions are outlined below.

**Francesco Careri,** Leonardo Stella, Raja H.U. Khan, Moataz M. Attallah, Application of Machine Learning in Additive Manufacturing of a Novel Al Alloy Heat Exchanger, The International Journal of Advanced Manufacturing Technology, 2025, https://doi.org/10.1007/s00170-025-15389-y.

**Francesco Careri:** Conceptualisation, Data curation, Investigation, Methodology, Validation, Visualisation, Writing – original draft, Writing - review and editing.

**Leonardo Stella:** Data curation, Methodology, Software, Writing - review and editing.

**Raja H.U. Khan:** Conceptualisation, Funding acquisition, Supervision, Writing – review and editing.

**Moataz M. Attallah:** Conceptualisation, Funding acquisition, Methodology, Resources, Supervision, Writing – review and editing.

# Graphical Abstract

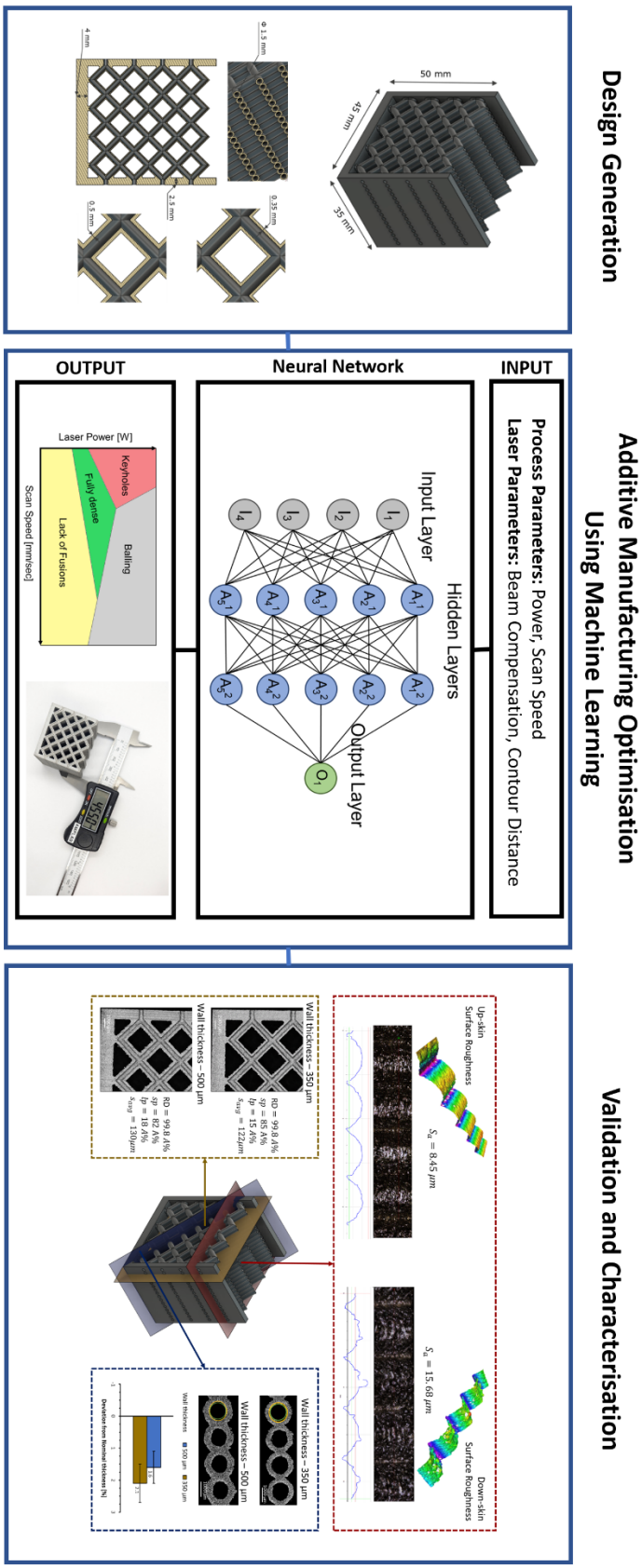

# Abstract

Additive Manufacturing (AM) of complex geometries faces limitations in the dimensional and geometrical accuracy, especially when the geometries are characterised by thin features designed to tailor the mechanical and thermal properties of novel Heat Exchangers (HXs). In this work, a novel, complex, thin hollow-walled lattice compact HX was fabricated using the Powder Bed Fusion-Laser Beam on Metal (PBF-LB/M) process. Given the intricate relationships between process parameters and complex design, Machine Learning (ML) methods were utilised to optimise the manufacturing workflow. Although new ML models would be required for different cases to ensure optimal performance, the flexibility of such approaches allows for recalibration and re-optimisation whenever there are changes to material properties, geometry, or manufacturing settings. A process map for the A205 Aluminium alloy was generated, investigating metallurgical defects and surface quality. Optimal process parameters for defect-free materials were estimated using a Neural Network (NN). Further optimisation evaluated the influence of laser parameters, Beam Compensation (BC) and Contour Distance (CD), on the geometrical and dimensional accuracy of thin features, with a second NN predicting optimal BC and CD. Thickness deviations in hollow lattices were reduced to under 2%. A prototype of the novel HX using optimised parameters was successfully fabricated and characterised to evaluate manufacturing feasibility. The analysis of pores in thin features, potentially leading to leakage and part failure, was carried out through SEM analysis. While PBF-LB/M is well-established for HXs, this study demonstrates its capability for manufacturing highly complex, thin-walled designs when guided by ML-based optimisation.

## 4.1 Introduction

There is growing attention on Additive Manufacturing (AM) for the development of novel Heat Exchangers (HXs), aiming to enhance thermal properties while achieving compactness and lightweight designs. Among AM technologies, Laser-Powder bed Fusion (L-PBF) has emerged as a preferred manufacturing method for the fabrication of high-performance HXs, in particular for aerospace and automotive applications [1, 2], where the demand for high-efficiency, lightweight thermal management is critical. Other AM technologies, such as Directy Energy Deposition (DED-LB/powder) and Wire Arc Additive Manufacturing (WAAM), are also employed for HX production. However, their applicability is mainly suitable for larger components, characterised by simpler geometries and lower tolerance requirements [3]. While DED and WAAM offer advantages like increased build volume and faster production speed compared to L-PBF [4], their lower resolution and limited design flexibility make them unsuitable for the accurate production of highly complex HXs characterised by thin features. L-PBF offers instead high precision and the ability to produce intricate designs characterised by thin-walled features, making this technology suitable for complex high-efficiency HX applications. Conventional manufacturing strategies, including machining and brazing, impose limitations on design complexity and often require multiple steps, leading to increased production time. Additionally, conventional manufacturing processes have reached their limits in improving the weight-to-performance ratio of manufacturable components [5]. In traditional manufacturing, the design of relatively simple geometries often results in heavier components due to the need for joining multiple sections. Moreover, achieving fine, thin features or complex internal structures essential for optimising heat transfer performance is challenging with conventional processes. L-PBF offers solutions to these constraints by enabling the fabrication of complex geometries such as lattice structures [5, 6], which enhance the thermal properties of

HXs while maintaining structural integrity and reduced weight [7, 8]. Recent studies have demonstrated the potential of L-PBF in advancing HX performance. For example, Ning et al. compared AM and conventional manufacturing strategies for finned HXs, revealing that the additively manufactured component exhibited superior thermal properties compared to the conventional counterpart. Furthermore, topological optimisation, enabled by AM technologies such as L-PBF, has allowed the creation of micro-architected designs, such as gyroid structures, that are impossible to manufacture with traditional strategies. Mahmoud et al. explored in their study the geometrical and thermal performance of HX generated using gyroid lattice structures. The authors employed Computational Fluid Dynamics (CFD) to analyse the correlation between several designs and HX properties, such as pressure drop and thermal conductivity. Prototypes were fabricated using AlSi10Mg via L-PBF process and then compared to conventional HX designs. The additively manufactured prototypes outperformed the conventional counterparts, achieving superior thermal performance through optimised geometries and manufacturing parameters.

Despite the advancements in AM technologies, modelling and optimising the L-PBF process remain challenging due to the complex relationships between process parameters and part quality. In particular, the production of intricate geometries, achieving dimensional accuracy, structural integrity and defect-free components is difficult and influenced by process parameters such as laser power, scan speed, hatch spacing, and layer thickness [5, 9, 10]. Unoptimised process parameters tend to generate metallurgical defects such as porosity, keyholes and lack of fusion, which can compromise both mechanical properties and the overall performance of the HX. The process parameters significantly influence defect formation and dimensional accuracy by affecting the thermal gradient and heat input during the PBF-LB/M process [11]. The phenomena occurring during the process generate thermal stresses, possibly causing part

distortion and even failure. In addition to optimising process parameters, modern PBF-LB/M technologies employe baseplate preheating as a strategy to mitigate these challenges. This approach, if combined with process parameters optimisation, could guarantee a more uniform thermal history, reducing thermal gradients between the substrate and deposited layers [12]. As a result, a decrease in residual stresses could lead to a reduction of defect formation and distortion, enhancing part quality [13]. Furthermore, the complexity of HXs poses challenges in terms of geometrical accuracy, surface roughness, and powder removal [14]. Several studies have addressed the manufacturing limits of L-PBF for thin complex features characterising HXs. Wu et al. [15] addressed the manufacturing limits of thin walls using PBF-LB/M, focusing on the influence of several materials and scan strategies on thin walls. Micro-computed Tomography (CT) was performed to analyse the distribution of the porosity inside the thin walls and assess the influence of design, material and scan strategy on the dimensions, surface roughness, and structural integrity. The results of the study emphasised the importance of optimising process parameters to minimise defects and ensure high accuracy and performance. Similarly, Tan et al. [16] investigated the influence of process parameters on the geometrical and dimensional integrity of TiNi lattices produced via L-PBF. In particular, the authors carried out a full optimisation for the L-PBF process parameters and analysed the deviation in strut size. After identifying the optimal process parameters for high density, the best combination of parameters to enable the manufacturing of accurate thin struts was tested and evaluated through microscopy highlighting the achievement of geometrical control.

However, the complexity of L-PBF lies in the intricate physical phenomena occurring during the process. The challenges in processing modelling emphasise these challenges. Stavropoulos et al. [17] highlighted in their study the intensive computational burden when simulating the thermal and physical interaction during L-PBF essential to accurately predict melt pool and

porosity formation. The authors proposed a multi-scale thermal modelling approach based on the enthalpy method, showing an increased efficiency in predicting the critical phenomena occurring during the process achieving good accuracy. Similarly, Foteinopoulos et al. [18] demonstrated how space-partitioning and dynamic mesh adaptation could significantly reduce simulation times by over 70% while maintaining the accuracy of the outcomes. The authors optimised modelling approaches for the prediction of meltpool dynamics and temperature distributions during the L-PBF process, validating the method through computational and experimental case studies.

In addition to experimental and modelling approaches, methods such as Machine Learning (ML) and Artificial Intelligence (AI) offer powerful tools for the optimisation of L-PBF process parameters [19-21]. ML algorithms can analyse datasets of experimental results and simulation data to identify optimal process parameter combinations that minimise defects while ensuring geometric accuracy. Through the use of ML techniques, it is possible to predict the relationship between process parameters and part quality. Several ML techniques have been tested for the optimisation of L-PBF process parameters, such as Neural Networks (NN) [22-26], physics-informed NNs [27, 28], and Reinforcement Learning (RL) approaches [29, 30]. In the work of Mohammed et al. [31], for example, an artificial NN was developed to predict the porosity in L-PBF manufacturing parts. The authors trained the NN using X-ray CT images of the additively manufactured parts, augmented with synthetic data to improve the performance of the algorithm. The results obtained showed high accuracy, emphasising the deep learning model as a cost-effective method for quality enhancement in AM.

The role of ML and AI approaches along with advanced simulation in addressing the complexity of L-PBF processes and improving part quality is growing, emphasising their potential to enhance the decision-making process and reduce the resource and time-intensive

experimental methods [17, 18]. However, despite their potential, most ML and AI approaches for L-PBF prediction and optimisation have achieved limited success due to the significant dependency of process outcomes on part geometry and variability of the process.

This research aims to address these challenges, developing a robust L-PBF strategy for the production of a prototype of next-generation HX using thin, hollow lattice structures in Aluminium (Al) alloy. By integrating ML and AI-based optimisation techniques, the study aimed to identify the optimal overall L-PBF process parameters to minimise defects and ensure the geometrical and dimensional integrity of the thin features required for efficient heat transfer. Two different NN algorithms were developed and trained using experimental data. A NN model was used to predict the combination of the most important parameters responsible for the generation of metallurgical defects, i.e. laser power, scan speed and hatch spacing, in order to control the heat input during the manufacturing process and achieve highly dense components. Furthermore, another NN model was generated to optimise other laser parameters, beam compensation and contour distance, correlated to the geometrical and dimensional accuracy of the produced components. Finally, the overall optimised process parameters generated via the ML approach were experimentally validated and tested for the manufacturing of a novel HX design. The additively manufactured part was analysed using microscopy methods to investigate the reliability of the ML approaches in generating defect-free accurate components through L-PBF.

## 4.2 Material and Methods

The metal powder used in the study was a pre-alloyed A205 Al alloy, with a size range between 20-60 µm and an average value of 40 µm. The chemical composition of the A205 alloy was: Cu 4.49 wt.%, Si 0.1 wt.%, Mg 0.24 wt.%, Fe 0.04 wt.%, Ti 2.4 wt.%, B 0.91 wt.%, Ag 0.71 wt.%, with the balance being Al. The L-PBF technology used was a Concept Laser M2 Cusing

system, produced by General Electric (GE) Additive. The machine was equipped with a single continuous fibre laser source with a maximum power of 400W. The laser beam distribution was considered Gaussian, and the laser spot size was 67 µm. The L-PBF process parameters mostly related to geometrical and dimensional integrity, along with the generation of metallurgical defects were investigated. In particular, these process parameters are described in Figure 4.1.

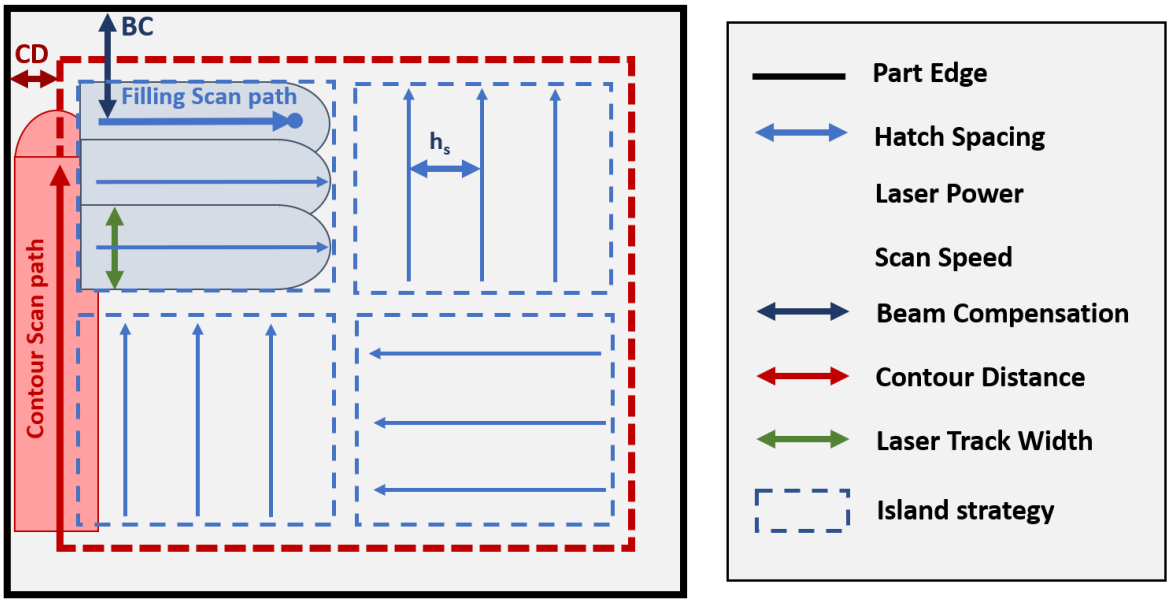


Figure 4.1. Schematisation of most important L-PBF process parameters.

Laser power (P), scan speed ($v_s$), hatch spacing ($h_s$), and layer thickness (t) are responsible for the metallurgical defects and mechanical properties. The different combinations of the laser power, scan speed and hatch spacing resulted in different levels of volumetric energy density (VED), the formula for which is described in Equation 4.1.

$$VED = \frac{P}{v_s \cdot h_s \cdot t} \qquad \text{Equation 4.1}$$

Furthermore, laser process parameters such as Beam Compensation (BC) and Contour Distance (CD) were studied due to their significant impact on the geometrical and dimensional integrity of thin features. BC refers to the adjustment made to the laser path in terms of the distance between the scanning patterns and the edge of the features, ensuring that the final dimensions

match the intended design. CD, on the other hand, controls the spacing between the contour laser scans at the edges of features, which is particularly important for achieving smooth, accurate surfaces on thin-walled structures along with dimensional accuracy. A high accuracy is essential during the manufacturing process of complex geometries such as HXs characterised by lattice structures. Consequently, an optimisation study was carried out using a combination of experimental campaign and ML techniques, in particular NN, to find the optimal overall process parameters to guarantee the feasibility of thin complex features and the tailoring of HXs properties.

### 4.2.1 Experimental method

The experimental campaign was carried out to generate data to train the ML algorithms. In particular, two different experimental studies were carried out. Initially a study of the influence of process parameters, i.e., laser power, scan speed, and hatch spacing, on the final density of the component was carried out, while using a fixed value of layer thickness of 30 μm. The Design of Experiments (DoE) was carried out using a Taguchi orthogonal array in order to generate a fractional factorial study with 25 combinations, randomising the combinations between the three factors and selecting the parameters with a VED below 200 J/mm$^3$.

Table 4.1. Details of the parametric study carried out for the generation of experimental data for the optimisation study of the L-PBF process parameters.

| **Factors** | **Factor Levels** | | | | | **Units** |
|---|---|---|---|---|---|---|
| | **A** | **B** | **C** | **D** | **E** | |
| **Laser Power** | 100 | 125 | 150 | 175 | 200 | W |
| **Scan Speed** | 750 | 1100 | 1450 | 1800 | 2150 | mm/s |
| **Hatch Spacing** | 0.0300 | 0.0525 | 0.0750 | 0.0975 | 0.120 | mm |

The method allowed analysis of all the factors and multiple levels using a selected small subset of combinations, ensuring at the same time that all the levels of all factors were equally considered in the study. No replicates were carried out during the study. The DoE details are summarised in Table 4.1. A wide range was analysed, from a low VED, of 13 J/mm$^3$, to a high value, of more than 100 J/mm$^3$. A chess-type scan strategy was used with islands of 5 x 5 mm, rotated at 45 degrees at each layer, and no contour line was used during the process. The analysis was performed on different types of specimens, in particular, single laser tracks were built to assess the effect of process parameters on the melt pool morphology and bulk samples were manufactured to analyse the influence on the mechanical and microstructural properties. The bulk samples were then sectioned parallel to the build direction, using a Buehler IsoMet 5000 cutting machine, and mounted in conductive bakelite using a Presidon ML-B mounting machine. The bulk samples were then metallographically prepared using a Struers Tegramin-25 polishing system. Finally, the characterisation of the materials was carried out with several techniques, explained in Section 4.2.4.

The influence of BC and CD on the geometrical and dimensional accuracy was evaluated with a full DoE with 5 different levels for each of the two factors, for a total of 25 sets of parameters. In particular, a single set of process parameters (P, $v_s$, $h_s$, t) was used. The detail of the levels used for the DoE is summarised in Table 4.2.

Table 4.2. Details of the parametric study carried out for the generation of experimental data for the optimisation study of the L-PBF laser parameters.

| **Factors** | **Factor Levels** | | | | | **Units** |
|---|---|---|---|---|---|---|
| | **A** | **B** | **C** | **D** | **E** | |
| **BC** | 0 | 0.025 | 0.050 | 0.075 | 0.100 | mm |
| **CD** | 0 | 0.025 | 0.050 | 0.075 | 0.100 | mm |

The scan strategy used in the study was a chess type, with the number of contours set to a value of 2. Furthermore, a benchmark was designed to characterise the manufacturability and optimisation of the accuracy of several thin features, in particular thin walls. The benchmark design along with the details of the thin features, and metallographic characterisation, along with the details of the thin features analysed are represented in Figure 4.2.

The benchmarks were removed from the substrate and sectioned in 3 equal parts at a distance of 5 mm along the build direction. The samples were then manually grinded and polished, and then characterised with several techniques as described in Section 4.2.4.

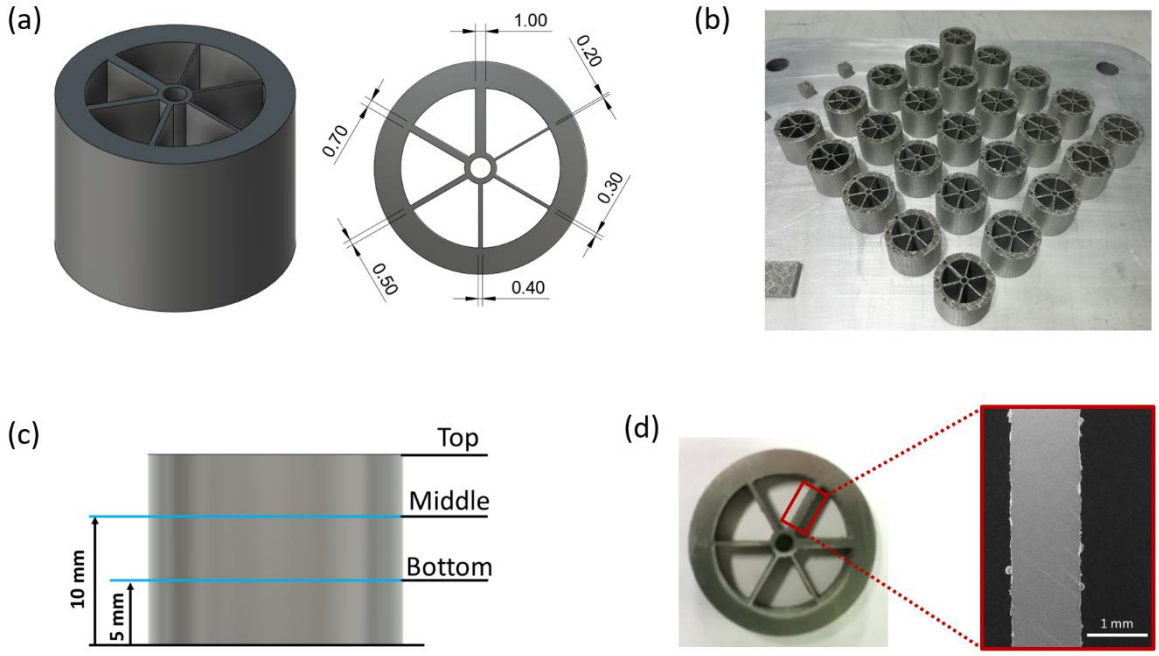


Figure 4.2. Benchmark design and characterisation for the parametric study of BC and CD. a) Benchmark design and thin features details; b) L-PBF manufacturing; c) sectioning strategy for SEM analysis; d) example of a measurement carried out via SEM microscope.

In particular, each of the two investigated parameters, BC and CD, were made to vary between a minimum of 0 µm and a maximum of 100 µm with an interval of 25 µm, for a total of five levels, while the contour hatching space was set at the same value as the CD due to slicing software limitations.

A predetermined contour number of two (2) was used for all samples, while a chess-type raster with islands of 5 x 5 mm was chosen as the scanning strategy, given its popularity in the AM industry due to its ability to ensure low residual stresses, with a rotation of 45° of each layer to ensure minimum residual stresses[24, 25], in order to reduce the failure risk of builds.

### 4.2.2 ML methods

The NN used in the study consisted of two hidden layers, each consisting of five nodes. Each node in either the hidden layers or the output layer was characterised by two activation functions, the Rectified Linear Unit (ReLU) and the sigmoid function, and a set of weights, used to tune the NN.

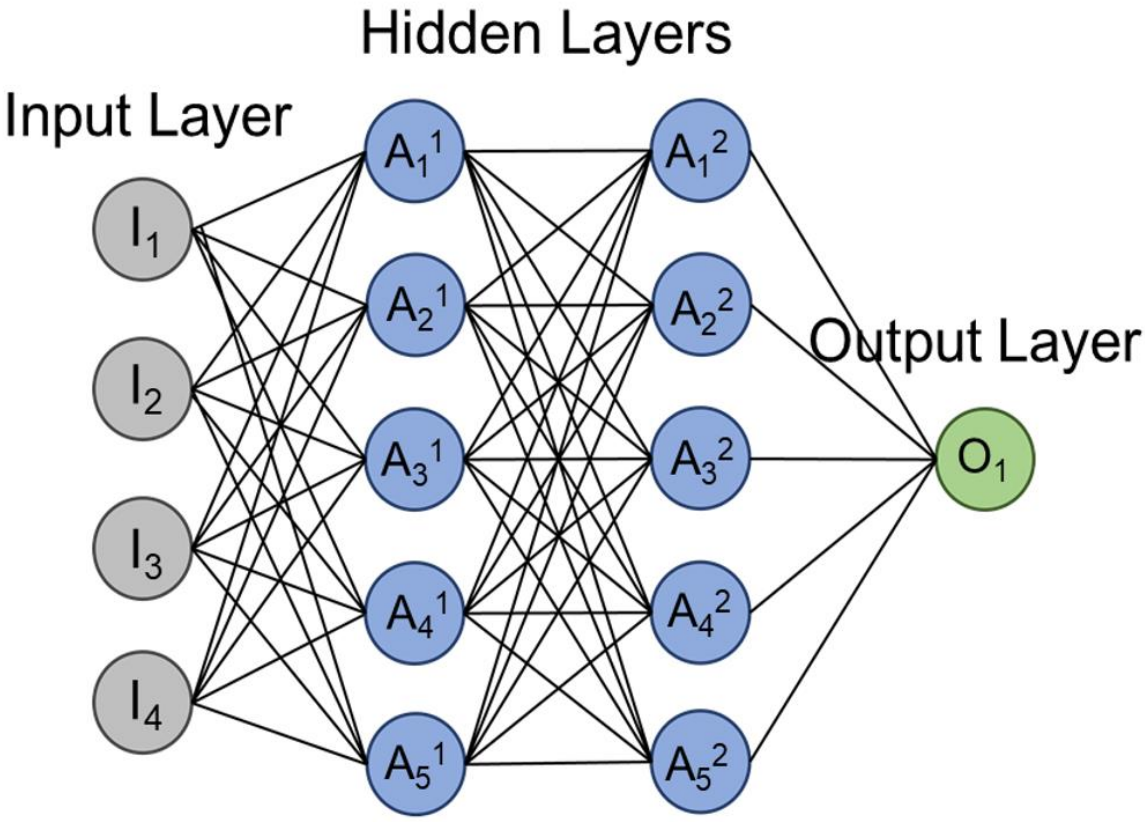


Figure 4.3. Schematisation of the Neural Network used in the study, characterised by 5 nodes and 2 hidden layers.

The input parameters for the prediction of optimal L-PBF process parameters for density were Laser Power, scan speed, hatch spacing and layer thickness, while the output was the relative density (RD) associated with the combination. The input for the optimisation of laser parameters ere BC and CD while the output was the deviation from the nominal dimension. The data was normalised using the min-max scaling method before the training of the model. A schematisation of the NN used in the study is represented in Figure 4.3.

The activation functions used for both NNs used in this study, the ReLU and the sigmoid function, are expressed in Equation 4.2 and Equation 4.3, respectively.

$$\boldsymbol{ReLU}(\boldsymbol{x}) = \boldsymbol{max}(\mathbf{0}, \boldsymbol{x}), \qquad \text{Equation 4.2}$$

$$\boldsymbol{Sigmoid}(\boldsymbol{x}) = \frac{1}{1 + e^{-x}}. \qquad \text{Equation 4.3}$$

In particular, each node in the hidden layer used the ReLU function because characterised by being less computationally expensive, where the sigmoid was used as an activation function for the final output layer, representing the expected RD, in order to increase the reliability of the model. As for the cost function, the Mean Squared Error (MSE) was used, being the most common cost function in NNs, and a backward propagation method was applied to improve the efficiency of the model. Finally, a tuning of the hyperparameters was performed to further improve the accuracy of the NN models, decreasing the possibility of incurring errors of overfitting and underfitting.

Along with the NN models, an AI approach was used to analyse the large amount of data received during the study of BC and CD, based on Computer Vision. Computer Vision enables the digitalisation of information deriving from images, video and other inputs, allowing a better analysis of data. In particular, an automated processing of images taken using an optical microscope was developed using the Canny Edge Detection Algorithm (CEDA) [32], to determine the wall thickness of the thin walls. Benefits such as increasing in data analysis

accuracy and processing speed were key points of the development of such a method. The methodology used in the development of the CEDA technique is represented in Figure 4.4. The image was initially fully converted to greyscale, with each pixel having a value in the range 0 – 255, where 0 was associated with black and 255 with white. The CEDA algorithm was then applied. This method is characterised by the automatic detection of the edge of the part being analysed, and the average thickness measurement was determined by counting the pixels enclosed by the innermost and outermost edge pixels. Initially, the measurement in pixels of the scale bar associated with the image was performed and divided by the number of pixels to obtain the individual width in mm of a single pixel. The scale bar was then cut out of the image because it would interfere with the edge detection. Finally, the CEDA was applied to produce overlaid edges, in blue in Figure 4.4, on top of the original image.

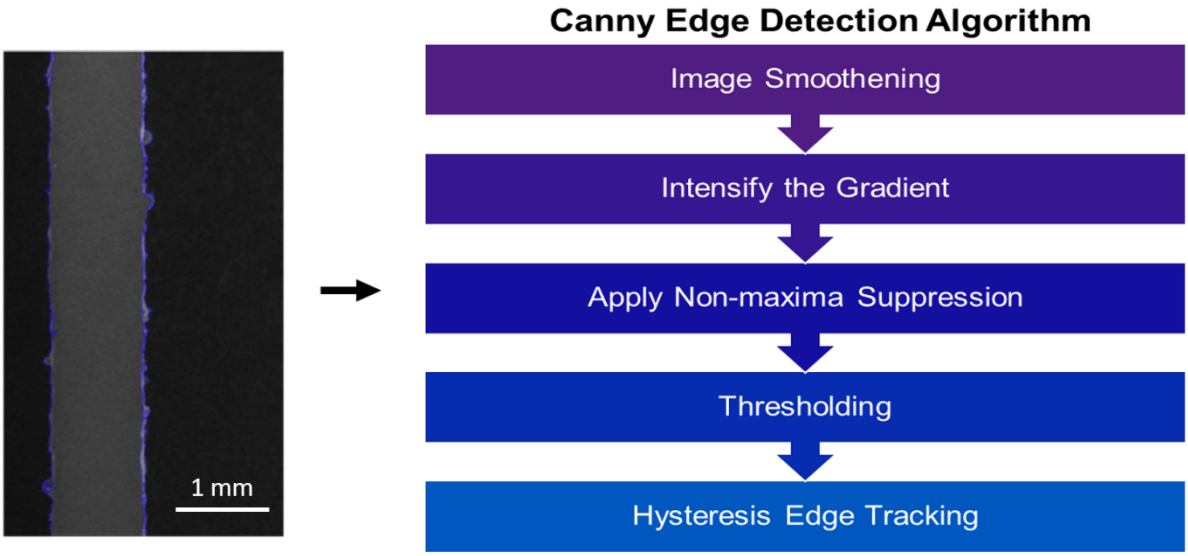


Figure 4.4. Schematisation of the Canny Edge detection Algorithm (CEDA) process for image analysis. The algorithm's five steps are, in order of application: Image smothering, where a Gaussian filter is applied to reduce the noise of the image; Intensify the Gradient, where the algorithm calculates areas in the image with an intensity change of the pixels; Non-Maxima Suppression, where the algorithm analyses the gradient direction of each pixel; Thresholding, where the algorithm marks the strong edges in the image based on thresholding; and Edge Tracking, where the algorithm identifies and reconstructs the edges of the object in the image.

The coordinates of the blue pixels were then obtained and a measurement of thickness for each of the pixels was carried out along the wall. Finally, the wall thickness was calculated as the average of all the measurements performed. While this approach ensured good repeatability for the specific material and case study analysed, a larger dataset and the investigation of other materials are necessary to generalise those ML-based approaches.

### 4.2.3 Novel HX design

The new generation of HXs by the application of hollow structures, fabricated via L-PBF has great potential for industrial development. Therefore, a novel geometry was generated characterised by a lattice structure of hollow tubes. A portion of a real component was designed, in order to assess the feasibility of the L-PBF process. A novel air-to-fluid HX was designed using the CAD design platform Autodesk Fusion 360, and the manufacturability was assessed in the study. A representation of the tested design is shown in Figure 4.5.

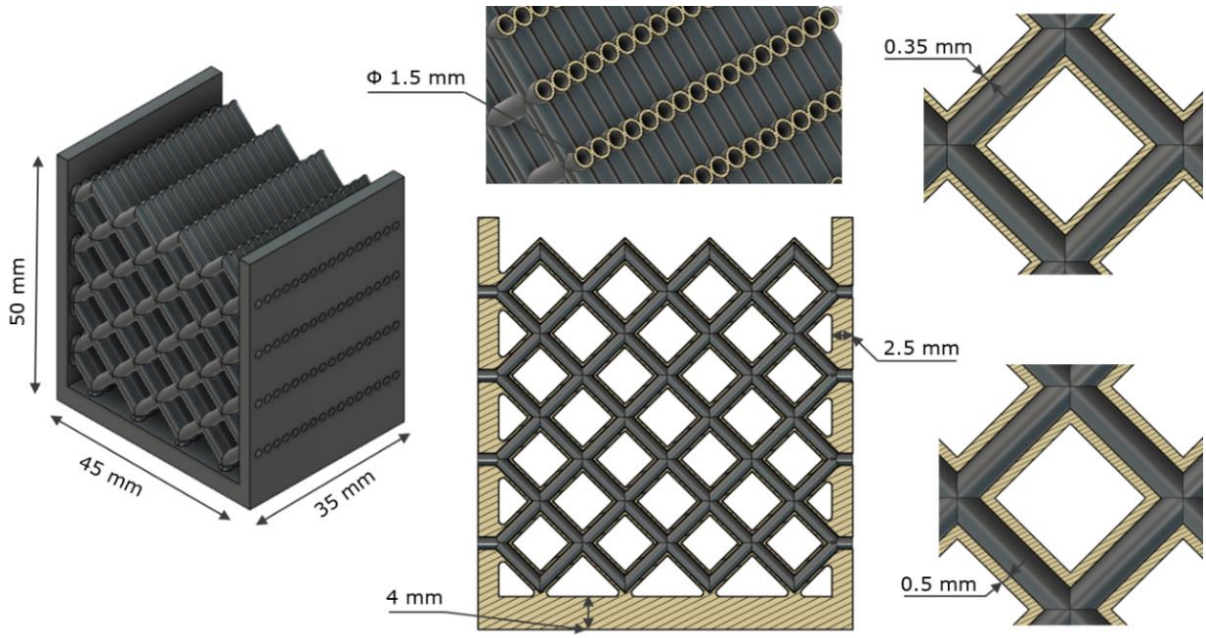


Figure 4.5. Design and details of the novel hollow lattice structure HX.

An air-to-fluid heat exchanger facilitates the transfer of heat between an air stream and a working fluid, typically in automotive, aerospace, and industrial applications. Usually, this type

of HXs consists of a network of finned tubes through which the fluid flows, while the surrounding air passes over the tubes, absorbing or releasing heat depending on the operational requirements. In particular, in this study, a compact HX composed of Face-Centered Cubic (FCC) lattice structures with hollow walled struts was designed. The component was characterised by two vertical plates of 2.5 mm, holding the inlet and outlet of the fluid. Two different wall thicknesses were selected, 350 µm and 500 µm, respectively, in order to estimate the limits of the L-PBF technology. The other design details were fixed for both configurations and described in Figure 4.5. In particular, the internal diameter of the tubes was 1.5 mm and 45-degree angles were applied to minimise the requirement of support structures. The lattice was designed on a flat 4mm thick bottom plate that takes into consideration the cutting process from the substrate, after the L-PBF manufacturing, and fillets with a radius of 0.5mm were used.

### 4.2.4 Characterisation methods

The characteristics of HX targeted for this study were dimensional and geometrical accuracy and low presence of metallurgical defects. In particular, achieving the desired accuracy and surface quality for HXs produced via PBF-LB/M is crucial. Improved accuracy ensures that the additively manufactured HXs meet operational specifications, such as flow rate and regime, and pressure drop, reducing or even eliminating the need for additional post-processing steps. This can significantly decrease the total manufacturing time and associated costs. Moreover, due to the high complexity of such HXs geometries, conventional post-processing technologies are often unsuitable. For instance, surface finishing operations, such as machining, cannot be effectively applied to the intricate internal structures and thin features that characterise the advanced HXs. The comprehensive analysis of the material properties for the process parameters optimisation and for the characterisation of the fabricated HX was carried out using

a range of advanced characterisations. Porosity and dimensional accuracy were assessed using both optical and electron microscopy. For optical microscopy, a Zeiss Axioskop 2 was utilised to obtain images of the material's surface and internal structure. This method allowed for the identification of larger pores and surface irregularities, while a Hitachi TM3030 tabletop scanning electron microscope (SEM) was used to investigate smaller pores and microstructural features that were not easily discernible through optical methods alone. The data acquired were then processed using a Java-based image analysis software, ImageJ. To evaluate the influence of process parameters on the mechanical properties of the material micro-hardness testing was conducted using a Wilson VH1202. Vickers testing method was employed, applying a load of 0.1 Kg. Finally, the surface quality of the fabricated parts was analysed using a 3D optical profilometer, the Alicona InfiniteFocus, which allows for the mapping of surface roughness, offering a three-dimensional visualisation and analysis of the surface features. Additional analysis such as mechanical tests was not included in this study, as optimal dimensional and geometrical accuracy and minimisation of porosity, mostly near the surface were targeted as primary requirements for increasing the life in operation of HXs.

## 4.3 Results and Discussion

### 4.3.1 Optimisation of Process parameters for Metallurgical defects

The optimisation of L-PBF process parameters was initially experimentally conducted. In particular, the laser track analysis included the assessment of two important properties of the meltpool to understand the phenomena during the L-PBF process. The full DoE was analysed, and the influence of laser power and scan speed on the generation of a single laser track was evaluated. A contour map was generated and is presented in Figure 4.6.

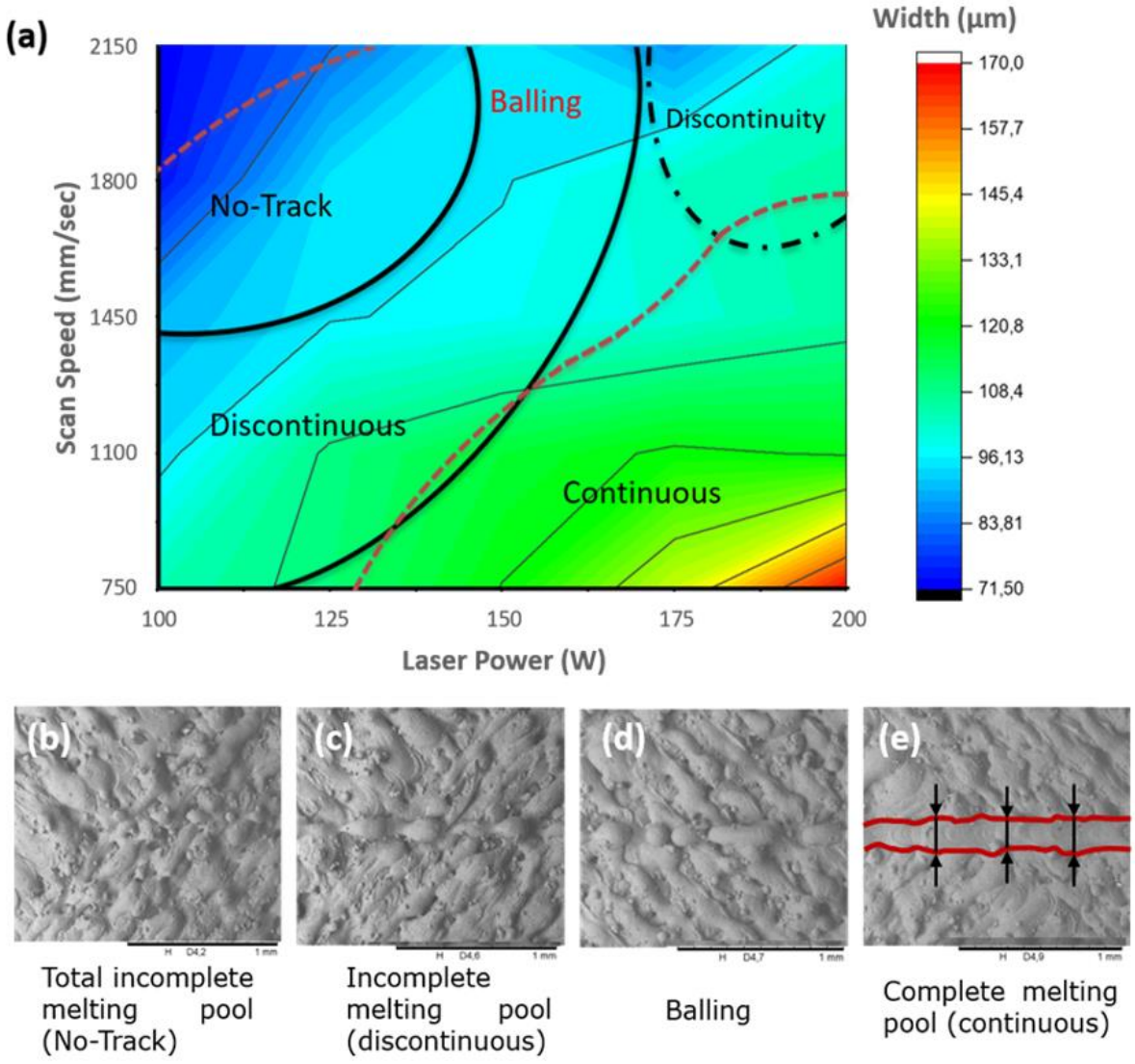


Figure 4.6. Laser track morphology map. a) morphology map; SEM image of b) incomplete laser track; c) discontinuous laser track; d) balling effect; e) continuo laser track.

The contour map shows the different types of laser tracks achieved with different process parameters. The results highlighted that low power and elevated scan speed reduce the quality of the meltpool, leading to poor formation of incomplete laser tracks. Furthermore, increasing in laser power showed the generation of continuous laser tracks, but the presence of balling phenomena was found for very high scan speed values. The interaction between the process parameters was further investigated using bulk samples. In particular, the density was evaluated by using microscopy analysis, and the trend of the RD vs the VED is shown in Figure 4.7.

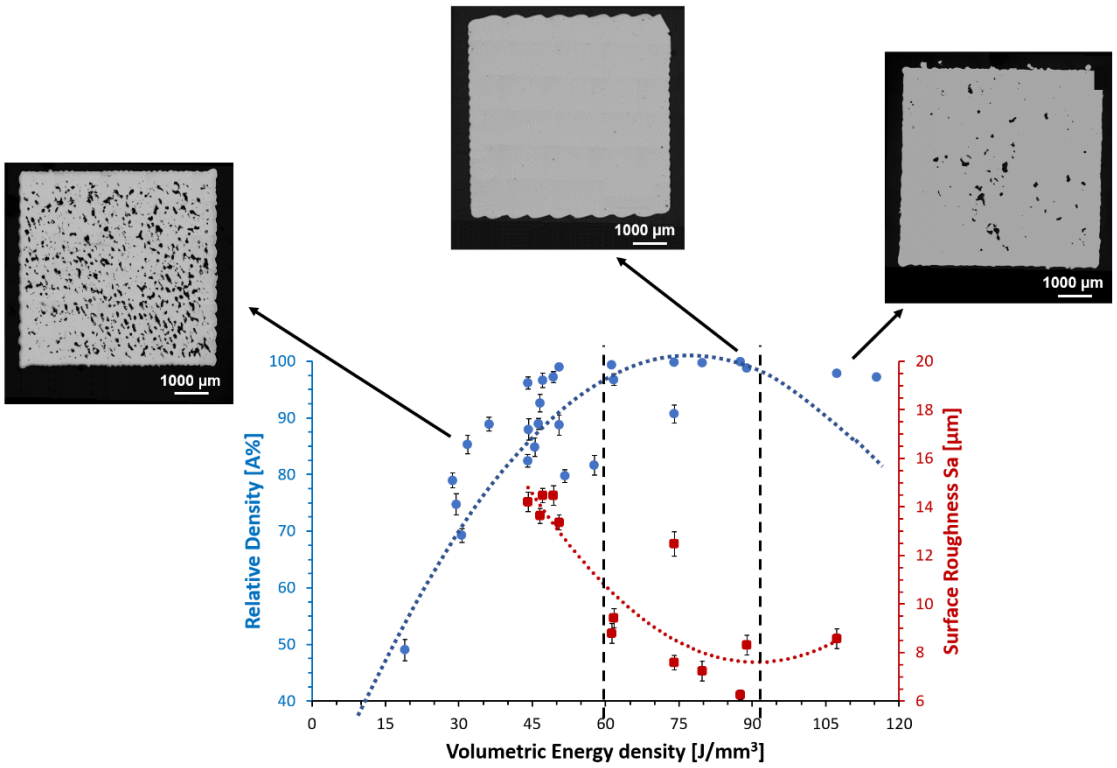


Figure 4.7. Metallurgical characterisation of the experimental analysis. Relative density analysis and Surface roughness analysis vs volumetric energy density.

Furthermore, surface roughness was measured on the high-density samples. The results highlighted an optimal process window for the material in the range of 60-90 J/mm$^3$. In particular, a low RD at low VED was found, and the characterisation showed a large lack of fusion effects in the material. Higher values of RD were measured by increasing the VED, reaching the best condition near 90 J/mm$^3$, while excessive VED led to the formation of keyholes, decreasing the total RD. The optimal process parameters for RD were also characterised by lower average surface roughness, with values of around 50% less than unoptimised process parameters.

The data obtained by the experimental results were normalised and fed to a NN. The hyperparameters producing the most reliable output were obtained after 2500 iterations, reaching a learning rate of 0.03. Using the previously determined optimal hyperparameters, the NN model was trained using the full set of data acquired during the experimental analysis, i.e.

combination of process parameters and corresponding properties. The NN training process required relatively minimal computation effort, with a total time of a few minutes to complete. By training the model on experimental data, the NN was able to predict outcomes based on specific parameter combinations, providing information regarding the importance of each parameter in reducing porosity and achieving the desired density. The NN model highlighted complex interactions among the three investigated process parameters, effectively capturing both favourable and adverse influences on material densification.

The prediction of the ML algorithm successfully identified a region of combination space with high RD, while confirming the generation of metallographic defects correlated to low density for the combination of low laser power associated with high scan sped and hatch spacing values. The validated NN model was then used to provide new optimal process parameters leading to the manufacturing of A205 alloy with high density and good overall properties. In particular, to validate the model, combinations specifically generated to produce metallurgical defects were also included. The results are shown in Figure 4.8.

The NN model was characterised by a mean squared error (MSE) of 0.017, highlighting the ability of the algorithm to accurately predict the influence of experimentally untested process parameters on metallurgical defects. As shown in Figure 4.8, the model exhibited greater accuracy in predicting the RD of process parameters in the optimal process window, while showing a higher MSE in predicting the exact RD below 90%. This discrepancy was attributed to dataset limitations, as approximately 80% of the data points used to train the NN represented RD above 90%. Despite this imbalance, the NN model accurately forecasted the likelihood of an ineffective build and provided the generation of L-PBF strategies to reduce metallurgical defects and enhance the properties of the A205 Al alloy.

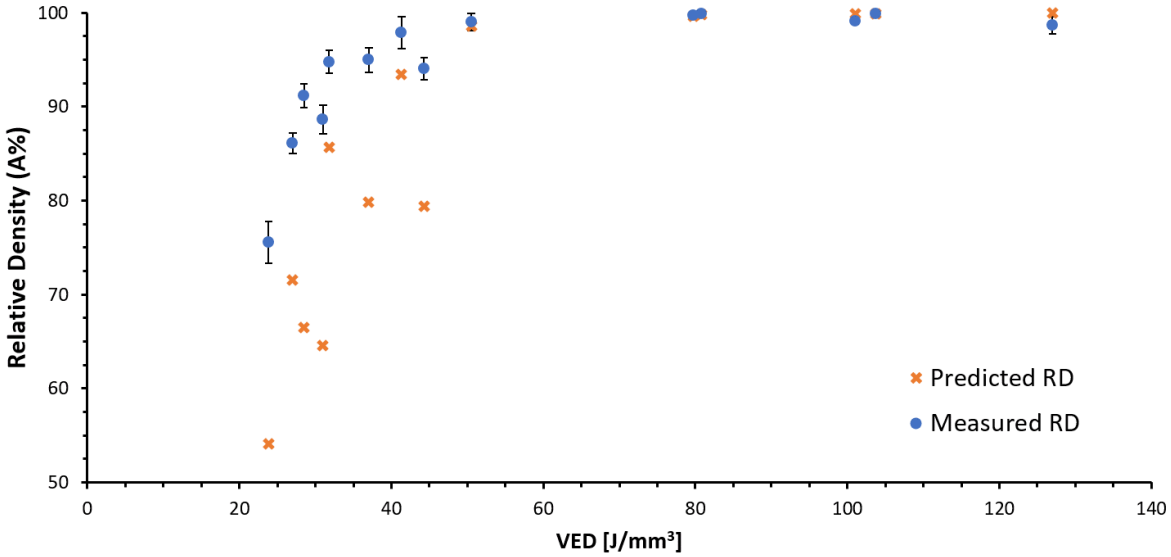


Figure 4.8. Validation results of the NN used for the optimisation of L-PBF process parameters for density showing Predicted and measured RD vs VED.

The best combination of process parameters was utilised in the manufacturing of the new hollow lattice HX.

### 4.3.2 Optimisation of Laser parameters for Accuracy

The optimisation of laser parameters, BC and CD, is essential when manufacturing thin features. Therefore, the influence of BC and CD on the accuracy of several types of thin features was initially assessed experimentally to generate data to train an NN algorithm. In particular, the benchmark was designed to evaluate the limits of the L-PBF system in the feasibility of several wall thicknesses. The optimal combination of process parameters (Power, scan speed, hatch spacing, and layer thickness) was used, and the parametric study carried out only varying BC and CD. A large amount of data was extracted from the analysis of the thin features, and therefore, the Computer Vision approach was used to evaluate the average thickness of the thin walls manufactured using several BC and CD combinations. The results are represented in Figure 4.9.

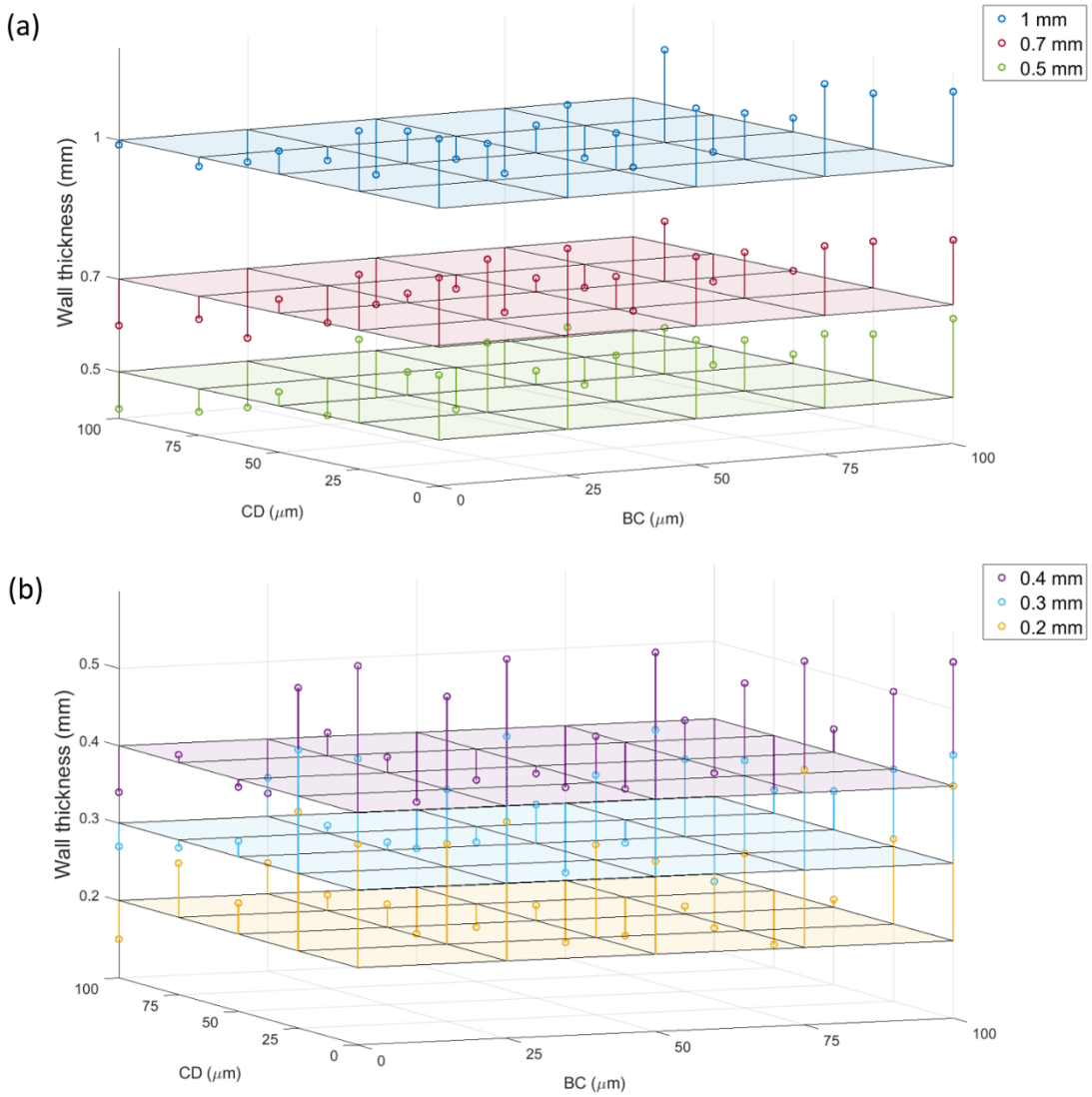


Figure 4.9. Influence of BC and CD in the dimensional accuracy. Measured thickness values for each combination of BC and CD against the nominal value for a) wall thickness of 1 mm, 0.7 mm, and 0.5 mm; b) wall thickness of 0.4 mm, 0.3 mm, and 0.2 mm.

The results highlighted a similar trend for different wall thicknesses, identifying the CD as the main parameter influencing the accuracy of thin features. The NN was then applied to predict the optimal BC and CD for the generation of several wall thicknesses. The NN was trained using the data generated during the experimental analysis. The prediction of optimised laser parameters to generate several thin walls was then evaluated. In particular, wall thicknesses

from 1 mm to 0.2 mm were tested, and the deviation from the nominal value was calculated. The results are shown in Figure 4.10.

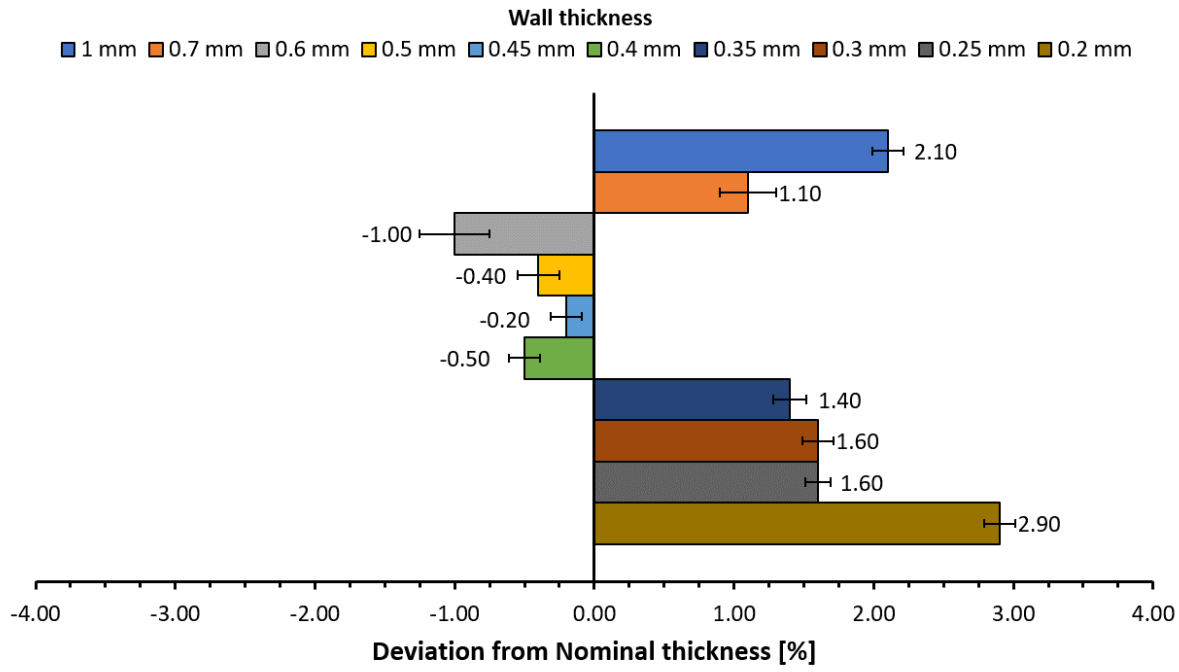


Figure 4.10. Validation results of the NN used for the optimisation of L-PBF laser parameters for accuracy. The results in terms of deviation from the nominal thickness are represented for thin features characterised by several thicknesses.

The results highlighted the ability of the NN to predict optimised parameters for reducing the deviation and improving the dimensional accuracy of thin features. In particular, the NN optimisation was more reliable for thicknesses between 0.6 and 0.4 mm, characterised by a negative deviation of less than 1%. While for wider and thinner thicknesses a positive deviation was found, with the real dimension higher than nominal. This was correlated to the interaction of filling and contour scanning, generating phenomena hard to understand without a physical model. While for thinner thicknesses, characterised by only contour strategy, the surface roughness led to an increase in real dimension and consequently in the deviation from the nominal target.

### 4.3.3 Characterisation of Manufacturability of Novel HX Design

The novel hollow walled lattice structure HXs with different wall thicknesses, 350 μm and 500 μm, were manufactured using the optimal process parameters generated using the NN models during the study and summarised in Table 4.3. The total manufacturing time of such novel HX including the entire workflow, from data generation and model development to validation and production, can be summarised as follows: i) data generation required approximately 2 weeks through an experimental campaign in which the collection of data on microstructural properties, geometrical and dimensional accuracy was carried out; ii) design and model development required approximately 1.5 weeks, including the developing of the ML algorithms, training of NN models, and validating the predicted optimal parameters through experimental tests; iii) manufacturing of the novel HX required approximately 0.5 weeks, including steps such as build preparation and setup, printing, depowdering, removal from the substrate, and cleaning the channels from powder debris.

Table 4.3. Summary of the overall L-PBF process parameters optimised using the ML-based strategy for the manufacturing of the novel HXs characterised by a thin hollow-walled lattice structure.

| | **L-PBF Process Parameters** | | | | | **L-PBF Laser Parameters** | | |
|---|---|---|---|---|---|---|---|---|
| **Parameters** | P [W] | Vs [mm/s] | Hs [mm] | T [mm] | VED [J/mm3] | BC [mm] | CD [mm] | Contour number |
| **Value** | 200 | 1100 | 0.075 | 0.03 | 80 | 0.04 | 0.055 | 2 |

The HXs were successfully produced demonstrating the feasibility of the L-PBF manufacturing process. Figure 4.11 depicts the novel HXs from different perspectives.

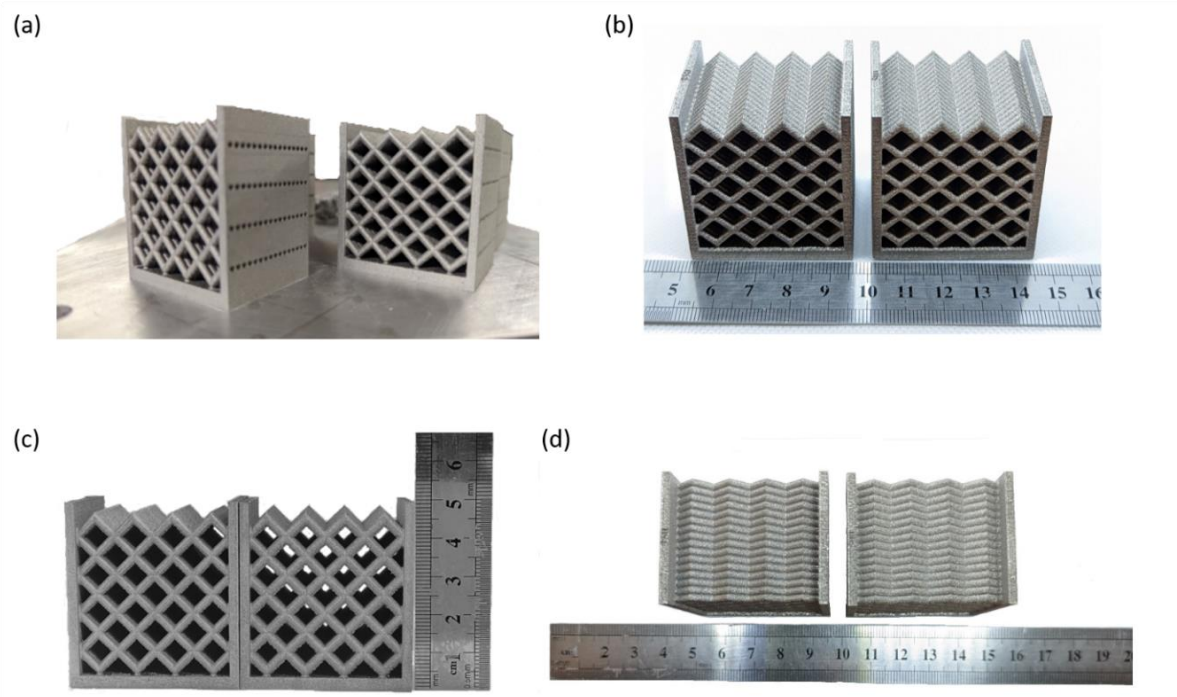


Figure 4.11. L-PBF manufactured novel HXs with 2 wall thicknesses. a) HXs on the substrate; b) orthogonal view; c) frontal view; d) top view.

Both HXs were sectioned and analysed to assess the quality of the design and thin features, and the presence of defects. In particular, a frontal section was used to analyse the presence of pores resulting in possible leakage failure, while a section at 45 degrees was performed to analyse the dimensional and geometrical accuracy of the hollow thin-walled struts composing the HXs. The results are shown in Figure 4.12.

The analysis of defects was assessed on all the sectioned surfaces. Porosity analysis was carried out to evaluate the metallurgical defect generation due to the optimised process parameters. The resulting RD was 99.8 A% for both of the HXs analysed. The evaluation of different types of pores was assessed using ImageJ. In particular, all the pores with a diameter lower than 100 μm were considered small pores (sp), while higher ones were considered large pores (lp). The analysis of the types of pores carried out for both HXs highlighted a high presence of small pores, and no presence of cracks or large pores along the surface was discovered. In particular, the amount of sp and lp was 85% and 15% in density for the HX characterised by a wall

thickness of 350 µm, respectively, while 82% and 18% for the HX with a wall thickness of 500 µm.

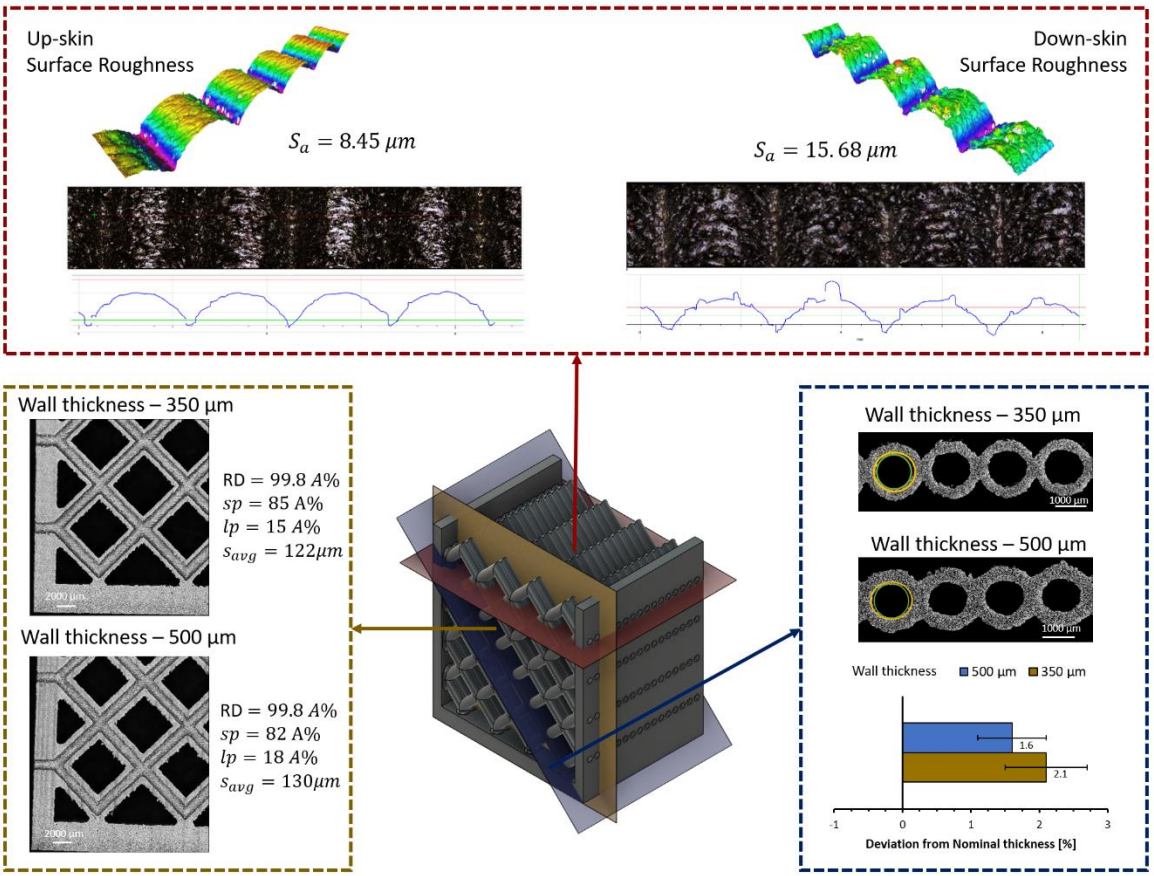


Figure 4.12. Characterisation of the manufacturability of the novel HX design characterised by a wall thickness of 350 µm and 500 µm in terms of porosity and density, dimensional and geometrical accuracy of thin features, and surface roughness.

Furthermore, the average pore size ($s_{avg}$) was calculated, showing consistency with the quantity of porosity analysed, with values of 122 µm and 130 µm, for HX with a wall thickness of 350 µm and 500 µm, respectively. The results emphasised the effectiveness of the optimised process parameters via ML models, leading to components with few metallurgical defects. Furthermore, the analysis carried out on the dimensional and geometrical accuracy of the hollow struts showed a good correlation between nominal and real dimensions. In particular, the dimensional deviation was lower for the wall thickness of 500 µm, highlighting a better control for thicker geometries with an average deviation of 1.6% compared to the 2.3% of the HX with a wall

thickness of 350 μm. Overall, the average deviation was smaller than 2.5% in all the analysed features, highlighting the high dimensional accuracy achieved in manufacturing thin features. The deviation in the geometrical shape was also calculated as less than 1% for both HXs, emphasising the manufacturability of hollow thin-walled lattice structures. Finally, the surface roughness of the upskin and downskin was evaluated to evaluate the influence of the optimal process parameters on the surface quality of the component. An average value of Sa=8.45 μm and Sa=15.68 μm was evaluated for the up-skin and down-skin, respectively, calculated for the HX characterised by a wall thickness of 350 μm.

## 4.4 Conclusions

The development of an L-PBF strategy for the manufacturing of a novel hollow lattice structure HX was carried out using ML-based models. The evaluation of the effectiveness of using ML approaches in AM and more in particular L-PBF technology to optimise the process parameters for the manufacturing of high-dense, high-fidelity HX characterised by thin features was performed. The main results of the study can be summarised as follows:

- The optimisation of L-PBF process parameters, power, scan speed, and hatch spacing, for the A205 Al alloy was carried out using a NN approach. The model was trained using the limited data generated during the experimental campaign and tuned in order to estimate the influence of each process parameter and several combinations on the achievable relative density of the alloy. The NN was then validated, showing good accuracy in detecting the optimal process window of process parameters for high density. However, due to the limited data set generated during the experimental campaign, further studies are needed in order to generate a larger training data set to increase the reliability of the NN.

- A second optimisation study, focusing on the laser parameters, BC and CD, was performed using a Computer Vision approach, the CEDA, and an ML-based technique, the NN. The manufacturing of thin walls characterised by several thicknesses was carried out and the average wall thickness associated with each combination of the two laser parameters was evaluated using the CEDA. The data was then fed to the NN for training. The validation of the NN model was finally performed to evaluate the potential of the new method in finding the optimal combinations of Bc and CD to decrease the dimensional deviation from the nominal thickness. The results highlighted a positive accordance between the outputs of the NN and the experimental measurements.
- The novel HX designs characterised by two wall thicknesses of 350 μm and 500 μm were successfully manufactured using the overall optimal L-PBF process parameters generated using the ML-based models.
- The characterisation of the thin features composing the novel HXs was assessed using several techniques. The porosity and density analysis highlighted a positive effect of the optimal process parameters in decreasing the generation of large pores. A relative density of 99.8% was achieved, with an average size of the pores of less than 150 μm for both manufactured HXs. The geometrical and dimensional accuracy in the fabrication of the thin features was also performed. The results showed a high fidelity in the manufacturing of complex features with thin wall thicknesses. In particular, a dimensional deviation of 1.6% and 2.3% was found for the hollow struts of the HX characterised by wall thicknesses of 350 μm and 500 μm, respectively, while the geometrical deviation was less than 1% for both analysed HXs. Finally, the surface roughness of the hollow lattice structure features of the HX with a wall thickness of 350 μm was assessed. The results highlighted a good compromise between the average

surface roughness of up-skin and down-skin, with values of Sa=8.45 µm and Sa=15.68 µm, respectively.

The results emphasised the significant role of ML in the optimisation process of L-PBF technology for the manufacturing of the new generation of HXs characterised by thin complex features. By reducing the experimental burden and enhancing the overall quality of the produced components, ML approaches offered optimised solutions for PBF-LB/M manufacturing of thermal management systems in fields such as aerospace and automotive. Although further studies are necessary to ensure the robustness and reliability of ML approaches for optimisation, as well as to generate models capable of predicting optimised parameters beyond their training range, such as physical-informed Neural Networks, the findings of this work demonstrate the potential of the methods. This research serves as a foundation for integrating ML-based strategies for one of the most widely adopted processes in the modern industry, promoting improvement in efficiency and flexibility in industrial manufacturing operations of thermal management systems.

## Acknowledgements

*This work is part of the C-AM AOHE project funded by the European Union's Horizon H2020-CS2-CFP08-2018-01 research and innovation program under grant agreement No 831880. This work was also supported in part by the EPSRC Centre for Doctoral Training in Topological Design, funded by the UK Engineering and Physical Sciences Research Council (grant EP/S02297X/1) based at the University of Birmingham.*

*The authors would like to thank Mr Thomas Astley and Mr Oliver Halliday for their valuable contributions to the development and validation of machine learning and computer vision techniques implemented in this work.*

# References

[1] F. Careri, R.H.U. Khan, C. Todd, M.M. Attallah, Additive manufacturing of heat exchangers in aerospace applications: a review, Applied Thermal Engineering, 235 (2023) 121387.

[2] I. Kaur, P. Singh, State-of-the-art in heat exchanger additive manufacturing, International Journal of Heat and Mass Transfer, 178 (2021) 121600.

[3] P. Stavropoulos, H. Bikas, T. Souflas, K. Tzimanis, C. Papaioannou, N. Porevopoulos, Additive manufacturing in the automotive industry, 3D Printing, CRC Press, 2023, pp. 453-470.

[4] P. Stavropoulos, AM Processes, in: P. Stavropoulos (Ed.) Additive Manufacturing: Design, Processes and Applications, Springer International Publishing, Cham, 2023, pp. 45-93.

[5] S.A. Niknam, M. Mortazavi, D. Li, Additively manufactured heat exchangers: a review on opportunities and challenges, The International Journal of Advanced Manufacturing Technology, 112 (2021) 601-618.

[6] S. Mahmoudinezhad, M. Sadi, H. Ghiasirad, A. Arabkoohsar, A comprehensive review on the current technologies and recent developments in high-temperature heat exchangers, Renewable and Sustainable Energy Reviews, 183 (2023) 113467.

[7] H.Z. Zhong, T. Song, C.W. Li, R. Das, J.F. Gu, M. Qian, Understanding the superior mechanical properties of hollow-strut metal lattice materials, Scripta Materialia, 228 (2023) 115341.

[8] X. Peng, Y. Huo, G. Zhang, L. Cheng, Y. Lu, J. Li, Z. Jin, Controlled mechanical and mass-transport properties of porous scaffolds through hollow strut, International Journal of Mechanical Sciences, 248 (2023) 108202.

[9] A. Muley, M. Stoia, D. Van Affelen, V. Reddy, V. Duggirala, S. Locke, Recent Advances in Thin-Wall Additively Manufactured Heat Exchangers, ASME 2021 International Mechanical Engineering Congress and Exposition, 2021.

[10] J. Wong, A. Qureshi, P. Mertiny, Complex Lattice Structure-Based Heat Exchangers Through Additive Manufacturing: Opportunities and Challenges, ASME 2022 Pressure Vessels & Piping Conference, 2022.

[11] L. Fournet-Fayard, C. Cayron, I. Koutiri, P. Lapouge, J. Guy, C. Dupuy, A.-F. Obaton, Thermal analysis of parts produced by L-PBF and correlation with dimensional accuracy, Welding in the World, 67 (2023) 845-858.

[12] C.L.A. Leung, R. Tosi, E. Muzangaza, S. Nonni, P.J. Withers, P.D. Lee, Effect of preheating on the thermal, microstructural and mechanical properties of selective electron beam melted Ti-6Al-4V components, Materials & Design, 174 (2019) 107792.

[13] B.Y. Benchabane, Y. Belkacemi, M.e.A. Belouchrani, H. Kebir, Thermomechanical modelling of residual stresses and distortion in laser powder bed fusion: Assessment of the effect of build plate preheating on the behaviour of Inconel 718, Optics & Laser Technology, 181 (2025) 111641.

[14] J. Noronha, M. Qian, M. Leary, E. Kyriakou, M. Brandt, Hollow-walled lattice materials by additive manufacturing: Design, manufacture, properties, applications and challenges, Current Opinion in Solid State and Materials Science, 25 (2021) 100940.

[15] Z. Wu, S.P. Narra, A. Rollett, Exploring the fabrication limits of thin-wall structures in a laser powder bed fusion process, The International Journal of Advanced Manufacturing Technology, 110 (2020) 191-207.

[16] C. Tan, S. Li, K. Essa, P. Jamshidi, K. Zhou, W. Ma, M.M. Attallah, Laser Powder Bed Fusion of Ti-rich TiNi lattice structures: Process optimisation, geometrical integrity, and phase transformations, International Journal of Machine Tools and Manufacture, 141 (2019) 19-29.

[17] P. Stavropoulos, G. Pastras, T. Souflas, K. Tzimanis, H. Bikas, A Computationally Efficient Multi-Scale Thermal Modelling Approach for PBF-LB/M Based on the Enthalpy Method, Metals, 12 (2022) 1853.

[18] P. Foteinopoulos, A. Papacharalampopoulos, P. Stavropoulos, Additive manufacturing simulations: An approach based on space partitioning and dynamic 3D mesh adaptation, Additive Manufacturing Letters, 11 (2024) 100256.

[19] L. Meng, B. McWilliams, W. Jarosinski, H.-Y. Park, Y.-G. Jung, J. Lee, J. Zhang, Machine Learning in Additive Manufacturing: A Review, JOM, 72 (2020) 2363-2377.

[20] S.L. Sing, C.N. Kuo, C.T. Shih, C.C. Ho, C.K. Chua, Perspectives of using machine learning in laser powder bed fusion for metal additive manufacturing, Virtual and Physical Prototyping, 16 (2021) 372-386.

[21] J. Liu, J. Ye, D. Silva Izquierdo, A. Vinel, N. Shamsaei, S. Shao, A review of machine learning techniques for process and performance optimization in laser beam powder bed fusion additive manufacturing, Journal of Intelligent Manufacturing, 34 (2023) 3249-3275.

[22] M. Marrey, E. Malekipour, H. El-Mounayri, E.J. Faierson, A Framework for Optimizing Process Parameters in Powder Bed Fusion (PBF) Process Using Artificial Neural Network (ANN), Procedia Manufacturing, 34 (2019) 505-515.

[23] B. Fotovvati, M. Balasubramanian, E. Asadi, Modeling and Optimization Approaches of Laser-Based Powder-Bed Fusion Process for Ti-6Al-4V Alloy, Coatings, 10 (2020) 1104.

[24] E. Maleki, S. Bagherifard, M. Guagliano, Application of artificial intelligence to optimize the process parameters effects on tensile properties of Ti-6Al-4V fabricated by laser powder-bed fusion, International Journal of Mechanics and Materials in Design, 18 (2022) 199-222.

[25] Z. Zhang, C.K. Sahu, S.K. Singh, R. Rai, Z. Yang, Y. Lu, Machine learning based prediction of melt pool morphology in a laser-based powder bed fusion additive manufacturing process, International Journal of Production Research, 62 (2024) 1803-1817.

[26] D. Yan, E.T. Lee, S. Pasebani, Z. Fan, A Study of the Laser Powder Bed Fusion Manufactured Surface Roughness Prediction and Optimization Based on Artificial Neural Network, ASME 2023 18th International Manufacturing Science and Engineering Conference, 2023.

[27] B. Uhrich, N. Pfeifer, M. Schäfer, O. Theile, E. Rahm, Physics-informed deep learning to quantify anomalies for real-time fault mitigation in 3D printing, Applied Intelligence, 54 (2024) 4736-4755.

[28] Y. Du, T. Mukherjee, T. DebRoy, Physics-informed machine learning and mechanistic modeling of additive manufacturing to reduce defects, Applied Materials Today, 24 (2021) 101123.

[29] F. Ogoke, A.B. Farimani, Thermal control of laser powder bed fusion using deep reinforcement learning, Additive Manufacturing, 46 (2021) 102033.

[30] A.M. Faizan Mohamed, F. Careri, R.H.U. Khan, M.M. Attallah, L. Stella, A novel porosity prediction framework based on reinforcement learning for process parameter optimization in additive manufacturing, Scripta Materialia, 255 (2025) 116377.

[31] A.S. Mohammed, M. Almutahhar, K. Sattar, A. Alhajeri, A. Nazir, U. Ali, Deep learning based porosity prediction for additively manufactured laser powder-bed fusion parts, Journal of Materials Research and Technology, 27 (2023) 7330-7335.

[32] J. Canny, A Computational Approach to Edge Detection, IEEE Transactions on Pattern Analysis and Machine Intelligence, PAMI-8 (1986) 679-698.

# CHAPTER 5. Development of novel Heat Treatment Strategies for L-PBF Fabricated A205 High-Strength Al Alloy

This chapter is part of a scientific paper that has been published in the Journal 'Materials Science and Engineering A'. The paper's details and co-authors' contributions are outlined below.

**Francesco Careri,** Raja H.U. Khan, Talal Alshammari, Moataz M. Attallah, Development of a Novel Heat Treatment in L-PBF fabricated High Strength A205 Al Alloy: Impact on Microstructure-Mechanical Properties, Materials Science and Engineering: A, 2025, 148278, ISSN 0921-5093, https://doi.org/10.1016/j.msea.2025.148278.

**Francesco Careri:** Conceptualisation, Data curation, Investigation, Methodology, Visualisation, Writing – original draft, Writing - review and editing.

**Raja H.U. Khan:** Conceptualisation, Supervision, Writing – review and editing.

**Talal Alshammari:** Investigation, Visualisation.

**Moataz M. Attallah:** Conceptualisation, Funding acquisition, Methodology, Resources, Supervision, Writing – review and editing.

# Graphical Abstract

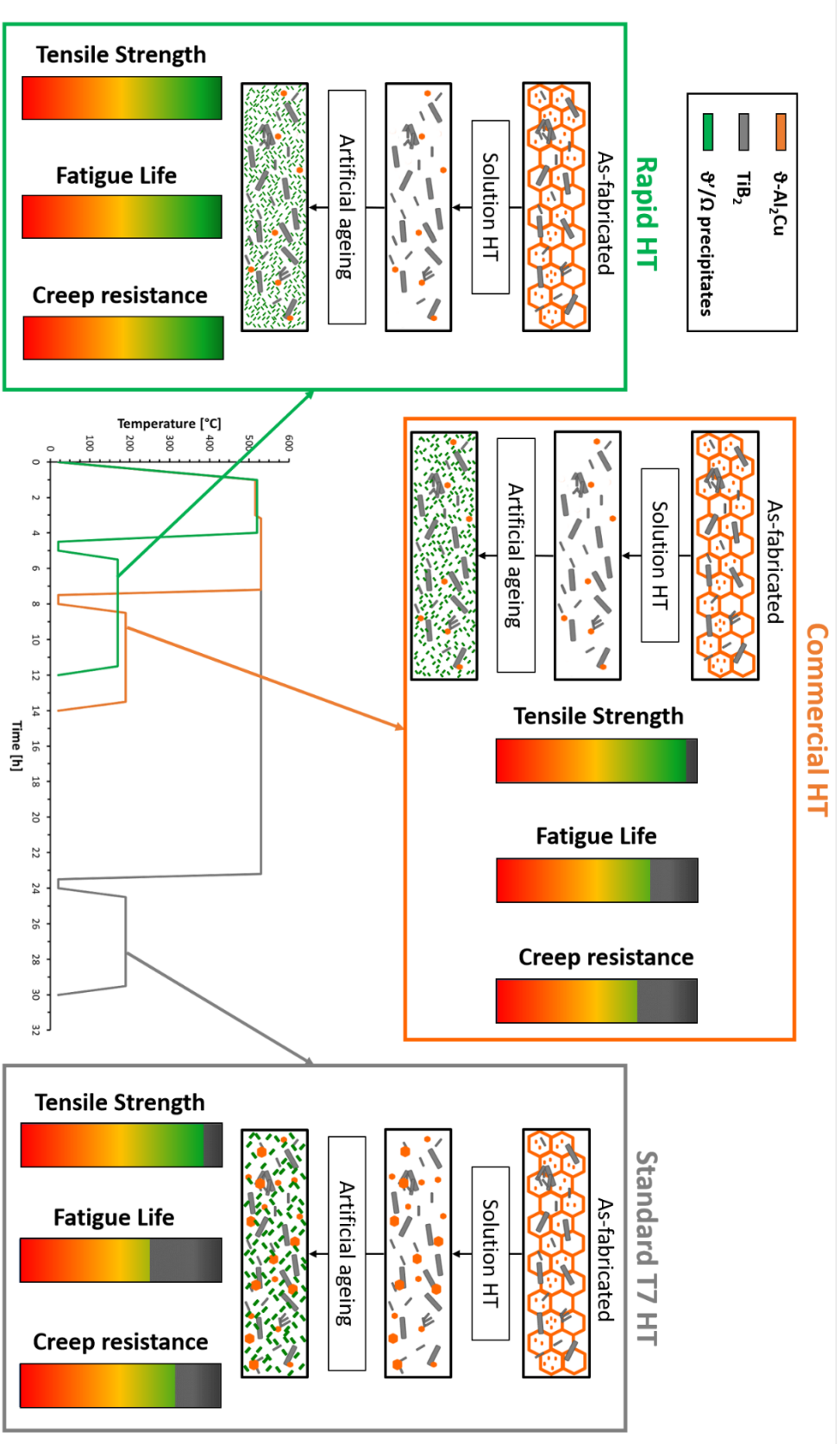

## Abstract

Recent advances in the additive manufacturing of high-strength aluminium alloys have enabled the replacement of cast components in industrial sectors such as aerospace and automotive. However, a major challenge facing additively manufactured alloys is the lack of standardised heat treatments (HT) to optimise mechanical properties. This study investigates the development of a novel HT and its influence on the microstructure and mechanical properties of the A205 Aluminium alloy, fabricated by Laser-Powder Bed Fusion (L-PBF). The A205 alloy was subjected to the Standard T7 HT, a Commercial HT, and the newly developed Rapid HT. Microstructural analysis, using Scanning electron microscopy (SEM) and Electron backscatter diffraction (EBSD), showed a decrease in grain growth for the Commercial HT and Rapid HT compared to the Standard T7, with average grain sizes of 2.4 μm, 2.3 μm, and 3.2 μm, respectively. TEM analysis revealed a higher volume fraction and finer Ω-AlCuAgMg and ϑ'-$Al_2Cu$ precipitates in the Rapid HT compared to the other HTs. The mechanical tests highlighted a higher UTS for the newly developed Rapid HT, achieving 465 MPa, compared to the values of 422 MPa and 449 MPa for Standard T7 HT and Commercial HT, respectively. Additionally, the Rapid HT showed an increase in fatigue life of around 189% and 125% and in creep life of around 33% and 80% compared to Standard T7 HT and Commercial HT, respectively. Finally, a strengthening mechanism model was applied to correlate microstructure evolution and mechanical properties, emphasising the strengthening role of precipitates and confirming segregations in Standard T7 HT.


## 5.1 Introduction

Additive Manufacturing (AM) is a rapidly developing technology with the potential to revolutionise the manufacturing process and the tailoring of properties for complex geometries.

In particular, the AM of high-strength alloys along with topological optimisation tools can produce lightweight, high-performance parts, significantly impacting industrial sectors such as space, aerospace, and automotive [1, 2]. Aluminium alloys (Al alloys) have gained significant attention in various engineering applications due to their excellent mechanical properties, low density, and corrosion resistance. Among these, the additively manufactured (AMed) high-strength AlCu-based alloy reinforced with $TiB_2$, commercially known as A205 or A20X™, stands out as a strong alternative to cast Al alloys, thanks to its superior mechanical properties at high temperatures and enhanced corrosion resistance [1, 3]. The A205 alloy, fabricated using Laser-Powder Bed Fusion (L-PBF), exhibits superior properties, particularly at elevated temperatures, compared to AlSi10Mg, which is currently the most commonly used alloy in the additive manufacturing (AM) of aluminium parts across various industrial sectors [4]. The as-fabricated A205 alloy is characterised by ultra-fine equiaxed microstructure with no apparent segregations and contains both nano- and micro-sized $TiB_2$ [5]. This alloy is heat-treatable, meaning it achieves its maximum potential in terms of mechanical properties and performance when subjected to post-processing thermal treatments. Unfortunately, standard heat treatments (HTs) developed for cast or wrought materials are not compatible with additively manufactured aluminium alloys due to differences in the microstructure of as-fabricated materials [6-8].

Recently, numerous studies have focused on examining the influence of standard HTs on the A205 alloy and comparing them with cast materials. Shakil et al. [9] analysed the correlation between the microstructure and micromechanical properties of A205 using standard HTs. In particular, they assessed the differences between cast and additively manufactured (AMed) materials subjected to a Solution HT and a standard T7 HT. The AM material exhibited high hardness due to grain refinement strengthening. However, the heat-treated AM material showed less strength compared to its cast T7 counterpart. The authors attributed the lower strength of

AM T7 to the formation of precipitation-free zones (PFZs). PFZs typically form along grain boundaries and can degrade both mechanical performance and corrosion resistance. The study highlighted that PFZs play a crucial role, particularly when the grain size is fine. Avateffazeli et al. [10] examined the correlation between standard heat treatments (HTs) and mechanical properties, focusing on the tensile strength of L-PBF A205 compared to its cast counterpart. The authors highlighted differences in the yield point phenomena between the two configurations after the same T7 HT, noting a slightly better strength improvement for the cast T7 material, but greater ductility for the AMed material. Additionally, Avateffazeli et al. recently analysed the effect of the same standard HT on the fatigue behaviour [11], as well as the response of the additively manufactured A205 alloy to very high cycle fatigue (VHCF) after T7 heat treatment [12]. The authors generated stress-life (S-N) data for both as-fabricated and T7 HT materials, discovering significant strengthening during the HT process compared to the as-fabricated condition. The S-N curves showed some overlap near the transition zone and for infinite life cycles, but overall, the fatigue life of T7 HT specimens was superior at all stress levels, indicating the effectiveness of precipitate strengthening. Finally, the creep behaviour of T7 heat-treated AM A205 and its cast counterpart was first investigated by Shakil et al [13] using room temperature indentation creep testing. Shakil et al. study concluded that the cast material exhibited better creep resistance, highlighting a correlation between creep properties and the number density of Ω phases, as well as the extent of precipitate-free zones (PFZ). The cast counterpart was found to have a higher density of precipitates and a lower fraction of PFZs compared to the additively manufactured material subjected to the same T7 HT. Kulkarni et al. [14] later made a first attempt at uniaxial creep testing and DIC-augmented bending creep tests at 200°C. Furthermore, in another study [15], Kulkarni et all. investigated the precipitate

evolution during heat treatments of A205 Al alloy demonstrating the composition of Ω phase composed by Al-Cu-Mg-Ag.

Due to the observed impact of standard heat treatments (HTs) on the mechanical properties, particularly fatigue and creep performance, of additively manufactured A205 compared to its cast counterpart, recent research has shifted towards the development and optimisation of tailored post-thermal treatments specifically designed for L-PBF A205 aluminium alloy. Barode et al. [16], in particular, proposed a revision of standard HTs for this high-strength alloy. The authors demonstrated that the T7 treatment was not the most suitable thermal treatment for A205, and they introduced a new HT, comparing the results with the standard T7 HT. Their study highlighted the possibility of using a single-step solution heat treatment (SS-ST) in place of the standard multi-step (MS-ST) process. The SS-ST resulted in finer precipitation-strengthening phases, leading to improved strength and ductility. It also enabled the almost complete dissolution of Cu-rich phases into the matrix, which is crucial for achieving strengthening during the ageing process. Based on their findings, the authors emphasised the need for new HTs specifically tailored for L-PBF fabricated A205 to achieve superior mechanical properties compared to standard HTs.

Despite the available data in the literature, inconsistencies and a lack of comprehensive investigations into the overall characterisation of mechanical properties in relation to post-thermal treatments for L-PBF produced A205 remain. Thus, further research is required to fully understand the phenomena occurring during HTs of AM aluminium alloys, in order to optimise and develop tailored post-thermal treatments. This study aims to develop an innovative post-thermal treatment strategy for A205 fabricated via L-PBF to enhance its overall mechanical properties and overcome the performance limitations observed in materials subjected to standard HTs. A comprehensive evaluation of the mechanical performance of both vertically

and horizontally fabricated L-PBF materials, specifically in terms of strength, fatigue, and creep, was conducted for the newly developed Rapid HT. The results were compared with the Standard T7 HT, used for cast alloys, as well as the Commercial HT currently available for additively manufactured A205. The correlation between mechanical properties, microstructure, and thermal treatment strategies was investigated by analysing the microstructure evolution of each HT using advanced characterisation techniques, including Electron Backscatter Diffraction (EBSD) and Transmission Electron Microscopy (TEM). Furthermore, the relationship between microstructural evolution and mechanical properties was quantitatively assessed by analysing various strengthening mechanisms. These included contributions from grain boundaries, $TiB_2$ particles, Ω and ϑ'-$Al_2Cu$ precipitates, solid solution strengthening, and clusters, both in the as-fabricated and heat-treated conditions. The findings provided insights into the role of grain size and precipitation phases in the alloy's strengthening mechanisms, allowing for the development and optimisation of a novel post-thermal processing strategy specifically tailored for L-PBF A205 alloy.

## 5.2 Material and Methods

The material used in the study was a pre-alloyed version of A205 (AlCu-TiB2) alloy, featuring a lower content of Ti and B compared to the standard version. The chemical composition of the alloy used in the study, analysed using Inductively Coupled Plasma (ICP) according to the ASTM standard E3061-17 [17], along with a comparison to the standard A205 version, is presented in Table 5.1.

A Concept Laser M2 Cusing L-PBF machine with a 400W laser was used to fabricate the A205 samples. The powder used in the study was recycled, and the alloy was characterised by a wide processing window, achieving high relative density with minimal metallurgical defects. In this study, a layer thickness of 0.030 mm was used, and the L-PBF process parameters were

optimised to achieve a relative density of 99.9%, ensuring good repeatability in material production.

Table 5.1. Material composition for the A205 powder used in the study and comparison with composition of standard A205 [18].

| Element | Percentage (wt.%) | |
|---|---|---|
| | A205 alloy | Nominal Value [18] |
| **Al** | Balance | Balance |
| **Cu** | 4.8 | 4.2-5.0 |
| **Mg** | 0.3 | 0.2-0.33 |
| **Si** | 0.06 | 0.1 max |
| **Fe** | 0.03 | 0.08 max |
| **B** | 0.92 | 1.25-1.55 |
| **Ti** | 2.25 | 3.00-3.85 |
| **Ag** | 0.77 | 0.6-0.9 |

The development and optimisation of the novel Rapid HT parameters were conducted in several stages. Specifically, the solution and artificial ageing treatments were performed at fixed temperatures, which were selected based on data obtained from Differential Scanning Calorimetry (DSC) analysis of the as-fabricated material, as shown in Figure 5.1.

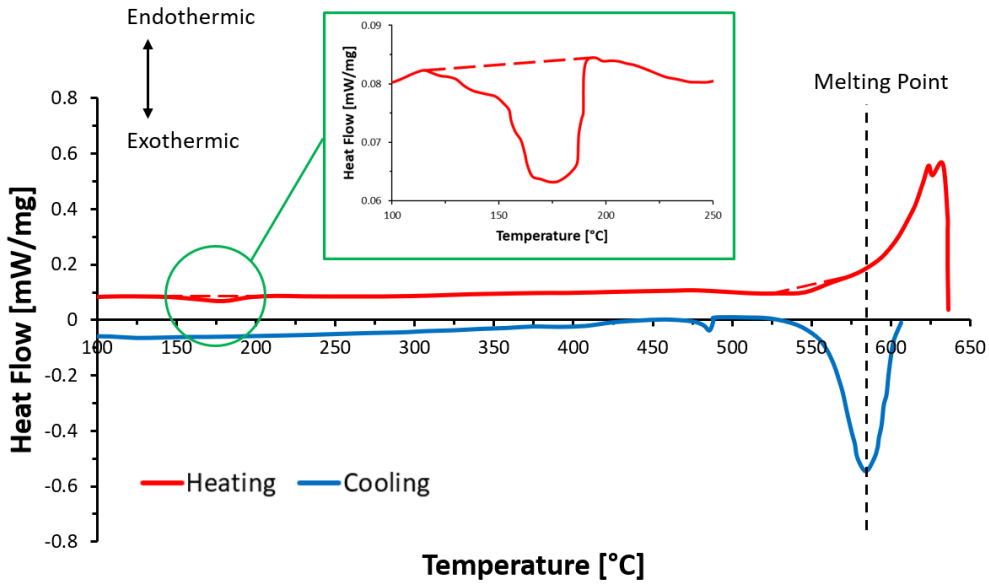


Figure 5.1. DSC analysis of as-fabricated A205 alloy material.

As shown in Figure 5.1, an exothermic peak corresponding to the precipitation of Ω and ϑ' strengthening phases occurred between 170°C and 350°C, while the precipitates at the grain boundaries melt around 530°C [19]. The temperatures for the solution and artificial ageing steps were selected based on the DSC results, with the solution temperature set below 530°C and the artificial ageing temperature set at 170°C. A single-step solution HT was carried out using a Carbolite Gero CWF 1200 furnace at a fixed temperature of 520°C, with a dwell time of up to 24 hours, to assess the influence of solution treatment on the dissolution of Cu-rich phases typical of as-fabricated conditions. The most promising candidates after the solution treatments were evaluated through micro-hardness testing with a Wilson VH1202, while microstructural analysis was performed using a Benchtop Hitachi TM3030 Scanning Electron Microscope (SEM) equipped with Energy Dispersive X-ray (EDX) capabilities and X-ray Diffraction (XRD) analysis conducted with a Benchtop PROTO AXRD. Subsequently, the samples were subjected to an artificial ageing step using an Elite oven at a fixed temperature of 170°C for up to 24 hours. The optimal combination of solution and ageing conditions was determined via micro-hardness analysis. Cuboid samples were fabricated using optimised L-PBF process parameters and heat treated using: i) newly developed Rapid HT, ii) Standard T7 HT [20] and iii) Commercial HT [21].

The microstructure evolution, including changes in grain size and phase distribution during the post-thermal treatments, was assessed using various equipment. In particular, EBSD analyses were performed using a JEOL JSM-7000F to evaluate differences in grain size and orientation after the three tested HTs. Additionally, TEM analysis was conducted with a JEOL JEM-F200 equipped with EDX to acquire high-magnification images for analysing the evolution of strengthening phases and correlating these changes with the mechanical performance of each of the three HTs.

The mechanical properties, tensile and fatigue, were tested at room temperature using a Zwick/Roell 1484 and a Phoenix resonant testing machine, respectively, while the creep test was carried out using an Instron 8862. The tensile test specimens, illustrated in Figure 5.2a, were designed and tested in accordance with the ASTM standard E8/E8M – 22 [22], for both vertical and horizontal orientations. The tests were performed at room temperature with three repetitions for each condition, at a loading speed of 0.39 mm/min. An extensometer was fitted on the gauge length of the sample to acquire the displacement during the entire test.

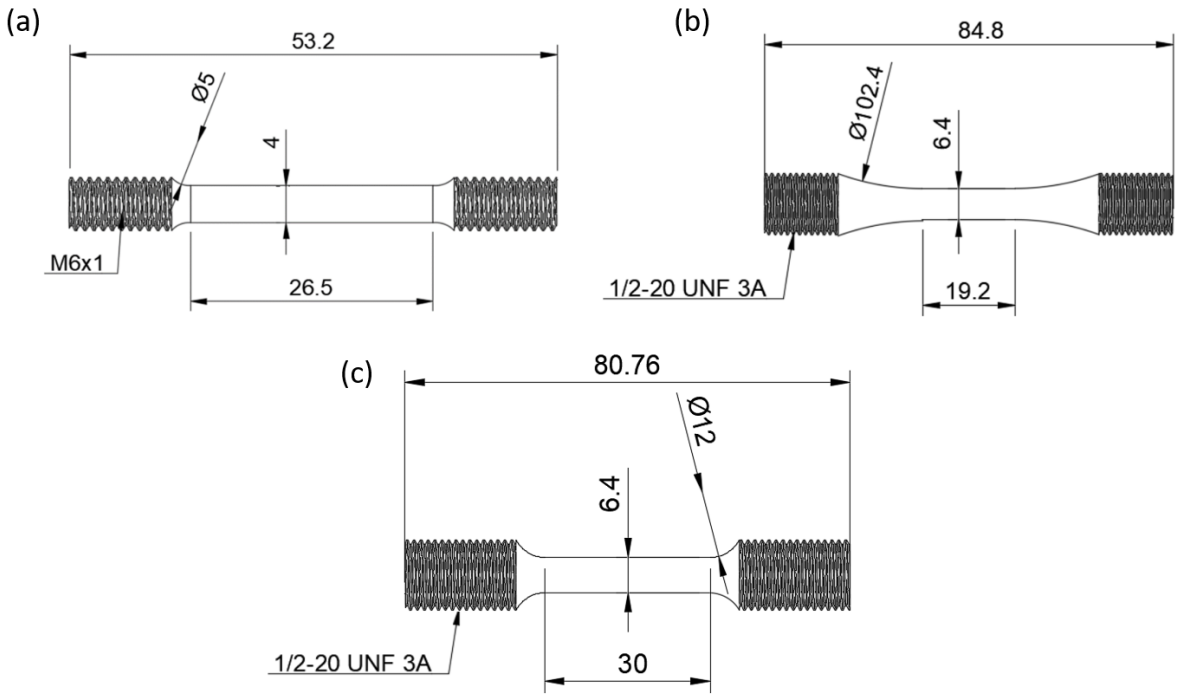


Figure 5.2. Mechanical test specimens. Designed specimens for a) tensile test, b) fatigue test and c) creep test according to ASTM standards.

The fatigue test specimens, depicted in Figure 5.2b, were designed and tested following the ASTM standard E466 – 21 [23], also in both vertical and horizontal orientations. The tests were performed using a fixed load set at 60% of the yield stress (180 MPa) of the as-fabricated vertical condition. Similar to the tensile tests, three repetitions were conducted for each orientation at room temperature. The fractography of tensile and fatigue tests was performed using SEM analysis.

The creep test, represented in Figure 5.2c, was performed on specimens designed and tested according to the ASTM standard E139–11 [24]. In particular, the creep tests were performed only on specimens manufactured along the horizontal build direction to minimise the effect of metallurgical defects such as pores. A uniaxial load of 200 MPa was applied at a fixed temperature of 180°C. The specimens were first subjected to an initial preload until reaching the test temperature, followed by a stabilisation period of 30 minutes to ensure temperature homogenisation. The creep test was then performed in force control mode, employing a high load to minimise the duration of the test. Finally, a strengthening mechanisms method was applied to as-fabricated and heat treated conditions to evaluate the influence of HTs on the mechanical properties of the A205 alloy.

## 5.3 Results and Discussion

### 5.3.1 Development of the new Rapid HT

The development of the novel post-thermal treatment involved conducting each of the two steps individually while analysing the evolution of the microstructure and phases. In particular, micro-hardness measurements were employed to evaluate the optimal conditions of each step, followed by further characterisations to determine and select the parameters for the HT. Initially, the study was focused on the single step of solution treatment at 520°C up to 24 hours, followed by water quenching. The results of the initial study are presented in Figure 5.3, which highlights the evolution of hardness and the segregations typical of the as-fabricated material during the solution treatment at varying time intervals.

The initial microstructure was characterised by fine equiaxed grains, typical of the material, with a significant presence of $TiB_2$, exhibiting agglomerations referred to as clusters, along with grain boundaries enriched in Cu [5, 25]. The dissolution of these Cu-rich phases during the

solution step was essential to ensure the precipitation of a substantial amount of strengthening phases during the following artificial ageing step.

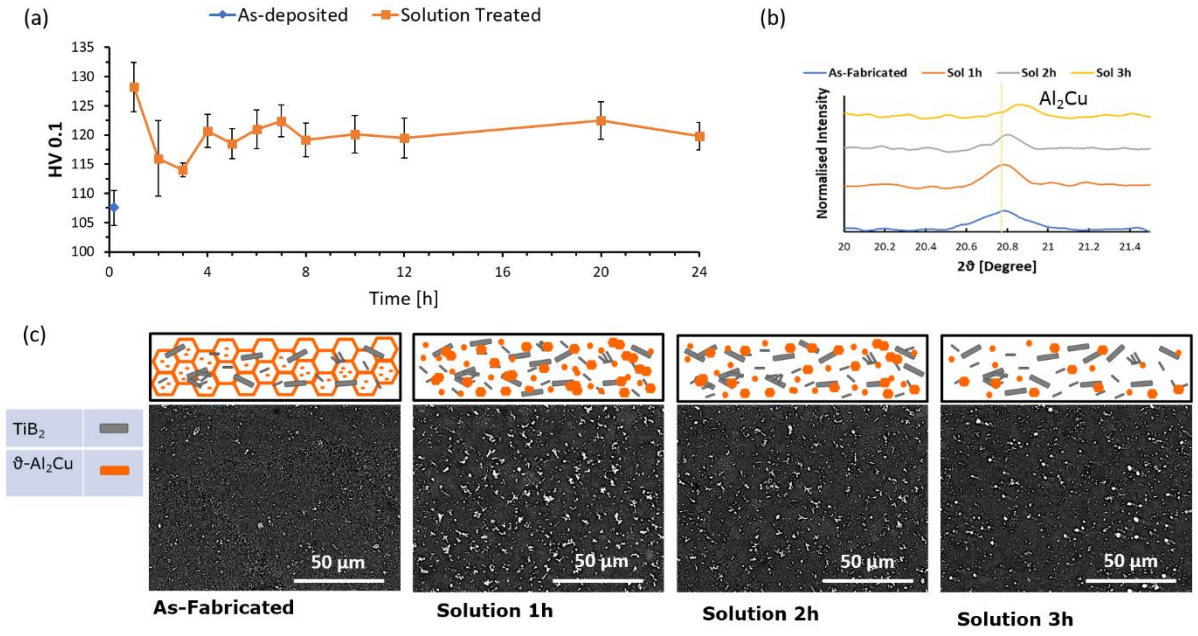


Figure 5.3. Evolution during the solution treatment at several dwell times of additively manufactured A205 in terms of a) Micro-hardness, b) phase peak reduction and c) intermetallic phases.

The results obtained for the solution step highlighted an evolution in hardness during the early dwell times of treatment, with a plateau reached after 4 hours of solution treatment at 520°C. Therefore, the first 3 hours of solution HT were analysed greater in detail to identify the best candidate and assess the influence of solution treatment on the microstructure of the A205 Al alloy. In particular, the analysis of intermetallic particles, shown in Figure 5.3, was conducted via SEM and XRD. A quantitative analysis was carried out using the image processing software ImageJ to calculate the area fraction of Cu-rich phases and segregations present in both as-fabricated and solution treated conditions. The volume fraction calculated in the as-fabricated was around 0.215, while for the solution dwell times of 1, 2, and 3 hours, the percentage was approximately 0.056, 0.046, and 0.032, respectively. The SEM image analysis indicated a significant decrease in cu-rich ϑ-$Al_2Cu$ phases after 3 hours of solution HT at 520°C. The XRD analysis confirmed the results obtained via SEM image analysis. The intensity peak of the ϑ

phases was analysed in detail in order to qualitatively evaluate the dwell time with the least amount of segregations [16]. In particular, the intensity peak was found to reduce along with the increase of dwell time and, with the lowest peak observed after 3 hours of solution treatment, confirming the almost complete dissolution of Cu-rich phases, which were predominantly concentrated around the grain boundaries, into the Al matrix. Furthermore, the shift of the peak position was associated with a change in lattice parameters.

The three solution treatments were then followed by the artificial ageing step at 170°C for up to 24 hours to investigate the effect of different solution dwell times on the precipitation process of the strengthening phases. New as-fabricated samples, coming from the same batch of the previously analysed specimens, were treated using the three different solution dwell times (1, 2, and 3 hours), quenched in water, and immediately subjected to the artificial ageing step to avoid any delay that could lead to the initiation of natural ageing of the A205 Al alloy at room temperature. After the artificial ageing step, the average hardness was analysed, and the results are shown in Figure 5.4.

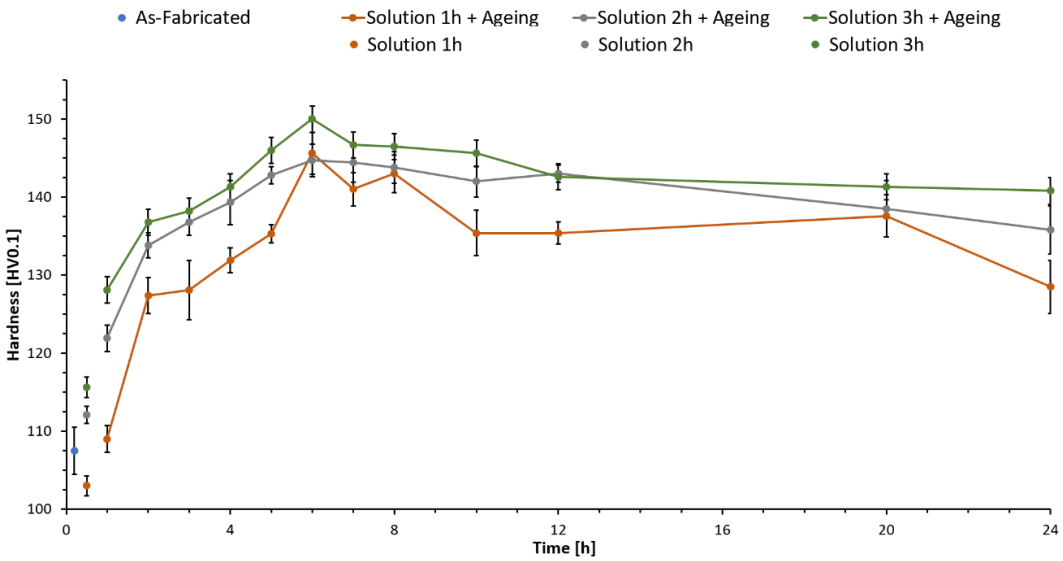


Figure 5.4. Micro-hardness evolution of the solution treated A205 subjected to the artificial ageing step for several dwell times.

The results highlighted a similar trend in the development of micro-hardness across all three tested conditions. In particular, the hardness increased with an increase in dwell time, reaching its peak-ageing time during the artificial ageing step after 6 hours of treatment. All three conditions exhibited the same dwell peak time for the artificial ageing step, with differences only in the micro-hardness values. The highest hardness value was recorded for the samples previously treated with a solution step of 3 hours, followed by an artificial ageing step of 6 hours, achieving an average micro-hardness of 152 $HV_{0.1}$. Consequently, the novel Rapid HT was selected for further comparison with the Standard T7 HT and the Commercial HT. The details of each HT tested in the study are summarised in Table 5.2.

Table 5.2. Details of the steps of each of the three tested post-thermal treatments.

| **Heat Treatment Step** | **Standard T7 HT [20]** | **Commercial HT [21]** | **Rapid HT** |
|---|---|---|---|
| **Solution** | 515°C for 2h<br>then<br>530°C for 20h<br><br>Water Quenching | 505°C for 2h<br>then<br>530°C for 4h<br><br>Water Quenching | 520°C for 3h<br><br>Water Quenching |
| **Artificial ageing** | 190°C for 5h<br><br>Natural Cooling | 190°C for 6h<br><br>Natural Cooling | 170°C for 6h<br><br>Natural cooling |

The novel Rapid HT process was characterised by a reduction in total processing time of approximately 67% and 25% compared to the Standard T7 and HT Commercial HT, respectively.

### 5.3.2 Microstructural Evolution

The samples were successfully treated using the three different HTs and an initial comparison was carried out via SEM imaging and micro-hardness analysis. Figure 5.5 shows the different microstructures of the as-fabricated and heat treated samples. The quantity of segregation and $TiB_2$ clusters, indicated by the yellow arrows in Figure 5.5a, was the least in the new Rapid HT. The Commercial HT was also characterised by a small number of clusters and segregations, while the sample treated using the Standard T7 HT displayed a considerable number of clusters and segregations, with overgrowned phases.

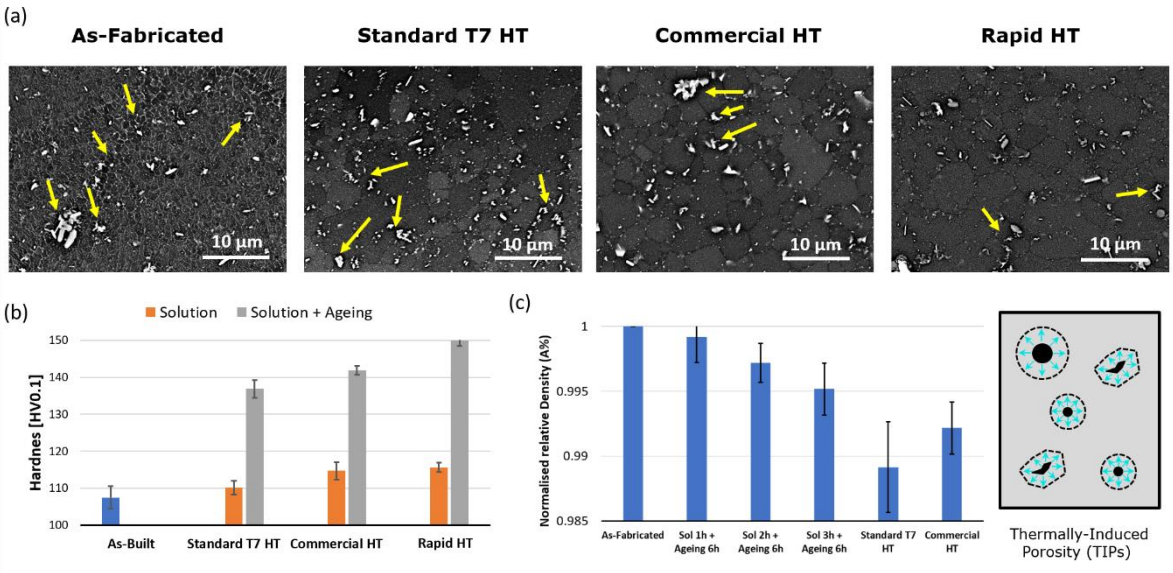


Figure 5.5. Initial analysis and comparison between the three tested HTs conditions. a )SEM images of microstructure with yellow lines indicating the presence of segregation and $TiB_2$ clusters for all the tested conditions; b) micro-hardness comparison; and c) normalised relative density analysis compared to the as-fabricated condition.

The analysis of porosity following the HTs, depicted in Figure 5.5c, highlighted another issue related to the AM of metal alloys. Using the density (A%) of the as-fabricated material as a baseline, the density analysis of the heat treated materials showed a consistent decrease in average value. The lower density value was correlated with the formation of Thermally-Induced Porosity (TIP), caused by the expansion of the shield gas trapped in the pores created during the L-PBF manufacturing process [26]. TIP can be detrimental to the material, as a lower

density indicates a high number of pores that can act as nucleation sites during mechanical performance [27]. In particular, the results indicated a significant presence of TIP after the Standard T7 HT, while the density values for the Rapid HT and Commercial HT were lower but closer to the as-fabricated density. A possible cause of the large number of TIP may be associated with the recycled powder used in the study, which could have introduced moisture and facilitated the formation of oxides, increasing the generation of micro-pores and metallurgical defects into the as-fabricated condition, ultimately leading to the formation of TIP after the HTs [28].

Finally, a comparison in terms of micro-hardness was conducted between the different HTs. Figure 5.5b highlighted the increase in the strength of the heat treated materials compared to the as-fabricated condition. The novel Rapid HT exhibited the highest micro-hardness value, reaching an average of 150 $HV_{0.1}$, while the Standard T7 HT and the Commercial HT were characterised by hardness values of 142 $HV_{0.1}$ and 137 $HV_{0.1}$, respectively. Hardness can be related to mechanical properties, particularly strength. Therefore, the differences in micro-hardness among the three tested conditions were analysed in greater detail using EBSD and TEM to better understand the evolution of the microstructure and strengthening phases during the tested HTs, correlating these results to the mechanical performance of the three HTs.

The EBSD analysis was performed to analyse the average grain size, which influences the mechanical properties of the material. The average initial grain size of the as-fabricated A205 was approximately 1.4 μm.

The microstructures of the three tested HTs, characterised by random texture, and equiaxed grains, are shown in Figure 5.6. The grain size analysis indicated a significant grain growth

phenomenon for the Standard T7 HT, which predominantly occurred during the solution step.

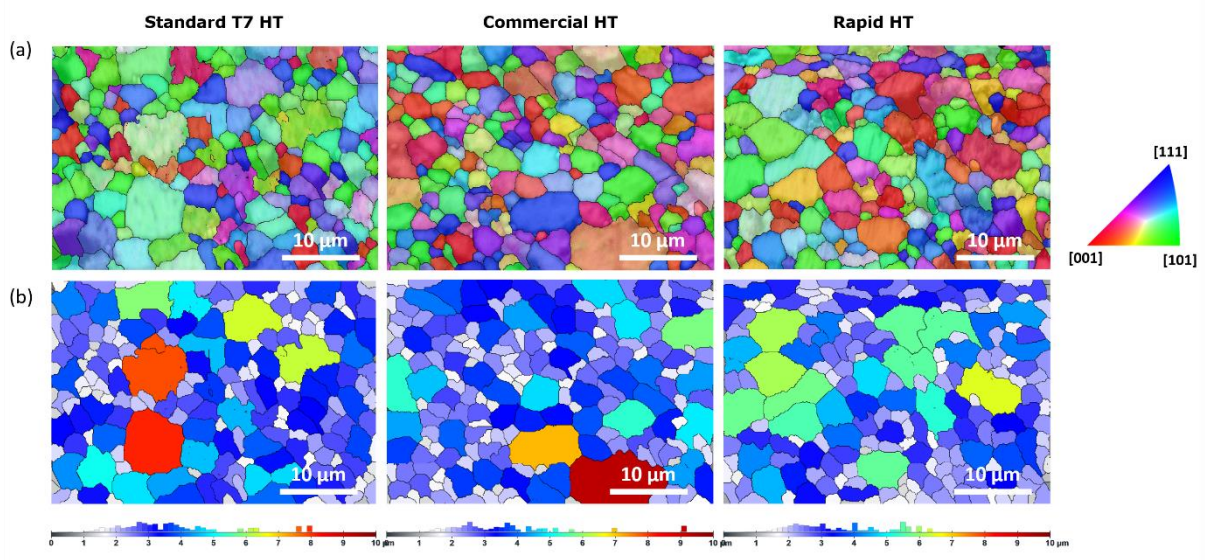


Figure 5.6. EBSD micrographs showing the grain structure and grain size of the three tested HT conditions, Standard T7 HT, Commercial HT, and Rapid HT.

The extended duration at high temperatures resulted in an increase in grain size, reaching an average of 3.2 µm. On the contrary, the average sizes for the other HTs remained closer to the value of the as-fabricated condition, with values of 2.4 µm for the Commercial HT, and 2.3 µm for the Rapid HT. The presence of $TiB_2$ within the matrix contributed to a pinning effect on the grain boundaries, thereby mitigating the grain growth phenomenon.

Finally, the strengthening phases following the three HTs were analysed using images acquired through TEM. By providing high-resolution imaging at the atomic scale, TEM allowed for a detailed examination of the strengthening precipitates, which are crucial for the alloy's mechanical properties. Additionally, due to the size of these phases, the resolution of the SEM was insufficient to identify and study the evolution of the strengthening phases or to facilitate a comparison among the three tested HTs.

The TEM-EDX map, presented in Figure 5.7, highlighted the presence of needle-shaped strengthening precipitates that are rich in Cu, with some instances showing enrichment in silver (Ag) and magnesium (Mg). Based on existing literature, these precipitates were most likely

identified as Ω and ϑ'-$Al_2Cu$, which are recognised as the most stable precipitates in Al-Cu alloy [16]. Additionally, the presence of precipitates enriched with Mg is consistent with the formation of S'-$Al_2CuMg$ [29, 30]. Collectively, these phases play a critical role in determining the mechanical performance of the material [31].

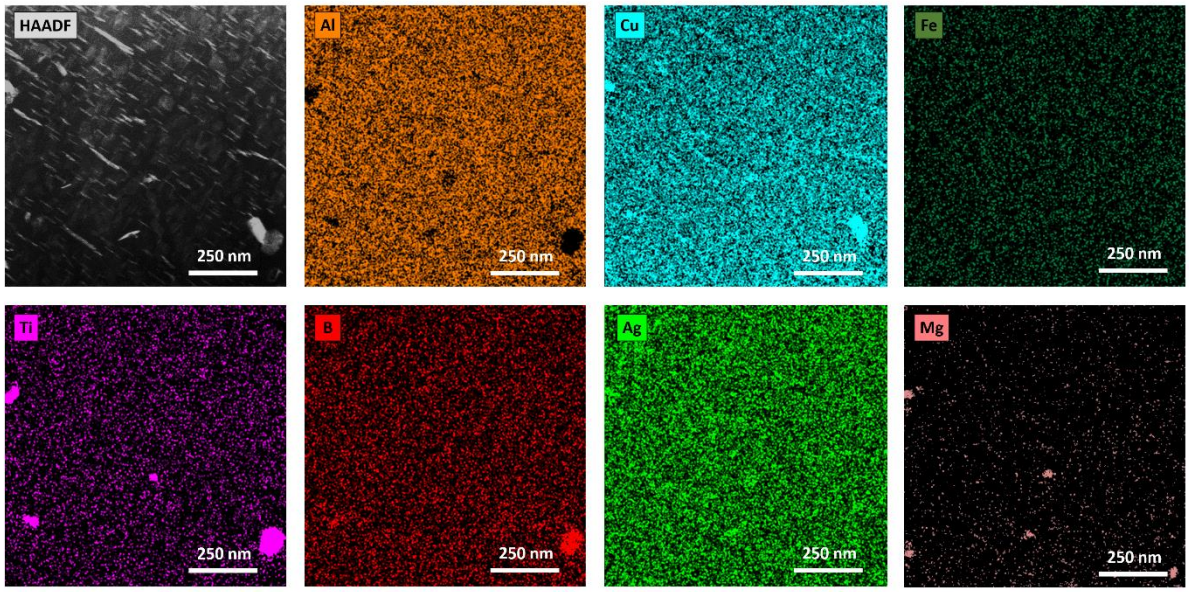


Figure 5.7. High-resolution HAADF-STEM micrograph of the new Rapid HT and EDX mapping showing the common elements related to the strengthening phases and TiB2 particles.

The $Al_2Cu$ phases hold the same chemical composition as the eutectic ϑ forming during the L-PBF process and are typically generated from a supersaturated solid solution. The Ω phase exhibits a high degree of coherency with the Al matrix, leading to the formation of plate-like precipitates aligned along the {111} plane. In contrast, the ϑ' and S' phases are semi-coherent with the Al matrix, consisting of thin plate-like structures aligned on the {100} plane and on the {210} plane of the matrix, respectively [31].

A comparison of the strengthening phases across the three tested HTs was carried out employing High-Angle Annular Dark-Field (HAADF) imaging. In particular, Figure 5.8 shows high-resolution images of a grain boundary triple point, along with high-magnification images that highlight the needle-shaped precipitates formed after each HT.

Figure 5.8a displays the presence and distribution of coarse ϑ phases and micro-$TiB_2$ particles across the three HT conditions. In particular, while a few segregations are visible at the grain boundaries are visible for all three HTs, the distribution and volume fraction of the coarse precipitates vary significantly among the conditions.

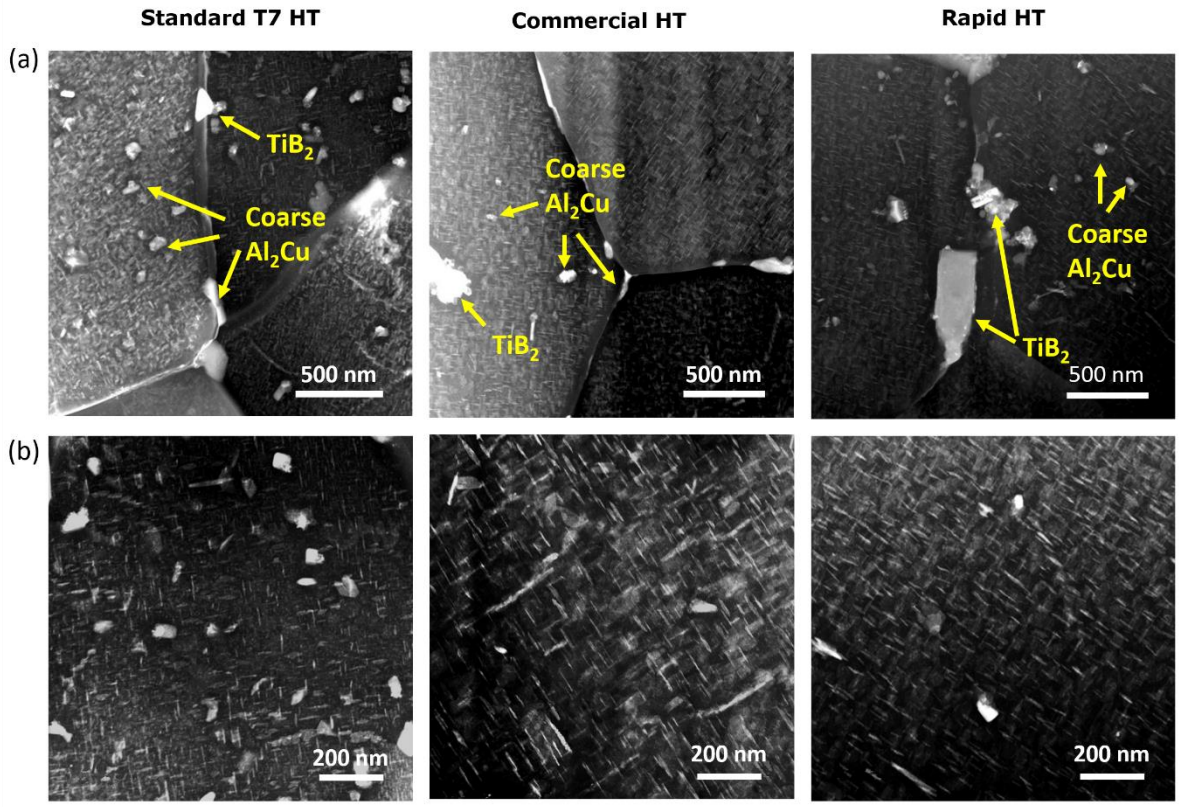


Figure 5.8. HAADF TEM-imaging of the three tested conditions, for a) a grain boundary triple point and b) precipitates phases and $TiB_2$ particles.

In the Standard T7 HT, $TiB_2$ particles are prominently observed along the grain boundaries, with large, coarse ϑ-$Al_2Cu$ precipitates dispersed throughout the matrix. The high presence of these coarse precipitates suggested incomplete dissolution of the ϑ during the long solution step, followed by over-ageing during the artificial ageing step. Such growth of the precipitates could potentially diminish their strengthening effectiveness due to reduced particle density. Similarly, the Commercial HT also exhibited coarse $Al_2Cu$ precipitates and $TiB_2$ particles. However, the distribution of these precipitates was found to be more refined, with fewer large,

coarse ϑ-$Al_2Cu$ compared to the Standard T7 HT, suggesting more controlled conditions in the HT steps. In contrast, the newly developed Rapid HT was characterised by a smaller presence of coarse ϑ-$Al_2Cu$, while still retaining $TiB_2$ particles along grain boundaries. The result highlighted a more effective tailoring of the HT steps, which minimised precipitate coarsening and achieved higher distributions of finer strengthening precipitates within the matrix.

The results were further sustained by the high-magnification analysis, which allowed a detailed evaluation of the evolution of strengthening phases across the three HTs. A quantitative comparison in terms of size and volume fraction of the Ω- $Al_2Cu$ and ϑ'-$Al_2Cu$ precipitates is summarised in Table 5.3.

Table 5.3. Quantitative analysis and comparison of the density and size of the strengthening precipitates formed after the three tested HTs.

| **Heat Treatment Condition** | **Precipitate Volume Fraction** | | **Precipitate Size** | | | |
|---|---|---|---|---|---|---|
| | | | **Length [nm]** | | **Width [nm]** | |
| | **Average** | **Standard deviation** | **Average** | **Standard deviation** | **Average** | **Standard deviation** |
| **Standard T7 HT** | 0.018 | 0.003 | 68.8 | 1.9 | 2.7 | 0.02 |
| **Commercial HT** | 0.021 | 0.003 | 48.8 | 1.8 | 1.8 | 0.05 |
| **Rapid HT** | 0.028 | 0.002 | 45.6 | 0.8 | 1.8 | 0.01 |

The Standard T7 HT showed lower volume fractions of precipitate formation, indicating significant coarsening of the precipitates. The Commercial HT analysis highlighted a more uniform distribution of finer precipitates throughout the matrix. Finally, the novel post-thermal treatment strategy, Rapid HT, appeared to promote a greater volume fraction of finely dispersed precipitates, effectively preventing excessive coarsening.

### 5.3.3 Mechanical Performance

A comprehensive analysis of the mechanical properties of the A205 alloy was performed. The study aimed to compare the three tested HTs and understand the influence of post-thermal treatments on mechanical performance.

Tensile test analysis was performed and Figure 5.9 shows the results obtained. A comparison of these conditions revealed significant differences in ultimate tensile strength (UTS), yield strength (YS), and elongation (EL).

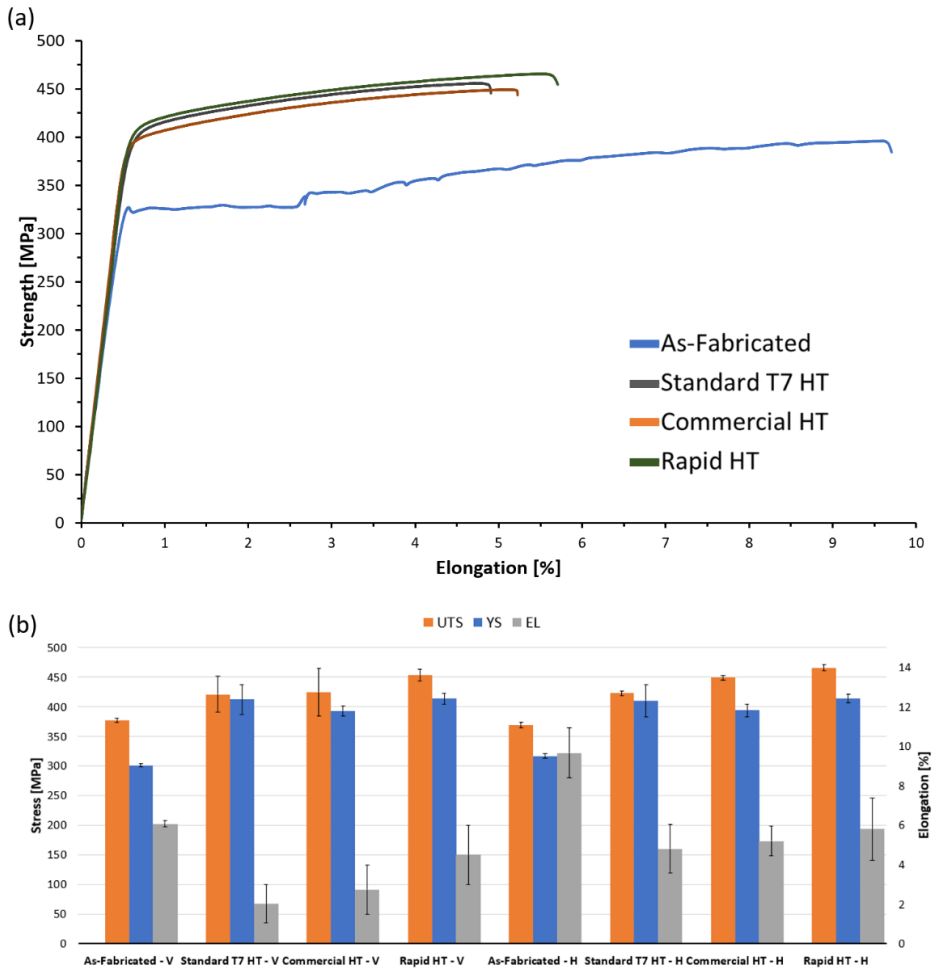


Figure 5.9. Tensile properties of A205 alloy in as-fabricated condition and following the three tested HTs. (a) Stress-strain curves for the horizontal (H) build orientation, comparing as-fabricated, standard

T7 HT, Commercial HT, and Rapid HT; (b) Comparison of the ultimate tensile strength (UTS), yield strength (YS), and elongation (EL) for both Vertical (V) and Horizontal (H) conditions.

The as-fabricated condition exhibited relatively lower YS and UTS values, for both vertical (V) and horizontal (H) conditions, while showing good elongation and, therefore, ductility. The tensile curve, represented in Figure 5.9a, was characterised by the typical stress-strain profile of additively manufactured A205 alloy, as also demonstrated in the literature [16, 25, 32]. In particular, the tensile behaviour showed inhomogeneous deformation between the initial elastic region and the final homogeneous flow region, while producing a series of serrations after the elastic response, reflecting heterogeneous deformation within the material. The sudden jump observed in the stress-strain curve of the as-fabricated sample at approximately 2.5 % elongation is attributed to a slippage of the extensometer during the tensile test.

All three tested HTs, on the other hand, exhibited a more typical tensile profile, with similar behaviour in both vertical and horizontal conditions, confirming the isotropic behaviour of the material after L-PBF and the subsequent HTs. The Commercial HT and the Rapid HT showed similar behaviour, with a substantial increase in YS and UTS which indicated enhanced strength following the HTs. In particular, the newly developed Rapid HT achieved the highest YS and UTS in the horizontal orientation, with values of 413 MPa and 465 MPa, respectively. The novel HT also showed an improvement in elongation when compared to the Standard T7 HT, suggesting a better balance between strength and ductility. The issues with the elongation were correlated with the significant presence of TIP, which occurred during the high temperatures of solution steps. Additionally, the recycled powder could have increased the likelihood of micro-pores formation, not identified during the analysis of the as-fabricated condition, which increased the number of TIP during the solution steps [28]. The results emphasised a decrease in TIP for the Rapid HT, leading to an increase in EL values compared to the other HTs. To

better understand the behaviour of the different HTs and to analyse the influence of the TIP on the strength of the material, a fractography analysis was carried out.

The fractography analysis presented in Figure 5.10 offered valuable insights into the fracture behaviour of the A205 alloy following tensile testing. In the as-fabricated condition, the analysis of the fracture surface indicated ductile fracture mechanisms, primarily driven by microvoid coalescence (MVC).

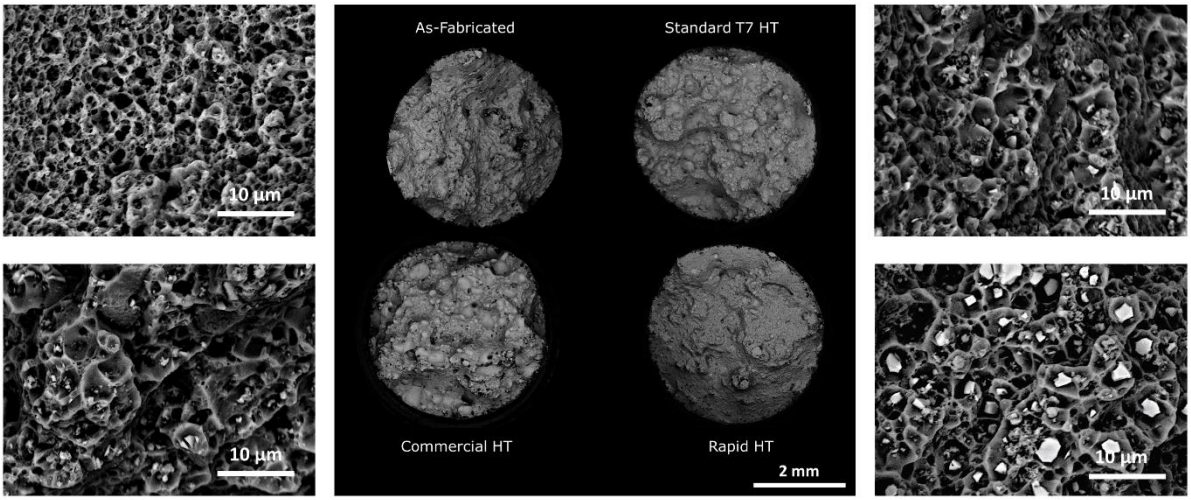


Figure 5.10. Fractography analysis of A205 alloy after tensile testing in the as-fabricated condition and following Standard T7 HT, Commercial HT, and Rapid HT.

The micrographs also revealed the presence of pores, particularly in regions where the fracture propagated, suggesting a lack of consolidation during fabrication. After the Standard T7 HT, the fracture surface displayed a more refined texture, with an increased presence of voids and larger dimples, indicating a reduction in ductility compared to the as-fabricated condition. A similar trend was also found for the Commercial HT, which exhibited further refinement of the dimple size, and a decrease in the number of voids. Finally, the novel Rapid HT showed the most compact and uniform fracture surface, characterised by fine dimples and fewer large voids, suggestive of a high-energy fracture mechanism. The reduction in void size and more uniform fracture pattern suggested that the Rapid HT strategy optimised the alloy's

microstructure, leading to the highest tensile strength observed in the tensile tests, while still maintaining a reasonable level of ductility.

The fatigue performance at room temperature was also analysed, and the results are presented in Figure 5.11a. A relatively high load was applied to the tested conditions to reduce the total test duration. A fractography analysis was also performed and the results are represented in Figure 5.11b.

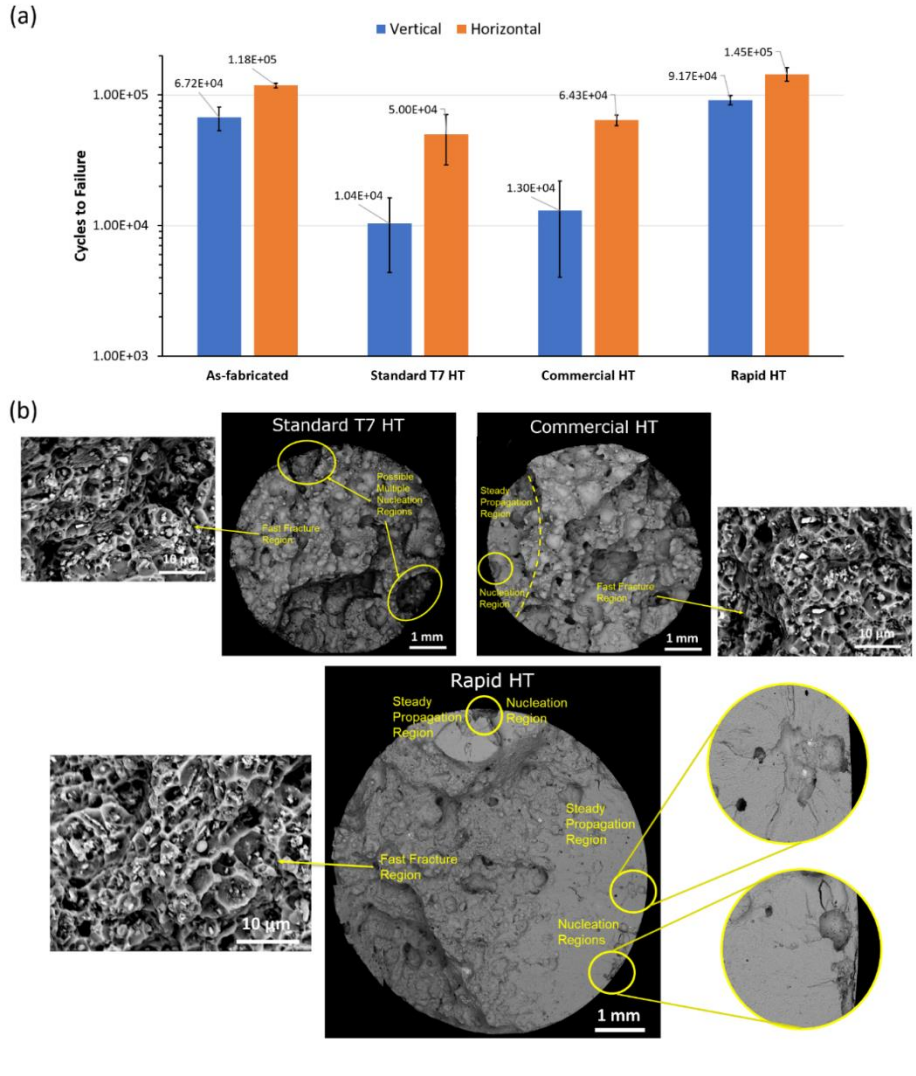


Figure 5.11. Fatigue test results and fractography analysis of A205 alloy in as-fabricated condition and after different HTs. (a) Cycles to failure comparison for vertical and horizontal build orientations in the as-fabricated condition, Standard T7 HT, Commercial HT, and Rapid HT; (b) Fractography analysis of fatigue fracture surfaces highlights key regions of nucleation, steady crack propagation, and fast fracture region.

The results of the fatigue tests highlighted a good performance of the as-fabricated condition, with a high number of cycles to failure observed for both vertical and horizontal build directions. This behaviour can be attributed to several characteristics of the material following the L-PBF process. In particular, the as-fabricated condition exhibited smaller pore sizes compared to the heat-treated conditions. Additionally, the high ductility observed in the tensile tests contributed to the enhanced overall fatigue performance. For all the heat treated conditions, the horizontal direction showed an improvement in fatigue behaviour, which was associated with the orientation of the load relative to the direction of the pores. Specifically, in the horizontal direction, the load was applied perpendicularly to the orientation of the pores, which helped improve fatigue life. The Standard T7 HT exhibited the fewest number of cycles to failure, likely due to microstructural changes observed after the HT. The overgrowned ϑ' precipitates, the large number and size of TIP, and the relatively brittle behaviour contributed to early crack initiation and propagation. The lower fatigue performance was confirmed by the fractography analysis, which revealed a large fast fracture area with multiple nucleation sites, indicating premature crack initiation and limited fatigue life. The Commercial HT resulted in a slightly higher fatigue life compared to the Standard T7 HT, although exhibiting a similar fracture morphology, with several distinct nucleation sites and a small crack propagation region, leading to a prominent fast fracture area. In contrast, the novel Rapid HT demonstrated the most significant improvement in fatigue life for both vertical and horizontal orientations. Compared to the Standard T7 HT and Commercial HT, the Rapid HT showed an increase in fatigue life of approximately 189% and 125%, respectively. The fractography analysis revealed a more stable crack propagation region with fewer nucleation sites, which were initiated at surface pores. These defects likely originated from the contour process parameters, reducing the overall fatigue life [33]. Nevertheless, the results suggested a more controlled and delayed crack

propagation process, in line with the significantly improved fatigue life observed for the Rapid HT compared to the other HTs. The reduction in TIP defects, along with the formation of fine precipitates during the Rapid HT allowed the alloy to acquire a better balance between strength and ductility, thereby enhancing the fatigue performance of the alloy.

Finally, creep tests were also conducted, focusing only on horizontal specimens in order to minimise the influence of pores and metallurgical defects that persisted after the HTs. This approach was used to isolate the effect of the precipitates formed during each of the three HTs. As described before, an accelerated test was performed under a high load of 200 MPa at 180°C to reduce the testing time. A comparison of the creep test results is shown in Figure 5.12.

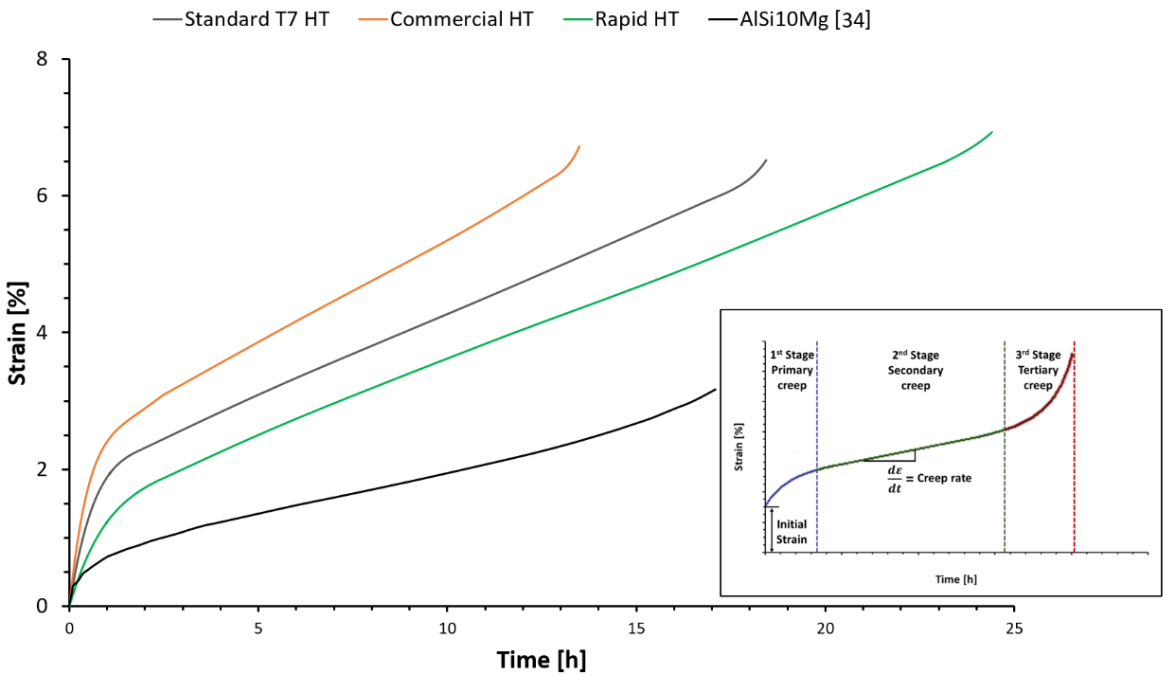


Figure 5.12. Accelerated Creep test results at 200 MPa and 180°C for AlSi10Mg in as-fabricated condition [34], and A205 alloy after three different HTs, Standard T7 HT, Commercial HT, and Rapid HT.

The results of the creep test for the A205 following the three HTs highlighted distinct behaviours. All three conditions exhibited a similar trend in the primary creep phase, followed by a short tertiary creep phase that led to rapid failure. The majority of creep life occurred during the secondary steady creep phase. The Commercial HT showed the poorest creep

performance, with failure occurring after around 14 hours, and it was characterised by a higher creep rate compared to the other HTs. The lower creep resistance of the Commercial HT was likely due to its smaller grain size, which negatively affected its ability to resist creep deformation [35]. The Standard T7 HT demonstrated an improvement in creep life, lasting about 18 hours, with a slower creep rate compared to the Commercial HT. This behaviour was attributed to the larger grain size resulting from grain coarsening during the heat treatment, which improved the material's resistance during the steady-state creep phase [14]. The Rapid HT was characterised by a similar creep rate to the Standard T7 HT, with a longer secondary creep phase, even with a small grain size similar to the Commercial HT. Among the three HTs, the novel Rapid HT exhibited the best creep performance, with a total creep life approaching 25 hours, showing an increase in creep life of approximately 33% and 80% compared to the Standard T7 HT and Commercial HT, respectively. The result represented a notable achievement when compared to the limited studies available on A205 alloy [13, 14], as well as to other materials like AlSi10Mg, which is widely used in L-PBF [34]. The evaluation of the creep curve for AlSi10Mg in as-fabricated condition, shown in Figure 5.12, highlighted the improvement in creep behaviour of the A205 alloy after heat treatment. The as-fabricated AlSi10Mg is typically characterised by columnar grains, with an average dendritic size five times larger than the A205 alloy [36]. Dendritic grains generally provide better creep performance compared to equiaxed grains due to the higher grain boundary area [37, 38]. While AlSi10Mg benefits from its silicon-rich microstructure and fine cellular structure, the A205 alloy, especially with optimised heat treatment, offers enhanced high-temperature stability through precipitation strengthening. Compared to AlSi10Mg, the A205 alloy exhibited higher overall creep strain; however, the Rapid HT variant of A205 demonstrated significantly improved creep resistance and prolonged lifetime under sustained loading. The superior

performance of the A205 alloy heat treated with the Rapid HT demonstrated the success of this newly developed post-thermal treatment in enhancing the alloy's resistance to high-temperature creep deformation while maintaining a fine equiaxed grain structure, essential for optimising mechanical properties at room temperature. The improved creep performance of the Rapid HT was attributed to the uniform distribution, small size, and high homogeneous volume fractions of precipitates formed during the artificial ageing step. These finely dispersed precipitates inhibited grain boundary sliding, slowed down creep propagation, and enhanced the overall creep resistance of the alloy [39], even though the grain size remained relatively small, similar to that of the Commercial HT.

### 5.3.4 Strengthening mechanism

The comprehensive study of the mechanical properties of the additively manufactured A205 alloy highlighted the significant influence of HTs. The microstructural evolution following each HT affected the tensile, fatigue and creep performance of the alloy, revealing notable variations in both the ductility and strength of the material. These differences in mechanical performance were closely correlated with the presence of segregations and the formation and growth of the precipitate phases, Ω-$Al_2Cu$ and ϑ'-$Al_2Cu$. Furthermore, changes in solid solution and grain size after each of the HT, along with the pre-existing $TiB_2$ particles, further contributed to the overall strengthening of the material. In particular, the yield strength of the alloy, manufactured in the vertical orientation, was estimated through the cumulative effect of individual strengthening mechanisms associated with the A205 alloy in as-fabricated conditions and after different HTs. This approach was supported by the studies conducted by Jiang et al. [40] and Barode et al. [19]. The proposed equation is presented below.

$$\sigma_{YS} = \sigma_0 + \sigma_{TiB_2} + \sigma_{\Omega/\vartheta'} + \sigma_{GB} + \sigma_{SS} + \sigma_{co-cluster} \quad (1)$$

where $\sigma_0$ was the lattice friction of pure Al, $\sigma_{TiB_2}$ was the strengthening contribution from the $TiB_2$ particles, $\sigma_{\Omega/\vartheta'}$ was the contribution from the plate-like Ω-$Al_2Cu$ and ϑ'-$Al_2Cu$ precipitates, $\sigma_{GB}$ was the grain boundary strengthening, $\sigma_{SS}$ was the solid solution strengthening, and $\sigma_{co-cluster}$ was the contribution from the presence of disordered clusters in the matrix related to the presence of Mg and Ag.

The lattice friction in pure Al $\sigma_0$ was considered as 20 MPa for all the conditions [40], while the other strengthening contributions were calculated using the proposed equations.

The contribution of the $TiB_2$ ceramic particles present in the matrix to the overall strengthening of the A205 alloy in the different conditions was estimated through the sum of multiple mechanisms. This cumulative effect was expressed mathematically, as shown in Eq. 2. The volume fraction ($V_P$), the average particle diameter ($d_p$), and the inter-particle distance (λ) were calculated from the SEM images of the as-fabricated material and considered unchanged even after the HTs. The values of ($V_P$), ($d_p$), and (λ) were 1.74%, 0.53 μm, and 3.49 μm, respectively.

$$\sigma_{TiB_2} = \sigma_{LB} + \sigma_{Orowan} + \sigma_{Modulus-TiB_2} + \sigma_{CTE} \quad (2)$$

where $\sigma_{LB}$ was the load-bearing strengthening, estimating the load transferred from the matrix to the $TiB_2$ particles distributed in the matrix, and expressed in Eq. 3.

$$\sigma_{LB} = V_P \frac{1}{2} \sigma_m \quad (3)$$

with $\sigma_m$ representing the yield strength of the matrix, and considered as 289 MPa [19, 40].

The contribution due to the Orowan strengthening $\sigma_{Orowan}$ was calculated as in Eq. 4.

$$\sigma_{Orowan} = \frac{0.13 G_m b}{\lambda} \ln \frac{d_p}{2b} \quad (4)$$

where $G_m$ was the shear modulus of the Al matrix, and b was the burger vector, considered as 26.9 GPa, and 0.286nm, respectively.

The increment correlated to the elastic mismatch between the TiB2 particles and the matrix, $\sigma_{Modulus-TiB_2}$ was estimated using the Eq. 5.

$$\sigma_{Modulus-TiB_2} = \sqrt{3}\alpha_{mt} G_m b \sqrt{\frac{6V_P}{bd_p}\varepsilon_y} \quad (5)$$

where $\alpha_{mt}$ was representing the dislocation strengthening coefficient, estimated as 0.5 [19], and $\varepsilon_y$ the yield strain of the as-fabricated condition.

Finally, the last contribution to the $\sigma_{TiB_2}$ was represented by the strengthening due to the Coefficient of thermal expansion (CTE) mismatching between the TiB2 particles and the matrix, $\sigma_{CTE}$. Of the equations constituting the $\sigma_{TiB_2}$, this last increment value was different for each of the different conditions. The equation representative of the $\sigma_{CTE}$ was reported in Eq. 6.

$$\sigma_{CTE} = \beta_{CTE} G_m b \sqrt{\frac{12\Delta_{CTE}\Delta_T V_P}{bd_p(1-V_P)}} \quad (6)$$

where $\beta_{CTE}$ was a geometrical constant equal to 1.25, an$\Delta_{CTE}$d was the difference in CTE of the Al matrix and $TiB_2$ particles, equal to $16.8x10^{-6}$ $K^{-1}$. $\Delta_T$ was instead calculated taking into consideration the difference between the room temperature and the temperature representative of each condition. In particular, the temperature correlated to the as-fabricated condition was considered as the melting temperature of the alloy, equal to 655°C, while for the HT the max temperature of the solution step was used. By quantifying the individual contributions from those mechanisms, Eq. 2 helped to explain the enhanced mechanical properties of the alloy, particularly the yield strength, in relation to the $TiB_2$ particles distributed throughout the matrix. The strengthening contribution from the precipitates was considered specifically for the heat-treated conditions, as the precipitates are formed during the heat treatment process. It was assumed that the observed precipitates were either Ω-$Al_2Cu$ or ϑ'-$Al_2Cu$. The increment in strength resulting from the presence of these precipitates was calculated using Eq. 7 [19, 41].

$$\sigma_{\Omega/\vartheta'} = \frac{1.211 M d_t \gamma_i^{3/2}}{t_t^2} \sqrt{\frac{b f_v}{\Gamma}} \quad (7)$$

where the Taylor factor for polycrystalline materials (M) was equal to 3.06, the line tension of the dislocations in the matrix (Γ) was approximated to $1.1 \times 10^{-15}$ MPa·m$^2$, and $\gamma_i$ was interfacial energy, equal to 0.14 J/m$^2$ [19, 31]. The precipitate dimensions were presented in terms of volume fraction ($f_v$), average thickness ($t_t$), and average diameter ($d_t$), calculated as in Table 5.3.

The contribution in strengthening correlated to the grain size was calculated using the Hall-Petch effect [19, 42], and it is reported in Eq. 8.

$$\sigma_{GB} = k d^{1/2} \quad (8)$$

where k was the Hall-Petch coefficient, characterised by a range of values depending on the microstructure, and considered as in the study of Barode et al. [19] as 0.17 $MPa\sqrt{m}$ and 0.14 $MPa\sqrt{m}$ for the as-fabricated and the heat treated conditions, respectively. The average grain size (d) instead was considered using the data from the EBSD map anlysis.

The solid solution strengthening contribution $\sigma_{SS}$ was related to Cu and Mg contribution and calculated using Eq. 9.

$$\sigma_{SS} = \sum_{i=element} k_i \; c_{ss,i}^n \quad (9)$$

with n equal to a constant value of 1, and $k_i$ the contribution of each element, and in particular $k_{Cu}$ equal to 13.8 MPA/wt% and $k_{Mg}$ equal to 18.6 MPA/wt% [19, 40, 43]. The concentrations of Cu and Mg in the as-fabricated condition were considered as in the work of Barode et al. [19], as 1.58 wt% and 0.16 wt%, respectively. Regarding the HTs conditions, only for the Standard T7 HT was considered. The concentration of Mg after the HT was considered

negligible, while for the Cu a concentration of 3.3 wt% was estimated according to the study of Gazivov et al. [31].

Finally the strengthening due to the presence of clusters $\sigma_{co-cluster}$, mainly Ag and Mg, in the matrix, was calculated based on 2 contributions depending on the modulus mismatching and the coherent strengthening, and it is reported in Eq 10.

$$\sigma_{co-cluster} = \sigma_{Modulus-cluster} + \sigma_{cs-cluster} \tag{10}$$

with

$$\sigma_{Modulus-cluster} = 1.4\alpha_{mc}^{3/2}\Delta_G^{3/2} f^{1/2} b \left(\frac{r}{b}\right)^{\frac{3\beta_{mc}}{2}-1} (2\pi\Gamma)^{-1/2} \tag{11}$$

where $\alpha_{mc}$ and $\beta_{mc}$ were obtained from the work of Starink et al. [44] and the constant values were 0.096 and 0.76, respectively. The difference between the shear modulus of the clusters and the Al matrix $\Delta_G$ was considered as 2.6 GPa [19, 40]. The volume fraction (f) and the average radius (r) of the Ag and Mg cluster were considered as in the work of Barode et al. [19] equal to 0.0034 and 1.8 nm for the as-fabricated condition, and 0.0071 and 1.8 nm for the Standard T7 HT, respectively, based on studies on similar alloys [19, 45-47]. The second contribution was calculated as follows:

$$\sigma_{cs-cluster} = M\alpha_\varepsilon (G_m \varepsilon_c)^{3/2} \left(\frac{rf}{0.5 G_m b}\right)^{1/2} \tag{12}$$

where $\alpha_\varepsilon$ was a constant associated with the FCC metals as Al alloy with a value of 2.6 [19, 48], and $\varepsilon_c$ was the strain associated with the clusters present in the matrix and approximated to 1% [19, 40].

For more details about the strengthening mechanism equations used in this study please refer to the work of Jiang et al. [40] and Barode et al. [19].

The results of the strengthening mechanism model for the A205 alloy, both in as-fabricated and heat treated conditions, provided valuable insights into the various factors contributing to the

yield strength. These findings are summarised in Table 5.4, which schematises the different contributions to the yield strength observed in each condition. The results highlighted the complex interplay of microstructural features, including the presence of segregations, precipitate formation, and the influence of $TiB_2$ particles, all of which significantly affected the mechanical performance of the alloy. In the as-fabricated condition, the contribution of the precipitates was neglected, as they were not detected during the analysis. For the heat treated conditions, it was initially hypothesised that the contributions from the solid solution and clusters were absent due to the dissolution of segregations during the Solution step of the HTs, followed by the precipitation of Ω and ϑ'.

Table 5.4. Results of the several strengthening mechanism contributions for the tested conditions, as-fabricated, Standard T7 HT, Commercial Ht, and Rapid HT and comparison with experimental YS of vertical tensile samples.

| **Contributions** | **As-fabricated** | **Standard T7 HT** | **Commercial HT** | **Rapid HT** |
|---|---|---|---|---|
| $\boldsymbol{\sigma_0}$ | 20 | 20 | 20 | 20 |
| $\boldsymbol{\sigma_{TiB_2}}$ | 60.81 | 56.95 | 56.95 | 56.68 |
| $\boldsymbol{\sigma_{\Omega/\vartheta'}}$ | 0 | 125.32 | 216.08 | 233.1 |
| $\boldsymbol{\sigma_{GB}}$ | 143.67 | 78.27 | 90.37 | 92.32 |
| $\boldsymbol{\sigma_{SS}}$ | 24.78 | 45.54 | 0 | 0 |
| $\boldsymbol{\sigma_{co-cluster}}$ | 44.05 | 66.12 | 0 | 0 |
| $\boldsymbol{\sigma_{YS}}$ | 293.3 | 392.2 | 383.4 | 402.1 |
| $\boldsymbol{YS_{experimental}}$ | **300.9 ± 12.4** | **405.8 ± 17.1** | **392.9 ± 10.7** | **413.7 ± 10.6** |

A missing contribution was discovered for the Standard T7 HT, and, therefore, the calculations for the potential contributions of these two factors were performed. The results of these

calculations indicated the presence of a solid solution of Cu in the Al matrix following the Standard T7 HT. This phenomenon was likely correlated to the extended dwell time of the Solution step along with the over-ageing step, typically associated with the Standard T7 HT. These conditions resulted in the excessive overgrowing and partial dissolution of strengthening precipitates. Therefore, residual Cu was retained in a solid solution state, with some of the Cu-rich phases dissolved back into the Al matrix [31]. Furthermore, the contribution from clusters of Ag and Mg indicated the possible existence of segregations that remained in the matrix after the standard T7 HT.

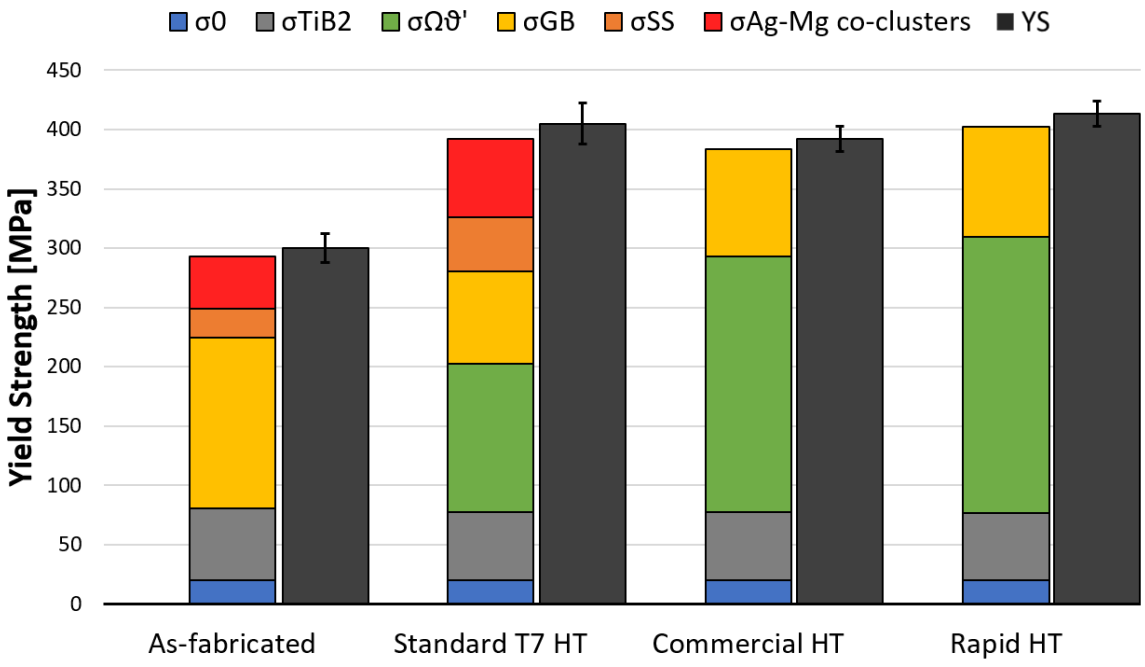


Figure 5.13. Comparison of the Yield strength calculated using the strengthening mechanism contributions model and the experimental value, for each of the tested conditions, as-fabricated, Standard T7 HT, Commercial HT, and Rapid HT.

A visual analysis of the quantitative study of the strengthening contributions to the total yield strength of the alloy is presented in Figure 5.13. The estimated yield strength ($\sigma_{YS}$) was characterised by the same trend as the experimentally determined yield strength (YS), demonstrating an average error lower than 5%. In the as-fabricated condition, the grain boundaries were found to play a significant role due to their ability to delay dislocation motion,

particularly in microstructures characterised by fine grains, such as the A205 alloy processed by L-PBF. In contrast, the Standard T7 HT exhibited a balanced contribution of all the strengthening factors, revealing issues associated with standard HTs of additively manufactured A205 alloy, which showed segregations and a high amount of Cu in solid solution state through the Al matrix, along with a substantial increase of the grain size. Finally, for both the Commercial HT and Rapid HT, the results highlighted as prominent strengthening factors the contributions from the Ω and ϑ' precipitates and the grain boundary. In particular, a significant contribution from $\sigma_{\Omega/\vartheta'}$ was observed for the Rapid HT, highlighting the effectiveness of the optimised tailored HT in the formation of high volume fraction of very fine strengthening precipitates in the A205 Al alloy.

## 5.4 Conclusions

The development of a novel customised post-thermal treatment for the Al alloy A205 produced by L-PBF was successfully completed. A comparison between standard HTs and the newly developed Rapid HT was performed, in terms of microstructural evolution and mechanical performance. In particular, the influence of the solution and artificial ageing steps of three different HTs, Standard T7 HT, Commercial HT, and novel Rapid HT, on the precipitate formation and microstructural characteristics were evaluated through various analyses. The main results of the study can be summarised as follows:

- A novel Rapid HT was successfully developed for the L-PBF A205 alloy. The HT was designed taking into consideration the DSC of the material, aiming to generate a high volume fraction of fine precipitates while maintaining a fine grain structure, thereby increasing the overall mechanical performance of the alloy at both room temperature and high temperature. The optimal Rapid HT conditions were found to involve a single

solution step of 520°C for 3 hours, followed by water quenching and an artificial ageing step of 170°C for 6 hours.

- Comparative analysis of the microstructural evolution across the three tested HTs revealed differences in grain size and precipitate distribution and formation. In particular, the EBSD results highlighted that the Standard T7 HT induced overcoarsening, while the Commercial HT and Rapid HT were characterised by relatively fine grains structure. Furthermore, TEM analysis showed a clear difference in the generation of Ω and ϑ'. The Standard T7 HT did not induce homogeneous phase distribution, showing a high number of overgrown precipitates and segregations, which were detrimental to the mechanical properties of the A205 alloy. In contrast, the Commercial HT was characterised by a more homogeneous distribution of ϑ' precipitates with a relatively fine size. On the other hand, the newly developed Rapid HT promoted the formation of finer precipitates, increasing both the distribution and volume fraction of these precipitates. The differences in grain size, phase distribution, and size were directly correlated with the observed variations in the mechanical performances of the three tested HTs.
- The comparison of the tensile strength of the HTs highlighted that the formation of TIP during the solution step of the three HTs resulted in a decrease in the elongation of the material. Nevertheless, the newly developed Rapid HT achieved high strength, with a YS and UTS of 413 Mpa and 465 MPa, respectively, while maintaining relatively good levels of elongation compared to the other HTs, similar to the Commercial HT. The Standard T7 HT resulted in brittle behaviour.
- Fatigue tests at a fixed load of 180 MPa were carried out at room temperature to understand the effect of the three HTs on the fatigue life of the A205 produced by L-

PBF. The results highlighted an increase in the number of cycles to failure for the novel Rapid HT compared to the as-fabricated condition, showing a higher fatigue life of around 189% and 125% compared to the Standard T7 HT and Commercial HT, respectively. The presence of localised porosity near the surface region of the specimen induced a crack initiation. However, the high density of fine precipitates in the matrix, combined with the fine grain size, resulted in slow and homogeneous steady propagation, allowing an increase in the fatigue performance of the alloy. On the other hand, the presence of TIP was detrimental for Standard T7 HT, while the Commercial HT achieved moderate performance.

- The creep test analysis at a temperature of 180° and a load of 200 MPa performed to compare the influence of the three HTs demonstrated that the newly developed Rapid HT exhibited the highest resistance to creep, attributed to the high density of fine precipitates that acted as pins and slowed down dislocation motion, while still maintaining a fine grain size. In particular, the creep life of the Rapid HT exceeded 24 hours, with an increase in creep performance of around 33% and 80% compared to the Standard T7 HT and Commercial HT, respectively. The Commercial HT was characterised by the least creep resistance, with poor performances correlated to the fine grain size combined with a lower volume fraction of precipitates. The Standard T7 HT exhibited moderate creep performance due to its higher grain size.
- Finally, the strengthening mechanisms correlating the microstructure and the yield strength of the material were quantitatively analysed for all the tested conditions. In particular, the as-fabricated condition was characterised by the lowest YS, primarily relying on the contribution of solid solution and grain boundary strengthening. The Standard T7 HT enhanced the YS promoting the formation of Ω and ϑ', although the

contributions of solid solution and clusters highlighted the presence of segregations, and Cu in solid solution state in the Al matrix, highlighting a reduced formation of strengthening precipitates. The Commercial HT showed a higher contribution from precipitate strengthening compared to the grain boundary. Finally, the newly developed Rapid HT achieved the highest YS, driven by the significant increase in precipitate formation alongside grain boundary strengthening.

The results of the study indicated that the microstructure of the A205 alloy can be significantly tailored through post-thermal treatment strategies. A novel Rapid HT characterised by a single solution step was proposed, offering a combination of strength and ductility, leading to optimal overall performance, especially when compared to the as-fabricated and standard post-thermal treatments. Furthermore, the reduction in total processing time of approximately 67% compared to the Standard T7 HT, and 25% compared to the Commercial HT, may result in lower resource consumption, leading to cost reductions and improved environmental sustainability.

## Acknowledgements

*This work is part of the C-AM AOHE project funded by the European Union's Horizon H2020-CS2-CFP08-2018-01 research and innovation program under grant agreement No 831880. This work was also supported in part by the EPSRC Centre for Doctoral Training in Topological Design, funded by the UK Engineering and Physical Sciences Research Council (grant EP/S02297X/1) based at the University of Birmingham.*

*The authors would like to acknowledge the support of the Henry Royce Institute through the Student Equipment Access Scheme at the University of Sheffield. The authors would also like to thank Dr Jiahui Qi for facilitating and assisting in the TEM analysis at the University of Sheffield.*

*The authors would like to thank Dr Timothy Doel for facilitating and assisting in the mechanical tests at the School of Materials and Metallurgy, University of Birmingham, UK.*

## References

[1] P.A. Rometsch, Y. Zhu, X. Wu, A. Huang, Review of high-strength aluminium alloys for additive manufacturing by laser powder bed fusion, Materials & Design, 219 (2022) 110779.

[2] F. Careri, R.H. Khan, C. Todd, M.M. Attallah, Additive manufacturing of heat exchangers in aerospace applications: a review, Applied Thermal Engineering, (2023) 121387.

[3] S.C. Altıparmak, V.A. Yardley, Z. Shi, J. Lin, Challenges in additive manufacturing of high-strength aluminium alloys and current developments in hybrid additive manufacturing, International Journal of Lightweight Materials and Manufacture, 4 (2021) 246-261.

[4] R. Montanari, A. Palombi, M. Richetta, A. Varone, Additive Manufacturing of Aluminum Alloys for Aeronautic Applications: Advantages and Problems, Metals, 13 (2023) 716.

[5] S. Li, B. Cai, R. Duan, L. Tang, Z. Song, D. White, O.V. Magdysyuk, M.M. Attallah, Synchrotron Characterisation of Ultra-Fine Grain TiB2/Al-Cu Composite Fabricated by Laser Powder Bed Fusion, Acta Metallurgica Sinica (English Letters), 35 (2022) 78-92.

[6] J. Fiocchi, A. Tuissi, C.A. Biffi, Heat treatment of aluminium alloys produced by laser powder bed fusion: A review, Materials & Design, 204 (2021) 109651.

[7] E. Sert, A. Öchsner, L. Hitzler, E. Werner, M. Merkel, Additive Manufacturing: A Review of the Influence of Building Orientation and Post Heat Treatment on the Mechanical Properties of Aluminium Alloys, in: H. Altenbach, A. Öchsner (Eds.) State of the Art and Future Trends in Material Modeling, Springer International Publishing, Cham, 2019, pp. 349-366.

[8] M. Laleh, E. Sadeghi, R.I. Revilla, Q. Chao, N. Haghdadi, A.E. Hughes, W. Xu, I. De Graeve, M. Qian, I. Gibson, M.Y. Tan, Heat treatment for metal additive manufacturing, Progress in Materials Science, 133 (2023) 101051.

[9] S.I. Shakil, A.S. Zoeram, H. Pirgazi, B. Shalchi-Amirkhiz, B. Poorganji, M. Mohammadi, M. Haghshenas, Microstructural-micromechanical correlation in an Al–Cu–Mg–Ag–TiB2 (A205) alloy: additively manufactured and cast, Materials Science and Engineering: A, 832 (2022) 142453.

[10] M. Avateffazeli, P.E. Carrion, B. Shachi-Amirkhiz, H. Pirgazi, M. Mohammadi, N. Shamsaei, M. Haghshenas, Correlation between tensile properties, microstructure, and processing routes of an Al–Cu–Mg–Ag–TiB2 (A205) alloy: Additive manufacturing and casting, Materials Science and Engineering: A, 841 (2022) 142989.

[11] M. Avateffazeli, S.I. Shakil, M.F. Khan, H. Pirgazi, N. Shamsaei, M. Haghshenas, The effect of heat treatment on fatigue response of laser powder bed fused Al-Cu-Mg-Ag-TiB2 (A20X) alloy, Materials Today Communications, 35 (2023) 106009.

[12] M. Avateffazeli, S.I. Shakil, A. Behvar, M.M. Attallah, J. Simsiriwong, A. Tridello, D.S. Paolino, M. Haghshenas, Very high cycle fatigue of laser powder bed fused Al-Cu-Mg-Ag-TiB2 (A20X) Alloy: Stress relief and aging treatments, International Journal of Fatigue, 183 (2024) 108281.

[13] S.I. Shakil, A.S. Zoeram, M. Avateffazeli, M. Roscher, H. Pirgazi, B. Shalchi-Amirkhiz, B. Poorganji, M. Mohammadi, M. Haghshenas, Ambient-temperature time-dependent deformation of cast and additive manufactured Al-Cu-Mg-Ag-TiB2 (A205), Micron, 156 (2022) 103246.

[14] A. Kulkarni, D. Srinivasan, P. Ravanappa, V. Jayaram, P. Kumar, Creep behavior of additively manufactured high strength A205 aluminum alloy, Additive Manufacturing Letters, 6 (2023) 100142.

[15] A. Kulkarni, D. Srinivasan, S. Kumar, P. Kumar, V. Jayaram, Precipitate evolution and thermal stability of A205 fabricated using laser powder bed fusion, Journal of Materials Science, 58 (2023) 2310-2333.

[16] J. Barode, A. Vayyala, E. Virgillito, A. Aversa, J. Mayer, P. Fino, M. Lombardi, Revisiting heat treatments for additive manufactured parts: A case study of A20X alloy, Materials & Design, 225 (2023) 111566.

[17] A. E3061-17, Standard Test Method for Analysis of Aluminum and Aluminum Alloys by Inductively Coupled Plasma Atomic Emission Spectrometry (Performance Based Method), 2017.

[18] Eckart, A20X™ – the strongest aluminium alloy. Worldwide. https://eckart.net/de/en/microsite/am (accessed on 07 March 2022).

[19] J. Barode, A. Vayyala, A. Aversa, L. Yang, J. Mayer, P. Fino, M. Lombardi, Natural and artificial aging behaviour of Al-Cu-Mg-Ag-Ti-B (A205) alloy processed by laser powder bed fusion: Strengthening mechanisms and failure analysis, Materials Today Communications, 39 (2024) 108978.

[20] Heat Treating of Aluminum and Its Alloys, in: G.E. Totten (Ed.) Heat Treating of Nonferrous Alloys, ASM International, 2016, pp. 0.

[21] A.X. Aeromet, New Shorter Heat Treatment Cycle for Additive Manufactured Parts, 2021. https://a20x.com/new-shorter-heat-treatment-cycle-for-additive-manufactured-parts/. (accessed on 07 September 2021).

[22] A. E8/E8M-22, Standard Test Methods for Tension Testing of Metallic Materials, 2022.

[23] A. E466-21, Standard Practice for Conducting Force Controlled Constant Amplitude Axial fatigue test of Metallic Materials, 2021.

[24] A. E139-11, Standard Test Methods for Conducting Creep, Creep-Rupture, and Stress-Rupture Tests of Metallic Materials, 2018.

[25] M. Ghasri-Khouzani, H. Karimialavijeh, M. Pröbstle, R. Batmaz, W. Muhammad, A. Chakraborty, T.D. Sabiston, J.P. Harvey, É. Martin, Processability and characterization of A20X aluminum alloy fabricated by laser powder bed fusion, Materials Today Communications, 35 (2023) 105555.

[26] E. Strumza, S. Hayun, S. Barzilai, Y. Finkelstein, R. Ben David, O. Yeheskel, In situ detection of thermally induced porosity in additively manufactured and sintered objects, Journal of Materials Science, 54 (2019) 8665-8674.

[27] A.Y. Al-Maharma, S.P. Patil, B. Markert, Effects of porosity on the mechanical properties of additively manufactured components: a critical review, Materials Research Express, 7 (2020) 122001.

[28] P. Moghimian, T. Poirié, M. Habibnejad-Korayem, J.A. Zavala, J. Kroeger, F. Marion, F. Larouche, Metal powders in additive manufacturing: A review on reusability and recyclability of common titanium, nickel and aluminum alloys, Additive Manufacturing, 43 (2021) 102017.

[29] C.-L. Tai, M.-C. Chen, T.-F. Chung, Y.-L. Yang, S.-L. Lee, T.-C. Tsao, Z. Shi, J. Lin, T.-C. Su, H.-R. Chen, J.-R. Yang, The nano-structural characterization of Ω and S phases in Al-5.1Cu-1.0 Mg-(0.4Ag) AA2024 aluminum alloys, Materials Science and Engineering: A, 881 (2023) 145361.

[30] Y. Liu, X. Han, S. Wang, B. Wei, W. Li, Subtle atomistic processes of S-phase formation in Al-Cu-Mg alloys, Journal of Alloys and Compounds, 838 (2020) 155677.

[31] M. Gazizov, R. Kaibyshev, Precipitation structure and strengthening mechanisms in an Al-Cu-Mg-Ag alloy, Materials Science and Engineering: A, 702 (2017) 29-40.

[32] H. Karimialavijeh, M. Ghasri-Khouzani, A. Chakraborty, M. Pröbstle, É. Martin, Direct aging of additively manufactured A20X aluminum alloy, Journal of Alloys and Compounds, 968 (2023) 172071.

[33] H. Karimialavijeh, M. Ghasri-Khouzani, A. Das, M. Pröebstle, É. Martin, Effect of laser contour scan parameters on fatigue performance of A20X fabricated by laser powder bed fusion, International Journal of Fatigue, 175 (2023) 107775.

[34] N. Read, W. Wang, K. Essa, M.M. Attallah, Selective laser melting of AlSi10Mg alloy: Process optimisation and mechanical properties development, Materials & Design (1980-2015), 65 (2015) 417-424.

[35] Y. Zhang, X. Yang, Comparison of grain size dependence on the creep performance of a Mg–Y alloy along different loading directions, Materials Science and Engineering: A, 893 (2024) 146155.

[36] A. Hadadzadeh, B.S. Amirkhiz, B. Langelier, J. Li, M. Mohammadi, Microstructural consistency in the additive manufactured metallic materials: A study on the laser powder bed fusion of AlSi10Mg, Additive Manufacturing, 46 (2021) 102166.

[37] V.P. Narayana Samy, M. Schäfle, F. Brasche, U. Krupp, C. Haase, Understanding the mechanism of columnar–to-equiaxed transition and grain refinement in additively manufactured steel during laser powder bed fusion, Additive Manufacturing, 73 (2023) 103702.

[38] B. Shassere, D. Greeley, A. Okello, M. Kirka, P. Nandwana, R. Dehoff, Correlation of Microstructure to Creep Response of Hot Isostatically Pressed and Aged Electron Beam Melted Inconel 718, Metallurgical and Materials Transactions A, 49 (2018) 5107-5117.

[39] R.N. Lumley, A.J. Morton, I.J. Polmear, Enhanced creep performance in an Al–Cu–Mg–Ag alloy through underageing, Acta Materialia, 50 (2002) 3597-3608.

[40] F. Jiang, L. Tang, S. Li, H. Ye, M.M. Attallah, Z. Yang, Achieving strength-ductility balance in a laser powder bed fusion fabricated TiB2/Al–Cu-Mg-Ag alloy, Journal of Alloys and Compounds, 945 (2023) 169311.

[41] J.F. Nie, B.C. Muddle, Microstructural design of high-strength aluminum alloys, Journal of Phase Equilibria, 19 (1998) 543-551.

[42] N. Hansen, Hall–Petch relation and boundary strengthening, Scripta Materialia, 51 (2004) 801-806.

[43] S. Bai, X. Yi, Z. Liu, On the role of Ag additions on the initial solute hardening and competitive precipitation of Al-Cu-Mg alloys, Journal of Alloys and Compounds, 945 (2023) 169339.

[44] M.J. Starink, S.C. Wang, The thermodynamics of and strengthening due to co-clusters: General theory and application to the case of Al–Cu–Mg alloys, Acta Materialia, 57 (2009) 2376-2389.

[45] T. Honma, S. Yanagita, K. Hono, Y. Nagai, M. Hasegawa, Coincidence Doppler broadening and 3DAP study of the pre-precipitation stage of an Al–Li–Cu–Mg–Ag alloy, Acta Materialia, 52 (2004) 1997-2003.

[46] S.P. Ringer, K. Hono, I.J. Polmear, T. Sakurai, Nucleation of precipitates in aged AlCuMg(Ag) alloys with high Cu:Mg ratios, Acta Materialia, 44 (1996) 1883-1898.

[47] M. Murayama, K. Hono, Three Dimensional Atom Probe Analysis of Pre-Precipitate Clustering in an Al-Cu-Mg-Ag Alloy, Scripta Materialia, 38 (1998) 1315-1319.

[48] K. Ma, H. Wen, T. Hu, T.D. Topping, D. Isheim, D.N. Seidman, E.J. Lavernia, J.M. Schoenung, Mechanical behavior and strengthening mechanisms in ultrafine grain precipitation-strengthened aluminum alloy, Acta Materialia, 62 (2014) 141-155.

# CHAPTER 6. Development of Novel Surface Strategies for L-PBF Fabricated A205 and AlSi10Mg High-Strength Al Alloys

This chapter is part of a scientific paper that has been published in the Journal 'Surface and Coatings Technology'. The paper's details and co-authors' contributions are outlined below.

**Francesco Careri,** Alessandro Sergi, Pavel Shashkov, Raja H.U. Khan, Moataz M. Attallah, Plasma electrolytic oxidation (PEO) as surface treatment for high strength Al alloys produced by L-PBF: Microstructure, performance, and effect of substrate surface roughness, Surface and Coatings Technology, Volume 489, 2024, 131122, ISSN 0257-8972, https://doi.org/10.1016/j.surfcoat.2024.131122.

**Francesco Careri:** Conceptualisation, Data curation, Investigation, Methodology, Visualisation, Writing – original draft, Writing - review and editing.

**Alessandro Sergi:** Data curation, Methodology, Writing - review and editing.

**Pavel Shashkov:** Methodology, Resources, Writing – review and editing.

**Raja H.U. Khan:** Conceptualisation, Funding acquisition, Supervision, Writing – review and editing.

**Moataz M. Attallah:** Conceptualisation, Funding acquisition, Methodology, Resources, Supervision, Writing – review and editing.

The published paper was slightly modified from the published version to increase formatting and visualisation.

# Graphical Abstract

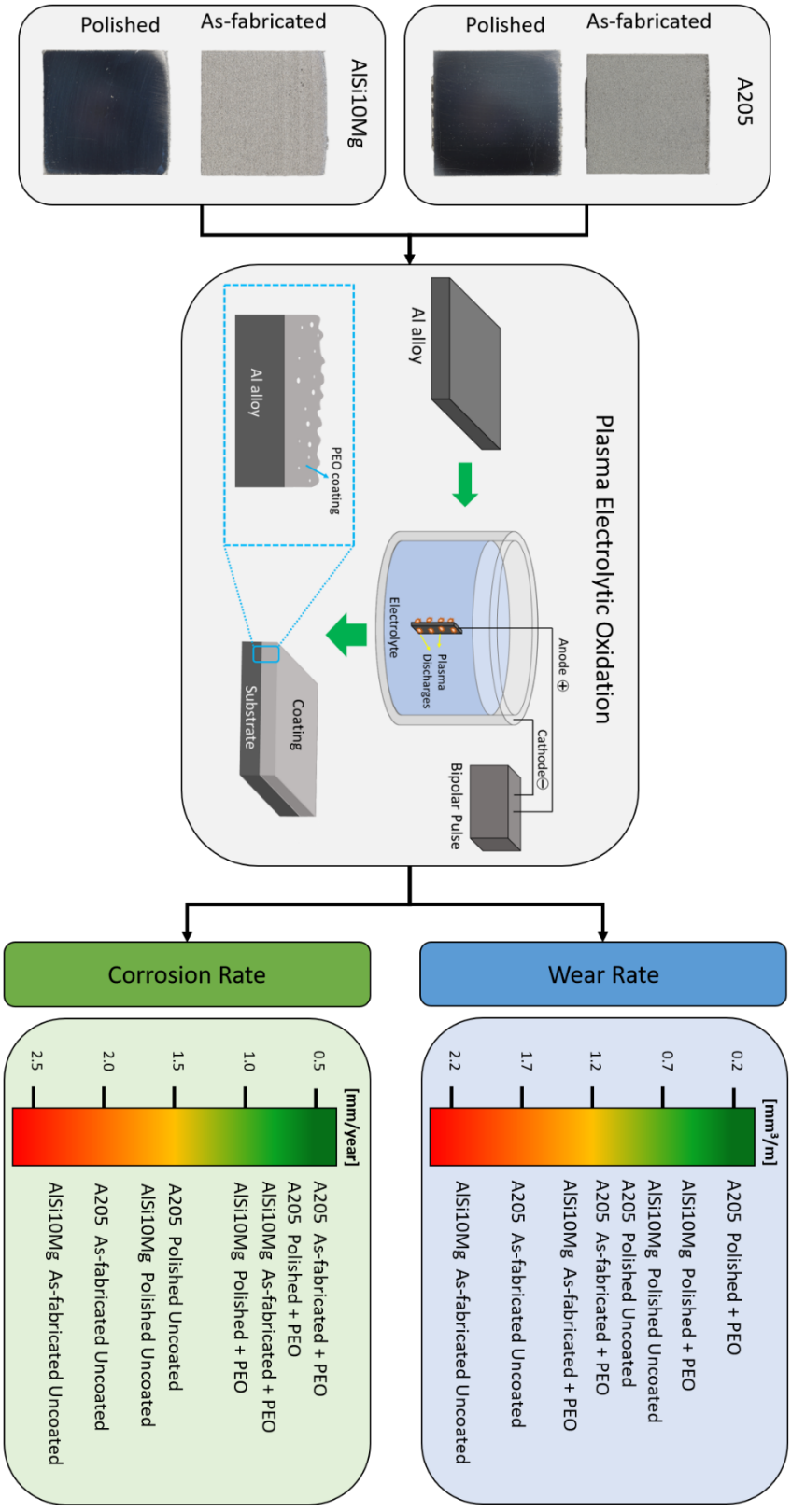

# Abstract

In recent years, additive manufacturing of Aluminium alloys has achieved remarkable developments, allowing for the replacement of casted components in industrial fields such as aerospace and automotive. However, the main issue affecting these alloys during operation at high temperatures and in critical environments is poor corrosion and wear resistance. The present work aims to produce a coated layer using an innovative surface treatment, Plasma Electrolytic Oxidation (PEO), on two high-strength Al alloys, AlSi10Mg and A205, processed by Laser-Powder Bed Fusion (L-PBF), in order to increase the corrosion and wear performance of the material. For each material, PEO coating was produced on two different surface conditions (as-fabricated and polished) and characterised in terms of morphology and composition through scanning electron microscopy (SEM) and digital microscope analysis. A PEO coating thickness of over 40 μm was achieved for both alloys, while the porosity was found around 13% and 3% for AlSi10Mg and A205, respectively. Additionally, nano-hardness analyses were carried out to understand the differences compared to the virgin material, highlighting an increase in hardness of the PEO coating at least 10 greater than the substrate for both materials. Finally, friction and corrosion tests were performed. The results in terms of wear rate and corrosion rate were compared with those obtained on uncoated manufactured samples. In particular, an increase in the wear and corrosion performance of 26.4% and 37.5%, respectively for the AlSi10Mg, and 88.4% and 53.1% for the A205, were evaluated. It was demonstrated that the presence of the oxidised layer improved the mechanical properties of the surface and, accordingly, the general performance of the material. Furthermore, performing a surface polishing treatment before PEO treatment helped to further increase the tribological and corrosion properties.

## 6.1 Introduction

Additive Manufacturing (AM) is considered one of the most promising technologies capable of manufacturing complex and customised parts, eliminating or reducing the limitations of conventional processing methods. In addition, parts are fabricated with layer technology that allows a decrease in design-to-manufacture time [1, 2]. Consequently, over the past decades, the technology has evolved, with the introduction of processes such as Laser-Powder Bed Fusion (L-PBF). This is a technique where powder is spread layer by layer onto a build plate, and an energy source, a laser beam, melts the powder in a protective atmosphere at specified locations to create the desired geometry [3, 4].

Aluminium (Al) alloys are used in a wide range of applications due to their strength-to-weight ratio. Therefore, AM of Al alloys has become of great interest in aerospace and automotive industries where lightness and reliability are essential prerogatives [5]. In particular, Al-Si alloys constitute nearly 80% of the Al casting alloys. Among them, AlSi10Mg is the most frequently investigated Al alloy [6]. AlSi10Mg is an age-hardening alloy with excellent properties in terms of hardness and strength, ideal for applications in which good thermal properties and low weight are required. Its application in AM is well-known due to the rapid increase in research on all aspects generated by AM processes and the differences with the casted counterpart [7, 8]. The main advantage of additive manufacturing of AlSi10Mg is the high cooling rate during the process, which allows to obtain a refined grain structure and the precipitation of intermetallic phases, enhancing the mechanical properties compared with the casted material [9, 10].

The other frontrunner in the AM development for high-strength applications is the Al-Cu based alloy A205. A205 is a metal matrix composite (MMC) alloy based on the Al-Cu system with the introduction of Titanium (Ti) and Boron (B) that allows the in-situ formation of Titanium

diboride $TiB_2$, acting as a solidification pin and grain refinement to eliminate the cracking issue of Al-Cu alloys and increasing the mechanical performance of the alloy. Furthermore, the addition of $TiB_2$ allows the formation of equiaxed grains after the L-PBF process, not achievable in the AlSi10Mg [11, 12]. The presence of $TiB_2$ together with the other intermetallic phases in this alloy makes the high-strength A205 alloy a promising candidate for aerospace and automotive structural and high-temperature applications up to 200°C. However, a major issue for the Al alloys is represented by wear and corrosion properties. Due to the intrinsic conditions of the process, the parts produced through AM possess several features in terms of both surface roughness and microstructure, that greatly influence the wear and corrosion properties of the components during the operation, especially in an adverse environment. Besides, the typical defects related to the AM technology (i.e. porosity, microcracks, anisotropy) could cause issues with the material's performance against wear and corrosion [13]. Consequently, in recent years the attention of many researchers has focused on surface treatment techniques aimed at improving the corrosive and wear properties of these alloys. Currently, the main common techniques include the use of coatings or anodising process to give the surface superior protective properties. Among these, the most promising and eco-friendly is Plasma Electrolytic Oxidation (PEO), also called micro-arc oxidation (MAO).

Considered an advanced anodising technique, PEO gives a solid oxide layer on the surface which guarantees more stable and long-term properties, in terms of mechanical properties, wear, and corrosion resistance [14]. The PEO process involves introducing the component to be treated in a non-toxic alkaline solution free of heavy metals. Then, once the electrodes have been introduced, and connected to an electrical source, which may be AC or DC depending on the type of process desired, the oxide film is generated by the presence of strong electrical discharges localised on the surface. The growth of this oxide film is granted under the high

local temperature involved in the process, which enables the generation of oxides of the substrate elements [15, 16]. Additionally, for difficult materials, where the use of an aqueous solution could lead to the formation of undesirable compounds in the coating, the process can be carried out in molten salt, to reduce the issues of the produced coating and the need for cooling and decomposition of the electrolytes [17]. Due to the sustainability and intrinsic simplicity of the process, many studies have been conducted to understand the basic principles of treatment, and still, other works have focused on the optimisation of process parameters. Tavares et al. [18] investigated the influence of different process parameters on the microstructure and wear properties, evaluating different duty cycles and treatment times. The results obtained highlighted a direct correlation between time exposure and the typical volcano shape of the surface. In addition, the duty cycle affects the thickness of the PEO layer. Pillai et al. [19] investigated two different kinds of PEO treatment on the AA6061 alloy and found that in every case the PEO layer achieves greater hardness than the substrate, improving the corrosion resistance of the materials. Furthermore, surface preparation to modify the initial surface condition of the substrate can significantly influence the final properties of the PEO coatings [20, 21].

On the other hand, the impact of surface preparation and PEO treatment on Al alloy fabricated via L-PBF is not yet fully understood, despite these materials are nowadays applied in several manufacturing sectors. Some studies have been found to focus on the study of the effects of the PEO treatment on AlSi materials additively manufactured. Rogov et al. [22] applied AC PEO treatment to an additively manufactured and cast AlSi alloy. The results demonstrated that for both configurations, subjected to the same PEO coating process, despite the difference in the initial microstructure, no divergences were found. Therefore, the approach used with the PEO of casted Al alloys is also valid for the alloys processed through Additive Manufacturing. In

addition, Pezzato et al. [23] found in their work on additively manufactured AlSi10Mg treated with PEO, that after the PEO coating, the specimens showed higher corrosion resistance than the untreated counterparts. Moreover, the authors emphasised the possibility of successfully coating on components characterised by different microstructures and porosities, not possible with traditional techniques such as anodising. On the other hand, despite the growing interest in the characterisation of A205 for several applications, there is still a lack of academic research regarding the impact of PEO on this material. A limited number of studies [24, 25] were found on the use of PEO process for Al-Cu alloys, focusing mostly on the coating growth mechanism and surface characterisation. Instead, several studies were reported on the high-strength 7075 Al alloy [26-29], similar in mechanical properties to the A205. In particular, Abdel-Gawad et al. [26] compared the oxidised film properties and corrosion behaviour of different Al alloys used in military applications, among which the Al7075 and the Al2024, another Al-Cu alloy, belonging to the same family as A205. The authors reported a reduced oxidised layer thickness for the Al2024, due to the high Cu content that decreases the current efficiency. However, the Cu content increased the hardness of the PEO layer and the wear performance.

Despite the advantages of using PEO treatments in combination with surface preparation of L-PBF AlSi10Mg and A205 alloys, the literature contains limited studies on such investigations. Thus, this study will focus on the evaluation of several factors, including surface conditions and different anodising conditions, to gain a comprehensive knowledge of the quality of PEO coating and the tribological and corrosion performance of the PEO-coated AlSi10Mg and A205 alloys fabricated via L-PBF.

## 6.2 Materials and Methods

### 6.2.1 Material and PEO characterisation

AlSi10Mg and A205 Al alloy powders, obtained by argon atomisation with an average particle size of 40µm, were employed to manufacture the samples used in the study. Specifically, the chemical composition of the two powders used in the study is reported in Table 6.1.

Table 6.1. Chemical composition for both materials used in the study, AlSi10Mg and A205.

| | **Chemical Composition [w%]** | | | | | | | | |
|---|---|---|---|---|---|---|---|---|---|
| **Name** | **Al** | **Si** | **Mg** | **Cu** | **Fe** | **Ti** | **B** | **Ag** | **Ni** |
| **AlSi10Mg** | Bal. | 11 | 0.45 | <0.1 | - | - | - | - | <0.05 |
| **A205** | Bal. | 0.1 | 0.24 | 4.49 | 0.04 | 2.4 | 0.91 | 0.71 | - |

The fabricated bulk specimens were rectangular, measuring 25 x 25 x 5 mm in size. An initial L-PBF parametric study was carried out for each material to achieve the lowest porosity and highest property in terms of surface roughness and hardness obtainable through this AM technology. Additionally, Plasma Electrolytic Oxidisation (PEO) treatment was performed by CAMBRIDGE NANOLITIC LIMITED, specialising in coating technologies. The material was treated in two different surface configurations: as-built and polished. For the polished configuration, the surface of the sample was initially subjected to grinding and polishing processes, drastically reducing the roughness downstream of the additive process. Both materials were PEO coated using 3 different alkaline solutions containing different concentrations of phosphate and silicate. Specifically, we refer to (i) Lean (L) electrolyte, an alkaline solution including < 1g/l of phosphate and <0.5 g/l of silicate; (ii) Medium (M) electrolyte, an alkaline solution including <1 g/l of phosphate and <1.5 g/l of silicate; and (iii) Rich (R) electrolyte, an alkaline solution including <2.5 g/l of phosphate and <5 g/l of silicate.

The 3 different alkaline solutions worked for the A205 material, while only one, the R electrolyte, was able to process the PEO coating for the AlSi10Mg due to the alloy composition, rich in Si, which integration in the oxide layer led to excessive electrical losses during the coating process and complex formation of the oxidation layer. Regarding the electrical modes used for the PEO process, all coatings were performed in a soft sparking mode using sequences of bipolar pulses with voltages up to 650 V. Considering the as-built counterparts, the analyses were carried out on a total of 12 different configurations of Al alloys analysed in this study, as reported in Table 6.2.

Table 6.2. Configurations analysed for L-PBF of AlSi10Mg.

| **Material** | **Surface Condition** | **Coating Condition** | **PEO Alkaline Solution** |
|---|---|---|---|
| **AlSi10Mg** | As-fabricated | Uncoated | - |
| **AlSi10Mg** | Polished | Uncoated | - |
| **AlSi10Mg** | As-fabricated | PEO Coating | Rich (R) |
| **AlSi10Mg** | Polished | PEO Coating | Rich (R) |
| **A205** | As-fabricated | Uncoated | - |
| **A205** | Polished | Uncoated | - |
| **A205** | As-fabricated | PEO Coating | Lean (L) |
| **A205** | Polished | PEO Coating | Lean (L) |
| **A205** | As-fabricated | PEO Coating | Medium (M) |
| **A205** | Polished | PEO Coating | Medium (M) |
| **A205** | As-fabricated | PEO Coating | Rich (R) |
| **A205** | Polished | PEO Coating | Rich (R) |

Initially, the coating thickness was evaluated using a digital Elcometer 456, designed to provide accurate coating thickness measurements as a non-destructive method. Subsequently, for each condition, the cross-section and surface were manually cleaned using ethanol to avoid

damaging the thin oxidised coating layer and evaluated with different methods. SEM analysis was conducted using a Benchtop Hitachi TM3030 in order to determine the thickness of the coating and its bonding with the substrate. The SEM images were then analysed using a java-based image processing software (ImageJ) to evaluate the porosity of each coating layer produced. The surface roughness of each condition was measured using an optical profilometer (Alicona InfiniteFocus G5) and then compared. Phase compositions of the PEO coating layer and as-built conditions were evaluated through X-ray diffraction (XRD). The diffractometer used was a Benchtop PROTO AXRD, equipped with a copper line-focus X-ray tube, and the analysis was performed using a Bragg-Brentano (BB) geometry. The parameters used for the analysis were: $2\theta$= 20° - 100°, step size= 0.05°, and dwell time= 1 s. All acquired data were then post-processed with software for image processing and XRD curve analysis. Furthermore, nano-hardness analysis was performed to assess the quality of the oxidised layer and its difference with the substrate. In particular, nano-hardness measurements were necessary due to the thin oxidised layer produced by PEO. The nano-hardness analysis was conducted using a Micro Materials NanoTest system equipped with a Berkovich tip, applying a load of 10 mN and a holding time of 5 seconds. A total amount of 20 points with a distance of 5 μm were measured for the best configuration of each PEO-coated material. The average value was then determined by calculating the mean of the nano-hardness data points obtained at identical positions along three lines.

### 6.2.2 Tribological and Corrosion Resistance evaluation

A wear test was performed on every sample condition previously analysed to assess the general quality of the PEO coating and the differences with the as-built counterparts. The wear tests were conducted according to the ASTM G133-22 standard [30], using a Phoenix Tribology Tester. Specifically, the test was carried out using $Al_2O_3$ balls with a diameter of 10mm, a fixed

load of 10N, a sliding velocity of 5mm/s, and 500 cycles, at room temperature. Using the dedicated tribometer software supplied with the equipment, the coefficient of friction (CoF) was evaluated. Moreover, SEM and Alicona optical profilometer analysis were used to acquire images of the wear track to evaluate the general quality and assess the differences in terms of wear mechanisms among the different samples. Furthermore, Alicona optical profilometer was used to calculate the wear volume loss, and the wear rate of each condition tested. In particular, the wear rate was evaluated according to the ASTM G133-12 standard [30] and it was calculated in terms of wear volume loss per unit distance of sliding calculated as linear slide distance times the duration of the test, as shown in Equation 6.1.

$$WR = \frac{V_f}{d_s} = \frac{A \cdot L}{N \cdot L} \qquad \text{Equation 6.1}$$

where $V_f$ and $d_s$ are the wear volume loss and the unit distance of sliding, A is the average cross-section area of the track, L is the length of the stroke, and N is the total number of cycles, respectively.

Salt fog corrosion tests were conducted on the best configuration of each material, in both surface configurations (as-fabricated and polished), to provide corrosion resistance information regarding the PEO coating and the as-fabricated counterpart. The test determines the effects of prolonged exposure to a salt atmosphere or salt fog experienced in normal operations on the tested equipment. The test was carried out following the ASTM B117-19 standard [31]. In particular, the exposing condition included a salt fog test duration of 96 hours in a salt environment prepared by dissolving sodium chloride in water. Visual inspections were carried out every 24 hours to evaluate the effect of the salt environment on the samples. The parameters used for the salt fog test are summarised in Table 6.3.

Table 6.3. Salt Fog Test Parameters details.

| **Parameter** | **Value/Detail** |
|---|---|
| **Salt Solution Concentration** | 4.0 – 6.0 % by weight |
| **Atomised Salt pH** | 6.5 – 7.2 |
| **Collection Rate of Atomised Salt** | 1.0 – 3.0 ml/hour |
| **Chamber Temperature** | 33 – 37 °C |

The samples were cleaned using clean running water to remove salt deposits from the surface and dried. The corrosion product was removed following the ASTM G1-03 standard [32] via an ultrasonic bath using a solution of $HNO_3$ in water ($HNO_3$ concentration 70% by volume) at 90°C for 10 minutes, and the corrosion rate based on mass loss was calculated. In particular, the average corrosion rate was obtained, according to the ASTM G1-03 standard [32], as shown in Equation 6.2.

$$CR = \frac{K \cdot W}{A \cdot t \cdot \rho} \qquad \text{Equation 6.2}$$

where CR is the corrosion rate, K is a constant with a constant value depending on the unit in which the corrosion rate is calculated, W is the mass loss, A the surface area, t is the time of the corrosion test, and ρ the density of the material. Finally, the samples were characterised using a digital microscope (Keyence VHX-7000 4K) to evaluate the extent of the damage caused by the salt fog test.

## 6.3 Results and Discussions

### 6.3.1 Characterisation of the coating layer

Both surfaces and cross-sections of samples processed by PEO treatment were characterised to estimate the success of the coating process and the influence of the initial surface condition.

Figure 6.1 illustrates the SEM image of the typical coating layer surface. The surface analysis shows a typical volcano structure with a high presence of craters. These craters were formed during the coating process due to the formation of oxide inside the plasma which, condensing as a liquid, collapses and tends to erupt on the surface before completely solidifying [33]. The initial surface condition, and consequently the related roughness upstream of the surface treatment process, influenced the volcanic structure of the pancake morphology. In particular, the polished configurations have ensured a decrease in the size and number of craters. A smooth surface, therefore, seems to act favourably on the PEO coating process as a decrease in the number of craters leads to a decrease in surface defects [34]. Further evidence of the effect of the initial conditions on the coating process is the measurement of the roughness carried out through an Alicona optical profilometer. The comparison between the different configurations (as-fabricated and polished) for both materials is shown in Figure 6.1.

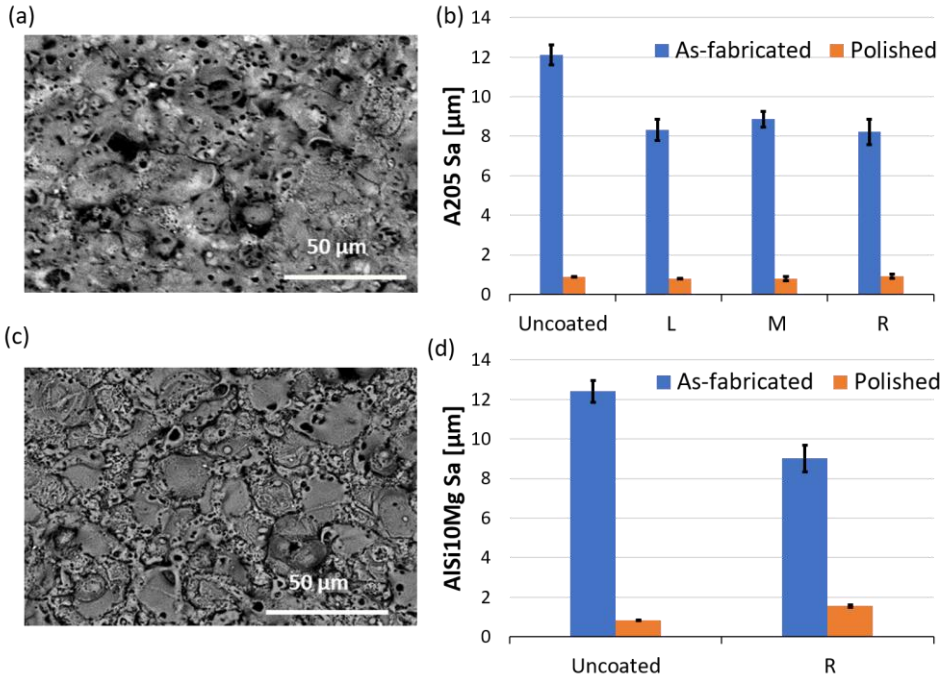


Figure 6.1. Characterisation of PEO coating layer. Representative morphology of the PEO coating surface of (a) as-fabricated and (c) polished configuration of A205; roughness analysis for (b) A205 and (d) AlSi10Mg alloys.

Considering the roughness downstream of the L-PBF process as a reference value, it is evident how the polishing surface treatment and the coating greatly influence the resulting final condition. The PEO coating acted as a smoothing process for the as-built configuration, with a considerable decrease in the final roughness downstream of the surface treatment. The numerous explosions generated by the strong electrical discharges during the generation of the plasma state acted as an erosion tool and consequently reduced the surface roughness value. As for the conditions initially subjected to the polishing process, the condition downstream of the PEO shows a roughness different from the reference value and even a different behaviour compared to the as-built samples. The coating treatment for the polished condition of AlSi10Mg causes an increase in surface roughness, however similar to the initial value, while for the A205 no considerable changes were found. A clear improvement in surface quality for both materials can be associated with an initial polishing condition, with a value that falls below 1.5 μm even downstream of the coating process. Consequently, an efficient manufacturing strategy should require surface treatments to be performed upstream of the PEO process.

X-ray diffraction analysis of the surface was performed to evaluate the phase composition of the oxidised layers. As shown in Figure 6.2, downstream of the PEO treatment, different aluminium oxides $Al_2O_3$ were formed for both materials AlSi10Mg and A205, which guarantees high performance for the oxidised surface [35]. The results highlighted the success of the surface treatment, as the ultimate goal was the generation of a thin layer of alumina which significantly contributes to increasing the tribological properties of the materials' surface. PEO coatings consist mostly of α and γ alumina [36, 37], which ensure the generation of a coating characterised by high hardness. In particular, for A205 Al alloy, the different PEO solutions did not affect the final composition of the oxidised layer; however, variations in the peaks of the

different phases were observed. These variations affected the final properties of the coating and were analysed via wear performance.

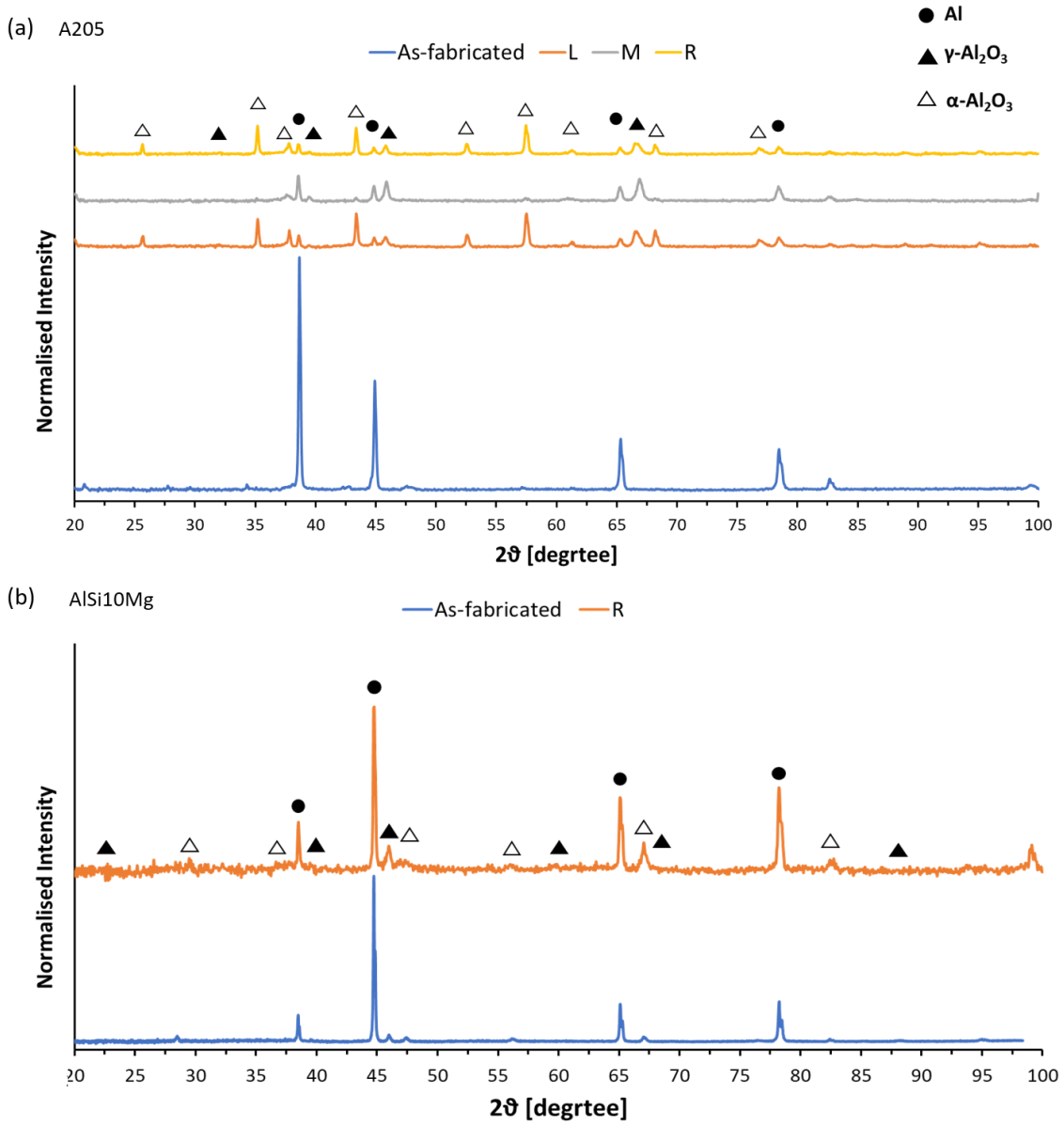


Figure 6.2. X-ray diffraction analysis of all studied conditions for (a) A205 and (b) AlSi10Mg alloys.

The morphology of the coatings was also evaluated by analysing the cross-section and comparing the results with the values provided by an Elcometer. The cross-section can provide information on the nature of the layer and, above all, on the porosity.

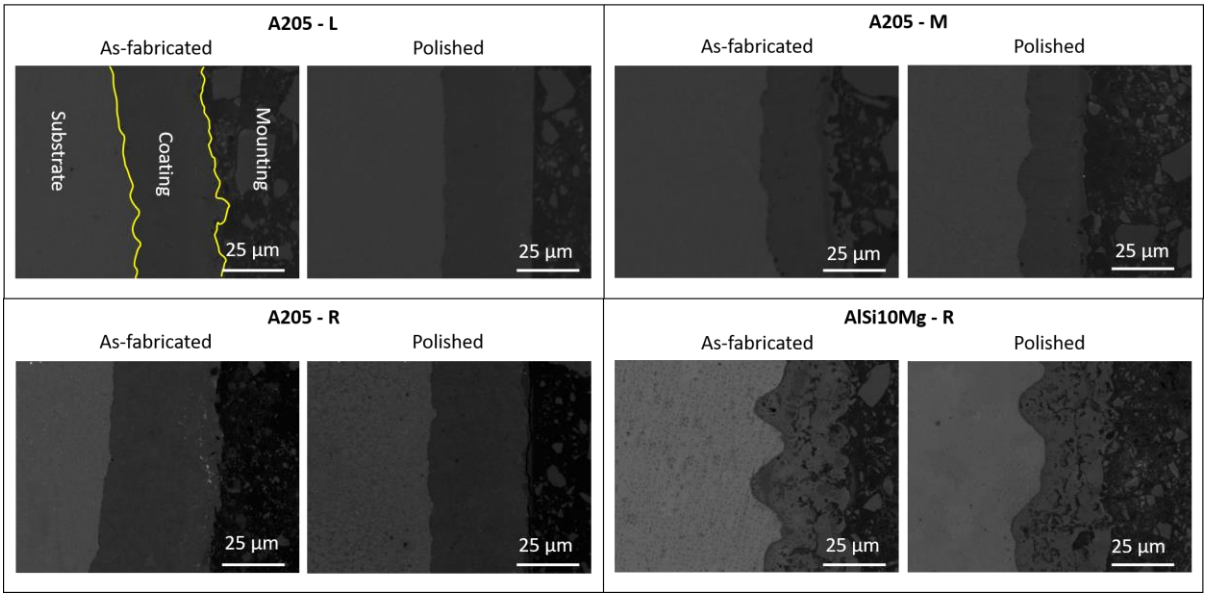


Figure 6.3. SEM images of the cross-section of PEO coatings of A205 and AlSi10Mg for As-Fabricated and PEO coated conditions.

This is particularly important as it affects all the characteristics of the coated layer, from hardness to permeability, which is crucial during operation in corrosive environments, as well as thermal properties [38]. For both materials, the coatings were found to be well-formed and adherent to the substrate, as shown in Figure 6.3. The results highlighted the feasibility of the PEO process in generating a successful oxidised layer for the A205, despite the well-known challenges in achieving a uniformly distributed coating layer due to the presence of $TiB_2$ reinforcement within the Al matrix [39].

Figure 6.4 highlights the details of the coating layer of the different configurations of both materials. In particular, considering the two different configurations analysed after PEO treatment (CT and CTP), considerable variation in thickness was found, reaching for the best configurations with a value of over 40µm of thickness for both materials. The analysis demonstrated that for both materials, the substrate initially subjected to polishing treatment did not have a great effect on the layer thickness, however, it was characterised by a decrease in micropores compared to the specimens PEO-coated in the as-fabricated surface condition.

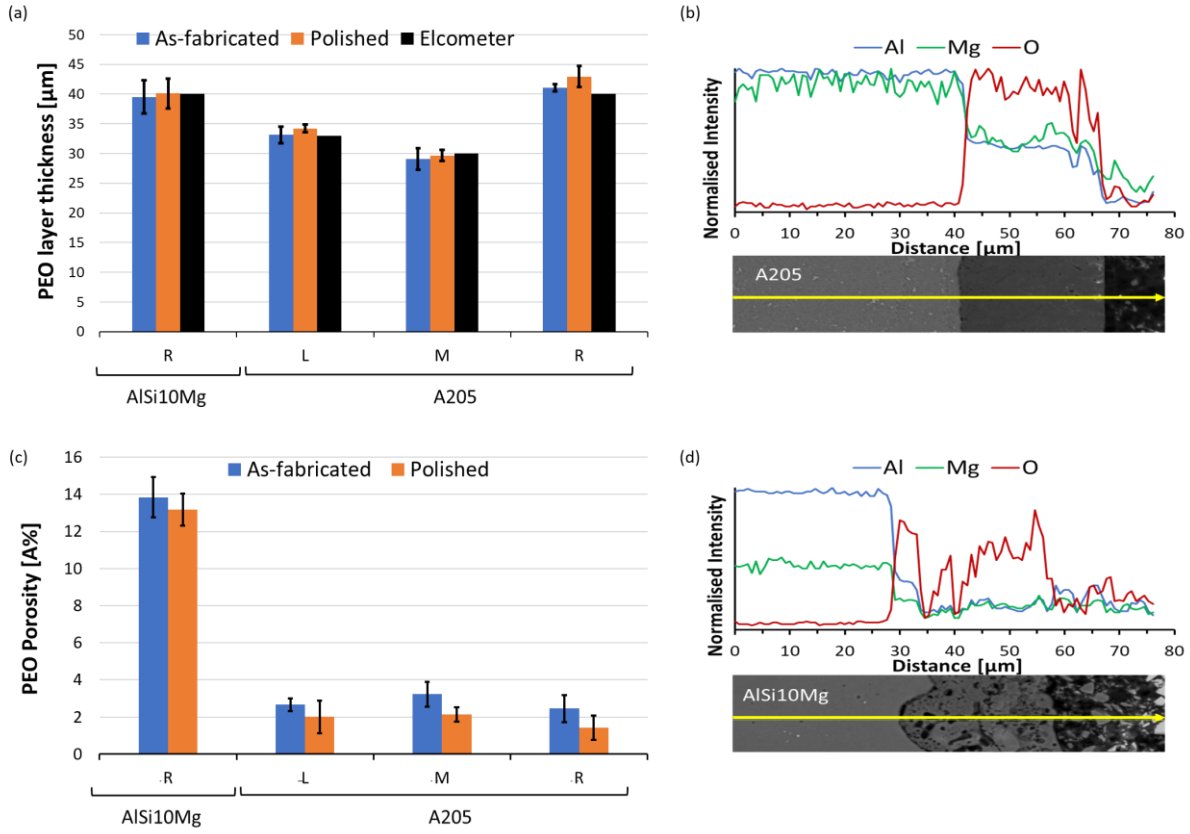


Figure 6.4. Analysis of the PEO coating layer. (a) analysis of the coating thickness, (b) EDX line for A205, (c) analysis of the porosity of the coating, and (d) EDX line for AlSi10Mg.

Furthermore, differences in the coating structure were assessed for the two alloys. In particular, while for the A205 alloy mostly a dense layer was found, with a low value of porosity, less than 3%, the analysis carried out on the PEO-coated AlSi10Mg highlighted the formation of a porous layer with values of around 13%. Comparing the PEO coating of AlSi10Mg and A205, the results highlighted a high presence of internal coating porosity for the AlSi10Mg, while for the A205, the different PEO solutions affected only the total thickness of the oxidised layer. The presence of a porous region at the top surface of the oxidised layer and the substrate/coating interface could facilitate the penetration of corrosive media and the failure of the coated layer from the substrate [40]. For both materials, it was found that a decrease in the initial roughness (polished samples) favoured the passage of electrolytes during the PEO process and led to a slight increase in the growth of the oxidised layer.

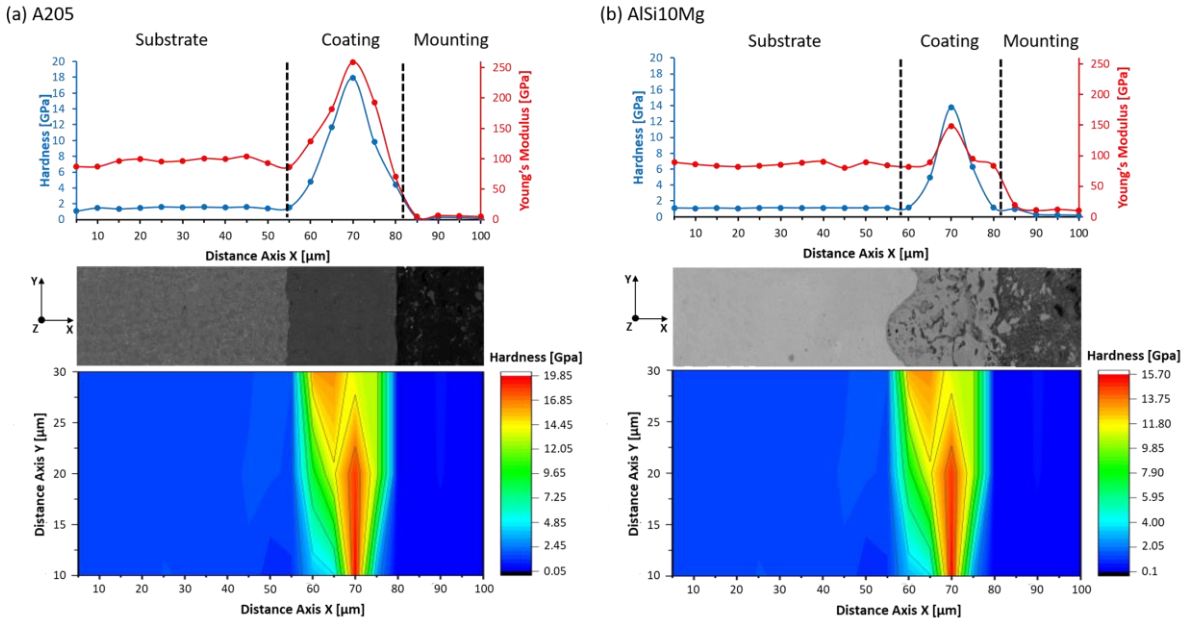


Figure 6.5. Nano-hardness and Young's Modulus analysis of the PEO coating layer for (a) A205 and (b) AlSi10Mg alloys.

The morphology and composition of the PEO coating can have a considerable impact on the characteristics of the oxidised layer. The mechanical properties were determined through the use of nano-hardness analysis. In particular, the polished configurations for both materials were chosen due to the higher overall quality shown by the metallographic analysis (Figure 6.4), and for the A205 Al alloy, the best configuration characterised by the higher PEO layer thickness (alkaline R) was selected. Figure 6.5 shows the average values of hardness and Young's Modulus estimated through the nanohardness load-displacement curve and calculated from the substrate up to the surface of the coated layer for both materials. Young's Modulus is related to the stiffness of the material and gives us insights into the materials' response to tensile and compressive loading. Additionally, the evaluation of Young's Modulus is important in coatings to understand the levels of stresses induced by a certain substrate strain [41]. In particular, the trend of Young's Modulus followed the trend of hardness for both specimens, reaching values of 258.8 GPa and 148.2 GPa for A205 and AlSi10Mg, respectively. For both AlSi10Mg and A205, the average values of the hardness of the substrate are comparable with the values

obtained from the L-PBF process [42, 43], while the difference with the oxidised layer, rich in alumina, was evident. The hardness value increased approaching the substrate/coating interface, further highlighting the good adhesion between the substrate and the oxidised layer.

As depicted in Figure 6.5b, for the AlSi10Mg, despite the presence of porosity, the hardness in the central area of the PEO coating presents a peak with a value 10 times greater than that of the substrate. The A205 PEO coating layer resulted in higher hardness with an average value of 17.9 GPa compared to the calculated value of 13.8 GPa of AlSi10Mg material, highlighting the positive effect of the PEO process on this material. The results could be explained by the lower presence of porosity and a better generation of PEO coating with the formation of small micro-cracks, typical of the oxidised layer produced by the PEO process. Furthermore, for both materials, different regions characterised by dissimilar hardness values were found. This result demonstrates the composite nature of the coating, containing non-uniform distributions of γ-$Al_2O_3$ and α-$Al_2O_3$, usually harder, reflecting the differences in hardness along the coating thickness [44]. The higher presence of α-$Al_2O_3$ found during the XRD analysis (Figure 6.2) increased the overall hardness of the A205 PEO-coated layer. The high hardness properties were considered a sign of the improvement of the quality of the external surface of the two materials tested, leading to the acquisition of superior surface properties, analysed by evaluating the wear and corrosion behaviours of both materials. At the same time, the combination of γ-$Al_2O_3$ and α-$Al_2O_3$ could trigger a combined effect of soft and hard phases to better accommodate deformation without failure and therefore lead to an increase in the performance of the PEO coating.

### 6.3.2 Tribology behaviour

The tribological properties were examined to understand the influence of PEO coating and initial surface conditions in improving the surface properties of the material. Reciprocating

sliding wear tests were performed on all the conditions analysed. Figure 6.6 shows a comparison of the average coefficients of friction (CoF) and calculated wear rates for several material configurations. In particular, the volume loss was used to evaluate the wear rate of the samples after the tribological test. The wear loss was analysed using an Alicona optical profilometer.

The base materials showed different behaviours. The A205 alloy demonstrated a lower CoF and wear rate compared to AlSi10Mg. In particular, a decrease in wear rate of 43.2% and 88.4% for the A205, and 36% and 26.4% for the AlSi10Mg, as-fabricated and polished condition, respectively was evaluated. The behaviour was associated with the different chemical compositions of the two materials. The addition of Cu, together with the generation of $TiB_2$ during the L-PBF process, led to an enhancement of the tribological performance of the material. Despite this improvement, as highlighted in Figure 6.6a, the A205 alloy initially exhibited a low CoF value but then rapidly increased without having a steady stage, most likely caused by the detachment of the reinforcement element ($TiB_2$) from the matrix [45]. The average values of both the CoF and wear rate decrease after the PEO coating process compared with the uncoated conditions.

The results highlighted that the PEO coating layer of the AlSi10Mg was hard but at the same time fragile and resulted in a higher CoF and wear rate compared to the A205 alloy. In particular, for the latter, the PEO coating process using different solutions led to different behaviours. The Alkaline R resulted in the best condition with the lowest CoF and wear rate, with levels reaching 0.2 and 0.11, respectively.

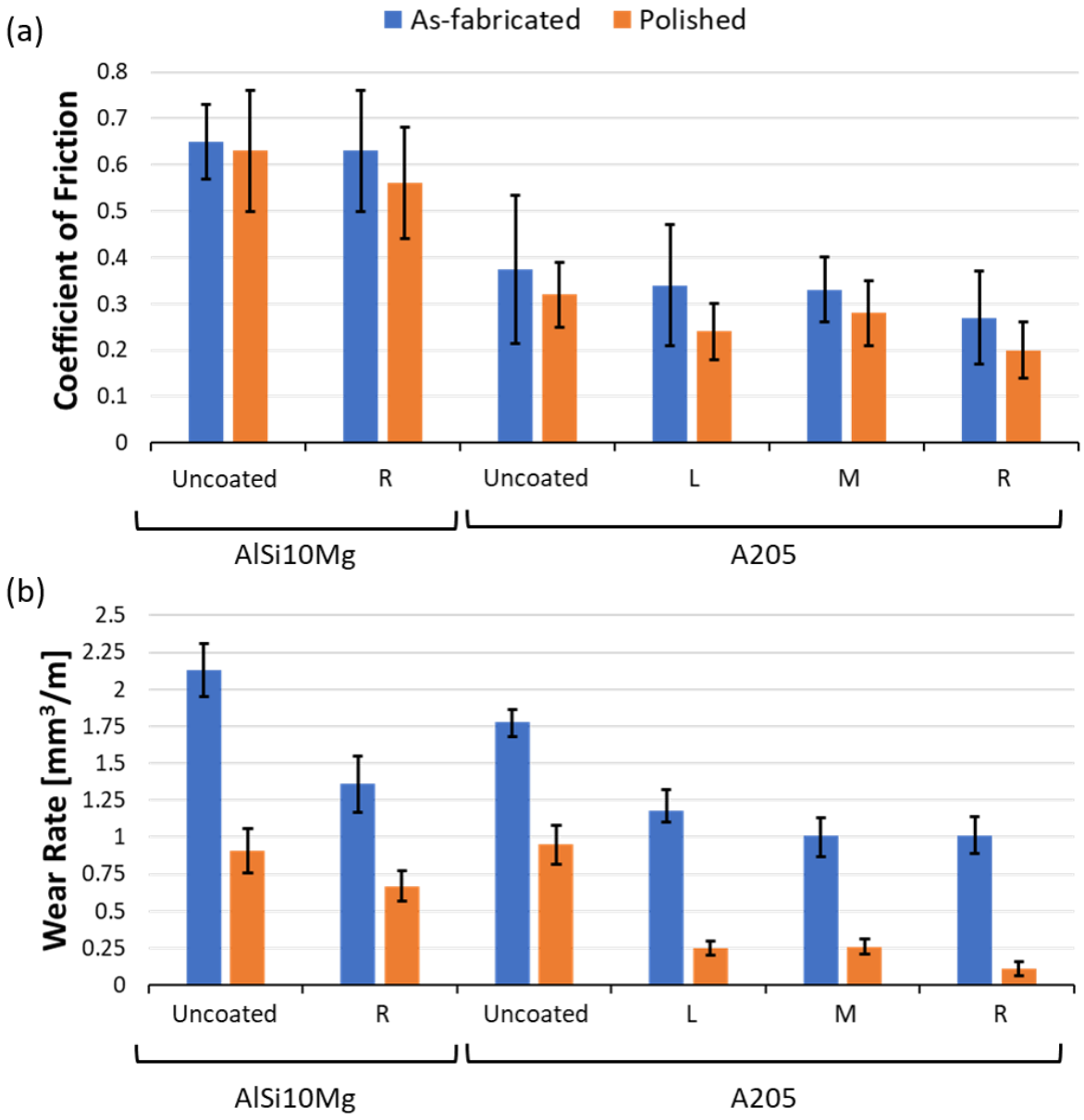


Figure 6.6. Wear test analysis. (a) coefficient of friction and (b) calculated wear rate for all conditions analysed in the study.

The results concerning the tribological test with the best properties for both A205 and AlSi10Mg alloys are shown in Figure 6.7.

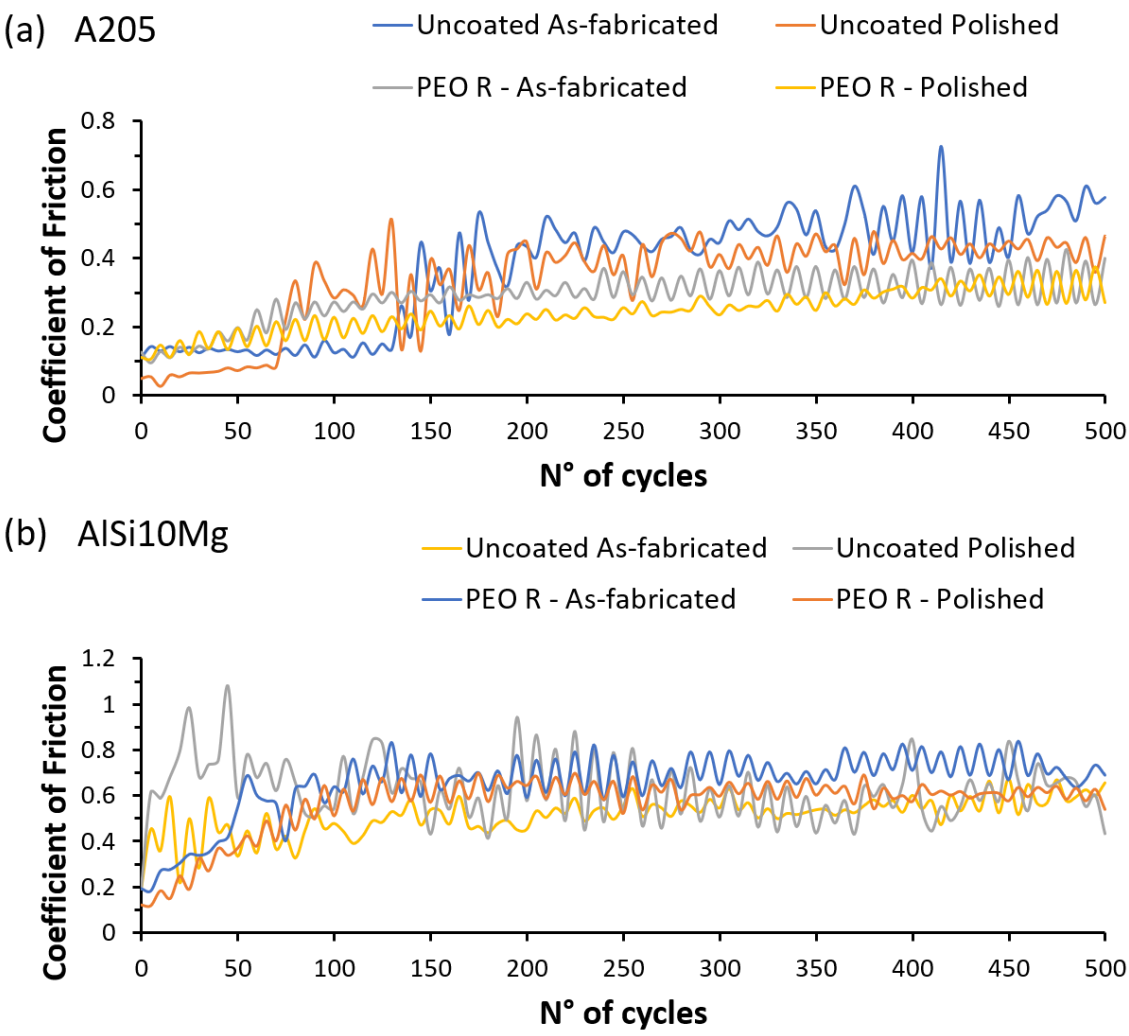


Figure 6.7. CoF of the best conditions for (a) A205 and (b) AlSi10Mg alloys.

In particular, downstream of the PEO coating process, the CoF decreases for both materials, even though lower values are reached for the A205 alloy. The presence of copper in the alloying element increases the effect of the PEO layer, leading to a major enhancement of the tribological properties of the material compared to the AlSi10Mg. The CoF trend of PEO R A205 at high cycles highlighted still the presence of the coating layer, without reaching its breakdown conditions.

The analysis of the wear tracks for the best conditions of PEO-coated A205 and AlSi10Mg, and the comparison with the uncoated ones, are represented in Figure 6.8.

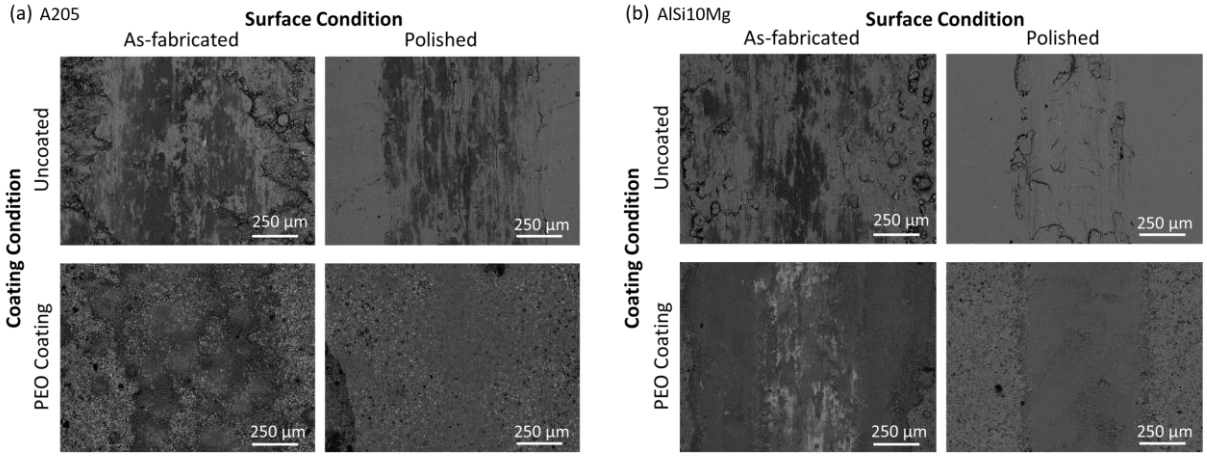


Figure 6.8. SEM of the wear tracks for the best condition (coating using electrolyte R) of (a) A205 and (b) AlSi10Mg alloys.

For both materials, the SEM micrographs of the uncoated as-fabricated condition showed a high presence of debris around the wear track. These debris were formed due to the action of abrasive and adhesive wear phenomena. The results highlighted a reduction in the abrasive wear phenomenon after only the polishing process of the uncoated samples.

Regarding the PEO-coated configuration, the results indicated an improvement in the tribological behaviour of the materials, with a total absence of debris and, in the case of the polished configuration, a smooth track characterised by a low average value. The wear phenomenon was more severe in the AlSi10Mg polished after the PEO process, due to the higher friction forces following the higher CoF in combination with the observed porosity of the coating layer. The PEO coating led to a reduction of the material transferred to the boundaries of the wear tracks and a substantial decrease in the level of volume loss, gaining high tribological properties after the PEO coating process.

### 6.3.3 Corrosion performance

The corrosion behaviour of both materials was assessed through a salt fog test. In particular, in the best conditions, PEO-coated using the R alkaline solution, together with uncoated specimens, were subjected to a corrosion test for a duration of 96 hours and then analysed.

Figure 6.9 shows the macroscopic corrosion morphology of uncoated and PEO-coated samples before and after the corrosion test for A205 and AlSi10Mg, respectively.

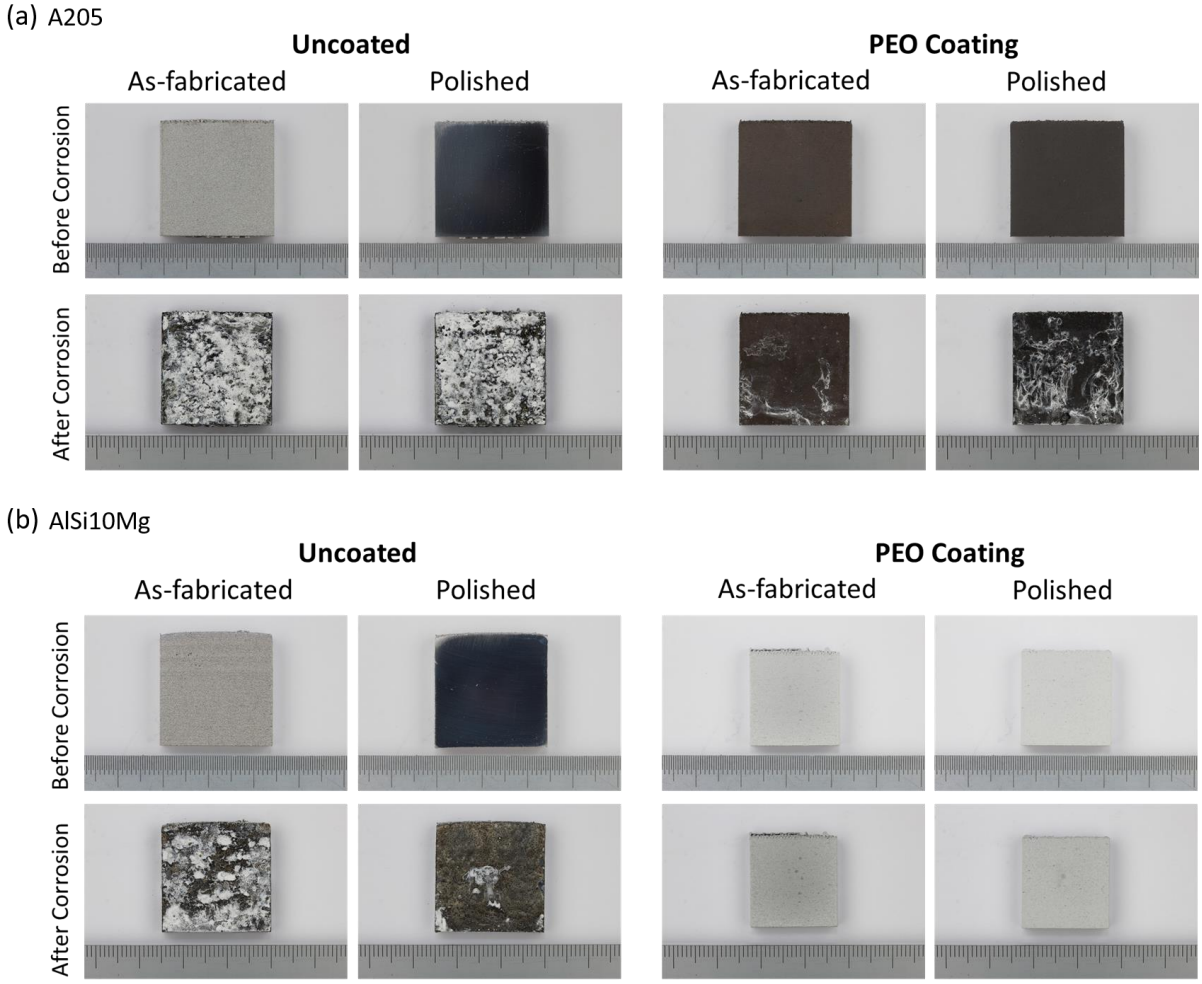


Figure 6.9. Macroscopic corrosion morphology analysis before and after salt fog test for (a) A205 and (b) AlSi10Mg alloys.

For both materials, there is an evident presence of corrosion products. In particular, for the A205, a larger fraction of corrosion product was observed. The increase in degradation of the base material was visible, and the surface was mostly covered by corrosion products. The distribution was fairly uniform for the A205 alloy, while non-uniform for the AlSi10Mg alloy. The macroscopic corrosion morphology and the corrosion rate were assessed after the chemical removal of corrosion products from the samples. In particular, Figure 6.10 shows the corrosion rate calculated according to the ASTM G1-03 standard [32].

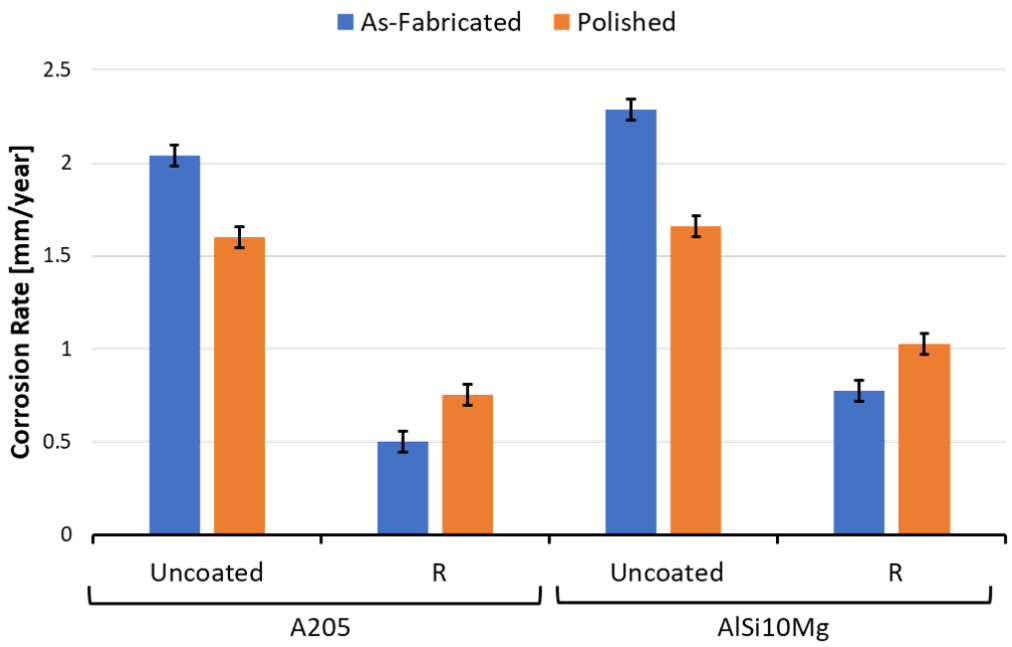


Figure 6.10. Corrosion rate analysis for uncoated and PEO coated A205 and AlSi10Mg subjected to salt fog test for 96 h.

The uncoated as-fabricated condition showed a similar trend. In particular, the A205 corrosion performance was slightly better than the AlSi10Mg. The A205 Al alloy should present enhanced corrosion properties compared to other AM Al alloys, due to its isotropic microstructure characterised by ultrafine grains and the presence of Ti and $TiB_2$ phases [46]. Regarding the PEO-coated conditions, the results highlighted a notable decrease in the corrosion rate for both Al alloys, compared with their uncoated counterpart. The corrosion rate for the PEO-coated samples was decreased by 75.4% and 53.1% for the A205, as-fabricated and polished conditions, respectively, while the corrosion rate was decreased by 66.2% and 37.5% for the AlSi10Mg, as-fabricated and polished condition, respectively. The PEO-coated A205 showed better corrosion behaviour compared to the AlSi10Mg, and a similar trend. In particular, the trend is reversed if compared to the outcomes of the uncoated specimens, with as-fabricated samples having a lower corrosion rate than the polished counterpart. The cause of this phenomenon can be attributed to the initial surface roughness of the substrate prior to the

PEO coating process. The high surface roughness appeared to enhance the formation of phenomena during the PEO process that led to an increase in the bonding strength between substrate and PEO coating, leading to better corrosion performance [47].

The analysis of types of corrosion that occurred during the salt fog test was assessed using digital microscope analysis. Figure 6.11 represents the surface morphology of both A205 and AlSi10Mg alloys, respectively.

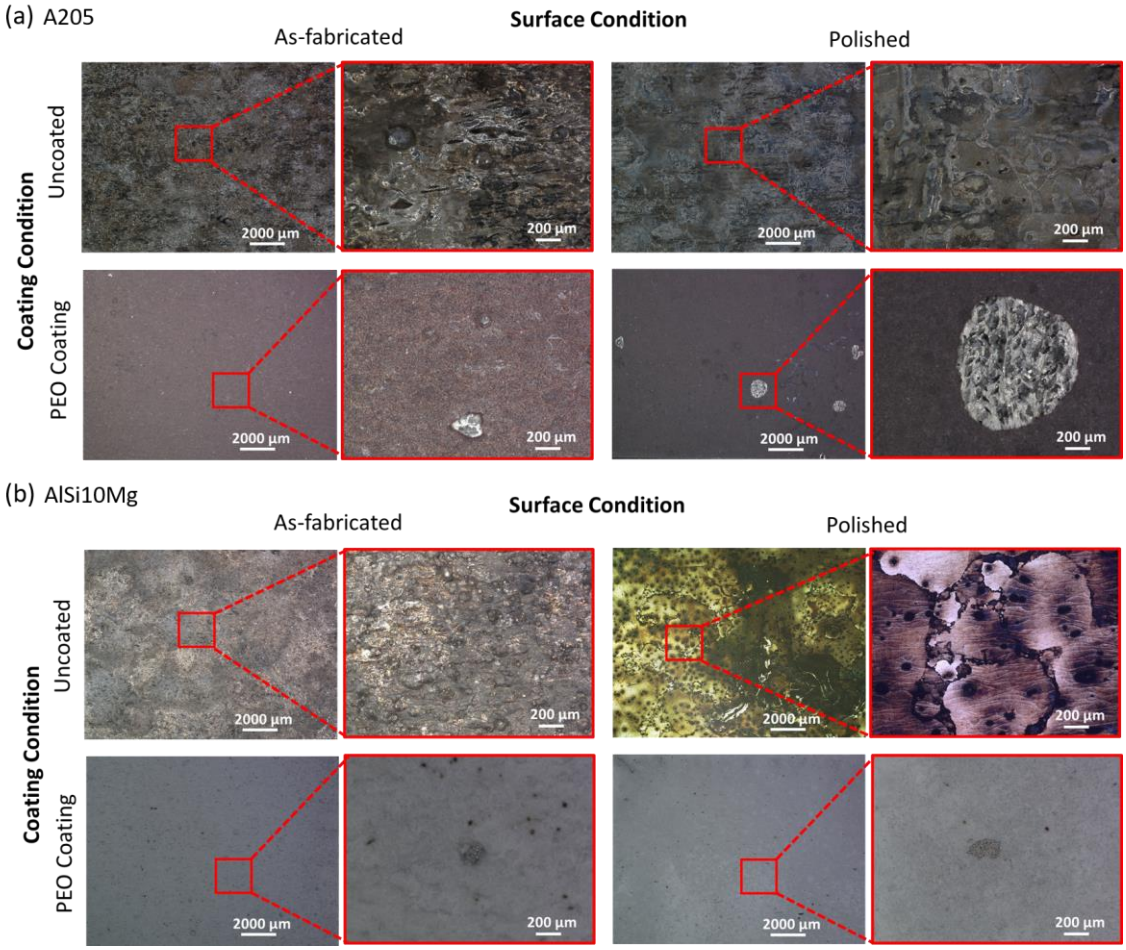


Figure 6.11. Surface morphology of uncoated and PEO-coated material after the salt fog test of 96 h for (a) A205 and (b) AlSi10Mg alloys.

For both materials, the main corrosion mechanism appeared to be pitting, at different stages of development. The corrosion of AlSi10Mg is highly related to the AM microstructure. In particular, the microstructure is characterised by a Si network, and the initiation of the corrosion is demonstrated to occur at the meltpool boundaries where there is a difference in potential

between the Al and Si phases, while the Si network provides a localisation of the corrosion attack [48]. This phenomenon was highlighted in the uncoated polished condition, where an accelerated corrosion process was found, potentially caused by the residual stresses introduced by the L-PBF. The A205 microstructure downstream the L-PBF process, characterised by fine grains and rich in Cu precipitates on the grain boundaries, reduced the corrosion rate of AM material thanks to the dissolution of Cu and Mg in the early stage of corrosion attack and the number of cathodic sites on the surface that could lead to localised corrosion, resulting in a slightly better corrosion performance compared to the AlSi10Mg. Furthermore, the presence of fine, well well-dispersed $TiB_2$ reinforcement particles acted as barriers against the propagation of corrosion, increasing the corrosion performance of the alloy [48].

For both materials, the uncoated as-fabricated condition exhibited higher levels of corrosion pitting compared to the polished configurations due to the higher surface area compared to the uncoated polished conditions. Finally, the results highlighted the great improvement provided by the PEO coating where only a few localised pitting corrosion zones. The analysis of the round spots in the PEO-coated specimens suggested that the saline corrosive moisture penetrated the porous outer of the coating and in some cases reached the substrate material, where the inner coating layer presented either porosity or weak bonding with the substrate.

## 6.4 Conclusions

The oxidised layer was successfully achieved for the two additively manufactured high-strength Al alloys, A205 and AlSi10Mg. The PEO process was carried out with different solutions to achieve remarkable PEO coating layer performance. Furthermore, the influence of the initial surface conditions, as-fabricated and polished, on the PEO coating's overall quality was assessed using different analyses. The main results of the study can be summarised as follows:

- The PEO coating was successfully applied to both materials A205 and AlSi10Mg, as highlighted by the XRD and SEM analyses. The initial surface condition, as-fabricated or polished, did not affect the development of PEO coating but affected the morphology. In particular, during the process, the generation of multiple phenomena such as thermal and plasma reactions led to surface smoothing, with a decrease in the average surface roughness. Both materials showed a similar trend in surface quality, with AM as-received values in the average downstream of the manufacturing process and increased post-PEO surface qualities.
- A reasonable PEO coating layer thickness was identified for both materials for all the different conditions analysed. In particular, the PEO process using the Rich (R) alkaline highlighted high adhesion between the substrate and oxidised layer, with low crack formations and high thickness (over 40 μm). Differences between the two materials were found during the analysis of the porosity of the produced PEO coating. In particular, a porosity of around 13% was assessed for the AlSi10Mg while a porosity of less than 3% was found for all the A205 configurations.
- The mechanical properties in terms of nano-hardness were evaluated for both materials using the best configuration, polished samples and alkaline R. The comparison between the core material and the PEO oxidised layer showed a massive increase in hardness, reaching values in accordance with the formation of Alumina highlighted by XRD. In particular, the A205 presented a higher hardness peak compared to the AlSi10Mg, thanks to the higher presence of $\alpha$-$Al_2O_3$. An hardness and Young's Modulus of 17.9 GPa and 258.8 GPa and 13.8 GPa and 148.2 GPa were found for A205 and AlSi10Mg alloys, respectively.
- The analysis of tribological performance showed a good increase of properties for the AlSi10Mg, compared with the AM uncoated configuration. Regarding the A205, the results

highlighted a considerable increase in the tribological performance, with a very low wear rate of 0.11 $mm^3/m$, for the polished configuration coated using the alkaline R. The initial surface condition strongly affected the performance, leading to a decrease in both CoF and wear rate. The results highlighted a decrease in wear rate of 43.2% and 88.4% for the A205, while 36% and 26.4% for the AlSi10Mg, as-fabricated and polished condition, respectively.

- The PEO coating enhanced the corrosion performance of both materials. In particular, the corrosion rate for the PEO coated samples was decreased by 75.4% and 53.1% for the A205, while 66.2% and 37.5% for the AlSi10Mg, as-fabricated and polished condition, respectively. Based on the analysis, the primary mechanism at play appeared to be the corrosion pitting mechanism for both uncoated and PEO coated Al alloys, with the uncoated samples subjected also to corrosion due to residual stresses typical of AM.
- The study highlighted that an initial surface condition similar to the one achieved downstream of the machining process (polished configuration) seems to increase the overall quality of the oxidised layer of the PEO process.
- Finally, the rich presence of Cu alloying element in the A205 composition increased the affinity with the PEO process, leading to a better PEO oxidised layer compared to the AlSi10Mg where the high percentage of Si undermined the electrical conductivity of the material and therefore the PEO coating process.

## Acknowledgements

*This work is part of the C-AM AOHE project funded by the European Union's Horizon H2020-CS2-CFP08-2018-01 research and innovation program under grant agreement No 831880. This work was also supported in part by the EPSRC Centre for Doctoral Training in Topological Design, funded by the UK Engineering and Physical Sciences Research Council*

*(grant EP/S02297X/1) based at the University of Birmingham. The authors would like to thank Dr Zhenxue Zhang for facilitating and assisting in the nano-hardness analysis at the School of Materials and Metallurgy, University of Birmingham, UK.*

## References

[1] T. Debroy, H.L. Wei, J.S. Zuback, T. Mukherjee, J.W. Elmer, J.O. Milewski, A.M. Beese, A. Wilson-Heid, A. De, W. Zhang, Additive manufacturing of metallic components – Process, structure and properties, Progress in Materials Science, 92 (2018) 112-224.

[2] S. Lathabai, Additive Manufacturing of Aluminium-Based Alloys and Composites, Elsevier, 2018, pp. 47-92.

[3] N.T. Aboulkhair, M. Simonelli, L. Parry, I. Ashcroft, C. Tuck, R. Hague, 3D printing of Aluminium alloys: Additive Manufacturing of Aluminium alloys using selective laser melting, Progress in Materials Science, 106 (2019) 100578.

[4] W.E. King, A.T. Anderson, R.M. Ferencz, N.E. Hodge, C. Kamath, S.A. Khairallah, A.M. Rubenchik, Laser powder bed fusion additive manufacturing of metals; physics, computational, and materials challenges, Applied Physics Reviews, 2 (2015) 041304.

[5] J. Zhang, B. Song, Q. Wei, D. Bourell, Y. Shi, A review of selective laser melting of aluminum alloys: Processing, microstructure, property and developing trends, Journal of Materials Science & Technology, 35 (2019) 270-284.

[6] R.K. Rhein, Q. Shi, S. Arjun Tekalur, J. Wayne Jones, J.W. Carroll, Effect of direct metal laser sintering build parameters on defects and ultrasonic fatigue performance of additively manufactured AlSi10Mg, Fatigue & Fracture of Engineering Materials & Structures, 44 (2021) 295-305.

[7] H. Wu, Y. Ren, J. Ren, L. Liang, R. Li, Q. Fang, A. Cai, Q. Shan, Y. Tian, I. Baker, Selective laser melted AlSi10Mg alloy under melting mode transition: Microstructure evolution, nanomechanical behaviors and tensile properties, Journal of Alloys and Compounds, 873 (2021) 159823.

[8] I.M. Kusoglu, B. Gökce, S. Barcikowski, Research trends in laser powder bed fusion of Al alloys within the last decade, Additive Manufacturing, 36 (2020) 101489.

[9] S.I. Shakil, A. Hadadzadeh, B. Shalchi Amirkhiz, H. Pirgazi, M. Mohammadi, M. Haghshenas, Additive manufactured versus cast AlSi10Mg alloy: Microstructure and micromechanics, Results in Materials, 10 (2021) 100178.

[10] Q. Yan, B. Song, Y. Shi, Comparative study of performance comparison of AlSi10Mg alloy prepared by selective laser melting and casting, Journal of Materials Science & Technology, 41 (2020) 199-208.

[11] H.R. Kotadia, G. Gibbons, A. Das, P.D. Howes, A review of Laser Powder Bed Fusion Additive Manufacturing of aluminium alloys: Microstructure and properties, Additive Manufacturing, 46 (2021) 102155.

[12] L. Xi, D. Gu, S. Guo, R. Wang, K. Ding, K.G. Prashanth, Grain refinement in laser manufactured Al-based composites with TiB2 ceramic, Journal of Materials Research and Technology, 9 (2020) 2611-2622.

[13] R. Revilla, D. Verkens, T. Rubben, I. De Graeve, Corrosion and Corrosion Protection of Additively Manufactured Aluminium Alloys—A Critical Review, Materials, 13 (2020) 4804.

[14] C. Berlanga-Labari, M.V. Biezma-Moraleda, P.J. Rivero, Corrosion of Cast Aluminum Alloys: A Review, Metals, 10 (2020) 1384.

[15] E. Matykina, R. Arrabal, M. Mohedano, B. Mingo, J. Gonzalez, A. Pardo, M.C. Merino, Recent advances in energy efficient PEO processing of aluminium alloys, Transactions of Nonferrous Metals Society of China, 27 (2017) 1439-1454.

[16] X. Huang, Plasma Electrolytic Oxidation Coatings on Aluminum Alloys: Microstructures, Properties, and Applications, Modern Concepts in Material Science, 2 (2019).

[17] S. Sela, K. Borodianskiy, Synthesis of ceramic surface on Zr alloy using plasma electrolytic oxidation in molten salt, Surfaces and Interfaces, 36 (2023) 102533.

[18] M.D.M. Tavares, J.D.O. Vitoriano, R.C.L.D. Silva, A.R. Franco, G.B.D. Souza, J.A.P.D. Costa, C. Alves-Junior, Effect of duty cycle and treatment time on electrolytic plasma oxidation of commercially pure Al samples, Journal of Materials Research and Technology, 8 (2019) 2141-2147.

[19] A.M. Pillai, R. Ghosh, A. Dey, K. Prajwal, A. Rajendra, A.K. Sharma, S. Sampath, Crystalline and amorphous PEO based ceramic coatings on AA6061: Nanoindentation and corrosion studies, Ceramics International, 47 (2021) 14707-14716.

[20] A. Fattah-alhosseini, R. Chaharmahali, Impressive strides in amelioration of corrosion behavior of Mg-based alloys through the PEO process combined with surface laser process: A review, Journal of Magnesium and Alloys, 11 (2023) 4390-4406.

[21] A. Fattah-alhosseini, M. Molaei, A review of functionalizing plasma electrolytic oxidation (PEO) coatings on titanium substrates with laser surface treatments, Applied Surface Science Advances, 18 (2023) 100506.

[22] A.B. Rogov, H. Lyu, A. Matthews, A. Yerokhin, AC plasma electrolytic oxidation of additively manufactured and cast AlSi12 alloys, Surface and Coatings Technology, 399 (2020) 126116.

[23] L. Pezzato, M. Dabalà, S. Gross, K. Brunelli, Effect of microstructure and porosity of AlSi10Mg alloy produced by selective laser melting on the corrosion properties of plasma electrolytic oxidation coatings, Surface and Coatings Technology, 404 (2020) 126477.

[24] A. Sobolev, T. Peretz, K. Borodianskiy, Synthesis and growth mechanism of ceramic coatings on an Al-Cu alloy using plasma electrolytic oxidation in molten salt, Journal of Alloys and Compounds, 869 (2021) 159309.

[25] H. Zhang, J. Geng, X. Li, Z. Chen, M. Wang, N. Ma, H. Wang, The micro-arc oxidation (MAO) behaviors of in-situ TiB2/A201 composite, Applied Surface Science, 422 (2017) 359-371.

[26] S.A. Abdel-Gawad, W.M. Osman, A.M. Fekry, Characterization and corrosion behavior of anodized Aluminum alloys for military industries applications in artificial seawater, Surfaces and Interfaces, 14 (2019) 314-323.

[27] C. Xia, J. Huang, J. Tao, S. Wang, L. Cai, M. Wang, D. Chen, H. Wang, The Preparation and Properties of the Brown Film by Micro-arc Oxidized on In-Situ TiB2/7050Al Matrix Composites, Coatings, 10 (2020) 615.

[28] N. Barati, J. Jiang, E.I. Meletis, Microstructural evolution of ceramic nanocomposites coated on 7075 Al alloy by plasma electrolytic oxidation, Surface and Coatings Technology, 437 (2022) 128345.

[29] A. Sobolev, T. Peretz, K. Borodianskiy, Fabrication and Characterization of Ceramic Coating on Al7075 Alloy by Plasma Electrolytic Oxidation in Molten Salt, Coatings, 10 (2020) 993.

[30] A. G133-22, Standard Test Method for Linearly Reciprocating Ball-on-Flat Sliding Wear, 2022.

[31] A. B117-19, Standard Practice for Operating Salt Spray (Fog) Apparatus, 2019.

[32] A. G1-03(2017)e1, Standard Practice for Preparing, Cleaning, and Evaluating Corrosion Test Specimens, 2017.

[33] T.W. Clyne, S.C. Troughton, A review of recent work on discharge characteristics during plasma electrolytic oxidation of various metals, International Materials Reviews, 64 (2019) 127-162.

[34] F. Xi, Y. Huang, Y. Zhao, Y. Liu, W. Dai, Y. Tian, Effects of Substrate Roughness on Microstructure and Fatigue Behavior of Plasma Electrolytic Oxidation-Coated Ti-6Al-4V Alloy, Materials (Basel), 15 (2022).

[35] V. Dehnavi, Surface modification of aluminum alloys by plasma electrolytic oxidation, (2014).

[36] L. Agureev, S. Savushkina, A. Ashmarin, A. Borisov, A. Apelfeld, K. Anikin, N. Tkachenko, M. Gerasimov, A. Shcherbakov, V. Ignatenko, N. Bogdashkina, Study of Plasma Electrolytic Oxidation Coatings on Aluminum Composites, Metals, 8 (2018) 459.

[37] V. Dehnavi, X.Y. Liu, B.L. Luan, D.W. Shoesmith, S. Rohani, Phase transformation in plasma electrolytic oxidation coatings on 6061 aluminum alloy, Surface and Coatings Technology, 251 (2014) 106-114.

[38] J. Curran, T. Clyne, Porosity in plasma electrolytic oxide coatings, Acta Materialia, 54 (2006) 1985-1993.

[39] D. Li, K. Gao, J. Liu, J. Huang, D. Zhao, Y. Gong, M. Wang, Z. Chen, H. Wang, Achieving Superior Corrosion Resistance of TiB2 Reinforced Al-Zn-Mg-Cu Composites via Optimizing Particle Distribution and Anodic Oxidation Time, Coatings, 13 (2023) 1780.

[40] D. Zeng, Z. Liu, S. Bai, J. Wang, Influence of Sealing Treatment on the Corrosion Resistance of PEO Coated Al-Zn-Mg-Cu Alloy in Various Environments, Coatings, 9 (2019) 867.

[41] N. Rösemann, T. Fiedler, H.-R. Sinning, M. Bäker, Determining Young's modulus of coatings in vibrating reed experiments using irregularly shaped specimens, Results in Materials, 2 (2019) 100022.

[42] N. Read, W. Wang, K. Essa, M.M. Attallah, Selective laser melting of AlSi10Mg alloy: Process optimisation and mechanical properties development, Materials & Design (1980-2015), 65 (2015) 417-424.

[43] M. Avateffazeli, S.I. Shakil, M.F. Khan, H. Pirgazi, N. Shamsaei, M. Haghshenas, The effect of heat treatment on fatigue response of laser powder bed fused Al-Cu-Mg-Ag-TiB2 (A20X) alloy, Materials Today Communications, 35 (2023) 106009.

[44] R.H.U. Khan, A. Yerokhin, X. Li, H. Dong, A. Matthews, Surface characterisation of DC plasma electrolytic oxidation treated 6082 aluminium alloy: Effect of current density and electrolyte concentration, Surface and Coatings Technology, 205 (2010) 1679-1688.

[45] H. Chi, L. Jiang, G. Chen, J. Qiao, X. Lin, G. Wu, The tribological behavior evolution of TiB2/Al composites from running-in stage to steady stage, Wear, 368-369 (2016) 304-313.

[46] M. Rafieazad, P. Fathi, A. Nasiri, M. Haghshenas, M. Mohammadi, Isotropic corrosion performance of the newly developed L-PBF-A205 aluminum alloy, Materials Letters, 291 (2021) 129541.

[47] J. Li, Y. Bian, X. Tu, W. Li, D. Song, Influence of surface roughness of substrate on corrosion behavior of MAO coated ZM5 Mg alloy, Journal of Electroanalytical Chemistry, 910 (2022) 116206.

[48] R.I. Revilla, D. Verkens, T. Rubben, I. De Graeve, Corrosion and Corrosion Protection of Additively Manufactured Aluminium Alloys-A Critical Review, Materials (Basel), 13 (2020).

# CHAPTER 7. Development of a novel ML Framework based on reinforcement Learning for L-PBF of High-Strength Al alloys

This chapter is part of a scientific paper that has been published in the Journal 'Scripta Materialia'. The paper's details and co-authors' contributions are outlined below.

Ahmed M. Faizan Mohamed, **Francesco Careri**, Raja H.U. Khan, Moataz M. Attallah, Leonardo Stella, A novel porosity prediction framework based on reinforcement learning for process parameter optimization in additive manufacturing, Scripta Materialia, Volume 255, 2025, 116377, ISSN 1359-6462, https://doi.org/10.1016/j.scriptamat.2024.116377.

**Ahmed M. Faizan Mohamed:** Data curation, Investigation, Methodology, Validation, Writing – original draft, Writing - review and editing.

**Francesco Careri:** Conceptualisation, Data curation, Investigation, Methodology, Visualisation, Writing – original draft, Writing - review and editing.

**Raja H.U. Khan:** Supervision, Writing – review and editing.

**Moataz M. Attallah:** Conceptualisation, Funding acquisition, Methodology, Resources, Supervision, Writing – review and editing.

**Leonardo Stella:** Conceptualisation, Funding acquisition, Methodology, Resources, Supervision, Writing – review and editing.

The published paper was slightly modified from the published version to increase formatting and visualisation.

# Graphical Abstract

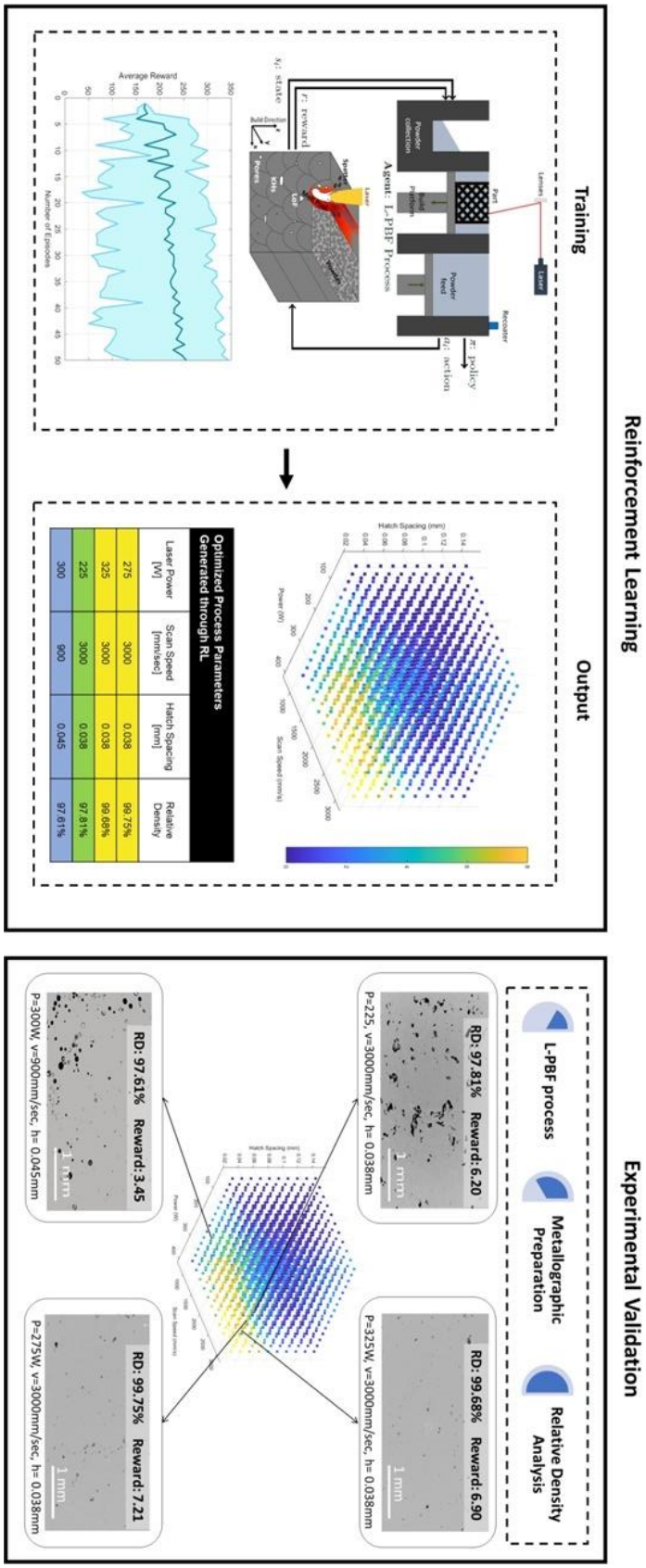

## Abstract

Machine learning (ML) has generated great interest in additive manufacturing (AM) thanks to its ability to predict complex patterns and behaviours through data. Examples include design optimisation, process control, and cost minimisation. In this paper, we develop a novel framework based on reinforcement learning (RL) for porosity prediction in metal laser-powder bed fusion (L-PBF). The novelty of this approach is twofold: it is the first approach that integrates RL in L-PBF for porosity prediction where the state space consists of permutations of three parameters (laser power, scan speed, and hatch spacing) for optimal parameter combinations; furthermore, through an appropriately formulated reward function, we embed physics-informed principles based on the Eagar-Tsai thermal model for training. The proposed framework has been experimentally validated on L-PBF high-strength A205 Al alloy. The experimental results demonstrated high fidelity with the predicted optimal parameters, despite few outliers, demonstrating the potential of this approach.


## 7.1 Introduction

In recent years, metal additive manufacturing (AM) has received great attention for its applications in several industrial sectors, including aerospace, biomedical and automotive [1]. Indeed, metal AM offers a range of benefits, from reducing the required material and prototyping costs to producing parts with intricate geometries or custom-designed products [2]. However, a critical issue in the wider adoption of metal AM is repeatability, which is due to the complex physics in the process, the different AM systems, and the choice of metal powders/alloys.

In general, AM technologies are characterised by a wide range of process parameters that can affect the quality of the manufactured components [3]. Traditionally, the process parameters

are experimentally optimised, which is costly. Therefore, leveraging on approaches such as machine learning (ML) and statistical methods is essential to reduce waste and resources [4]. Popular supervised learning methods, including linear regression and random forests [5, 6], have achieved a level of success in several applications. In the literature, we find more studies that use a range of methods to optimise the process parameters based on ML techniques [7-9]. A limitation associated with these methodologies is the reliance on large amounts of data for training, imposing significant costs in terms of time and resources. On the other hand, reinforcement learning (RL) is an ML paradigm where an agent learns through trial and error by interacting with an environment. The environment maps rewards to state-action pairs [10], and the agent learns by balancing short-term and long-term rewards. The strength of this approach lies in its independence from preliminary datasets. Despite its benefits, a major issue in RL is to define the problem in a precise manner such that the corresponding model is able to capture the complexity of the task. To the best of our knowledge, only the work by Dharmadhikari et al. [11] has attempted to leverage RL in AM. The authors propose an RL algorithm that optimises two process parameters for a steady-state melt pool depth in a Laser-Direct Energy Deposition system without depending on experimental data. Despite being the first of its kind, this work presents RL as a viable alternative for the AM process parameter optimisation problem.

Contribution. The contribution of this work are twofold. First, we develop a novel RL framework for process parameter optimisation for porosity detection. In particular, we focus on laser-powder bed fusion (L-PBF) as the AM technique. To address the control of process parameters on the formation of metallurgical defects, our work provides a systematic approach to determine the best parameter configuration in L-PBF. We consider relative density (RD) as the chosen quality measure, using the following parameters: laser power P, scan speed v, and

hatch spacing h. The relative density is the actual density of the part compared to the theoretical density, representing how dense the part is. Porosity is a primary cause of reduction in relative density and affects the mechanical properties and structural integrity of the part. Second, we thoroughly validate our framework, which optimises the relative density of an Aluminium (Al) alloy, the A205 alloy, known also as A20X$^{TM}$, by learning the optimal parameter configuration in the RL model. The RL agent receives a reward from the environment, which is a physics-informed analytical model that predicts the porosity for a given parameter configuration. This approach is depicted in Figure 7.1.

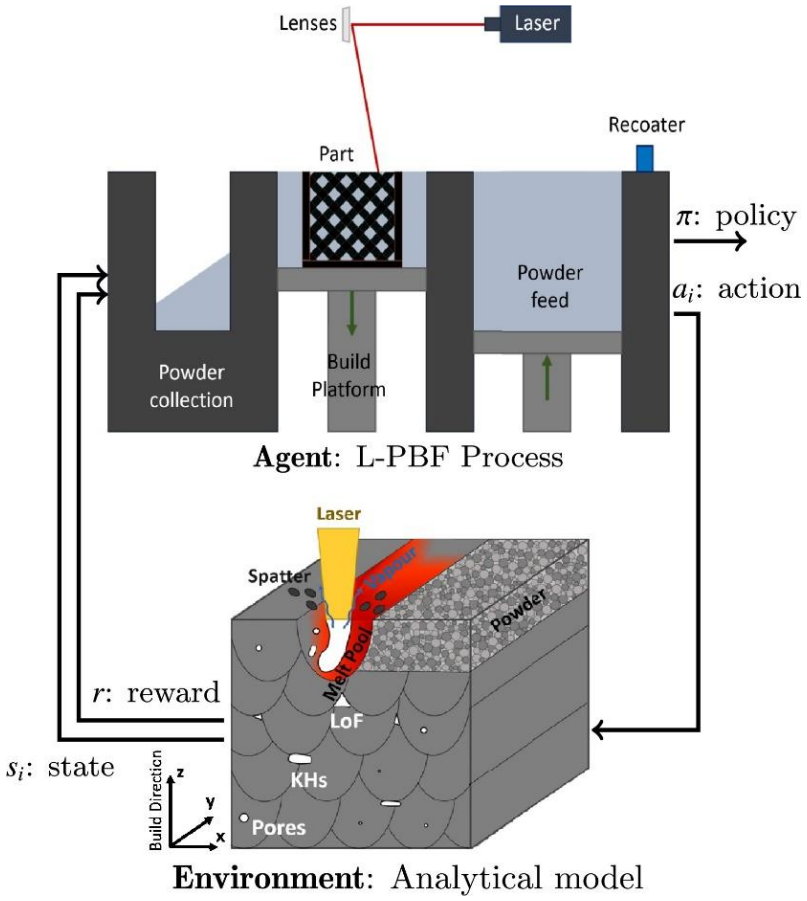


Figure 7.1. Agent-environment interaction of the traditional RL framework adapted for L-PBF optimisation. The environment is a physics-informed analytical model based on the Eagar-Tsai thermal model. The L-PBF process acts as the agent. Each state $s_i$ corresponds to a set of three values, one for each parameter. Each action ai represents the change in the parameters from one state to another. Each action is rewarded or penalised to a value that depends on the predicted relative density (RD). The policy $\pi$ retrieved is a path from states where the RD is lower to states where RD is higher.

## 7.2 Methodology

The RL environment consists of two main parts. First, a porosity model is used to estimate if a particular parameter configuration would yield defective or fully-dense parts. This porosity prediction model then serves as a guide for rewarding the state/action configurations explored by the agent. This allows the RL model to find the best set of parameters in the parameter space. The porosity model used in the study was proposed by Liu et al. [12]. The authors investigated the factors responsible for different types of porosity and introduced two dimensionless variables that were used to define the boundaries that contain the optimal processing window. In particular, the Eagar-Tsai thermal model was used to find the width of the melt pool at a specific location:

$$T(x,y,z,\theta) - T_0 \qquad \text{Equation 7.1}$$

$$= \frac{\alpha P}{\pi \rho c_p \sqrt{4\pi a}} \int_0^{\theta} \frac{(\theta-\tau)^{-\frac{1}{2}}}{2a(\theta-\tau)+\sigma^2} e^{-\frac{(x-v\tau)^2+y^2}{4a(\theta-\tau)+2\sigma^2} - \frac{z^2}{4a(\theta-\tau)}} d\tau$$

where (x, y, z) are the coordinates of the position in space exposed to a moving Gaussian heat source, and τ is the time integrated from 0 to θ. The remaining variables $c_p$, ρ, σ, a, α are the specific heat, density, laser spot deviation, thermal diffusivity, and absorptivity, respectively [11]. Based on the above equation, two dimensionless variables $\pi_1$ and $\pi_2$ can be calculated as follows:

$$\pi_1 = \frac{\pi\, dw}{2hp} \qquad \text{Equation 7.2}$$

$$\pi_2 = \frac{\gamma\, d}{v_x \mu \sigma} \qquad \text{Equation 7.3}$$

where w, d, p, γ, $v_x$, μ are the melt pool width, melt pool depth, powder thickness, surface tension, horizontal backflow velocity, and dynamic viscosity, respectively [12]. Equation 7.2 and Equation 7.3 are used to gauge the likelihood of occurrence of two types of porosity - lack

of fusion pores (LoFs) and keyhole pores (KPs), respectively. The boundaries of both dimensionless variables and the correlation with the type of porosity were then set according to [12]. In particular, for values of $\pi_1$ greater than 4 LoFs were minimised; and for values below 2, the frequency and severity of LoFs increased. The minimisation of KPs occurs for values of $\pi_2$ less than 800; the presence of KPs increased with an increase in $\pi_2$ values. The boundaries of $\pi_1$ and $\pi_2$ were used in the RL framework to generate the reward function employed to find the optimal parameter configurations.

The model used in the study was a tabular RL approach called Q-learning, where the agent is rewarded for exploring the environment by taking different actions in a given state. This approach is described by a Markov decision process (MDP) [13], which consists of a tuple [*L, A, P, R]*. *L* denotes the state space containing all possible parameter configurations. In our study, each state corresponds to a P-v-h value. *A* corresponds to the action set, consisting of all possible actions that can be taken by the agent. These actions are a combination of increasing, decreasing, or keeping each process parameter value constant. Keeping all three values constant is not permitted as it would not guide the agent towards exploring new states, hence the size of *A* is 26. *P*(s'|s,a) is the probability of the agent moving from state s to state s' through action a in a given timestep. *R* is the reward functions that maps rewards to state-action pairs. These rewards are stored in the form of Q-values within a tabular dataset called Q-table, which is used by the agent to determine the best policy, namely, choosing the best action in a given state. The equation used to update the Q-value of a state-action pair at timestep t is:

$$Q^{new}(s_t, a_t) \leftarrow Q(s_t, a_t) + \alpha_q \left[ r_t + \gamma_q \left( \max_a Q(s_{t+1,a}) \right) - Q(s_t, a_t) \right] \quad \text{Equation 7.4}$$

with $\alpha_q$ is the learning rate, $r_t$ is the reward obtained, $\gamma_q$ is the discount factor, and $\max_a Q(s_{t+1,\,a})$ is the maximum Q-value associated with the new state. The equation balances the reward

through a weighted sum of the old and future Q-values. A discount factor is also introduced to determine the importance given to the maximum Q-value in the new state, expressed as a short-term reward. In our framework, the agent explores the parameter space starting at an arbitrary state, considering each possible action, and choosing a trade-off between exploring and exploiting, i.e., between taking a random action and the best action. After taking an action, the agent receives a reward from the analytical model (the environment) and moves to the next state. After a fixed number of timesteps in the algorithm, the current episode terminates and a new episode begins. Over the episodes, the agent progressively learns the optimal policy, which corresponds to a trajectory in areas of the state-space that yield higher rewards, with the goal of reaching the state that is associated with the lowest porosity as determined by the porosity model.

The reward received by the agent for each action is based on a reward function calculated as:

$$R(\widehat{\pi_1}, \widehat{\pi_2}, VED) = \frac{5}{1 + e^{-6\widehat{\pi_1} - 0.8}} + \frac{5}{1 + e^{-12\widehat{\pi_2} - 0.75}} - \frac{2}{1 + e^{17 - 0.1VED}} - 2 - \frac{2}{1 + e^{5 - 0.1VED}} \quad \text{Equation 7.5}$$

where $\widehat{\pi_1}$ and $\widehat{\pi_2}$ are the values of π1 and π2 normalised in the range from 0 to 1, and VED is the volumetric energy density [14]. The first two components of Equation 7.5 provide information about the desirability of the $\pi$ values. The last two components introduce a penalty if the VED exceeds the desirable range. Using these reward values, the agent can iteratively update the Q-table and explore the parameter space while learning the location of the optimal parameters. Upon completion of the run, the output of the model would consist of the parameters generating L-PBF parts with minimal defects.

## 7.3 Results and Discussion

The material used in the study was a pre-alloyed A205 Al alloy powder with an average particle size of 0.40 μm. The properties of the metal powder, as reported in Table 7.1, were applied to the physical model embedded into the RL framework [15-17]. The L-PBF system considered in the study was a Concept Laser M2 Cusing equipped with a continuous infrared laser with a maximum power of 400 W.

Table 7.1. A205 material properties.

| **Material property** | **Value** |
|---|---|
| **Initial temperature (K)** | 292.15 |
| **Thermal Diffusivity ($m^2/s$)** | 0.000046 |
| **Density ($Kg/m^3$)** | 2850 |
| **Specific Heat Capacity (J/Kg·K)** | 900 |
| **Laser Spot Deviation (m)** | 0.0000167 |
| **Thermal Conductivity (W/m·K)** | 234 |
| **Melting Temperature (K)** | 819.45 |
| **Boiling Temperature (K)** | 2786 |
| **Powder bed Thickness (m)** | 0.00003 |
| **Dynamic Viscosity (Pa/s)** | 0.001548 |
| **Surface Tension (N·m)** | 0.871 |
| **Latent heat of Fusion (J/Kg)** | 269000 |

A comprehensive assessment of the model was conducted evaluating the two constituent components, the RL model and the porosity prediction model. In particular, for the RL model, the hyperparameters, $\alpha_q$, $\gamma_q$, and number of timesteps t, were tuned to optimise the model

performance. We tuned the hyperparameters and the resulting values were $\alpha_q = 0.2$, $\gamma_q = 0.5$, and $t = 50$.

The assessment of the convergence of the model was carried out across several numbers of episodes. As illustrated in Figure 7.2, the trend of the average reward is proportional to the number of episodes, wherein increments in the number of episodes are equivalent to the increase in the average reward. The plot highlights the constant learning of the agent during the exploration of the parameter space, and demonstrates a tendency to identify states characterised by high rewards.

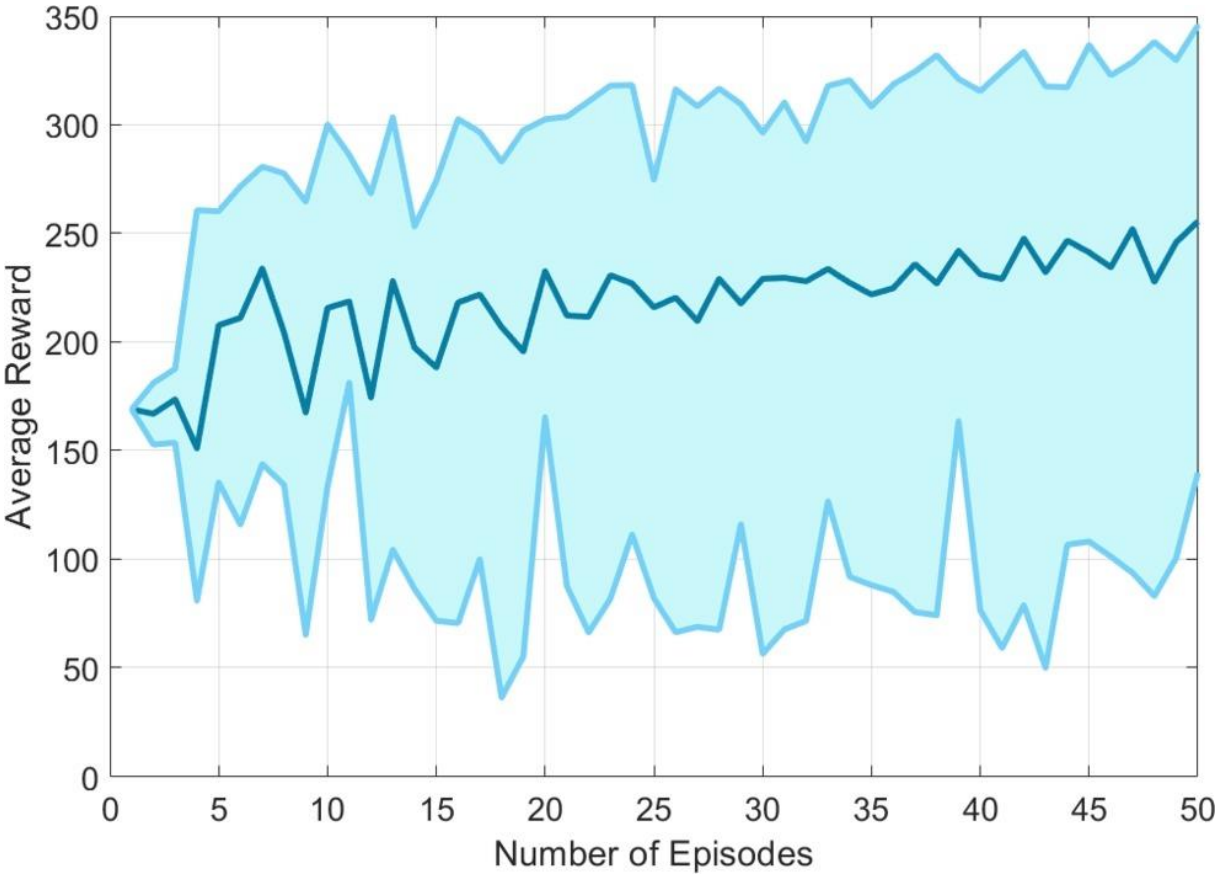


Figure 7.2. Average reward per episode received by the agent (dark blue line) vs standard deviation (light blue area). (For interpretation of the colors in the figure(s), the reader is referred to the web version of this article).

The porosity prediction model was validated through experimental investigation. Cuboid samples with a size of $mm^3$ were fabricated using the L-PBF M2 Cusing system with a fixed

layer thickness of 0.03 mm. The samples were then sectioned using an Electrical Discharge Machining (EDM) and subjected to grinding and polishing. Finally, the RD was analysed using a Scanning Electron Microscope (SEM) Hitachi 3030 and an image processing software, ImageJ. The space explored by the agent consisted of a combination of the three process parameters - laser power, scan speed, and hatch spacing. The details of the parameters are described in Table 7.2.

Table 7.2. Parameter space.

| **Parameter** | **Minimum** | **Maximum** | **Interval** |
|---|---|---|---|
| **Laser Power (W)** | 50 | 400 | 25 |
| **Speed (mm/s)** | 750 | 3000 | 150 |
| **Hatch Spacing (mm)** | 0.0375 | 0.150 | 0.0075 |

A total of 12 different parameter combinations were experimentally tested. The sensitivity of the physics-informed model was evaluated by comparing the ability to generate process parameters associated with low and high RD. This ability was assessed by plotting the Q-value associated with each state of the parameter space and depicted in Figure 7.3a. This figure can be considered as a processing window for the L-PBF manufacturability of the tested A205 alloy. Among the possible parameter combinations, we favored those with higher scan speeds as it aligned with our aim of improving efficiency and would result in faster build rates. Figure 7.3b shows the tested samples in the VED-RD plane.

As shown in Figure 7.3c, the micrographs associated with undesirable values of $\pi_1$ and $\pi_2$ were characterised by high porosity and, therefore, low RD. The process parameters in the ideal range of $\pi_1$ and $\pi_2$ produced as-fabricated material with high levels of RD, higher than 99.5%. During the experimental validation, a few outliers were present among the tested parameters.

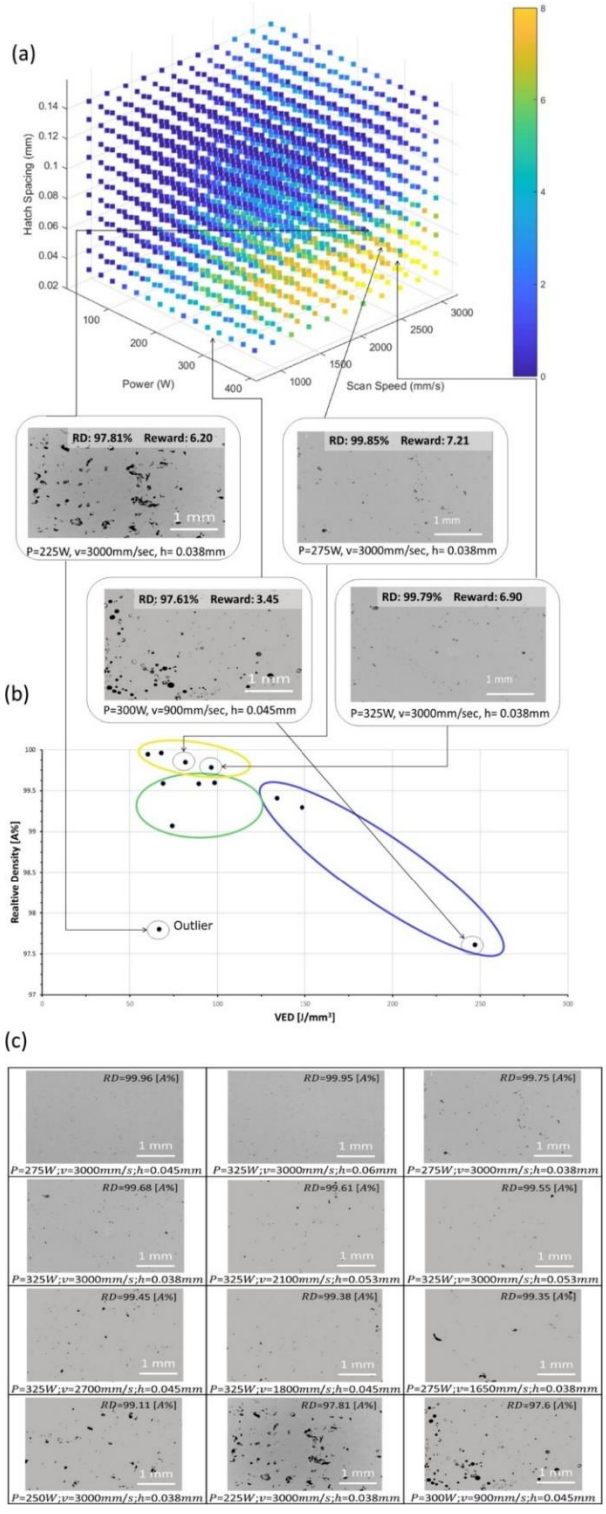


Figure 7.3. Results of the RL model applied to the optimisation of process parameters for the L-PBF manufacturability of A205 Al alloy. (a) Q-value associated with each state of the parameter space, to be considered as processing map, with four micrographs and their corresponding location on the map. (b) A scatterplot of RD against VED, with points grouped according to RD, along with four corresponding micrographs. (c) RD experimentally measured for some combinations of process parameters generated by the RL model and sorted from low to high values of RD.

Certain parameter combinations that were predicted to be in the region of low RD were experimentally tested and found to be near fully-dense. Numerous factors can explain this, including the position of the sample on the substrate or slightly inaccurate $\pi_1$ and $\pi_2$ ranges used in the porosity model. There are also other phenomena occurring during an L-PBF process which may explain these outliers, such as the Marangoni effect, where temperature gradients cause uneven melting. Cooling rate also affects porosity – too fast would lead to cracks whereas too slow may cause shrinkage porosity.

Furthermore, the high scan speed could lead to the triggering of numerous spatters, increasing the chance of the generation of porosity [18]. In future work, we are planning to investigate these aspects to make our approach more generalisable and robust.

## 7.4 Conclusion

To conclude, we have developed a novel RL framework to address the process parameter optimisation of the L-PBF technique for porosity defects minimisation. Our aim is to maximise the relative density by creating a process window for the manufacturability of the A205 Aluminium alloy, which would eliminate the need for an initial experimental investigation. In particular, a modified Eagar-Tsai function embedded within a porosity prediction model has been used to predict the occurrence of LoFs and KPs for several combinations of laser power, scan speed and hatch spacing. The model has been validated using experimental data analysis. The results highlight a conformity in the prediction of optimal process parameters, associated with high RD. Although the presence of few outliers highlights some limitation of the RL, the newly tested approach is able to narrow down the process parameter map of an alloy without the need for large datasets, decreasing time and resource costs.

The limitations of the RL approach and therefore the error in the prediction of the optimal process parameters could be addressed by better calibrating the range of the dimensionless

variables and increasing the accuracy of the data related to the material properties of the powder tested. The RL model itself can be improved using alternate functions such as proximal policy optimisation [19], or the use of multi-agent reinforcement learning in complex dynamical systems [20, 21] which would allow us to scale the complexity of the system under consideration. Furthermore, different physics models can be investigated, and their results compared with our approach. The study highlights our RL framework as a powerful tool for the investigation of the process parameters of an L-PBF system and its potential for solving issues related to AM and material development. Finally, we plan to investigate other properties of the parts produced by using our framework, including residual stress.

## Acknowledgements

*A.M.F.M. and L.S. have been supported by The Institute for Interdisciplinary Data Science and AI (IIDSAI), University of Birmingham, United Kingdom for Prime Pump Funding. F.C., R.H.U.K. and M.M.A. have been supported by the National Structural Integrity Research Centre (NSIRC), a postgraduate engineering facility for industry-led research into structural integrity established and managed by TWI Ltd, based in Cambridge, under the sponsorship of the C-AM AOHE project funded by the European Union's Horizon H2020-CS2-CFP08-2018-01 research and innovation program under grant agreement No 831880. F.C., R.H.U.K. and M.A. have been also supported by the EPSRC Centre for Doctoral Training in Topological Design, funded by the UK Engineering and Physical Sciences Research Council (grant EP/S02297X/1), based at the University of Birmingham.*

# References

[1] A. Vafadar, F. Guzzomi, A. Rassau, K. Hayward, Advances in Metal Additive Manufacturing: A Review of Common Processes, Industrial Applications, and Current Challenges, Applied Sciences, 11 (2021) 1213.

[2] B. Blakey-Milner, P. Gradl, G. Snedden, M. Brooks, J. Pitot, E. Lopez, M. Leary, F. Berto, A. Du Plessis, Metal additive manufacturing in aerospace: A review, Materials & Design, 209 (2021) 110008.

[3] H. Fayazfar, M. Salarian, A. Rogalsky, D. Sarker, P. Russo, V. Paserin, E. Toyserkani, A critical review of powder-based additive manufacturing of ferrous alloys: Process parameters, microstructure and mechanical properties, Materials & Design, 144 (2018) 98-128.

[4] L. Meng, B. McWilliams, W. Jarosinski, H.-Y. Park, Y.-G. Jung, J. Lee, J. Zhang, Machine learning in additive manufacturing: a review, Jom, 72 (2020) 2363-2377.

[5] B. Kappes, S. Moorthy, D. Drake, H. Geerlings, A. Stebner, Machine learning to optimize additive manufacturing parameters for laser powder bed fusion of Inconel 718, Proceedings of the 9th international symposium on superalloy 718 & derivatives: Energy, aerospace, and industrial applications, Springer, 2018, pp. 595-610.

[6] R.U. Rehman, U.K.u. Zaman, S. Aziz, H. Jabbar, A. Shujah, S. Khaleequzzaman, A. Hamza, U. Qamar, D.-W. Jung, Process Parameter Optimization of Additively Manufactured Parts Using Intelligent Manufacturing, Sustainability, 14 (2022) 15475.

[7] C. Lu, J. Shi, Relative density and surface roughness prediction for Inconel 718 by selective laser melting: central composite design and multi-objective optimization, The International Journal of Advanced Manufacturing Technology, (2022) 1-19.

[8] C. Lu, J. Shi, Simultaneous consideration of relative density, energy consumption, and build time for selective laser melting of Inconel 718: A multi-objective optimization study on process parameter selection, Journal of Cleaner Production, 369 (2022) 133284.

[9] D.R.T. Velázquez, A.L. Helleno, H.C. Fals, R.G. dos Santos, Prediction of geometrical characteristics and process parameter optimization of laser deposition AISI 316 steel using fuzzy inference, The International Journal of Advanced Manufacturing Technology, 115 (2021) 1547-1564.

[10] R.S. Sutton, A.G. Barto, Reinforcement learning: An introduction, MIT press, 2018.

[11] S. Dharmadhikari, N. Menon, A. Basak, A reinforcement learning approach for process parameter optimization in additive manufacturing, Additive Manufacturing, 71 (2023) 103556.

[12] B. Liu, G. Fang, L. Lei, X. Yan, Predicting the porosity defects in selective laser melting (SLM) by molten pool geometry, International Journal of Mechanical Sciences, 228 (2022) 107478.

[13] F. Garcia, E. Rachelson, Markov decision processes, Markov Decision Processes in Artificial Intelligence, (2013) 1-38.

[14] M.A. Buhairi, F.M. Foudzi, F.I. Jamhari, A.B. Sulong, N.A.M. Radzuan, N. Muhamad, I.F. Mohamed, A.H. Azman, W.S.W. Harun, M. Al-Furjan, Review on volumetric energy density: influence on morphology and mechanical properties of Ti6Al4V manufactured via laser powder bed fusion, Progress in Additive Manufacturing, 8 (2023) 265-283.

[15] I.F. Bainbridge, J.A. Taylor, The surface tension of pure aluminum and aluminum alloys, Metallurgical and Materials Transactions A, 44 (2013) 3901-3909.

[16] A. Dinsdale, P. Quested, The viscosity of aluminium and its alloys--A review of data and models, Journal of materials science, 39 (2004) 7221-7228.

[17] J. Trapp, A.M. Rubenchik, G. Guss, M.J. Matthews, In situ absorptivity measurements of metallic powders during laser powder-bed fusion additive manufacturing, Applied Materials Today, 9 (2017) 341-349.

[18] C. Qiu, C. Panwisawas, M. Ward, H.C. Basoalto, J.W. Brooks, M.M. Attallah, On the role of melt flow into the surface structure and porosity development during selective laser melting, Acta Materialia, 96 (2015) 72-79.

[19] J. Schulman, F. Wolski, P. Dhariwal, A. Radford, O. Klimov, Proximal policy optimization algorithms, arXiv preprint arXiv:1707.06347, (2017).

[20] T. Zhang, H. Gupta, K. Suprabhat, L. Stella, A multi-agent reinforcement learning approach to promote cooperation in evolutionary games on networks with environmental feedback, 2023 62nd IEEE Conference on Decision and Control (CDC), IEEE, 2023, pp. 2196-2201.

[21] K. Zhang, Z. Yang, T. Başar, Multi-agent reinforcement learning: A selective overview of theories and algorithms, Handbook of reinforcement learning and control, (2021) 321-384.

# CHAPTER 8. Conclusions

This research thesis investigated the development of L-PBF process strategies for the application of high-strength Al alloys in thermal management in the aerospace field. The key aspects of the work integrated material science and AM technologies by integrating advanced methodologies such as Machine Learning (ML). Unlike conventional manufacturing, L-PBF enables the creation of complex geometries with optimised features through topological optimisation, allowing the production of lighter, more efficient Heat Exchanger (HX) components with tailored mechanical and corrosion properties. However, the L-PBF process of high-strength Al alloys for HX production remains immature, with challenges such as reliable parameter optimisation, control of surface quality, and material performance. Therefore, research addressing challenges related to process optimisation, material properties, and performance enhancement is necessary to gain insights into the advancement of L-PBF technologies for aerospace applications. This chapter summarises the key findings of each study and highlights their significance in the field.

Initially, the effectiveness of ML approaches, and in particular Neural Network (NN) models, for the optimisation of L-PBF process parameters for high-strength Al alloys was demonstrated. Two NN models were trained using experimental data to predict the relationships between process parameters and material properties and accuracy. In particular, a reliable framework was generated and was able to identify optimal conditions for defect-free components. The second NN algorithm was generated together with Computer Vision techniques in order to gain precise dimensional control on thin-waled features, demonstrating the potential to reduce the dimensional and geometrical deviation, leading to enhanced manufacturing fidelity. The results of the study showed an improvement in density, reaching values of 99.8% for features characterised by different thicknesses. Furthermore, high dimensional accuracy with a

deviation of less than 1%, and good surface quality were achieved. The findings highlight the role of ML in enhancing the efficiency and quality of additively manufactured components and the reduction of experimental data necessary to find the optimal process windows for L-PBF technology.

Successively, the challenges in material properties were addressed in terms of mechanical, tribological and corrosion performance. These properties are essential in aerospace applications due to the extreme environments and the severe conditions the components operate. Therefore, post-processing treatments are required to meet the requirements necessary for the application of thermal management systems in the aerospace field.

The lack of thermal post-processing treatments for the high-strength A205 Al alloy was addressed. In particular, a novel heat treatment (HT) was developed and validated, demonstrating superior performance compared to standard and commercial HTs, and highlighting the need for customised new HTs for high-strength Al alloys. The newly developed optimised HT, named rapid HT, involved a single solution step at 530°C for 3 hours followed by water quenching. The step of artificial ageing was performed at 170°C for 6 hours, followed by natural cooling in air. The HT significantly improved the mechanical properties of the A205, achieving a yield strength (YS) of 413 MPa and an ultimate tensile strength (UTS) of 465 MPa, while maintaining good elongation and fatigue life. A comparison analysis with the other HTs was carried out and the results revealed the propensity for the novel HT to promote the formation of fine strengthening precipitates with a highly uniform distribution, and a fine equiaxed grain structure, leading to higher fatigue performance and creep resistance. The novel HT also demonstrated a 67% reduction in processing time compared to the standard HT, highlighting its potential for cost and energy savings.

A surface post-processing treatment was then studied to investigate topological surface modification of the high-strength Al alloy surfaces manufactured via L-PBF for high performance in extreme environments. In particular, Plasma Electrolytic Oxidation (PEO) was successfully applied to the A205 and AlSi10Mg alloys. Different surface conditions and electrolyte solutions were evaluated and the results demonstrated that polished surfaces yielded higher-quality coatings with reduced porosity and increased adhesion. The Rich alkaline solution produced superior PEO layers, with a porosity of less than 3% for A205 and around 13% for AlSi10Mg. The coatings were then characterised and the findings revealed significant increases in hardness for both materials, achieving 17.9 GPa for A205 and 13.8 GPa for AlSi10Mg. Wear and corrosion resistance were also enhanced, with corrosion rates reduced by up to 75.4% for A205 and 66.2% for AlSi10Mg in the as-fabricated and polished conditions compared to the uncoated conditions.

Finally, the development of a novel advanced ML framework, Reinforcement Learning (RL) was applied to the L-PBF process for process parameters optimisation to minimise porosity defects and maximise relative density. Using a modified Eagar-Tsai thermal model integrated into an RL-based approach, optimal process parameters were identified with minimal experimental input, significantly reducing time and resource requirements. The results demonstrated the effectiveness of RL in narrowing the process parameter window for the high-strength A205 Al alloy while achieving high relative density. Although limitations such as prediction accuracy and model generalisability were found, the study highlighted the potential for scaling the RL framework using alternative methods, such as proximal policy optimisation and multi-agent RL.

The research carried out has advanced the knowledge and understanding of AM technologies, with a particular focus on L-PBF, for high-strength Al alloys. The findings have contributed to

addressing the current challenges in AM, leading to insights for the development of optimised manufacturing and post-processing strategies for demanding applications such as thermal management systems in aerospace and automotive applications.

## 8.1 Future Work

Despite the findings achieved in this research and the advancement in understanding AM processes, post-processing treatments and the role of ML in the optimisation process for high-strength Al alloys, there are several more possibilities for future exploration that could build upon the studies and results presented in this thesis.

The integration of ML in process optimisation, including NNs and RL, has shown promising results in predicting and improving material properties and manufacturing efficiency. Additional advancements could be pursued in the following areas:

- Expanding ML frameworks to include additional process parameters, such as layer thickness and scan strategies, to capture more complex interactions. This would allow for the optimisation of process parameters for higher production rates, making L-PBF processes competitive with traditional manufacturing strategies.
- Incorporating multi-objective optimisation techniques and high-fidelity physics-based modelling to find solutions for conflicting issues and improve efficiency. The use of advanced ML algorithms incorporating models correlated to the multiple phenomena happening simultaneously during the L-PBF process could increase the efficiency of ML in finding the best optimisation for different requirements of different application fields.
- Developing transfer learning methods to adapt trained ML models for new materials, reducing the need for extensive re-training. The implementation of ML models using a

wide database composed of several materials could lead to a better understanding of relationships between materials, process parameters and manufacturing technology, improving the chances for the development of tools for customised optimisation of novel materials.

The research highlighted the importance of thermal and surface post-processing treatments to improve and tailor the material characteristics and properties. Regarding the study on the development of the novel HT, future work could include:

- Applying the novel HT to industrial A205 alloy, analysing the mechanical, thermal and electrical properties. A study on the evolution of pores and defects after HT could lead to more information useful for gaining insights on HT for additively manufactured materials.
- Applying HIP HTs to reduce the porosity size and distribution, comparing the mechanical performance with the HT developed in an air furnace. It would be beneficial to understand the pros and cons of the newly developed HT applied using a HIP furnace.
- Exploring protocols for further optimisation and standardisation of novel HTs for additively manufactured materials. Further studies on the application and influence of customised HTs for materials manufactured via AM are necessary to re-evaluate the standard thermal treatments currently in use.

Regarding the study on the influence of PEO as surface treatment for high-strength Al alloys produced through L-PBF, future work could include:

- Investigating the effect of the PEO process on materials subjected to different HTs. High-strength Al alloys rarely are used in as-fabricated conditions, and therefore an analysis of the effect of PEO coating and characterisation of oxidised layer in samples

treated using currently available HTs is necessary to evaluate the capabilities of such surface treatment process.

- Investigating the performance of PEO-coated alloys under extreme conditions. Further characterisations such as corrosion at high pressure and high temperature and mechanical tests in a broad range of conditions can provide information regarding the benefits of surface treatment application on high-strength Al alloys produced by AM technologies in long-term applications.
- Investigating the scalability of the PEO process in order to address industrial production challenges. Studies on the effect of PEO in large complex components and characterisation of limits of the technology in achieving uniform stable oxidised layer in internal features are essential to explore the possibility of using the PEO process as technology to improve performance in automotive and aerospace fields.